Title
Exploring the Supermassive Black Hole at the Galactic Center and the Stars in its Environment

Author
Chen, Zhuo

Publication Date
2022

Peer reviewed|Thesis/dissertation

UNIVERSITY OF CALIFORNIA
Los Angeles

Exploring the Supermassive Black Hole at the Galactic Center and the Stars in its Environment

A dissertation submitted in partial satisfaction
of the requirements for the degree
Doctor of Philosophy in Astronomy and Astrophysics

by

Zhuo Chen

2022

ABSTRACT OF THE DISSERTATION

Exploring the Supermassive
Black Hole at the Galactic Center
and the Stars in its Environment

by

Zhuo Chen
Doctor of Philosophy in Astronomy and Astrophysics
University of California, Los Angeles, 2022
Professor Andrea M. Ghez, Chair

As the closest galactic nucleus, the Galactic center provides a unique opportunity for learning about the supermassive black hole at the center of the Milky Way, Sgr A*, and its environment. High-angular-resolution observations in the near-infrared further this advantage. This thesis presents an investigation of the long-term near-infrared accretion properties of Sgr A*, and characterizes the star formation history in this extreme environment. This work utilizes the unique data gathered by the UCLA Galactic Center Group over 25 years to answer fundamental questions about the supermassive black hole and the formation of stars around it.

First, we investigate the near-infrared variability of Sgr A* with the longest time baseline yet considered. The recently improved speckle holography technique has led to the capability to detect Sgr A* in the early years of the group's monitoring program. We carry out a new analysis of speckle imaging data (1995 - 2005) obtained from the Keck observatory, enabling new detections of Sgr A* in the near-infrared over a decade that was previously

inaccessible at these wavelengths. We report that the near-infrared brightness of Sgr A* and its variability are consistent over 22 years, which addresses variability timescales that are 10 times longer than earlier published studies. The power spectral density of Sgr A* shows a plateau between ∼80 days and 7 years, further confirming that it is uncorrelated in time beyond the previously-proposed, single power-law break of ∼245 minutes. We also investigate and note that the closest approach of the extended and dusty object G1, experiencing tidal disruption, had no apparent effect on the near-infrared emission from the accretion flow onto Sgr A*.

Second, we report the first star-formation history study of the Milky Way's nuclear star cluster (NSC) which includes observational constraints from a large sample of stellar metallicity measurements from Gemini and VLT. Along with stellar photometry and spectroscopically derived stellar temperatures, a Bayesian inference approach is developed to derive the NSC's star formation history. By including metallicity measurements, the low-temperature red giants that were previously difficult to constraint are now accounted for, and the best fit favors a two-component model. The dominant (∼93% of the mass), metal-rich component has an age of 5^{+3}_{-2} Gyr, which is likely ∼3 Gyr younger than earlier studies with fixed (solar) metallicity; this younger age challenges the co-evolution models of the supermassive black hole, the NSC and the bulge. The minor component (∼7%) is metal-poor and its age is uncertain though likely less than that of the dominant component. We present updated estimates of the number of compact objects at the Galactic center and their rates of mergers in order to inform interpretations of gravitational-wave detections. Of particular note, when metallicity measurements are included, the predictions result in 2 - 4 times fewer neutron stars compared to earlier predictions that assume solar metallicity, introducing a possible new path to understand the so-called "missing pulsar problem" at the Galactic center.

The dissertation of Zhuo Chen is approved.

Smadar Naoz

Mark R. Morris

Tuan Do

Andrea M. Ghez, Committee Chair

University of California, Los Angeles

2022

To my family

TABLE OF CONTENTS

1 Introduction **1**

1.1 Technology-driven discoveries 1

1.2 Near-infrared variability of Sgr A* 4

1.3 Star formation history of the nuclear star cluster 6

2 Consistency of the Infrared Variability of SGR A* over 22 yr **10**

3 The Star Formation History of the Milky Way's Nuclear Star Cluster . **30**

4 Conclusions **82**

LIST OF FIGURES

1.1 Image of the central region of the Milky Way galaxy. The Galactic center hosts a supermassive black hole (SMBH), Sgr A*, embedded in a dense and massive nuclear star cluster (NSC) at the center. The Galactic center is the only resolved nucleus in the local universe to study the composition and dynamics of the extreme environment close to a SMBH. The NSC is an old star cluster that dominates the inner $\sim$ 5 pc of the Milky Way galaxy (**left**). The central region within 1 pc is extremely dense with a density of $\sim 10^6\ M_\odot/pc^3$ (**middle**). The Galactic center is the only place where we can study in detail the accretion properties of SMBHs, and the possible interactions of the central SMBH with objects experiencing tidal disruption like G1 and G2 (**right**). 2

1.2 Comparison of the different high angular resolution techniques used to image the Galactic center. The early data has been analyzed with the shift-and-add (**left**) and speckle holography (**middle**). AO data taken at a similar time is shown in (**right**). The position of Sgr A* is marked in each panel. 3

1.3 H-R diagram with MIST isochrones (Choi et al., 2016) for ages 3 Gyr ('dashed') and 10 Gyr ('solid') with colors showing the different metallicities of [M/H] = +0.5 (orange), [M/H] = 0 (blue). Age and metallicity are degenerate parameters in star formation history. Generally, the stellar population with lower effective temperature (T_{eff}) and fainter brightness (Ks magnitude) can be interpreted as either old or high metallicity. 8

ACKNOWLEDGMENTS

I sincerely appreciate all the great help and support I have ever received at UCLA during my PhD life. First and foremost I would like to thank my advisors Andrea Ghez and Tuan Do for inspiring me and supporting me all the time. You spent an enormous amount of time leading me from an undergrad to finally a doctor, and a better scientist. I can still remember the moment when I joined the group in my junior year though the research program and how much I have learnt during that summer. You are the ones who really introduced me to the field of astronomy. You are always extremely supportive in both research and the plans to future career paths. I am immensely grateful for working with you during past 6 years.

I would like to thank my thesis committee, Mark Morris and Smadar Naoz, who always made great efforts to help me in research and career planning. Thank Shoko Sakai, Matt Hosek, Gunther Witzel for patiently helping me with any detailed questions I had in the research. Thank all of my group members, current or former, at the Galactic Center Group, Eric Becklin, Jessica Lu, Rainer Schödel, Kelly Kosmo O'Neil, Devin Chu, Abhimat Gautam, Breann Sitarski, Greg Martine, Anna Ciurlo, Rory Bentley, Arezu Dehghanfar, Laly Gallego-Cano, Siyao Jia, Aurelien Hees, Wendy Ravenhill, Juleen Moon. Thank Anja Feldmeier-Krause for great help with the dataset analysis. Thank Stephanie Krilov for the assistance during the hard time. I want to thank my girls, Kelly, Bao-Minh, Sanaea and Veronica, who are always willing to share my delight and listen to my frustrations. And I would like to thank the entire Astronomy graduate fellow students at UCLA for the great help and the supportive atmosphere during my time here. I appreciate the professors of the Division of Astronomy and Astrophysics for their assistance and help all the time.

I would like to thank my parents, Guanjun Chen and Lihua Pan, who have always supported my decisions and trusted whatever I wanted to pursue. I am extremely grateful to my love Yizhang Wu for your support, care and love whenever I need. I cannot finish this wonderful journey without you.

I acknowledge that results presented in this thesis are based on published works with additional coauthors.

Chapter 2 of this dissertation is a reprint of Chen et al. (2019). We are grateful for the helpful and constructive comments from the referee. The primary support for this work was provided by NSF, through grant AST-1412615, and UCLA, through faculty salaries. Additional support was received from the Heising- Simons Foundation, the Levine-Leichtman Family Foundation, the Preston Family Graduate Fellowship (held by B.N.S and A.G.), UCLA Galactic Center Star Society, UCLA Cross– disciplinary Scholars in Science and Technology (CSST) Fellowship, NSF Research Experiences for Undergraduates (REU) grant No. PHY-1460055, and the European Union's Seventh Framework Programme (FP7/2007-2013)/ERC grant agreement No. [614922] (R.S.). This research was based on data products from the Galactic Center Orbit Initiative (GCOI), which is hosted at UCLA and which is a key science program of the Galactic Center Collaboration (GCC). These data products were derived from data originally obtained from W. M. Keck Observatory. The W. M. Keck Observatory is operated as a scientific partnership among the California Institute of Technology, the University of California, and the National Aeronautics and Space Administration. The authors wish to recognize that the summit of Maunakea has always held a very significant cultural role for the indigenous Hawaiian community. We are most fortunate to have the opportunity to observe from this mountain. The Observatory was made possible by the generous financial support of the W. M. Keck Foundation.

Chapter 3 of this dissertation is a version of Chen et al., (submitted). We would like to thank Smadar Naoz, Kelly Kosmo O'Neil, Bao-Minh Hoang, and other members of the UCLA Galactic Center group for providing helpful comments and discussions. The primary support for this work was provided by NSF AAG grant NSF AAG AST-1909554. Additional support was received from the UCLA Galactic Center Star Society. This research uses the Galactic Center Orbit Initiative (GCOI) catalogue based on the data obtained from W. M. Keck Observatory.

VITA

2016	Graduated Nanjing University Bachelor of Arts, Astronomy and Space Science
2016–2022	Teaching Assistant Stars & Nebulae, Nature of Universe, Life in Universe University of California, Los Angeles
2016–2022	Graduate Student Researcher University of California, Los Angeles
2016–2020	Astronomy Live! Educational Outreach University of California, Los Angeles
2018	Master of Science, Astronomy University of California, Los Angeles
2020–2022	PhD Candidate Astronomy and Astrophysics University of California, Los Angeles

PUBLICATIONS

Chen Z., Gallego-Cano E., Do T., Witzel G., Ghez A., Schödel R., Sitarski B. N., Becklin E. E., Lu J. R., Morris M. R., Dehghanfar A., Gautam A. K., Hees A., Hosek M. Jr., Jia S., Mangian A. C., Matthews K. "Consistency of the Infrared Variability of SGR A* over 22 yr", 2019, ApJ, 882, 28

Bentley R. O., Do T., Kerzendorf W. E., Chu, D. S., **Chen Z.**, Konopacky Q., Ghez A. "Measuring the α-abundance of subsolar-metallicity stars in the Milky Way's central half-parsec: testing globular cluster and dwarf galaxy infall scenarios", 2022, ApJ, 925, 77

Do T., Witzel G., Gautam A. K., **Chen Z.**, Ghez A., Morris M. R., Becklin E. E., Ciurlo A., Hosek M. Jr., Martinez G., Matthews K., Sakai S., Schödel R. "Unprecedented Near-infrared Brightness and Variability of Sgr A*", 2019, ApJ, 882, 27

Do T., Hees A., Ghez A., Martinez G., Chu, D. S., Jia S., Sakai S., Lu J. R., Gautam A. K., Kosmo O'Niel K., Becklin E. E., Morris M. R., Matthews K., Nishiyama S., Campbell R., Chappell S., **Chen Z.**, Ciurlo A., Dehghanfar A., Gallego-Cano E., Kerzendorf W., Lyke J., Naoz S., Saida H., Schödel R., Takahashi M., Takamori Y., Witzel G., Wizinowich P. "Relativistic redshift of the star S0-2 orbiting the Galactic center supermassive black hole", 2019, Science, 365, 6454

Do T., Ghez A., Lu J. R., Morris M. R., Hosek M. Jr., Hees A., Naoz S., Ciurlo A., Armitage P., Beaton R. L., Becklin E. E., Bellini A., Bentley R. O., Chakrabarti S., **Chen Z.**, Chu, D. S., Dehghanfar A., Gammie C., Gautam A. K., Genzel R., Greene J., Hora J., Kerzendorf W. E., Libralato M., Nishiyama S., Kosmo O'Niel K., Ozel F., Perets H., Psaltis D., Quataert E., Ramirez-Ruiz E., Rich R. M., Rasio F., Sakai S., Smith H., Weinberg N. N., Witzel G. "Envisioning the next decade of Galactic Center science: a laboratory for the study of the physics and astrophysics of supermassive black holes" , 2019, Astro2020: Decadal Survey on Astronomy and Astrophysics, science white papers, no. 530

CHAPTER 1

Introduction

The center of the Milky Way presents a unique laboratory for learning about the extreme environment of the center of galaxies. The Galactic center, ∼8 kpc (26,000 light years) away from the Earth, hosts a supermassive black hole (SMBH) with 4 million times mass of the Sun (e.g., Schödel et al. 2002; Ghez et al. 2008; Genzel et al. 2010; Boehle et al. 2016; Gillessen et al. 2017; Do et al. 2019), and the most massive and densest star cluster in our galaxy with over 20 million times mass of the Sun in stars (e.g., Launhardt et al. 2002; Schödel et al. 2014). This is the closest galactic nucleus where we can study in detail and learn about phenomena and physical processes in this extreme environment. Many of the discoveries at the Galactic center have been driven by the improvements of our imaging and spectroscopic technology in the near-infrared observations. In this thesis, I will explore two different areas related to the center of our galaxy: What is the nature of the brightness variations that we see from the supermassive black hole? What is the star formation history at the Galactic center?

1.1 Technology-driven discoveries

Recent advances in high angular resolution technology and methodology in the near-infrared (NIR) have revolutionized the understanding of the Galactic center over the last two decades. In the first decade, starting from 1995, the speckle imaging technique with 10m class telescopes allowed the first diffraction-limited images and enabled the discovery of a supermassive black hole (SMBH, Sgr A*) at the center of our Galaxy (Eckart & Genzel 1997; Ghez et

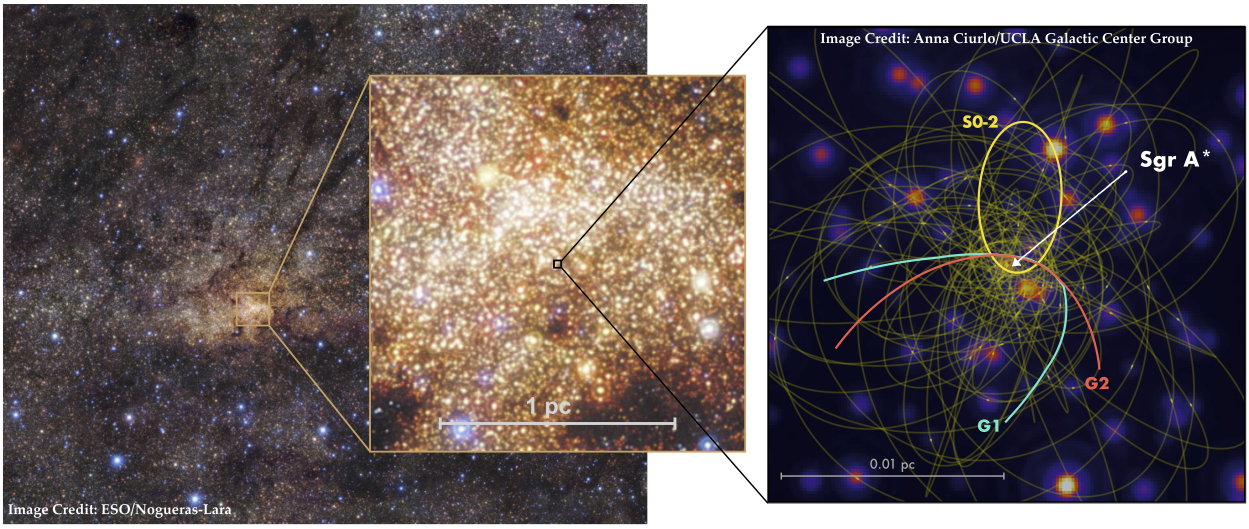

Figure 1.1: Image of the central region of the Milky Way galaxy. The Galactic center hosts a supermassive black hole (SMBH), Sgr A*, embedded in a dense and massive nuclear star cluster (NSC) at the center. The Galactic center is the only resolved nucleus in the local universe to study the composition and dynamics of the extreme environment close to a SMBH. The NSC is an old star cluster that dominates the inner $\sim$ 5 pc of the Milky Way galaxy (**left**). The central region within 1 pc is extremely dense with a density of $\sim 10^6\ M_\odot/pc^3$ (**middle**). The Galactic center is the only place where we can study in detail the accretion properties of SMBHs, and the possible interactions of the central SMBH with objects experiencing tidal disruption like G1 and G2 (**right**).

al. 1998, 2000, 2005a; Schödel et al. 2002). The speckle imaging technique utilizes large numbers of short exposures (0.1 s) to freeze the distorting effects of the Earth's atmospheric turbulence. This technique remarkably increases the resolution of ground-based telescopes and enables diffraction-limited images of targets. In the second decade, the advent of laser guide star Adaptive Optics (LGSAO) allowed much deeper observations, and thus enabled the first reported detection of Sgr A* at infrared wavelengths and the recognition of Sgr A* as a highly variable source (e.g., Genzel et al. 2003; Ghez et al. 2005b). The LGSAO technique utilizes an artificial guide star by a laser to measure the atmospheric distortions,

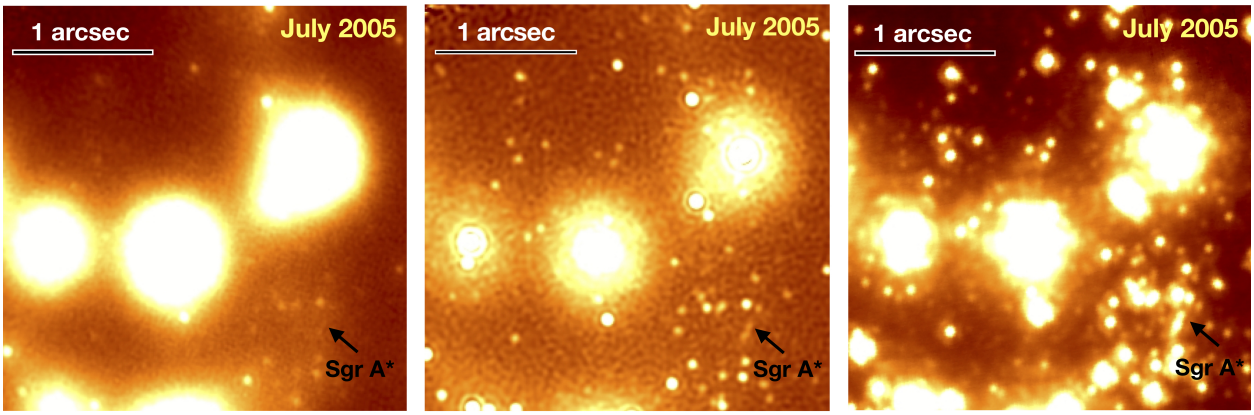

Figure 1.2: Comparison of the different high angular resolution techniques used to image the Galactic center. The early data has been analyzed with the shift-and-add (**left**) and speckle holography (**middle**). AO data taken at a similar time is shown in (**right**). The position of Sgr A* is marked in each panel.

and then compensate for them with a deformable mirror. See Figure 1.1 for the image of the central region of the Milky Way galaxy.

Prior to the epoch when AO systems were coming online, Sgr A* was not directly detected in the initial analysis of speckle images due to poorer sensitivity. Originally, the speckle images were reduced using the shift-and-add technique (SAA; Eckart et al. 1995; Eckart, & Genzel 1996; Ghez et al. 1998, 2000, 2005a; Hornstein et al. 2002; Lu et al. 2005; Rafelski et al. 2007). In this algorithm, the individual frames are shifted and aligned by using the brightest pixel of each frame and then averaged together to give a single output image. The sensitivity of these SAA maps typically had detection limits ($< K_{lim} > = 15.7$ mag; Boehle et al. 2016) comparable to or fainter than the average Sgr A* brightness ($< K_{SgrA*,AO} > = 16.1$ mag; Chen et al. 2019). However, the detection depth of a speckle image is dependent on the post-processing techniques that are used to combine individual frames. Recently, the analysis of the speckle data has been improved with the speckle holography technique (Primot et al. 1990; Schödel et al. 2013; Boehle et al. 2016). This technique performs deconvolution of

the observed, distorted images in the Fourier space with reliable instantaneous point-spread function (PSF) as measured from a set of reference sources. Compared to the SAA technique where only the brightest speckle from each frame contributes to the final diffraction-limited core of the image, the speckle holography technique uses the information from all the speckles. This approach increases the detection depth of the resulting speckle images to $K < 17$ mag, and opens up the possibility of detecting Sgr A* in early years. See Figure 1.2 for the comparison of the different techniques used to image the Galactic center.

The advent of LGSAO also allowed the first spectroscopic observations for faint stars near the supermassive black hole. With the introduction of spectroscopy came a surprising picture of the stellar population at Galactic center: the central SMBH is surrounded by an old NSC (e.g., Launhardt et al. 2002; Schödel et al. 2014) and a compact, young nuclear cluster (YNC, e.g., Ghez et al. 2003; Paumard et al. 2006; Do et al. 2013; Lu et al. 2013). More recently, the integral field spectroscopy with multi-object mode has revealed a remarkably wide range of metallicities and the most metal-rich stars in the Galaxy (e.g., Do et al. 2015; Feldmeier-Krause et al. 2017). The integral field spectroscopy provides spatially resolved spectra over a 2-dimensional field of view using the instruments called integral field units (IFUs). This technique speeds up the traditional observations with 2-dimensional region of the sky simultaneously, which allows large sample of spectroscopic measurements of stars. The AO spectroscopic sample size in the near field of the black hole is now large enough to combine with larger field seeing-limited sample, and comprehensively study the star formation history at the Galactic center with additional information such as metal abundances and stellar temperature.

1.2 Near-infrared variability of Sgr A*

SMBHs have been found to exist at the center of most galaxies. The origin and formation of these black holes, however, still remains an open field of research. The Galactic center

allows us to study in detail the accretion properties of a SMBH and its interaction of stars in this extreme environment at angular resolution orders of magnitude better than for any other galaxies. The accretion flow onto the SMBH at the Galactic center gives rise to its electromagnetic counterpart, Sgr A*, which has been monitored across a wide range of wavelengths at radio, submillimeter, infrared and X-ray (e.g., Balick & Brown 1974; Falcke et al. 1998; Hornstein et al. 2002; Yusef-Zadeh et al. 2006; Bower et al. 2015; Ponti et al. 2017; Gravity Collaboration et al. 2018). These multi-wavelength observations show that the luminosity associated with the black hole is roughly nine orders of magnitude below the Eddington luminosity, and is highly variable (e.g., Melia & Falcke 2001; Baganoff et al. 2003; Mauerhan et al. 2005; Eckart et al. 2008; Dodds-Eden et al. 2009, 2011; Yusef-Zadeh et al. 2012; Do et al. 2019).

The near-infrared (NIR) has proven to be a powerful window to monitor and characterize the variability of Sgr A*, and understand the physical and radiative mechanisms of the accretion processes onto a supermassive black hole (e.g., Witzel et al. 2018). Thanks to the AO technology, Sgr A* IR emission has been detected against the source confusion with nearby stars in this extremely dense region (Genzel et al. 2003; Ghez et al. 2004). The short-term variability of Sgr A* in the NIR regime has been well characterized as a red-noise power spectrum that is correlated in time (Press, 1978). A power-law power spectral density can well describe the variability over timescales from minutes to hours (e.g., Do et al. 2009; Dodds-Eden et al. 2011; Hora et al. 2014; Witzel et al. 2018). The latter timescale is corresponding to the single power-law break beyond which the variations show uncorrelated in time. The longest NIR timescale that has been measured thus far is 1.9 years (Meyer et al., 2009). The underlying physical processes that drive the variable accretion in low-luminosity black holes have not been conclusively understood. Now with the improved speckle holography technique, we are able to reexamine the speckle imaging data from 1995 to 2005 as obtained from Keck telescope. The deeper speckle images and the better knowledge of the position of Sgr A* as predicted from nearby stellar orbits will allow us to detect Sgr A*

in early years and to probe the long-term accretion behavior of the low-luminosity SMBH.

Furthermore, the speckle era (1995 - 2005) extends the time baseline for searching possible interactions with objects experiencing tidal disruption. One interesting object is the extended, dusty source G1 which went through the periapse in 2001 (e.g., Sitarski et al. 2014; Witzel et al. 2017). This object has similar observational properties to G2, which is the first example of a spatially resolved object tidally interacting with Sgr A*. See Figure 1.1. G2 was expected to increase the accretion flow onto Sgr A* during or a few years after the closest approach in early 2014 (e.g., Gillessen et al. 2012), however, no indication of such impact has so far been observed (e.g., Hora et al. 2014; Witzel et al. 2014, 2017, 2018; Pfuhl et al. 2015; Valencia-S. et al. 2015). The hypotheses for the nature of G1 are similar to those proposed to explain G2 (Pfuhl et al., 2015). By reexamining the speckle images which covered the time baseline of G1's periapse, we will be able to monitor and study whether G1 had impacted the the accretion flow and thereby caused an enhancement of accretion luminosity as it went through closest approach to Sgr A*.

This thesis provides an unprecedented view of the long-term variability of Sgr A* in the NIR. In Chapter 2 of this dissertation, I report new infrared measurements of Sgr A* over a decade in which it was previously inaccessible at these wavelengths. I reexamine the first decade (1995 - 2005) of Keck speckle data with our further-improved speckle holography analysis technique. This work enables direct Sgr A* detections in early years and a study addressing variability timescales 10 times longer than earlier published studies. I discuss how this work can be used to characterize the infrared variability pattern of Sgr A*, and the possible interactions of the central SMBH with objects experiencing tidal disruption.

1.3 Star formation history of the nuclear star cluster

Spectacularly dense and massive nuclear star clusters (NSCs) appear to be common in many galaxies. The formation and evolution of the stars in the NSC and their connections to the

central SMBH and the inner bulge, however, are still puzzling. The best studied NSC is at the center of our own Milky Way galaxy, only ∼8 kpc from Earth and surrounding a SMBH. The current picture of the NSC reveals an old stellar population, extending out a few pc with a mass of $\sim 2.5 \times 10^7\ M_\odot$ (e.g., Launhardt et al. 2002; Schödel et al. 2014). The NSC at the Galactic center enables us to resolve the stellar population and to study the composition and the nature of star formation in this extreme environment.

The star formation history of the NSC has been extensively probed over the last few decades. Previous studies suggested this extreme region host multiple stellar populations. Near-infrared surface brightness measurements were initially used to show the discontinuity between the bright nucleus and the bulge at ∼150 pc (Becklin & Neugebauer 1968; Kent 1992; Launhardt et al. 2002). The discovery of massive young stars in the central parsec shows the evidence for very recent star formation as young as < 5 Myr (Forrest et al. 1987; Allen et al. 1990). Later on, high angular resolution observations with robust photometric, astrometric and spectroscopic measurements enable the resolved stellar detections and spectrum. The star formation history of the NSC was then studies by constructing the Hertzsprung-Russell (H-R) diagram of the population using photometry and spectroscopically derived temperature of individual stars. These studies analyzed late-type stars including the asymptotic giant branch (AGB), red giant branch (RGB) and helium-burning red clump stars within the central few parsecs. They generally claimed that the majority of the stars in the NSC formed more than 5 Gyr ago (e.g., Blum et al. 2003; Maness et al. 2007; Pfuhl et al. 2011).

The current picture of the NSC star formation history is far from complete. One limitation in the understanding of the star formation history is that previous studies assumed that all stars have solar metallicity due to limited measurements of chemical abundances. However, age and metallicity are degenerate parameters in star formation history; by ignoring the effect of metallicties, the age estimates can be potentially biased. Generally, the stellar population with lower temperature and fainter brightness can be interpreted as either old or high metallicity. See Figure 1.3. Earlier works have noted such degeneracies, but were not able to

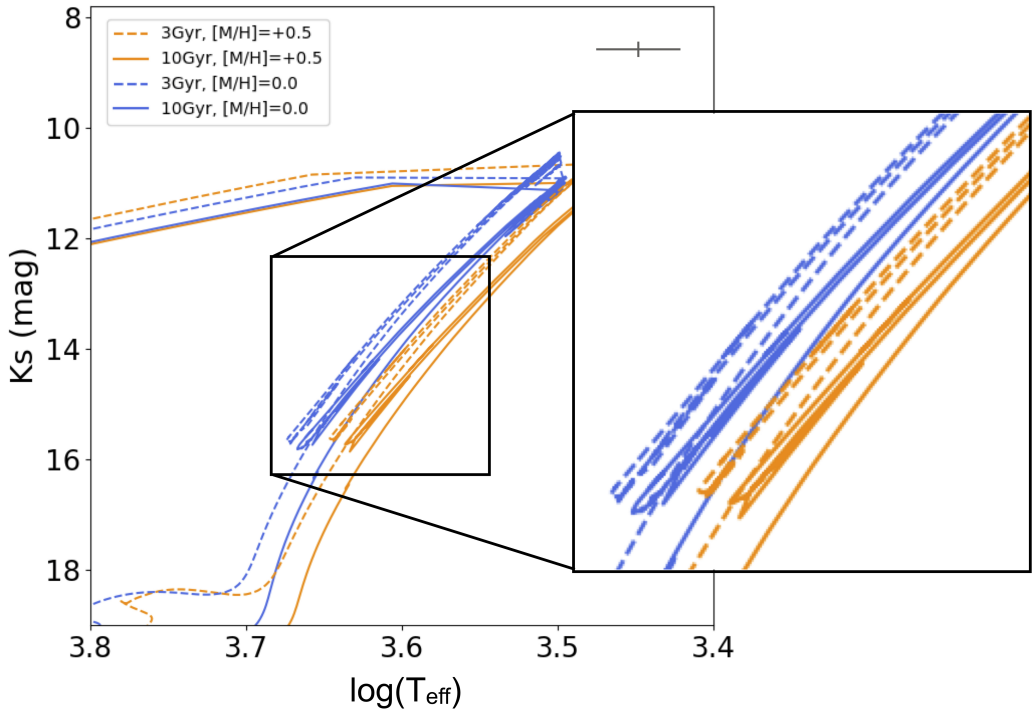

Figure 1.3: H-R diagram with MIST isochrones (Choi et al., 2016) for ages 3 Gyr ('dashed') and 10 Gyr ('solid') with colors showing the different metallicities of [M/H] = +0.5 (orange), [M/H] = 0 (blue). Age and metallicity are degenerate parameters in star formation history. Generally, the stellar population with lower effective temperature (T_{eff}) and fainter brightness (Ks magnitude) can be interpreted as either old or high metallicity.

account for them due to limited metallicity measurements of individual stars. More recent spectroscopic surveys presented a significant spread in metallicity, ranging from sub-solar to super-solar, for late-type stars in the NSC (e.g., Do et al. 2015; Feldmeier-Krause et al. 2017, 2020; Ryde & Schultheis 2015; Ryde et al. 2016; Rich et al. 2017). The broad metallicity distribution addresses the necessity of revisiting the star formation history. Now we are able to reconstruct the star formation history at the Galactic center using new information such as metal abundances measurements and temperature of stars.

Furthermore, dense nuclear star clusters are expected to interact with the central SMBH

and drive many dynamical processes, including a higher merger rates of compact object binaries that could be detected in the form of gravitational waves (e.g., Portegies Zwart & McMillan 2000; O'Leary et al. 2009, 2016; Antonini et al. 2014; Rodriguez et al. 2016b; Bartos et al. 2017b; Hoang et al. 2018). The extreme physical phenomena can only be observed in detail at the center of our galaxy, and help understand how this environment influences the compact object merger rates. The predicted type and mass of compact remnants have been explored over the last few decades (e.g., Morris 1993; Baumgardt et al. 2004; Alexander et al. 2007; Löckmann et al. 2010). One limitation is that predictions of compact objects and their merger rates have assumed a "Chabrier/Kroupa" IMF and a solar metallicity, which may have large impacts on the resulting compact remnant populations. Knowing the star formation history of the NSC is valuable because it allows us to make the most accurate predictions of the number of compact objects including stellar mass black holes, neutron stars and white dwarfs at the Galactic center, and their gravitational wave merger rates.

This thesis presents new investigations for the star formation history of Milky Way's NSC. In Chapter 3 of this dissertation, I report the first star formation history study of the NSC which includes constraints from a large sample of stellar metallicity measurements. I develop a Bayesian inference approach to derive the star formation history and other cluster properties of the NSC. I present the substantial impact of the metallicity constraints on the age estimates of the NSC and discuss how this work can be used to constrain the co-evolution of the NSC, the SMBH and the Galactic bulge, as well as the implication for the formation scenario of the NSC. I also report updated predictions of the number of compact objects at the Galactic center and their merger rates for detecting gravitational waves.

CHAPTER 2

Consistency of the Infrared Variability of SGR A* over 22 yr

The Galactic center is home to the closest known supermassive black hole (SMBH), Sgr A* (4×10^6 $M_\odot$, e.g., Schödel et al. 2002, 2003; Ghez et al. 2003, 2005b, 2008; Genzel et al. 2010; Boehle et al. 2016; Gillessen et al. 2009, 2017; Do et al. 2019), where we can study in detail the accretion behaviors of the SMBH and physical processes that occur in its vicinity. Sgr A* near-infrared (NIR) emission has been extensively monitored with adaptive optics observations since mid-2000 (e.g., Genzel et al. 2003; Ghez et al. 2004). While earlier data exists in form of speckle imaging as obtained from Keck telescope (1995 - 2005), Sgr A* was not detected in the initial analysis of the speckle images. This chapter is driven by the question of what is the long-term accretion properties of the low-luminosity SMBH? Chen et al. (2019) carried out a new analysis of speckle imaging data with the improved speckle holograph techniques, enabling new detections of Sgr A* IR over a decade in which it was previously inaccessible at these wavelengths. This study established a variability timescale ten times longer than any published studies. This analysis presents that the brightness of Sgr A* and its variability is consistent over 22 yr, indicating that the proposed 245 minutes still remains the dominant break timescale beyond which the variations show uncorrelated in time. This work also investigated possible interactions of spatially resolved objects experiencing tidal disruption with the central SMBH and reported no apparent effect on the NIR emission from accretion flow onto Sgr A*.

The Astrophysical Journal Letters, 882:L28 (19pp), 2019 September 10 https://doi.org/10.3847/2041-8213/ab3c68

Consistency of the Infrared Variability of SGR A* over 22 yr

Zhuo Chen[1,11], E. Gallego-Cano[2,3,11], T. Do[1,11], G. Witzel[1,4,11], A. M. Ghez[1,11], R. Schödel[2,11], B. N. Sitarski[1,5,11], E. E. Becklin[1,11], J. Lu[6,11], M. R. Morris[1,11], A. Dehghanfar[1,7,11], A. K. Gautam[1,11], A. Hees[1,8,11], M. W. Hosek, Jr.[1,11], S. Jia[6,11], A. C. Mangian[9,11], and K. Matthews[10,11]
[1] Department of Physics and Astronomy, UCLA, USA
[2] Intituto de Astrofísica de Andalucía (CSIC), Glorieta de la Astronomía s/n, E-18008 Granada, Spain
[3] Centro Astronómico Hispano-Alemán (CSIC-MPG), Observatorio Astronómico de Calar Alto, Sierra de los Filabres, 04550, Gérgal, Almería, Spain
[4] Max Planck Institute for Radio Astronomy, Auf dem Hügel 69, D-53121 Bonn (Endenich), Germany
[5] Giant *Magellan* Telescope Corporation, Pasadena, CA, USA
[6] Department of Astronomy, UC Berkeley, USA
[7] Institut de Planetologie et d'Astrophysique de Grenoble, 414 Rue de la Piscine, F-38400 Saint-Martin-d'Heres, France
[8] SYRTE, Observatoire de Paris, Université PSL, CNRS, Sorbonne Université, LNE, 61 avenue de l'Observatoire F-75014 Paris, France
[9] Department of Astronomy, University of Illinois, Urbana-Champaign, USA
[10] Division of Physics, Mathematics, and Astronomy, California Institute of Technology, USA
Received 2019 June 22; revised 2019 July 30; accepted 2019 August 17; published 2019 September 11

Abstract

We report new infrared (IR) measurements of the supermassive black hole at the Galactic Center, Sgr A*, over a decade that was previously inaccessible at these wavelengths. This enables a variability study that addresses variability timescales that are 10 times longer than earlier published studies. Sgr A* was initially detected in the near-infrared (NIR) with adaptive optics observations in 2002. While earlier data exists in form of speckle imaging (1995–2005), Sgr A* was not detected in the initial analysis. Here, we improved our speckle holography analysis techniques. This has improved the sensitivity of the resulting speckle images by up to a factor of three. Sgr A* is now detectable in the majority of epochs covering 7 yr. The brightness of Sgr A* in the speckle data has an average observed K magnitude of 16.0, which corresponds to a dereddened flux density of 3.4 mJy. Furthermore, the flat power spectral density of Sgr A* between ∼80 days and 7 yr shows its uncorrelation in time beyond the proposed single power-law break of ∼245 minutes. We report that the brightness and its variability is consistent over 22 yr. This analysis is based on simulations using the Witzel et al. model to characterize IR variability from 2006 to 2016. Finally, we note that the 2001 periapse of the extended, dusty object G1 had no apparent effect on the NIR emission from accretion flow onto Sgr A*. The result is consistent with G1 being a self-gravitating object rather than a disrupting gas cloud.

Key words: accretion, accretion disks – black hole physics – Galaxy: center – techniques: high angular resolution

1. Introduction

The Galactic Center (GC), approximately 8 kpc (Reid 1993) from Earth, is host to the closest known supermassive black hole (SMBH; Ghez et al. 1998, 2000, 2005b, 2008; Schödel et al. 2002; Gillessen et al. 2009, 2017; Boehle et al. 2016). This makes it an excellent laboratory for studying the accretion properties of SMBHs. The accretion flow onto the SMBH at the GC gives rise to its radiative counterpart, Sgr A*, which appears to be very under-luminous compared to active galactic nuclei (AGNs) with comparable masses (Melia & Falcke 2001). Several different theoretical models have been developed to describe Sgr A*'s accretion flow, including the well-known advection-dominated accretion flow model (Ichimaru 1977; Narayan & Yi 1994; Abramowicz et al. 1995; Narayan et al. 1995) and the radiatively inefficient accretion flow model (RIAF; Yuan et al. 2003), both of which account for the low efficiency of the radiation loss of accreting gas and imply a hot and geometrically thick accretion structure.

An additional complexity and opportunity for modeling Sgr A* emission is that it is a variable source. Thus far the near-infrared (NIR) has proven to be a powerful window for characterizing Sgr A*'s variability (Witzel et al. 2018). Sgr A* was first detected in the NIR in 2002 with the first adaptive optics (AO) measurements of the GC (Genzel et al. 2003; Ghez et al. 2004). The NIR short-term variability of Sgr A* is well characterized as a red-noise process (Press 1978). A power-law power spectral density (PSD) with a slope $\gamma_1 \approx 2$ can describe the variability on short timescales of minutes to hours (Do et al. 2009; Dodds-Eden et al. 2011; Witzel et al. 2012; Hora et al. 2014; Meyer et al. 2014). Witzel et al. (2018) reported a break in the PSD at a timescale of $\tau_b = 245^{+88}_{-61}$ minutes, which constitutes the characteristic timescale of the variability process. The power law and break timescales have been a powerful way to study black hole accretion physics over a large range of luminosity and mass scales (e.g., Eckart et al. 2006; Meyer et al. 2008, 2009; Do et al. 2009). Thus far, the longest NIR timescale of Sgr A* that has been measured is 1.9 yr (Meyer et al. 2009).

Prior to and during the epoch when AO systems were coming online (2002–2005, the Very Large Telescope), the GC was studied at high angular resolution comparable to that achieved with AO at NIR wavelengths with speckle data from 1995 to 2005 at Keck. The initial analysis used the shift-and-add technique (SAA; Eckart et al. 1995; Eckart & Genzel 1996; Ghez et al. 1998, 2000, 2005a; Hornstein et al. 2002; Lu et al. 2005; Rafelski et al. 2007). Sgr A* was not detected at this time owing to both the poorer sensitivity of these maps, which typically had detection limits ($\langle K_{\rm lim}\rangle = 15.7$ mag; Boehle et al. 2016) comparable to or fainter than the average Sgr A* brightness ($\langle K_{\rm SgrA*,AO}\rangle = 16.1$ mag; see Section 4.2), and the short time baseline of observations, which allowed only limited knowledge of the orbits

[11] Galactic Center Collaboration (GCC).

of nearby stars and the position of Sgr A* (Hornstein et al. 2002). Recently, the analysis of the speckle data has been improved with the speckle holography technique (Primot et al. 1990; Schödel et al. 2013; Boehle et al. 2016) to study two short-period stars, S0-38 and S0-2. This technique deepens the detection magnitude to $K < 17$ and opens up the possibility of detecting Sgr A* over a much longer time baseline.

Detecting Sgr A* during the speckle era (1995–2005) also extends the time baseline for discrete accretion events searches. Of particular interest is the spatially resolved dusty source G1, which underwent a tidal interaction with the central black hole as it went through periapse in 2001 (Sitarski et al. 2014; Pfuhl et al. 2015; Witzel et al. 2017). This event may have increased the gas accretion onto Sgr A*. This object is similar observationally to G2, a cold, gaseous, highly eccentric object orbiting Sgr A* that reached closest approach in early 2014 (Gillessen et al. 2012). G2 was originally posited to be a 3 Earth-mass pure gas cloud that would measurably impact the accretion flow and variability process as it was tidally sheared from the moment of periapse to ∼7 yr after periapse. However, no indication of this impact has so far been observed (e.g., Hora et al. 2014; Witzel et al. 2014, 2017, 2018; Pfuhl et al. 2015; Valencia-S et al. 2015), but the interaction phase may extend a few years (∼7 yr or more) beyond periapse passage (e.g., Pfuhl et al. 2015). One hypothesis is that G1 and G2 are part of the same gas streamer (Pfuhl et al. 2015). If this is the case, then G1 may have also impacted the accretion flow and thereby caused an enhancement of accretion luminosity as it went through closest approach to Sgr A*, and perhaps a few years after. While the AO measurements only started in 2002 and did not cover the time baseline of G1's periapse, the speckle data sets allow us to study whether G1 had any impact on the accretion flow related to its periapse passage. Moreover, two short-period stars, S0-2 and S0-16, went through the periapse (S0-16, 2000; S0-2, 2002) during the speckle era explored in this work, allowing us to test whether they had any kind of impact on the variability of Sgr A*.

In this work, we further develop the speckle holography technique to analyze our speckle data sets (1995–2005). We make the first report of NIR detection of Sgr A* prior to 2002. The details of the 10 years of data used in this work are described in Section 2. Section 3 presents the data analysis and methods, including the speckle holography image reconstruction and improvements, point sources extraction, photometric calibration, and Sgr A* identification from speckle holography images. Section 4 presents the results of Sgr A* detections, observed brightness, and its variability. Section 5 discusses the impact of G1's periapse, and also simulations to explore how the variability of Sgr A* in the speckle data is compared to that at later times. We conclude with a summary in Section 6 of the long-term activity of Sgr A* on timescales that are significantly longer than previous studies. Appendices A and B present details of photometry and source analyses used in this work for speckle holography images.

2. Data Sets

This Letter is based on speckle imaging that was taken as part of the Galactic Center Orbit Initiative (GCOI) and that was originally presented in Ghez et al. (1998, 2000, 2005a, 2008), Lu et al. (2005), Rafelski et al. (2007), and Boehle et al. (2016). From 1995 to 2005, the K[2.2 μm]-band speckle data sets of the Galaxy's central $\sim 5'' \times 5''$ region were obtained with the W. M. Keck I 10 m telescope and its NIR camera (NIRC; Matthews & Soifer 1994; Matthews et al. 1996). During each epoch, which combine observations ranging from 1 to 4 nights, roughly 10,000 short-exposure frames ($t_{\rm exp} = 0.1$ s) were obtained in datacubes consisting of 128 frames, which was the maximum number of frames that could be obtained in a single NIRC FITS file. Within each datacube, the time delay between the start time of each frame was 1.5 s in 1995 and 0.61 s thereafter. These series of short exposures were obtained with NIRC in its fine plate scale mode, with a scale of 20.396 ± 0.042 mas pixel^{-1} and a corresponding field of view of $5\farcs22 \times 5\farcs22$. The data were obtained with the telescope in stationary mode, which keeps the pupil fixed with respect to the detector and causes the sky to rotate over a datacube. Our starting point for this Letter's analysis is the individual frames that have had the instrumental effects removed (i.e., sky-subtracted, flat-fielded, bad-pixel-corrected, distortion-corrected) and that have been rotated to have a position angle of 0° on the plane of the sky (see details in Ghez et al. 1998, 2000). Table 1 summarizes the 27 speckle observation epochs.

3. Data Analysis and Methods

3.1. Image Reconstruction—A New Implementation of Speckle Holography

For this project, we have developed a new implementation of speckle holography. This builds on the work of Schödel et al. (2013), which has been applied to the GCOI data sets presented in Meyer et al. (2012; version 2_0) and Boehle et al. (2016; version 2_1) to study the short-period stars. In theory, the speckle holography technique uses the instantaneous PSF, which is measured from a set of reference sources, to deconvolve, in Fourier space, the distorted images and realize the contribution of all speckle information to the final diffraction-limited core, as follows:

$$O = \frac{\langle I_m P_m^* \rangle}{\langle |P_m^2| \rangle} \quad (1)$$

where O is the Fourier transform of the object, I_m and P_m are the Fourier transforms of the mth short-exposure image and of its instantaneous PSF, respectively, and the brackets denote the mean over N frames. P_m^* is the conjugate complex of P_m (Primot et al. 1990).

In practice, speckle holography images are constructed through an iterative process. A key component of this analysis uses the PSF fitting program StarFinder (Diolaiti et al. 2000; also see Section 3.2). Below we detail the steps to construct the speckle holography images (version 2_2), and show how they differ from the implementation used in Boehle et al. (2016; version 2_1).

1. Shift all short-exposure frames to align the brightest speckle of IRS 16C. Subtract a constant background, which is estimated for each individual frame, from each short-exposure frame for version 2_2.
2. Rebin the speckle frames from original 20 mas pixel^{-1} scale down to 10 mas pixel^{-1} scale. Bilinear and cubic interpolation are used in version 2_1 and version 2_2, respectively.
3. Combine and construct an SAA image from all datacubes per observing epoch.

Table 1
Summary of Speckle Holography Observations[a]

Date		Frames	K_{lim}[b]	N_{Real}	N_{pix}[c]	Sgr A* Pos. with Respect to Field of View (FoV)[e]		Original	K Systematic Phot. Zero-point	K Relative Phot.
(U.T.)	(Decimal)	Used	(mag)			ΔR.A. (arcsec)	ΔDecl. (arcsec)	Refs.[f]	Error[g] (mag)	Error[h] (mag)
1995 Jun 9–12	1995.439	5265	17.0	41	108042	−0.52	0.01	1	0.24	0.04
1996 Jun 26–27	1996.485	2283	15.8	49	82505	−1.22	−0.29	1	0.14	0.09
1997 May 14	1997.367	3426	16.8	51	92467	−0.90	−0.15	1	0.09	0.03
1998 Apr 2–3	1998.251	1718	15.8	39	95816	−0.57	−0.15	2	0.07	0.06
1998 May 14–15	1998.366	7675	16.8	45	102328	−0.45	−0.10	2	0.17	0.04
1998 Jul 3–5	1998.505	2040	16.4	43	116557	0.04	0.00	2	0.18	0.05
1998 Aug 4–6	1998.590	11032	17.1	47	109269	−0.41	0.04	2	0.18	0.04
1998 Oct 9, 11	1998.771	2000	16.6	45	97215	0.80	0.05	2	0.12	0.03
1999 May 2–4	1999.333	9423	17.2	52	107882	−0.45	−0.21	2	0.12	0.06
1999 Jul 24–25	1999.559	5690	17.4	54	100567	−0.46	−0.09	2	0.11	0.04
2000 Apr 21	2000.305	651	15.7	56	96248	0.84	0.11	3	0.09	0.04
2000 May 19–20	2000.381	15581	17.5	55	96853	−0.74	−0.24	3	0.08	0.03
2000 Jul 19–20	2000.584	10668	17.0	63	86452	−0.93	−0.12	3	0.15	0.04
2000 Oct 18	2000.797	2215	16.2	52	82315	−0.80	−0.42	3	0.09	0.05
2001 May 7–9	2001.351	6662	17.2	64	85028	−0.46	−0.20	3	0.17	0.02
2001 Jul 28–29	2001.572	6634	17.4	74	96872	−0.15	−0.22	3	0.15	0.02
2002 Apr 23–24	2002.309	13440	17.5	74	96953	−0.59	−0.17	3	0.12	0.05
2002 May 23–24	2002.391	11834	17.6	72	98552	−0.85	−0.08	3	0.14	0.05
2002 Jul 19–20	2002.547	4139	16.8	69	99994	−0.63	−0.39	3	0.17	0.05
2003 Apr 21–22	2003.303	3644	16.4	58	90963	−0.32	−0.40	3	0.18	0.06
2003 Jul 22–23	2003.554	2894	16.8	65	87265	−0.54	−0.24	3	0.08	0.01
2003 Sep 7–8	2003.682	6296	17.1	74	95367	−0.53	−0.44	3	0.14	0.03
2004 Apr 29–30	2004.327	6169	16.8	58	125423	−0.71	−0.21	4	0.17	0.04
2004 Jul 25–26	2004.564	13071	17.4	80	99819	−0.61	−0.41	4	0.15	0.04
2004 Aug 29	2004.660	2284	16.8	63	96172	−0.09	0.66	4	0.14	0.02
2005 Apr 24–25	2005.312	9553	17.1	70	105715	−0.36	−0.16	5	0.14	0.05
2005 Jul 26–27	2005.566	5606	16.8	84	108360	−0.26	−0.41	5	0.12	0.04

Notes.
[a] All numbers given in the table are based on speckle holography version 2_2 (see Section 3).
[b] K_{lim} is the magnitude that corresponds to the 95th percentile of all K magnitudes in the sample of real stars in the central $2'' \times 2''$ region (see Appendix B.1).
[c] N_{pix} refers to the number of pixels in a given image that meet a 0.8 of maximum frames used criteria.
[d] N_{ref} refers to the number of reference stars used to align the epoch of data.
[e] The center of the FoV is the weighted average of the detector pixels, with the weight being the number of frames used squared at each pixel in the final image. The offsets reported above are $(\boldsymbol{x}_{SgrA*} - \boldsymbol{x}_{centerFoV})$.
[f] 1: Ghez et al. (1998); 2: Ghez et al. (2000); 3: Ghez et al. (2005a); 4: Lu et al. (2005); 5: Rafelski et al. (2007).
[g] Systematic photometric zero-point errors were calculated after performing initial photometric system calibration described in Appendix A.1. The average zero-point uncertainty $\bar{\sigma}_{zp}$ is 0.14 mag in NIRC K bandpass.
[h] Relative photometric zero-point errors were determined by the relative photometry calibration using the stable calibrators (see Appendix A.2). The average zero-point uncertainty $\bar{\sigma}_{zp}$ for the relative photometry is 0.04 mag in NIRC K bandpass.

4. Extract astrometry and photometry of stars in the SAA images with StarFinder to identify potential PSF reference stars for the speckle holography analysis.
5. Select the brightest isolated sources as PSF reference stars for speckle holography. Each datacube typically has two to five reference sources (IRS 16NE, IRS 16C, IRS 16NW, IRS 16SW, IRS 33N), depending on the centering and image quality of the datacube.
6. Estimate the instantaneous PSF for each speckle frame from the median of the aligned and flux-normalized images of the reference stars. For each PSF, we subtract a constant value of $b_g + n \times \sigma$ ($n = 3$ for speckle images), where b_g is the background and σ is the noise. All resulting negative values in the PSF are set to 0. As a final step, a circular mask is applied to the PSF and the PSF is normalized to a total flux of 1. In version 2_2, we fixed a bug in StarFinder in which secondary stars that are not PSF reference stars were not being subtracted from the primary reference stars.
7. Improve the PSF estimate by subtracting all known secondary contaminating sources near the reference stars in each frame, using the preliminary PSFs from step (6) and information from step (4).

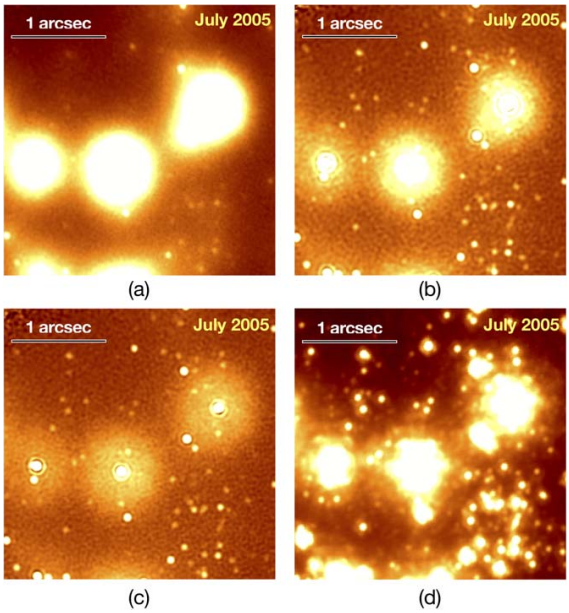

Figure 1. Comparison of the different high angular resolution techniques used to image the GC. The early data has been analyzed with (a) SAA, (b) the original implementation of speckle holography (version 2_1), and (c) the new implementation presented in this work (version 2_2). AO data taken at a similar time is shown in (d). The new speckle holography improves the sensitivity of the final images by up to a factor of three compared to the initial speckle holography.

8. Estimate the object Fourier transform O by applying Equation (1).
9. Apodize O with a model for the optical transfer function (OTF) of the telescope. Here we use a Gaussian function for 10 m aperture.
10. Reconstruct the image with inverse Fourier transform.
11. Repeat of the process from step (4) with the holographically reconstructed image, which has significantly higher quality than the initial SAA image.
12. Create multiple images for error estimation. In version 2_1, the data set for each epoch is divided into three equal-quality subsets to produce three speckle holography maps. In version 2_2, we use a bootstrapping method to produce 100 bootstrap data sets using sampling with replacement resulting in 100 speckle holography images produced from the same number of frames as the original data set.

The most important improvements of version 2_2 compared to version 2_1 are listed here.

1. Subtracting a constant sky background from each frame results in less background variation in the combined images, and in significantly suppressed edge effects near the edge of the FoV (Step 1).
2. Version 2_1 only used IRS 16C as PSF reference source. Version 2_2 uses up to five stars as PSF reference sources, depending on the instantaneous FoV (Step 5).
3. The bootstrapping method results in a more robust estimate of the astrometric and photometric uncertainties (Step 12).

Figure 1 shows the central region of the final reconstructed image from 2005 July. Compared to the earlier implementation of speckle holography and SAA analysis, the new analysis (version 2_2) has both improved the image quality and reduced the edge-effect artifacts.

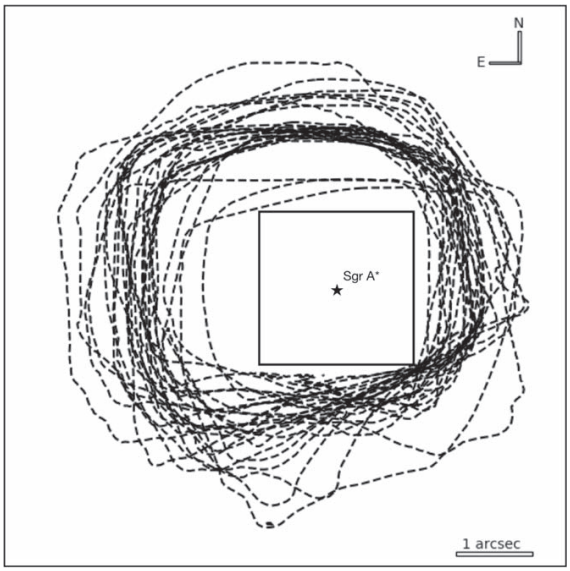

Figure 2. Comparison of the FoV for all the final speckle holography images. The dashed contours display the covered region for each epoch with contribution of over 80% of the individual frames. In order to minimize the edge effects, this study considers only the central $2'' \times 2''$ region center around Sgr A* outlined with the solid line.

3.2. Point Sources Extraction from Speckle Holography Images

Point sources are extracted from each epoch's final reconstructed image using StarFinder. Here, like in Section 3.1, we use the version of StarFinder utilized in Boehle et al. (2016) setting the cross-correlation threshold to 0.8, and a slightly lower minimum signal-to-noise ratio cut (3σ, versus 5σ). In order to estimate the astrometric and photometric uncertainties for the sources extracted, we perform StarFinder on 100 bootstrap images for each epoch and then calculate the standard deviation.

In order to minimize the impact of edge effects of speckle holography images, we restricted our analysis in the central $2'' \times 2''$ region center around Sgr A* for all epochs in the rest of this work. Owing to the observing strategy, in which stationary mode was used (see Section 2), the final image has significant variations in the number of individual frames that contributes to the each pixel toward the outer edge of the image. See contours in Figure 2.

Because speckle holography is a Fourier deconvolution technique, point-like artifacts can be produced in the middle of the FoV from edge effects, background, and PSF extraction. We therefore require sources to be detected above a minimum threshold number of bootstrap images to be considered real. This threshold is set by demanding that the probability of fake detections be less than 1% (see Appendix B.1). The bootstrap threshold for each epoch is reported in Table 2 and with an average of $10\% \pm 7\%$.[12]

[12] We note that this threshold is lower than in other GCOI studies because we have strong prior knowledge of the source (Sgr A*) location.

Table 2
Summary of Sgr A* Measurements

Date(UT)	Date (Epoch)	Bootstrap Fraction Cut[a]	Source Detection Limit[b] (mag)	Source Confusion with Sgr A*	K (mag)	K Error (mag)	Dereddened Flux (mJy)	Dereddened Flux Error (mJy)	Fraction of Bootstraps Detected	ΔT[c] (minutes)
1995 Jun 9–12	1995.439	0.26	17.0	S0-19	…	…	…	…	…	…
1996 Jun 26–27	1996.485	0.24	16.0	…	…	…	…	…	…	…
1997 May 14	1997.367	0.22	16.9	…	…	…	…	…	…	…
1998 Apr 2–3	1998.251	0.14	15.8	…	15.2	0.2	6.7	1.2	0.64	352
1998 May 14–15	1998.366	0.02	16.8	…	16.4	0.1	2.3	0.4	0.48	1653
1998 Jul 3–5	1998.505	0.12	16.7	…	16.0	0.1	3.4	0.7	0.34	1643
1998 Aug 4–6	1998.59	0.02	17.2	…	16.3	0.1	2.5	0.5	0.66	1624
1998 Oct 9,11	1998.771	0.06	16.6	…	15.7	0.1	4.5	0.7	0.44	2952
1999 May 2–4	1999.333	0.06	17.2	…	16.2	0.2	2.7	0.5	0.82	2949
1999 Jul 24–25	1999.559	0.02	17.5	…	15.9	0.1	3.8	0.6	0.88	1527
2000 Apr 21	2000.305	0.14	15.7	S0-16	…	…	…	…	…	…
2000 May 19–20	2000.381	0.02	17.6	S0-16	…	…	…	…	…	…
2000 Jul 19–20	2000.548	0.14	17.3	S0-16	…	…	…	…	…	…
2000 Oct 18	2000.797	0.12	16.4	S0-16	…	…	…	…	…	…
2001 May 7–9	2001.351	0.08	17.1	…	16.6	0.1	2.0	0.3	0.81	1443
2001 Jul 28–29	2001.572	0.02	17.4	…	15.8	0.1	4.0	0.6	0.96	1702
2002 Apr 23–24	2002.309	0.06	17.4	S0-2	…	…	…	…	…	…
2002 May 23–24	2002.391	0.02	17.8	S0-2	…	…	…	…	…	…
2002 Jul 19–20	2002.547	0.22	16.9	S0-2	…	…	…	…	…	…
2003 Apr 21–22	2003.303	0.04	16.3	S0-38	…	…	…	…	…	…
2003 Jul 22–23	2003.554	0.08	16.7	…	…	…	…	…	…	…
2003 Sep 7–8	2003.682	0.18	17.0	…	…	…	…	…	…	…
2004 Apr 29–30	2004.327	0.02	16.6	…	16.2	0.1	2.8	0.6	0.21	1578
2004 Jul 25–26	2004.564	0.04	17.5	…	16.7	0.2	1.9	0.4	0.75	1572

Table 2
(Continued)

Date(UT)	Date (Epoch)	Bootstrap Fraction Cut[a]	Source Detection Limit[b] (mag)	Source Confusion with Sgr A*	K (mag)	K Error (mag)	Dereddened Flux (mJy)	Dereddened Flux Error (mJy)	Fraction of Bootstraps Detected	ΔT[c] (minutes)
2004 Aug 29	2004.66	0.06	16.8	…	…	…	…	…	…	…
2005 Apr 24–25	2005.312	0.06	16.9	…	16.0	0.1	3.2	0.5	0.95	1633
2005 Jul 26–27	2005.566	0.16	16.9	…	15.8	0.1	4.0	0.6	0.66	1654

Notes.
[a] Bootstrap fraction cut of a real source detection in each epoch is obtained at which the probability of a false detection within within 10 mas radius is always <1%.
[b] Sgr A* detection limit is the 95th percentile of all K magnitudes in the sample which includes all sources with a bootstrap fraction higher than the bootstrap fraction cut in the central $2'' \times 2''$ FoV.
[c] Time duration of the observations that contributes to the final speckle image for Sgr A* detections.

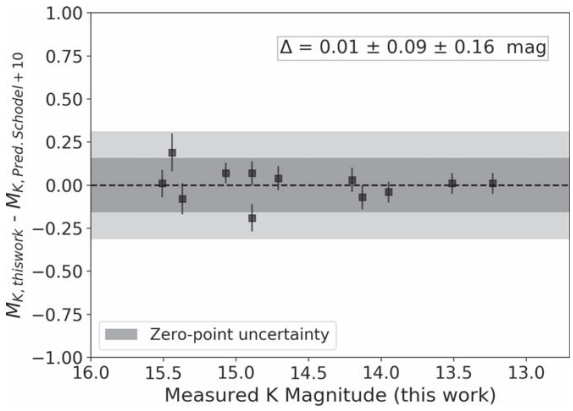

Figure 3. Difference between our measured K magnitude (from photometric system calibration) and the predicted K magnitude (bandpass corrected from Schödel et al. (2010) Ks) for calibrators used in Witzel et al. (2012). The measured K magnitudes are consistent with the predicted ones, with an average difference of 0.01 ± 0.09 mag and a zero-point uncertainty $\overline{\sigma}_{zp}$ of 0.16 mag (dark band; light band: $2\overline{\sigma}_{zp}$). This verifies that the early infrared (IR) measurements made based on speckle images are on the same photometric system as the later IR measurements obtained from AO.

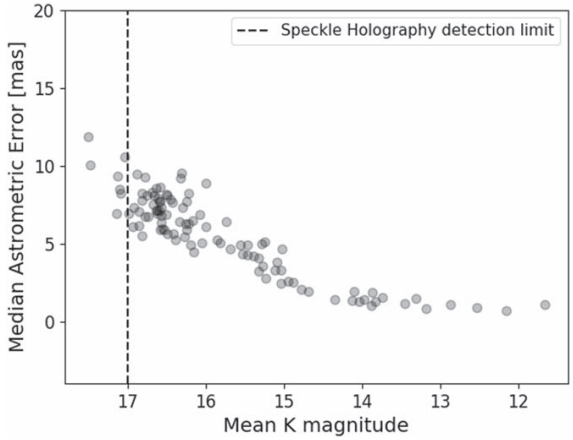

Figure 4. Astrometric uncertainty as a function of source brightness. While the brightest sources have an astrometric uncertainty of 1 mas, at the average speckle holography detection limit of K ∼17 mag, shown as the dashed line, the astrometric uncertainty is typically 10 mas.

3.3. Photometric Calibration

The list of extracted sources from speckle holography images is photometrically calibrated using a two-step procedure described in detail in Appendix A. This process results in an average photometric systematic zero-point uncertainty of 0.14 mag and an average relative photometric uncertainty of 0.04 mag respectively in NIRC K bandpass (see Table 1). While we use the standard photometry in Blum et al. (1996) as the initial system calibration, we find that our photometry of stars in the GC is consistent with both the photometric systems of Witzel et al. (2012) and Schödel et al. (2010) for the AO measurements of Sgr A* obtained between 2004 and 2017. The overall photometric difference between Schödel et al. (2010) and us is ∼1% with an average difference of only 0.01 ± 0.09 mag and a zero-point uncertainty of 0.16 mag. See Figure 3.

3.4. Comparison of Speckle Holography Implementation

This work has introduced an improved implementation of speckle holography. Appendix B.2 compares in detail the performances between the current and the old versions and shows the clear improvements of version 2_2. In particular, version 2_2 is 0.4 mag deeper on average but can be as much as a factor of three more sensitive in the extreme. From here on, we only consider the analysis based on the new speckle holography (version 2_2), which has an average detection limit of 16.9 mag (see Table 1).

3.5. Identification of Sgr A* from Source List

We use the following steps to identify Sgr A* in the source list.[13]

1. Determine the position of Sgr A* in each epoch from the offsets between Sgr A* and IRS 16C and S0-2 because they are bright enough (IRS 16C: $K = 9.8$ mag; S0-2: $K = 14.2$ mag) to always be identified and obtain the accurate positions in the image. The offsets were generated by aligning all of our speckle holography and AO data sets together. See Ghez et al. (2008), Gautam et al. (2019), Jia et al. (2019), and Sakai et al. (2019) for more details.
2. Search Sgr A* in the source list using the expected positions estimated in step (1). Sgr A* detected candidates are extracted if they are within the search radius of 10 mas. The search radius was determined by exploring the median astrometric error for all real detections in speckle epochs (Appendix B.1) in the central $2'' \times 2''$ region. See Figure 4. Empirically for sources with $K \sim 17$ mag (average speckle holography detection limit for all epochs, see Appendix B.2), the astrometric uncertainty is typically 10 mas. Based on this, we do not expect any real Sgr A* detections beyond 10 mas search radius.
3. Identify epochs where there is confusion with a known star that is passing within a 40 mas radius (Jia et al. 2019) away from Sgr A*.

4. Results

4.1. Sgr A* Detections

Results on the detections of Sgr A* in our 27 epochs of speckle holography imaging data fall into four categories: detections without source confusion (13); non-detections (5); confusion with brighter sources (8); and confusion with fainter sources (1). See Table 2 for details.

4.1.1. Detections without Source Confusion

Figure 5 presents the images of epochs with Sgr A* detections that are free from source confusion. The average observed magnitude of Sgr A* as obtained from these 13 epochs, which span the 7 yr period from 1998 to 2005, is $K = 16.0 \pm 0.4$ (standard deviation, std) with average relative photometric uncertainty of 0.1 mag, corresponding to the

[13] Here we use the source list excluding the most likely artifact sources identified in Appendix B.1.

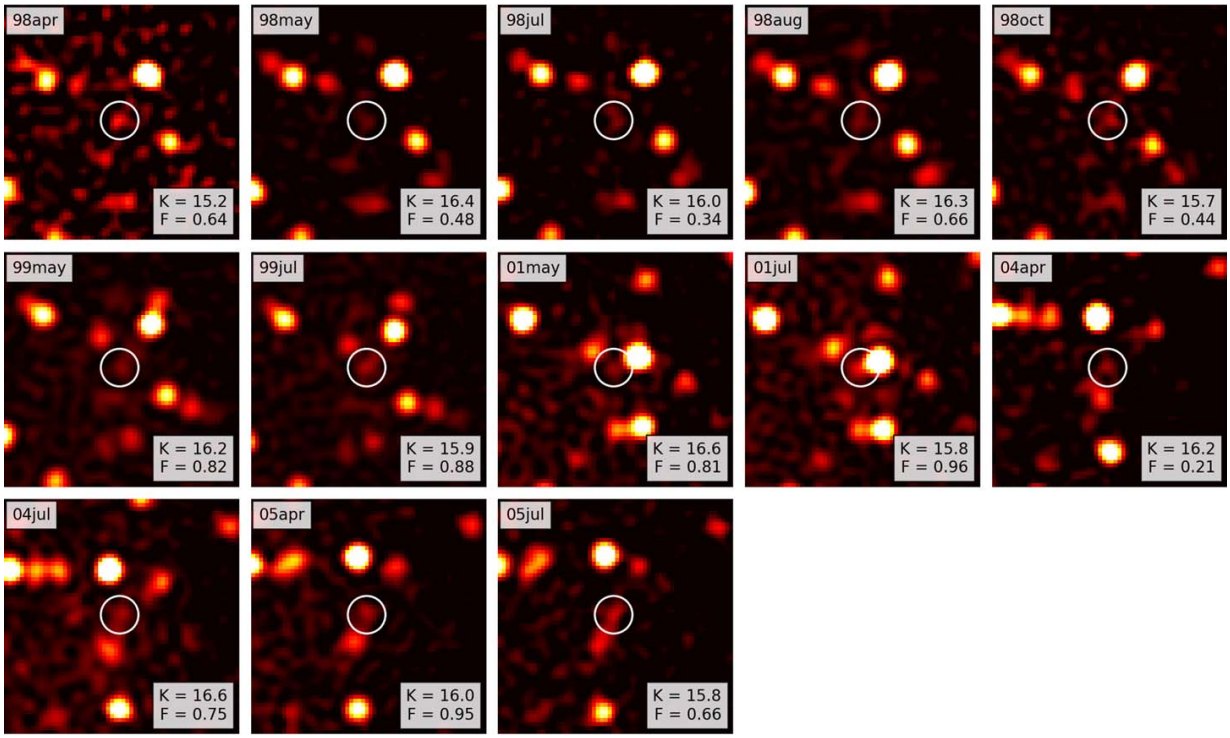

Figure 5. Speckle holography images with new Sgr A* detections (white circles). For each detection, the *K* magnitude (*K*) and the bootstrap fraction (*F*) are provided. These are the first IR detections of Sgr A* in the late 1990s and early 2000s.

average observed flux density of 0.35 ± 0.13 mJy with average relative photometric uncertainty of 0.04 mJy.

4.1.2. Non-detections

Among the 18 available epochs without source confusion (see Section 3.5), Sgr A* is not detected in five epochs. The brightness limit for Sgr A* in these epochs was determined by the source detection limit of that epoch (defined in Appendix B.1) and has values ranging from 16.0 to 17.0 mag.

4.1.3. Detections Confused with Brighter Sources

In eight epochs, Sgr A* was confused with a source brighter than its average value. As shown in Figure 6 confusion occurred with the following brighter stars: S0-2, $K_{\rm ave} = 13.6$ mag in 2002 April, May, and July; S0-19, $K_{\rm ave} = 15.0$ mag in 1995 June; S0-16, $K_{\rm ave} = 15.1$ mag in 2000 April, May, July, and October. These epochs were removed from further analysis.

4.1.4. Detections Confused with Fainter Sources

In one epoch, Sgr A* was confused with a source fainter than its average value (see Figure 6). In 2003 April, there is a source detection that is the combination of Sgr A* ($K_{\rm ave} = 16.0$ mag) and S0-38 ($K_{\rm ave} = 16.5$ mag). Because the confusing source is fainter, the constraints on Sgr A* can be obtained from the photometry ($K = 16.4$ mag) and the astrometry ($K = 16.7$ mag). These are comparable to the detection limit of this image ($K = 16.3$ mag). We therefore place a limit on Sgr A* in this epoch of 16.3 mag.

4.2. Sgr A* Brightness (1996–2005)

4.2.1. Average Brightness

Figure 7 shows all our detections and detection limits of Sgr A* from 1996 to 2005. We convert the observed values into dereddened flux densities using the relationship $F_{K_s} = 6.67 \times 10^5 \times 10.0^{-0.4 \times (K_s - A_{\rm ext,K_s})}$ mJy (Tokunaga 2000) and assuming $A_{\rm ext,K_s} = 2.46$ mag extinction (Schödel et al. 2010, 2011). Then we use the filter transformation $F_K = 1.29 F_{K_s}$, which is computed for the observed color of Sgr A* (H–$K = 2.6$ mag), to convert from K_s fluxes to K fluxes (see Table 3). See Appendix A.1 for more discussion of the filter transformations. Here, in order to present the absolute dereddened fluxes all uncertainties contain both the photometric systematic uncertainties and relative uncertainties (see Appendix A). The average detected dereddened flux density (ignore the brightness limit) is 3.4 ± 1.2 mJy (standard deviation) with average uncertainty of 0.6 mJy (0.4 mJy of relative photometric uncertainty only). If including the brightness limit, (a) treat brightness limit as a value: the upper limit of the dereddened flux density is 2.9 mJy; (b) treat brightness limit as zero: the lower limit is 2.3 mJy. The average from detections and the variance (see following Section 4.2.2) are consistent with the expectations from simulations based on more recent AO observations (2006–2017) as modeled from Witzel et al. (2018; see Section 5.2.2, and Figures 13 and 14).

4.2.2. Long Timescale Variance (40 days–7 yr)

We used the first-order structure function to characterize the variability of Sgr A* over the 7 yr. This approach is similar to

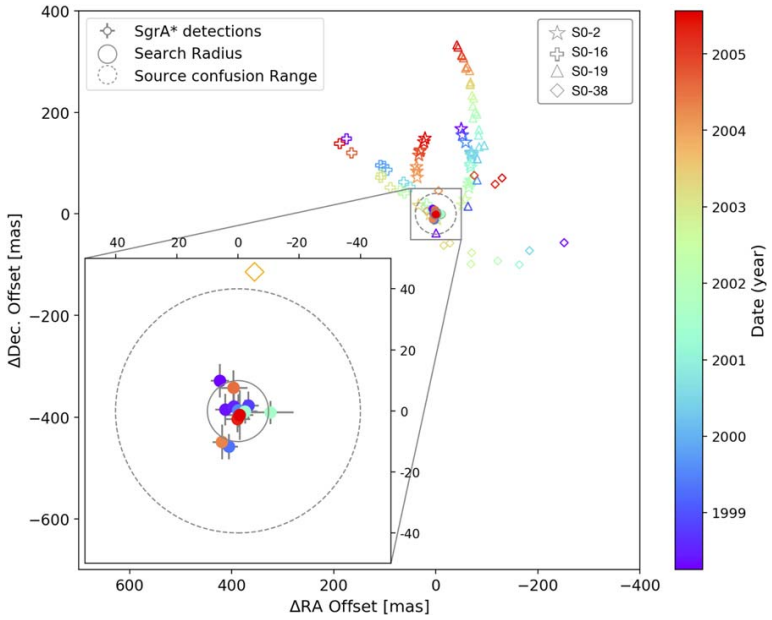

Figure 6. R.A. and decl. offsets of Sgr A* detections (points with errorbars) and of nearby star detections (symbols marked with names) relative to the predicted position of Sgr A* ((0, 0)). Different colors show the corresponding epochs. The inset panel zooms into the central part of the region. The gray solid circle marks the search radius of 10 mas (see Section 3.5) used to extract Sgr A* from the source list. The gray dashed circle shows the source confusion region (radius of 40 mas) within which nearby stars would cause bias and misdetection. We have removed confused Sgr A* detections and all nearby stars within this region in the inset panel. Overall, 13 detections of Sgr A* are free of source bias and used in this study.

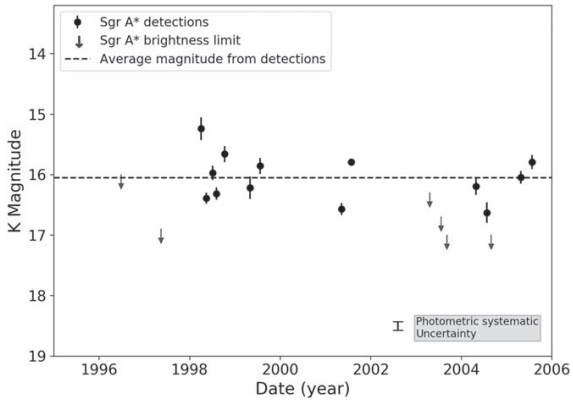

Figure 7. Light curve of Sgr A* from 1998 to 2005. The points with errorbars are the confirmed detections of Sgr A*. The arrows mark the brightness limit of Sgr A* in other non-detected epochs. The errorbar on the right bottom shows the average photometric systematic uncertainty of 0.14 mag. The average magnitude from the 13 detections is 16.0 mag.

Table 3
Filter Transformation for Sgr A*

Name	$K'_{\rm NIRC2} - K_{\rm NIRC}$	$K_{s,\rm NACO} - K_{\rm NIRC}$
Sgr A*	$0.367^{+0.01}_{-0.02}$	$0.275^{+0.01}_{-0.02}$

the analysis of the timescale and the intrinsic variability of active galactic nucleus (AGN) light curves (e.g., Simonetti et al. 1985; Hughes et al. 1992; Paltani 1999) and Sgr A* short time variability (e.g., Do et al. 2009; Witzel et al. 2012, 2018).

For the set of flux measurements shown in the light curve, $s(t)$, the first-order structure function $V(\tau)$ measures the flux density variance for a given time separation τ:

$$V(\tau) \equiv \langle [s(t+\tau) - s(t)]^2 \rangle. \quad (2)$$

We calculated $[s(t+\tau) - s(t)]^2$ using Sgr A* dereddened fluxes reported in this work for all possible pairs of time lags from real speckle observational time series. Then we put the variances into bins with a bin size of 100,000 minutes (~70 days). This yields nine bins covering the timescale between 42 days and 7.3 yr, and each bin contains at least five and as many as 19 data points. In each bin, we assigned the median lag time to be the lag time for that bin, and the average of the $V(\tau)$ values to be the value of the structure function at that lag. The error of the structure function for each bin is calculated from $\sigma_{\rm bin}/\sqrt{N_{\rm bin}}$. Here σ is the standard deviation of the $V(\tau)$ values and N is the number of points in that bin. The structure functions calculated with Sgr A* dereddened fluxes from observations are presented in Figure 8. The structure function is flat over timescale from 42 days to 7.3 yr, and has an average value of 3.1 mJy^2 with the standard deviation of 1.1 mJy^2.

5. Discussion

5.1. Impact of G1 Passage

Based on 7 yr of speckle holography data, we can use the variability of Sgr A* as the indication of the accretion activity between 1998 and 2005. During this time, the dusty source G1 went through the closest approach in 2001. This object has similar observational properties to G2, which is the first example of a spatially resolved object tidally interacting with Sgr A*. The

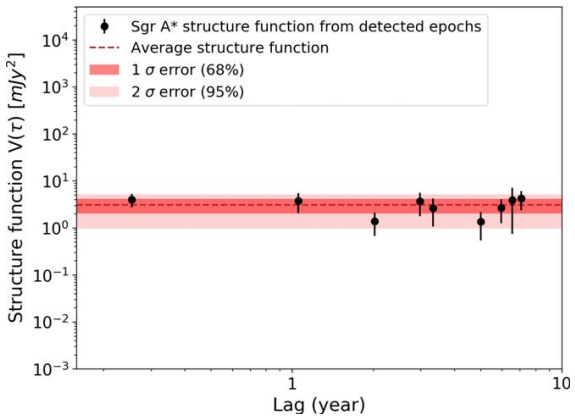

Figure 8. Sgr A* structure function $V(\tau)$. The average structure function from 13 detections is 3.1 ± 0.3 mJy^2 (red band).

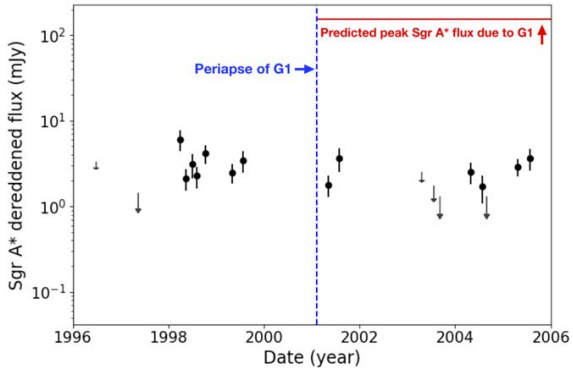

Figure 9. Impact of G1's closest approach on the brightness of Sgr A*. The blue dashed line marks the G1's periapse (2001), and red line marks the predicted peak Sgr A* flux due to the closest approach of G1. No brightening or flares of Sgr A*, i.e., no apparent impacts of G1 on the Sgr A* IR emission, were observed between 2001 and 2005.

hypotheses for the nature of G1 are similar to those proposed to explain G2. These predictions range from compact gas clouds to the product of binary mergers (Gillessen et al. 2012; Murray-Clay & Loeb 2012; Phifer et al. 2013). Predictions of compact gas clouds near Sgr A* suggest that they may increase the accretion flow onto Sgr A*. For G2, one prediction (Schartmann et al. 2012) is that if it is a gas cloud, it may be tidally disrupted and accrete onto Sgr A*, increasing the black hole's luminosity by up to a factor of 80. Because G1's tidal radius is even smaller than that of G2, it would be more influenced by the black hole. If G1 was a gas cloud and some of the gas had been accreted onto the black hole, we may expect the additional accretion at the periapse. We marked the time following of G1's periapse passage in Figure 9. Between 2001 and 2005, there is no increase in flux observed in Sgr A*. Sgr A* was quite steady with no evidence of large variations in brightness. The result is consistent with G1 being a self-gravitating object (such as a merger of two stars) as suggested by Witzel et al. (2017).

5.2. Long Timescale Variability of Sgr A*-IR

While the short-term variability of Sgr A* in the NIR is well characterized as a red-noise process, the long timescale variation has not been well probed. In order to explore if the observed long timescale variability shown in this work is consistent with models derived from shorter timescales, we simulate the NIR Sgr A* light curves with the model presented in Witzel et al. (2018; see Section 5.2.1). Section 5.2.2 presents the comparison of the simulations to the observations. See Section 5.2.3 for further discussion of the characteristic break timescale.

5.2.1. Light Curve Simulations

This model contains two key components. The first component describes the temporal characteristics using the PSD, which is modeled as a broken power law

$$\mathrm{PSD}(f) \propto \begin{cases} f^{-\gamma_0} & \text{for} \quad f < f_b \\ f^{-\gamma_1} & \text{for} \quad f \geqslant f_b, \end{cases} \tag{3}$$

where $\gamma_0 = 0$ (assumed), $\gamma_1 = 2.1 \pm 0.1$, $f_b = (4.1 \pm 0.7) * 10^{-3}$ minute^{-1} (which corresponds to a timescale of $\tau \sim 245$ minutes). See Figure 10 for the modeled PSD.

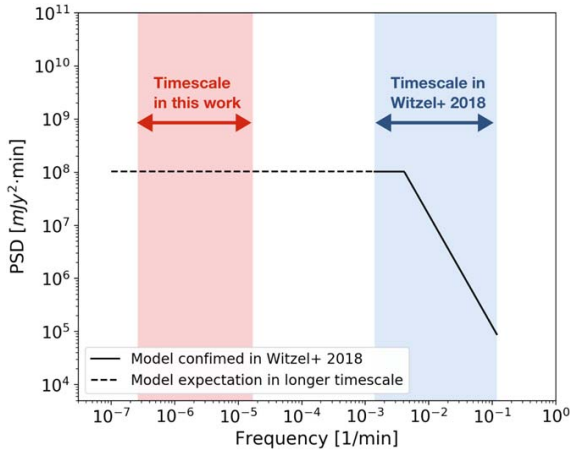

Figure 10. Modeled PSD of Sgr A* presented in Witzel et al. (2018). The solid line shows the broken power-law PSD that has been confirmed in previous short-term variability observations with a break timescale of $\tau \sim 245$ minutes. The dashed line shows the assumed flat PSD in a longer timescale. The blue band marks the timescale probed in existed studies, and the red band marks the timescale that we explored in this work.

The second component describes the distribution of fluxes with a log-normal probability density function (PDF)

$$\mathcal{P}[F](\mu_{\log n}, \sigma_{\log n})] = (\sqrt{2\pi} F \sigma_{\log n})^{-1} \cdot \exp\left(- \frac{\left[\ln\left(\frac{F(K)}{\mathrm{mJy}}\right) - \mu_{\log n} \right]^2}{\sqrt{2}\,\sigma^2_{\log n}} \right), \tag{4}$$

where Sgr A* flux density $F \in [0, \infty]$, log-normal mean in K-band $\mu_{\log n} \in [-\infty, +\infty]$, and log-normal standard deviation in K-band $\sigma_{\log n} \in [0, \infty]$.

Following the method in Timmer & Koenig (1995) and using the modeled parameters in Witzel et al. (2018), we are able to generate the simulated light curves of Sgr A* using the same time series sampling as the real observations following the time of

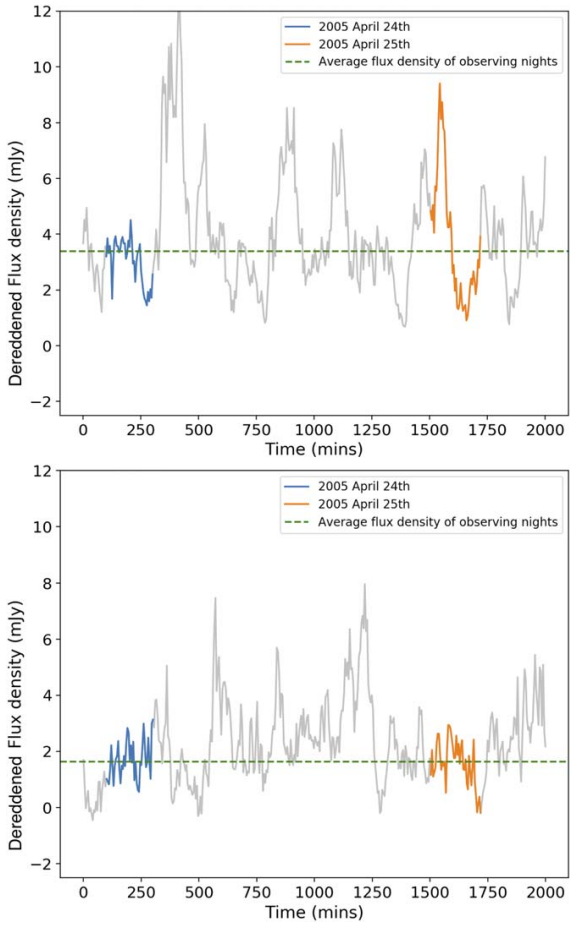

Figure 11. Two examples of the simulated Sgr A* light curve (gray curve) over the two real observing nights in 2005 April (blue and orange parts, respectively). The simulated light curves were generated following the modeled PSD and a log-normal flux distribution, and using the same time series sampling as the real observations (see Section 5.2). The horizontal line shows the average flux density from the two observing nights (blue and orange), which imitates the final combined image.

datacubes. Here we assigned the time of each datacube to be the time of first frame in that cube. We have tested the effects of only using the datacube time series instead of frame time series if considering time delay between each frame. No significant differences were found. We therefore use the datacube sampling for computational efficiency. To create each simulated light curve (with observed flux density), we added Gaussian-distributed noise ($\sigma = 0.035$ mJy, average uncertainty from speckle observations; see Section 4.1.1). In order to convert from observed fluxes at Kp (NIRC2 AO instrument used in this model from Witzel et al. 2018) to our observations at K (NIRC speckle instrument), we did filter transformation for Sgr A* of NIRC2 Kp–NIRC $K = 0.367\ \mathrm{mag}^{+0.01}_{-0.02}$ (see Table 3), similar to the bandpass correction described in Section 4.2.1 and Appendix A.1. As a final step, the dereddened flux of a simulated light curve was obtained following the process presented in Section 4.2.1. See Figure 11 for the examples of the final simulated light curve with dereddened flux.

5.2.2. Comparison of the Simulations to the Observations

We extracted the average flux density of every single simulated light curve (see Section 5.2.1), in order to imitate each real observational image that combines and averages the fluxes from all datacubes. For each epoch, we repeated the simulation 10,000 times using the posterior values from Witzel et al. (2018). See Figure 12 for the distribution of the average dereddened flux density of simulated light curves in 19 available epochs,[14] and Sgr A* observations for comparison.

Then we used simulated Sgr A* light curves to calculate the expectation of Sgr A* average flux and average structure function of our available epochs based on the model described above. In order to take into account the effect of detection limit of observations in simulations, we calculate the expectation of Sgr A* average flux and average structure function only with the simulated fluxes that are higher than the detection limit in that epoch. The steps are as follows.

1. Probe 19 available epochs that have either a detection or a detection limit.
2. Among all 10,000 simulations, for each one set of simulated flux densities from all 19 epochs, mark the epoch if the simulated flux density passes the corresponding Sgr A* detection limit. Calculate one average flux density and one series of structure functions (for all possible pairs of time lags) with only marked epochs. Then generate one Sgr A* average variance.
3. Repeat step (2) for all 10,000 sets of simulations. The number of epochs used to generate each average flux density and series of structure functions varies depending on how many simulated flux densities pass the detection limit in that round.

Figure 13 presents the comparison of Sgr A* average dereddened flux from 13 detected epochs and its expectation calculated above from simulations based on the model in Witzel et al. (2018). Figure 14 presents average structure function of Sgr A* detections and its expectation from simulations. The observed Sgr A* average flux density and average structure function are consistent with the predictions that are modeled from Witzel et al. (2018) with a power-law PSD and log-normal flux distribution. These results show that Sgr A* long-term variability status in the past (1998–2005) is well consistent with the extrapolation from shorter timescale AO-based observations at later time. Sgr A* has had similar brightness and variability characteristics over two decades.

5.2.3. Characteristic Break Timescale

In this work, the flat structure function of Sgr A* calculated from observations indicates that there is no need for a second PSD break in the longer timescale that we investigated here. Any significant increase of power in the PSD between ~80 days and 7 yr can be excluded. Previous studies of timescales from minutes to hours presented a break timescale in the NIR PSD of Sgr A* (Eckart et al. 2006; Meyer et al. 2008, 2009; Do et al. 2009) and the latest analysis (Witzel et al. 2018) reports a correlation timescale of ~245 minutes. Our result is consistent with the assumption of a zero-slope PSD after the correlation timescale based on the model from Witzel et al. (2018). Therefore, the 245 minute timescale remains the only

[14] With either a detection or a detection limit.

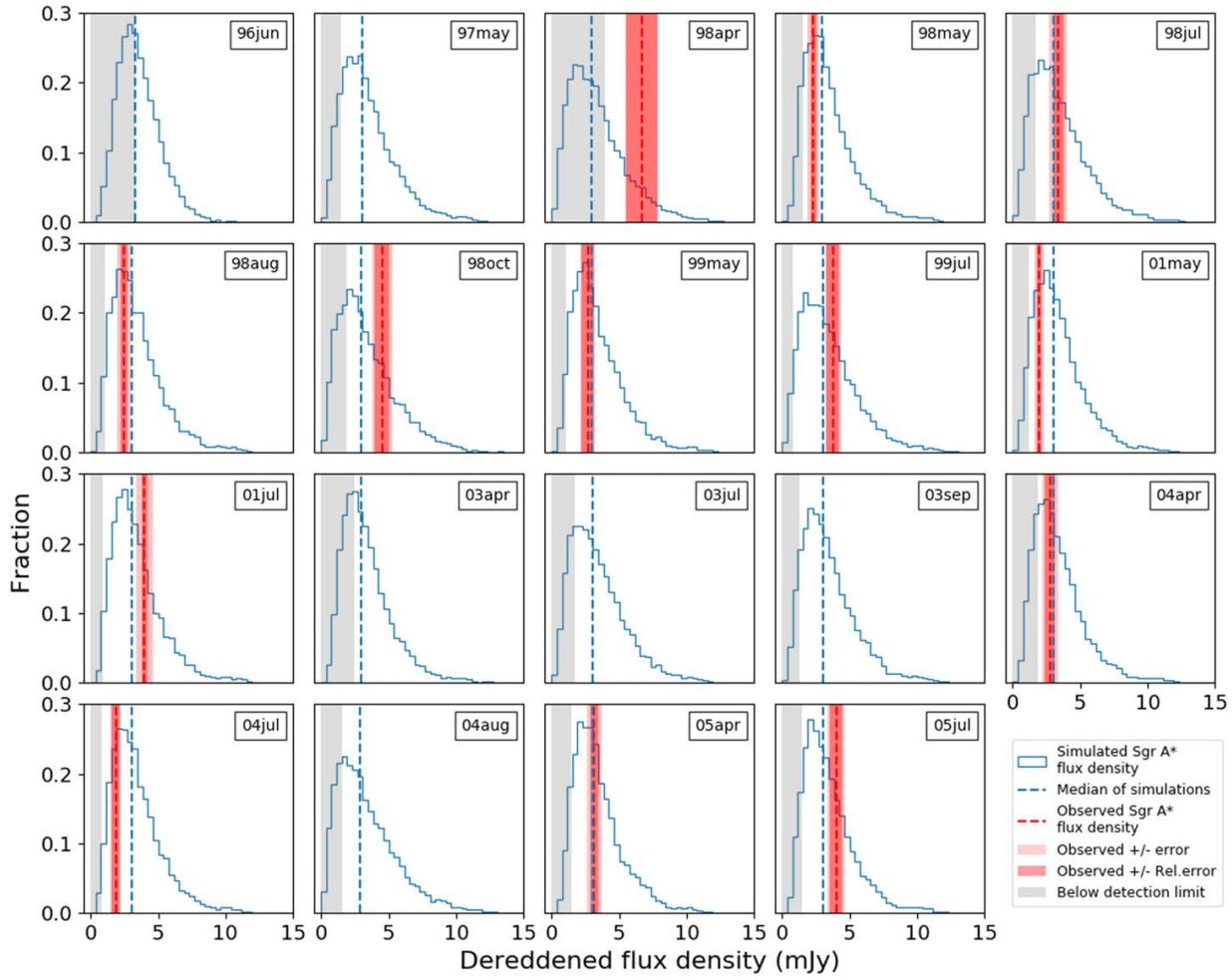

Figure 12. Distribution of average flux densities of 10,000 simulated light curves (Section 5.2.1) compared to the observations of Sgr A*. We probed 19 available epochs with either a detection or a detection limit. The blue curve presents the histogram of 10,000 average flux densities with the median shown as a blue dashed line. The red dashed line with bands marks the observed Sgr A* dereddened flux density with errors (light: total photometric error; dark: relative photometric error only; see Appendix A). The gray shaded region in each epoch presents the fluxes lower than the detection limit (defined in Appendix B.1).

confirmed break timescale in the NIR PSD of Sgr A*. Beyond this break timescale, Sgr A* appears to be uncorrelated with time, and the amplitude of the variations stop increasing.

The speckle era of Keck (1995–2005) that we have explored in this work overlaps with some AO data sets between 2002 and 2005 (VLT NAOS/CONICA 2002–2005; Keck NIRC2 2004–2005). The results of overlapping AO data sets do not show any significant deviations from the average flux obtained with speckle data sets in the same period. Witzel et al. (2018) has summarized and reported the analysis based on AO data sets (VLT NAOS/CONICA 2003-2010; Keck NIRC2 2004–2016). The results obtained from AO measurements appear to be consistent with the speckle results reported in this work.

The characteristic timescale of the X-ray variability of AGNs and black hole X-ray binaries (BHXRBs) has been similarly investigated (see, e.g., Uttley et al. 2002; Markowitz et al. 2003; Uttley & McHardy 2005). Previous studies hypothesized that the characteristic break timescales (the break frequency, observed in BHXRBs) of AGNs scale linearly with the mass of black holes with a correction factor of bolometric luminosity of the accretion flow (McHardy et al. 2006). This led to the conclusion that AGNs are scaled-up galactic black holes. Therefore, the variability of the SMBH at the GC, Sgr A*, serves well as the most under-luminous black hole system to test the scaling relationship of AGNs (Meyer et al. 2009; Witzel et al. 2018).

6. Conclusions

The long-term variability of the SMBH at the GC, Sgr A*, has been studied with the analysis of speckle data (1995–2005) obtained from the W. M. Keck I0 m telescope. The application of the speckle holography technique enables us to investigate Sgr A* with deeper detections than in any previous work. This study presents the first NIR detection of Sgr A* prior to 2002. We are able to monitor the long-term variability of Sgr A* in the NIR with a time baseline of 7 yr with analysis for astrometry and photometry of Sgr A*. We present a Sgr A* light curve from

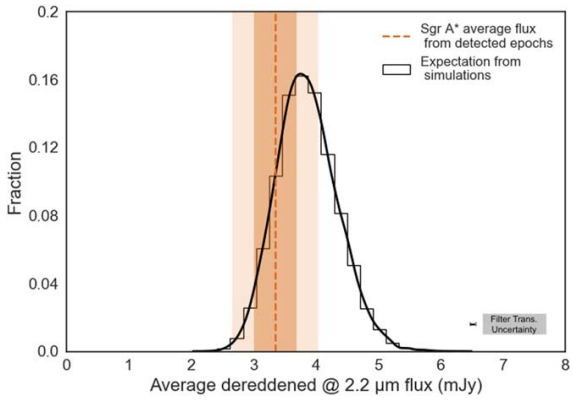

Figure 13. Sgr A* average flux from early observations (1996–2005) and its expectation from simulations based on more recent observations (2006–2017). The orange line with band marks the average dereddened flux calculated from 13 detected epochs with errors (dark: $\sigma/\sqrt{N_{\rm detections}}$; light: $2\sigma/\sqrt{N_{\rm detections}}$). The histogram with corresponding kernel density estimation presents the distribution of expected average flux density from simulations based on the model in Witzel et al. (2018). The errorbar on the bottom right shows the filter transformation uncertainty of 0.04 mJy. Sgr A* has had similar brightness over two decades.

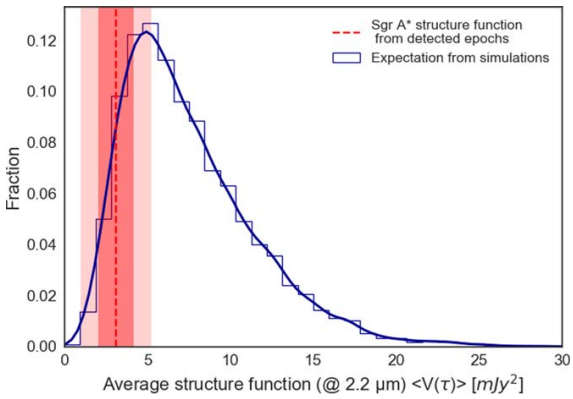

Figure 14. Sgr A* average structure function $V(\tau)$ from observations and its expectation from simulations. The red line with the band marks the average structure function calculated from 13 detected epochs with 1σ error and 2σ error, respectively (see the red points in Figure 8). The blue histogram with corresponding kernel density estimation presents the distribution of expected average structure function from simulations based on the model in Witzel et al. (2018; see the red bands in Figure 8). Sgr A* has had similar variability characteristics over two decades.

1998 to 2005, indicating that Sgr A* was stable and showed no extraordinary flux excursions during this time. The average observed magnitude of Sgr A* as obtained from the last 7 yr (1998–2005) of speckle holography data sets is $K = 16.0 \pm 0.4$ with average relative photometric uncertainty of 0.1 mag, corresponding to the average observed flux density of 0.35 ± 0.13 mJy with average uncertainty of 0.04 mJy. The average dereddened flux density is 3.4 ± 1.2 mJy with a total average photometric uncertainty of 0.6 mJy. The results agree very well with the average observed AO measurements of $K = 16.1 \pm 0.3$ (2005–2017), and are consistent with the extrapolation modeled from AO-based shorter timescale studies. Sgr A* is quite stable without significant change in this time baseline of 7 yr based on the structure function timing analysis, which indicates that 245 minutes still remains the dominant break timescale. Based on the results, the periapse passage of the object G1 did not result in any measurable change of the mean accretion rate onto Sgr A*.

The primary support for this work was provided by NSF, through grant AST-1412615, and UCLA, through faculty salaries. Additional support was received from the Heising-Simons Foundation, the Levine-Leichtman Family Foundation, the Preston Family Graduate Fellowship (held by B.N.S and A.G.), UCLA Galactic Center Star Society, UCLA *Cross–disciplinary Scholars* in *Science* and *Technology* (CSST) Fellowship, NSF *Research Experiences for Undergraduates* (REU) grant No. PHY-1460055, and the European Union's Seventh Framework Programme (FP7/2007-2013)/ERC grant agreement No. [614922] (R.S.). This research was based on data products from the Galactic Center Orbit Initiative (GCOI), which is hosted at UCLA and which is a key science program of the Galactic Center Collaboration (GCC). These data products were derived from data originally obtained from W. M. Keck Observatory. The W. M. Keck Observatory is operated as a scientific partnership among the California Institute of Technology, the University of California, and the National Aeronautics and Space Administration. The authors wish to recognize that the summit of Maunakea has always held a very significant cultural role for the indigenous Hawaiian community. We are most fortunate to have the opportunity to observe from this mountain. The Observatory was made possible by the generous financial support of the W. M. Keck Foundation.

Appendix A
Photometry used in this Work

In order to obtain photometry for sources from the speckle holography images, we performed a two-step procedure. In the first step (Appendix A.1), the photometric systematic scale is established with an uncertainty of 0.14 mag (1σ). In the second step (Appendix A.2), we select a set of stable secondary photometric calibrators to improve the relative photometry to ± 0.04 mag (1σ).

A.1. Photometric System Calibration

We perform photometric system calibration using four initial calibration stars (IRS 16C, IRS 33E, S2-16 and S2-17). These stars are the only ones that have both reference flux measurements as reported by Blum et al. (1996) and are located within our FoV. As Figure 15 shows, IRS 16C is ideally located close to the center of the FoV and therefore measured in every epoch. S2-17 and S2-16 are measured in almost every epoch, and in each epoch typically have more than half of the frames obtained. In contrast, IRS 33E is much closer to the edge of the final FoV and detected in only two-thirds the epochs, and in these epochs it typically has one-third of the frames.

There are three considerations made to convert Blum's measurements into flux predictions for the speckle holography measurements made with NIRC. First and most importantly, we applied an aperture correction to the Blum's measurements to account for the low resolution of their measurements. With $\sim 1''$ seeing, Blum's measurements include neighboring stars that are resolved in our speckle holography observations. Therefore, we did aperture correction by subtracting the fluxes

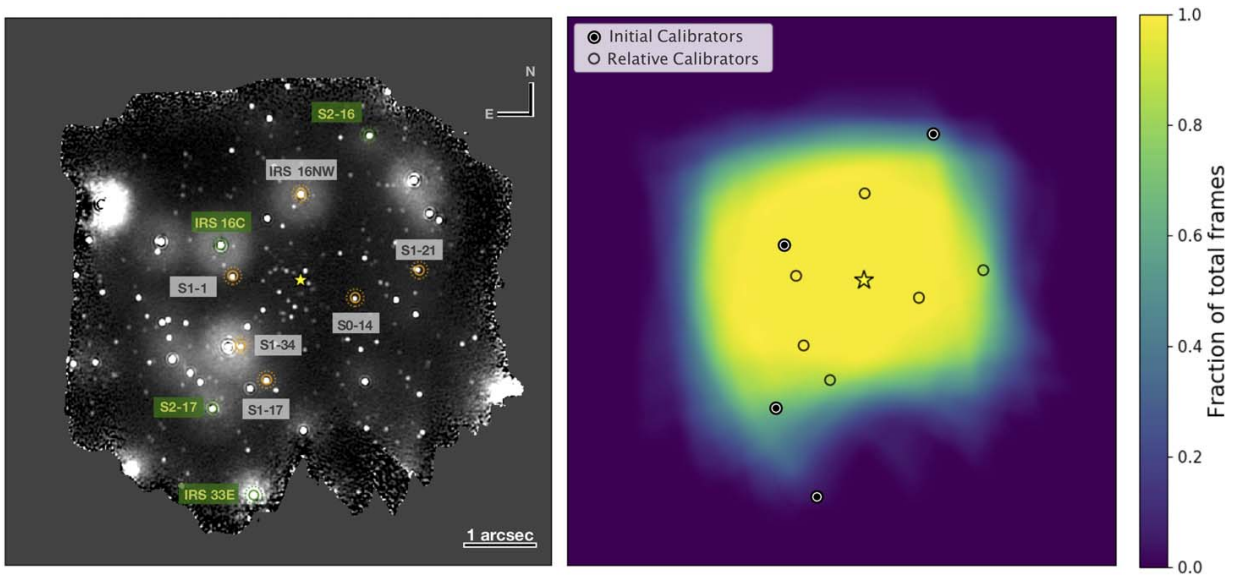

Figure 15. Location of photometric calibrators. Left panel: background is the speckle holography image from 2002 April observation. The four initial photometric calibrators used in photometric system calibration are marked with green circles. The six relative photometric calibrators are marked with orange circles. The yellow star symbol shows Sgr A*'s position. Right panel: the fraction of total frames used in each pixel for the final image from 2002 April observation. Filled circles show initial photometric calibrators, and the open circles show relative photometric calibrators. The relative calibrators are chosen to be isolated stars that uniformly cover the FoV with minimal edge effects.

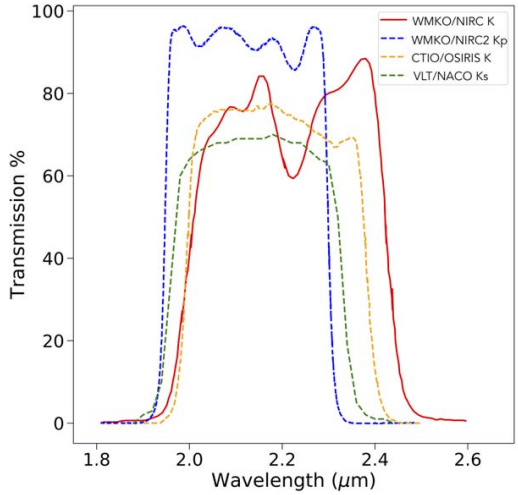

Figure 16. Comparison of the 2 μm bandpass filter used in this work. The transmission curves for the WMKO/NIRC/K (this work), WMKO/NIRC2/Kp (Gautam et al. 2019), CTIO/OSIRIS/K (Blum et al. 1996), and VLT/NAKO/*Ks* (Schödel et al. 2010). Owing to the different transmissions, there are photometric offsets between the filters (see Appendix A.1).

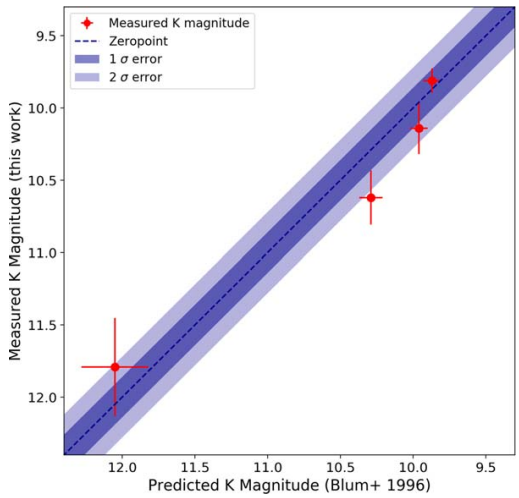

Figure 17. Comparison of our measured *K* magnitude (from photometric system calibration) to the predicted *K* magnitude (bandpass corrected from Blum et al. 1996) for all four initial calibrators (red points with errorbars). The resulting zero-point uncertainty is 0.14 mag (1σ).

of nearby sources within the radius of $\sim 0\farcs5$ aperture. The correction ranges from 0 to 0.3 mag. Second, owing to the slight differences between the bandpass used in Blum et al. (1996) and our NIRC *K* instrument (see Figure 16), there are photometric offsets between the filters. These offsets were calculated by convolving the extincted stellar model atmospheres with the filter functions (see Appendix A in Gautam et al. 2019 for more details). The offsets range from 0.06 to 0.11 mag. Third, the uncertainties in the predicted brightness of the four calibrators are increased by the known level of variability from the work in Gautam et al. (2019). The additional uncertainties range from less than 0.03–0.07 mag, which for each star is less than the uncertainty in the original Blum's measurements. Table 4 summarizes all these considerations and provides the final predictions.

The zero-point for each epoch, zp, was calculated as a weighted mean of the ratios between the calibrators' measured

Table 4
Calibration Stars

Star Name	Calib. Type	N[a] Epoch	Varia.[b] (mag)	$K_{\rm Blum+96}$	Aperture Corr.[c] (δmag)	$K_{\rm NIRC}$-$K_{\rm Blum+96}$	$K_{\rm NIRC,Pred.}$[d]	$K_{\rm NIRC}$ Init.[e]	$K_{\rm NIRC}$ Rel.[f]
IRS 16C	Phot.	27	0.040	9.86 ± 0.05	0.07 ± 0.001	−0.06 ± 0.01	9.87 ± 0.06[g] ± 0.04[h]	9.81 ± 0.04 ± 0.14	9.79 ± 0.08[i]
IRS 33E	Phot.	18	<0.035	10.02 ± 0.05	0 ± 0	−0.06 ± 0.01	9.96 ± 0.06 ± 0.04	10.14 ± 0.04 ± 0.14	10.04 ± 0.07
S2-17	Phot.	26	<0.034	10.03 ± 0.07	0.32 ± 0.007	−0.06 ± 0.01	10.29 ± 0.09 ± 0.04	10.62 ± 0.04 ± 0.14	10.64 ± 0.06
S2-16	Phot.	25	0.070	11.90 ± 0.22	0.26 ± 0.001	−0.11 ± 0.01	12.05 ± 0.23 ± 0.04	11.79 ± 0.09 ± 0.14	11.79 ± 0.10
IRS 16NW	Rel.	27	<0.031	…	…	…	…	10.00 ± 0.04 ± 0.14	10.00 ± 0.05
S1-17	Rel.	26	<0.030	…	…	…	…	12.24 ± 0.04 ± 0.14	12.24 ± 0.04
S1-34	Rel.	26	<0.029	…	…	…	…	12.92 ± 0.04 ± 0.14	12.93 ± 0.04
S1-1	Rel.	27	<0.029	…	…	…	…	12.85 ± 0.04 ± 0.14	12.86 ± 0.04
S1-21	Rel.	25	<0.030	…	…	…	…	13.26 ± 0.05 ± 0.14	13.23 ± 0.05
S0-14	Rel. & Veri.	26	<0.028	…	…	…	13.50 ± 0.03 ± 0.07	13.50 ± 0.04 ± 0.14	13.51 ± 0.05
S0-13	Veri.	27	<0.030	…	…	…	13.22 ± 0.04 ± 0.07	13.21 ± 0.04 ± 0.14	13.23 ± 0.04
S0-6	Veri.	27	<0.030	…	…	…	13.99 ± 0.03 ± 0.07	13.95 ± 0.04 ± 0.14	13.95 ± 0.04
S0-12	Veri.	27	<0.034	…	…	…	14.20 ± 0.04 ± 0.07	14.15 ± 0.04 ± 0.14	14.13 ± 0.05
S0-4	Veri.	27	<0.032	…	…	…	14.17 ± 0.04 ± 0.07	14.22 ± 0.04 ± 0.14	14.20 ± 0.05
S1-10	Veri.	27	<0.029	…	…	…	14.67 ± 0.04 ± 0.07	14.69 ± 0.04 ± 0.14	14.71 ± 0.04
S0-31	Veri.	27	<0.037	…	…	…	15.08 ± 0.05 ± 0.07	14.86 ± 0.06 ± 0.14	14.89 ± 0.07
S1-33	Veri.	27	<0.030	…	…	…	14.82 ± 0.04 ± 0.07	14.92 ± 0.04 ± 0.14	14.89 ± 0.04
S0-11	Veri.	27	<0.035	…	…	…	15.00 ± 0.04 ± 0.07	15.06 ± 0.05 ± 0.14	15.07 ± 0.06
S1-6	Veri.	27	0.069	…	…	…	15.25 ± 0.08 ± 0.07	15.35 ± 0.08 ± 0.14	15.44 ± 0.08
S0-27	Veri.	26	0.049	…	…	…	15.45 ± 0.05 ± 0.07	15.35 ± 0.07 ± 0.14	15.37 ± 0.10
S1-31	Veri.	26	<0.036	…	…	…	15.50 ± 0.05 ± 0.07	15.51 ± 0.05 ± 0.14	15.51 ± 0.09

Notes.
[a] Number of epochs detected in the speckle holography images.
[b] Additional uncertainty from variability (Gautam et al. 2019), which for each star is less than the uncertainty of the original Blum's measurements. Reported in Gautam et al. (2019).
[c] Aperture correction with a radius of 0.″5 (see Appendix A.1).
[d] Predicted NIRC K mag for four initial calibrators obtained from Blum et al. (1996) after aperture and bandpass correction; predicted NIRC K mag for 12 verification calibrators obtained from Schödel et al. (2010) after bandpass correction. See details in Appendix A.1.
[e] Measured NIRC K magnitude after initial photometric system calibration (see Appendix A.1).
[f] Measured NIRC K relative magnitude after relative photometric calibration (see Appendix A.2).
[g] Photometric uncertainty with additional variability uncertainty.
[h] Average photometric systematic zero-point uncertainty.
[i] Relative photometric uncertainty (see Appendix A.2). The average zero-point uncertainty for relative photometry is 0.04 mag.
References. Blum et al. (1996), Gautam et al. (2019).

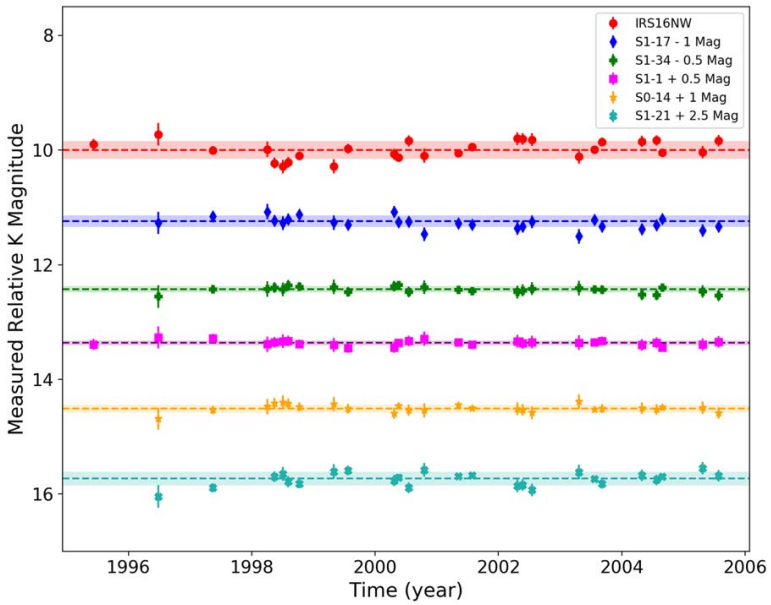

Figure 18. Light curve with measured relative *K* magnitude for each of the secondary calibrator star after relative photometric calibration. The line with band shows the weighted mean and the rms across all detected epochs. The relative photometry has an average uncertainty of 0.04 mag (1σ).

instrumental flux and reference flux ($d_i = f_{i,\mathrm{reference}}/f_{i,\mathrm{measured}}$):

$$\mathrm{zp} = \frac{\sum w_i * d_i}{\sum w_i}. \quad (5)$$

Here, w_i indicates the weight for calibrator i, derived from uncertainty in its reference flux ($\sigma_{f,i}$): $w_i = (\sigma_{f,i})^{-2}$. Zero-point uncertainties in the photometric calibration for each observation epoch, σ_{zp}, were derived from the weighted standard deviation of flux differences (between the calibrator stars' reference magnitudes and measured magnitudes) then divided by $\sqrt{N_{\mathrm{Calibs.}} - 1}$ (here $N_{\mathrm{Sys.Calibs.}} = 4$).

$$\sigma_{\mathrm{zp}} = \sqrt{\frac{\sum w_i (d_i - \mathrm{zp})^2}{\sum w_i}} \Big/ \sqrt{N_{\mathrm{Calibs.}} - 1}. \quad (6)$$

Each epoch's zero-point uncertainty is reported in Table 1. Overall, we achieved an average zero-point uncertainty $\overline{\sigma}_{\mathrm{zp}}$ for the photometric system calibration of 0.14 mag in NIRC *K* bandpass (see Figure 17).

As a final step, we verify that our speckle holography measurements are at the same photometric system as Witzel et al. (2018), whose model is used to simulated the NIR Sgr A* light curves in Section 5.2. Witzel et al. (2012) used and reported 13 stars as photometric calibrators, 12 of which are contained in our studies (see Appendix B). These measurements were tied to the absolute *Ks* observations reported in Schödel et al. (2010). Therefore, we transformed from the VLT NACO *Ks* to NIRC K (see Figure 16 for different transmissions) with bandpass corrections that are similar to that process described above. Figure 3 shows that our measured *K* magnitudes (after photometric system calibration) are highly consistent with the predicted *K* magnitudes (corrected from *Ks* photometric system), with an average difference of only 0.01 ± 0.09 mag (see Table 4).

A.2. Relative Photometric Calibration

We perform relative photometric calibration using the secondary calibrator stars identified by Gautam et al. (2019) that are detected in the FoV of our observations. These calibrator stars, IRS 16NW, S1-17,S1-34, S1-1, S0-14, and S1-21 (see the left panel of Figure 15), are selected to be non-variable and well-distributed in the FoV. The reference fluxes of these calibrators were obtained from the photometric system calibration described in Appendix A.1 (see Table 4). See Figure 18 for the light curve with measured relative *K* magnitude for each of the calibrator after relative photometric calibration. The derivation of the zero-point and uncertainties in the relative calibration is the same as for the photometric system calibration procedure (see Appendix A.1). We achieved an average uncertainty $\overline{\sigma}_{\mathrm{zp}}$ for the relative photometric calibration of 0.04 mag in the NIRC *K* bandpass. See Table 1 for the details of a single epoch.

Appendix B
Source Analyses for Speckle Holography

B.1. Bootstrap Fraction Threshold and Detection Limit

In order to define criteria for real detections, we can use the stellar photometric and astrometric information from the analysis of our extensive AO imaging data (e.g., Jia et al. 2019), which are on the order of three magnitudes deeper than the speckle images. We define a reference set of 88 sources (real stars) in the central $2'' \times 2''$ region with $K < 17.6$ mag (deepest speckle data sets limit) and detected as the same source in at least one-third of 39 AO epochs. The real sources typically have high bootstrap fractions, while the remaining detections have quite low bootstrap fractions. The bootstrap fraction of any given object is defined as

Table 5
Comparison between Speckle Holography version 2_1 and version 2_2

Date		$K_{\rm lim}$ (mag)		$N_{\rm Real\ Stars}$		$N_{\rm pix}$[b]		Max Frames		$N_{\rm ref}$[c]	
(U.T.)	(Decimal)	Value[d]	$\Delta\ m$[e]	Value	Ratio	Value	Ratio	Value	Ratio	Value	Ratio
1995 Jun 9–12	1995.439	17.0	1.15	41	1.21	108042	0.90	5286	1.24	19	0.95
1996 Jun 26–27	1996.485	15.8	0.36	49	1.40	82505	0.79	2336	0.52	22	1.10
1997 May 14	1997.367	16.8	0.48	51	1.21	92467	0.74	3486	2.99	25	0.83
1998 Apr 2–3	1998.251	15.8	0.25	39	1.00	95816	0.78	1730	0.83	24	0.81
1998 May 14–15	1998.366	16.8	−0.02	45	0.92	102328	0.82	7685	0.77	24	0.89
1998 Jul 3–5	1998.505	16.4	0.57	43	1.08	116557	0.83	2053	0.81	24	0.83
1998 Aug 4–6	1998.590	17.1	0.16	47	0.94	109269	N/A[f]	11047	0.46	23	0.77
1998 Oct 9, 11	1998.771	16.6	0.41	45	1.22	97215	0.81	2015	0.87	24	0.80
1999 May 2–4	1999.333	17.2	0.10	52	0.96	107882	0.77	9427	0.96	22	0.81
1999 Jul 24–25	1999.559	17.4	0.73	54	1.02	100567	0.76	5776	0.99	23	0.79
2000 Apr 21	2000.305	15.7	0.13	56	1.81	96248	0.78	662	0.21	21	0.84
2000 May 19–20	2000.381	17.5	0.39	55	0.89	96853	0.80	15591	0.98	23	0.79
2000 Jul 19–20	2000.584	17.0	0.32	63	1.29	86452	0.78	10678	0.98	23	0.82
2000 Oct 18	2000.797	16.2	0.51	52	1.73	82315	0.84	2247	0.88	17	0.74
2001 May 7–9	2001.351	17.2	0.53	64	1.28	85028	0.91	6678	0.85	21	0.84
2001 Jul 28–29	2001.572	17.4	0.22	74	1.21	96872	0.78	6654	0.99	23	0.85
2002 Apr 23–24	2002.309	17.5	0.65	74	1.30	96953	0.79	13469	0.98	23	0.82
2002 May 23–24	2002.391	17.6	0.51	72	1.22	98552	0.83	11860	0.99	21	0.78
2002 Jul 19–20	2002.547	16.8	0.59	69	1.73	99994	0.79	4192	0.72	22	0.81
2003 Apr 21–22	2003.303	16.4	0.32	58	1.49	90963	0.93	3715	0.89	23	0.96
2003 Jul 22–23	2003.554	16.8	0.25	65	1.41	87265	0.79	2914	0.96	24	0.86
2003 Sep 7–8	2003.682	17.1	0.60	74	1.57	95367	0.79	6324	1.00	20	0.77
2004 Apr 29–30	2004.327	16.8	0.15	58	1.07	125423	0.99	6212	0.51	26	1.00
2004 Jul 25–26	2004.564	17.4	0.48	80	1.45	99819	0.78	13085	0.99	22	0.85
2004 Aug 29	2004.660	16.8	0.60	63	1.54	96172	0.96	2299	0.75	25	0.93
2005 Apr 24–25	2005.312	17.1	0.24	70	1.46	105715	0.81	9644	0.88	24	0.89
2005 Jul 26–27	2005.566	16.8	0.81	84	2.33	108360	0.79	5642	0.96	23	0.92

Notes.
[a] $K_{\rm lim}$ is the magnitude that corresponds to the 95th percentile of all K magnitudes in the sample of real stars in the central $2'' \times 2''$ region (see Appendix B.1).
[b] $N_{\rm pix}$ refers to the number of pixels in a given image that meet a .8 of maximum frames used criteria.
[c] $N_{\rm ref}$ refers to the number of reference stars used to align the epoch of data.
[d] All values given in the table are the results of version 2_2.
[e] $\Delta m = K_{\rm lim,2\_2} - K_{\rm lim,2\_1}$, is the detection limit difference between the version 2_2 and the version 2_1. The average magnitude limit has been increased from $K = 16.5$ (version 2_1) to $K = 16.5$ (version 2_2).
[f] The number of pixels in 1998 August is removed due to an artifact in the old holography image.

the portion of bootstrap images (among overall 100 bootstraps) in which the object can be detected (see Step 4 in Section 3.5). We use the remaining sources to estimate the surface density of likely spurious detections in the central $2'' \times 2''$ region at each bootstrap fraction, below which the detection is treated as likely spurious. Assuming a random process we can thus compute the probability of obtaining a false detection within 10 mas search radius around its nominal position, which is a function of the bootstrap fraction threshold that is applied to each epoch (see Figure 19). To avoid false detections, we require that the bootstrap fraction cut of a real source detection in each epoch is obtained and has a probability of a false detection within a 10 mas radius that is always <1%. See Table 2 for the summary of the bootstrap fraction cut.

Then the source detection limit for each epoch is determined to be the 95th percentile of all K magnitudes in the sample, which includes all sources with a bootstrap fraction that is higher than the threshold in the central $2'' \times 2''$ FoV. The median of the detection limit for all epochs is 16.9 mag at K, which corresponds to observed flux of 0.15 mJy and dereddened flux of 1.4 mJy, respectively. See Table 2 for details.

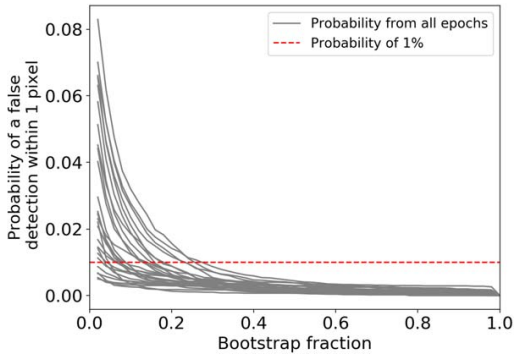

Figure 19. Probability of a false detection within 1 pixel (10 mas square) around its nominal position as a function of bootstrap fraction cut below which the detection is treated as likely spurious. Each gray line presents one epoch's probability function at all possible bootstrap fractions. The bootstrap fraction cut of a real detection in each epoch is set to be the value at which the probability of a false detection within 1 pixel is 1% (red line). This ensures that all detections are real.

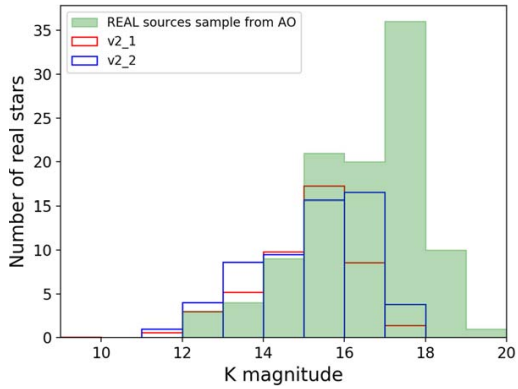

Figure 20. Comparison of the distribution of real detections based on their K-band magnitudes with the original speckle holography (version 2_1, red) and the new implementation presented here (version 2_2, blue). The green histogram shows the distribution of real sources sample defined in Appendix B.1 with their average K' magnitudes from AO observations. The number of real detections for each speckle holography version plotted here is the average from 27 speckle epochs. The new analysis results in deeper detection (∼0.4 mag deeper), and increases significantly the completeness of detection between $K = 15 \sim 17$ mag, where Sgr A* lies.

B.2. Comparison between Speckle Holography version 2_1 and version 2_2

We performed the real source analysis (see Appendix B.1) for both speckle holography version 2_1 and version 2_2, and then obtained the real source lists for two data sets, respectively. Here we compare speckle holography analysis version 2_1 and version 2_2 based on the real detection list in the central $2'' \times 2''$ region.

1. The speckle holography technique version 2_2 results in deeper detections. The average magnitude limit for speckle data has been increased from $K = 16.5$ (version 2_1) to $K = 16.9$ (version 2_2). See Table 5 for details of each epoch. See Figure 20.
2. In >80% epochs, the speckle holography technique version 2_2 results in more real detections. The average number of real detected stars in the central $2'' \times 2''$ region has been increased from $N = 46$ (version 2_1) to $N = 59$ (version 2_2). See Table 5 for details of each epoch.
3. The version 2_2 increases the completeness of detection between $K = 15 \sim 17$ mag, where Sgr A* lies (see Figure 20).
4. The halos around sources, especially bright ones, are reduced in the speckle holography version 2_2 data sets (see Section 3.1 and Figure 1).
5. For the speckle holography version 2_1 data sets, we obtain the uncertainties from running StarFinder on three sub-maps (standard deviation divided by square root 3). For the version 2_2 data sets, we calculate the uncertainties from running StarFinder on up to 100 bootstraps. This new bootstrapping technique gives mathematically more accurate uncertainties.

ORCID iDs

Zhuo Chen https://orcid.org/0000-0002-3038-3896
E. Gallego-Cano https://orcid.org/0000-0002-7452-1496
T. Do https://orcid.org/0000-0001-9554-6062
G. Witzel https://orcid.org/0000-0003-2618-797X
A. M. Ghez https://orcid.org/0000-0003-3230-5055
J. Lu https://orcid.org/0000-0001-9611-0009
M. R. Morris https://orcid.org/0000-0002-6753-2066
A. Dehghanfar https://orcid.org/0000-0003-0518-944X
A. K. Gautam https://orcid.org/0000-0002-2836-117X
A. Hees https://orcid.org/0000-0002-2186-644X
M. W. Hosek, Jr. https://orcid.org/0000-0003-2874-1196
S. Jia https://orcid.org/0000-0001-5341-0765
A. C. Mangian https://orcid.org/0000-0003-2385-6904

References

Abramowicz, M. A., Chen, X., Kato, S., Lasota, J.-P., & Regev, O. 1995, ApJL, 438, L37
Blum, R. D., Sellgren, K., & Depoy, D. L. 1996, ApJ, 470, 864
Boehle, A., Ghez, A. M., Schödel, R., et al. 2016, ApJ, 830, 17
Diolaiti, E., Bendinelli, O., Bonaccini, D., et al. 2000, Proc. SPIE, 4007, 879
Do, T., Ghez, A. M., Morris, M. R., et al. 2009, ApJ, 691, 1021
Dodds-Eden, K., Gillessen, S., Fritz, T. K., et al. 2011, ApJ, 728, 37
Eckart, A., Baganoff, F. K., Schödel, R., et al. 2006, A&A, 450, 535
Eckart, A., & Genzel, R. 1996, Natur, 383, 415
Eckart, A., Genzel, R., Hofmann, R., et al. 1995, ApJL, 445, L23
Gautam, A. K., Do, T., Ghez, A. M., et al. 2019, ApJ, 871, 103
Genzel, R., Schödel, R., Ott, T., et al. 2003, Natur, 425, 934
Ghez, A. M., Hornstein, S. D., Lu, J. R., et al. 2005a, ApJ, 635, 1087
Ghez, A. M., Klein, B. L., Morris, M., & Becklin, E. E. 1998, ApJ, 509, 678
Ghez, A. M., Morris, M., Becklin, E. E., Tanner, A., & Kremenek, T. 2000, Natur, 407, 349
Ghez, A. M., Salim, S., Hornstein, S. D., et al. 2005b, ApJ, 620, 744
Ghez, A. M., Salim, S., Weinberg, N. N., et al. 2008, ApJ, 689, 1044
Ghez, A. M., Wright, S. A., Matthews, K., et al. 2004, ApJL, 601, L159
Gillessen, S., Eisenhauer, F., Trippe, S., et al. 2009, ApJ, 692, 1075
Gillessen, S., Genzel, R., Fritz, T. K., et al. 2012, Natur, 481, 51
Gillessen, S., Plewa, P. M., Eisenhauer, F., et al. 2017, ApJ, 837, 30
Hora, J. L., Witzel, G., Ashby, M. L. N., et al. 2014, ApJ, 793, 120
Hornstein, S. D., Ghez, A. M., Tanner, A., et al. 2002, ApJL, 577, L9
Hughes, P. A., Aller, H. D., & Aller, M. F. 1992, ApJ, 396, 469
Ichimaru, S. 1977, ApJ, 214, 840
Jia, S., Lu, J. R., Sakai, S., et al. 2019, ApJ, 873, 9
Lu, J. R., Ghez, A. M., Hornstein, S. D., Morris, M., & Becklin, E. E. 2005, ApJL, 625, L51
Markowitz, A., Edelson, R., Vaughan, S., et al. 2003, ApJ, 593, 96
Matthews, K., Ghez, A. M., Weinberger, A. J., & Neugebauer, G. 1996, PASP, 108, 615
Matthews, K., & Soifer, B. T. 1994, ExA, 3, 77
McHardy, I. M., Koerding, E., Knigge, C., Uttley, P., & Fender, R. P. 2006, Natur, 444, 730
Melia, F., & Falcke, H. 2001, ARA&A, 39, 309
Meyer, L., Do, T., Ghez, A., et al. 2008, ApJL, 688, L17
Meyer, L., Do, T., Ghez, A., et al. 2009, ApJL, 694, L87
Meyer, L., Ghez, A. M., Schödel, R., et al. 2012, Sci, 338, 84
Meyer, L., Witzel, G., Longstaff, F. A., & Ghez, A. M. 2014, ApJ, 791, 24
Murray-Clay, R. A., & Loeb, A. 2012, NatCo, 3, 1049
Narayan, R., & Yi, I. 1994, ApJL, 428, L13
Narayan, R., Yi, I., & Mahadevan, R. 1995, Natur, 374, 623
Paltani, S. 1999, in ASP Conf. Ser. 159, BL Lac Phenomenon, ed. L. O. Takalo & A. Sillanpää (San Francisco, CA: ASP), 293
Pfuhl, O., Gillessen, S., Eisenhauer, F., et al. 2015, ApJ, 798, 111
Phifer, K., Do, T., Meyer, L., et al. 2013, ApJL, 773, L13
Press, W. H. 1978, ComAp, 7, 103
Primot, J., Rousset, G., & Fontanella, J. C. 1990, JOSAA, 7, 1598
Rafelski, M., Ghez, A. M., Hornstein, S. D., Lu, J. R., & Morris, M. 2007, ApJ, 659, 1241
Reid, M. J. 1993, ARA&A, 31, 345
Sakai, S., Lu, J. R., Ghez, A. M., et al. 2019, ApJ, 873, 65
Schartmann, M., Burkert, A., Alig, C., et al. 2012, ApJ, 755, 155
Schödel, R., Morris, M. R., Muzic, K., et al. 2011, A&A, 532, A83
Schödel, R., Najarro, F., Muzic, K., & Eckart, A. 2010, A&A, 511, A18
Schödel, R., Ott, T., Genzel, R., et al. 2002, Natur, 419, 694
Schödel, R., Yelda, S., Ghez, A., et al. 2013, MNRAS, 429, 1367
Simonetti, J. H., Cordes, J. M., & Heeschen, D. S. 1985, ApJ, 296, 46

Sitarski, B., Do, T., Witzel, G., et al. 2014, AAS Meeting, 223, 238.05
Timmer, J., & Koenig, M. 1995, A&A, 300, 707
Tokunaga, A. T. 2000, in Allen's Astrophysical Quantities, ed. A. N. Cox (4th ed.; Melville, NY: AIP), 143
Uttley, P., & McHardy, I. M. 2005, MNRAS, 363, 586
Uttley, P., McHardy, I. M., & Papadakis, I. E. 2002, MNRAS, 332, 231
Valencia-S, M., Eckart, A., Zajaček, M., et al. 2015, ApJ, 800, 125
Witzel, G., Eckart, A., Bremer, M., et al. 2012, ApJS, 203, 18
Witzel, G., Ghez, A. M., Morris, M. R., et al. 2014, ApJL, 796, L8
Witzel, G., Martinez, G., Hora, J., et al. 2018, ApJ, 863, 15
Witzel, G., Sitarski, B. N., Ghez, A. M., et al. 2017, ApJ, 847, 80
Yuan, F., Quataert, E., & Narayan, R. 2003, ApJ, 598, 301

CHAPTER 3

The Star Formation History of the Milky Way's Nuclear Star Cluster

The nuclear star cluster (NSC) at the Galactic center is the most massive and densest star cluster in the Milky Way, with a mass of $2 \times 10^7\ M_\odot$ (e.g., Launhardt et al. 2002; Schödel et al. 2014). Milky Way's NSC is the only resolved nucleus, enabling us to probe some of the exciting science topics associated with the fundamental physics of the SMBHs and how they impact the formation and evolution of nearby stars. This chapter is driven by the question of what is the star formation history of the NSC, and the related question of what is the number of compact objects at the Galactic center? Chen et al., (submitted) carried out the first star formation history study of the Milky Way's NSC which includes observational constraints from a large sample of stellar metallicity measurements. This study presents that the NSC population is best fitted with a two-component model. Roughly 93% of the stellar mass is metal-rich, with an age of ∼5 Gyr. This dominant component is likely to be ∼3 Gyr younger than previously thought if one assumed a solar metallicity for all stars, challenging the current formation and evolution scenarios at the Galactic center. The minor component ($\sim$ 7%) is metal-poor, with age being uncertain. This study makes updated predictions of number of compact objects (white dwarfs, neutron stars, stellar-mass black holes) in the NSC, and their merger rates for interpreting gravitation waves. Particularly, this study predicts 2 - 4 times fewer neutron stars compared to earlier predictions that assume solar metallicity, introducing a new path to understand the so-called "missing pulsar problem" at the Galactic center.

THE STAR FORMATION HISTORY OF THE MILKY WAY'S NUCLEAR STAR CLUSTER

Zhuo Chen,[1] Tuan Do,[1] Andrea Ghez,[1] Matthew Hosek Jr.,[1] Anja Feldmeier-Krause,[2] Devin Chu,[1] Rory Bentley,[1] Jessica R. Lu,[3] and Mark R. Morris[1]

[1]*Department of Physics and Astronomy, University of California, Los Angeles, USA*
[2]*Max Planck Institute for Astronomy, Königstuhl 17, D-69117 Heidelberg, Germany*
[3]*Department of Astronomy, University of California, Berkeley, USA*

Submitted to ApJ

ABSTRACT

We report the first star formation history study of the Milky Way's nuclear star cluster (NSC) that includes observational constraints from a large sample of stellar metallicity measurements. These metallicity measurements were obtained from recent surveys from Gemini and VLT of 770 late-type stars within the central 1.5 pc. These metallicity measurements, along with photometry and spectroscopically derived temperatures, are forward modeled with a Bayesian inference approach. Including metallicity measurements improves the overall fit quality, as the low-temperature red giants that were previously difficult to constrain are now accounted for, and the best fit favors a two-component model. The dominant component contains 93%±3% of the mass, is metal-rich ($\overline{[M/H]}$ ∼0.45), and has an age of 5^{+3}_{-2} Gyr, which is ∼3 Gyr younger than earlier studies with fixed (solar) metallicity; this younger age challenges co-evolutionary models in which the NSC and supermassive black holes formed simultaneously at early times. The minor population component has low metallicity ($\overline{[M/H]}$ ∼ -1.1 and contains ∼7% of the stellar mass. Using the estimated parameters, we infer the following NSC stellar remnant population (with ∼18% uncertainty): 1.5×10^5 neutron stars, 2.5×10^5 stellar mass black holes (BHs) and 2.2×10^4 BH-BH binaries. These predictions result in 2-4 times fewer neutron stars compared to earlier predictions that assume solar metallicity, introducing a possible new path to understand the so-called "missing pulsar problem". Finally, we present updated predictions for the BH-BH merger rates (0.01-3 $\mathrm{Gpc^{-3}yr^{-1}}$) for detecting gravitational waves.

Keywords: Star formation history, Metallicity, Galactic center, star clusters, late-type stars

1. INTRODUCTION

The innermost region of most galaxies is occupied by a spectacularly dense and massive assembly of stars, which forms the nuclear star cluster (NSC). The star formation in this region is believed to be affected by the central supermassive black hole (SMBH), but the physical mechanisms behind it are not entirely known. The center of the Milky Way galaxy is host to the closest example of a SMBH ($4.2 \times 10^6 M_\odot$, e.g., Ghez et al. 2008; Gillessen et al. 2009; Do et al. 2019), embedded in a NSC ($\sim 2.5 \times 10^7 M_\odot$, e.g., Launhardt et al. 2002; Schödel et al. 2014). Given its proximity, the Milky Way NSC provides a unique opportunity to resolve the stellar population and to study phenomena and physical processes which may be happening in other galactic nuclei.

The star formation history is crucial to our understanding of how the formation of stars connects to the formation of the central SMBH and the Galactic bulge. Previous studies have suggested that the star formation history of the NSC is complex. The stellar population of the NSC is composed of cool, evolved giants; and hot, young main-sequence/post-main-sequence stars. Blum et al. (2003) combined spectroscopic and photometric observations of the 79 most luminous asymptotic giant branch (AGB) and supergiant stars in the central 5 pc. They constructed the Hertzsprung-Russell (H-R) diagram from CO and H_2O molecular absorption features in H- and K-band spectra, and claimed that ∼75% of stars formed more than 5 Gyr ago. Maness et al. (2007) reported the first study using adaptive optics (AO) observations of 329 giants in the central 1 pc, including helium-burning red clump stars, red giants, and AGB stars. These stars with longer-lived evolutionary phases are better understood by theoretical evolutionary models. They derived stellar effective temperature (T_{eff}) using the prominent ^{12}CO 2.2935 μm $\nu = 2$ - 0 rovibrational bandheads, and favored a continuous star formation over the last 12 Gyr with a top-heavy initial mass

function (IMF). Pfuhl et al. (2011) presented AO observations of 450 giants (central 1 pc), and claimed a maximum star formation rate ∼10 Gyr ago to a deep minimum 1-2 Gyr ago, followed by a significant increase during the last few hundred Myrs. They favored a "canonical" Chabrier/Kroupa IMF (Kroupa 2002) which was found in the local universe and is consistent across different star formation regions, and reported that ∼ 80% of the stellar mass formed more than 5 Gyr ago.

The limitation in our current understanding of the NSC star formation history is that previous studies assumed that all stars have solar metallicity. However, possible degeneracies between stellar age and metallicity in the star formation history may potentially cause biases in the age estimates. Earlier works have noted such degeneracies, but were not able to account for them due to limited metallicity measurements. Recent spectroscopic surveys have revealed a significant spread in metallicity of late-type stars from the NSC, which motivates us to revisit the star formation history and its implications for the formation and evolution of the NSC. Do et al. (2015) reported an AO-fed sample (R ∼5,400) of 83 red giants with scaled solar metallicity measurements (henceforth described by $[M/H]$), ranging from sub-solar ($[M/H]$ < -1.0) to metal-rich stars ($[M/H]$ > +0.5). Feldmeier-Krause et al. (2017, 2020) confirmed the broad distribution ($[M/H]$ < -1.0 to $[M/H]$ > +0.3) on a larger sample (R ∼4,000), covering roughly half of the enclosed area of the NSC (R_{eff} ∼ 4.2 pc, Schödel et al. 2014). Ryde & Schultheis (2015) and Rich et al. (2017) also reported a broad distribution with $[Fe/H]$ measurements (R ∼24,000), spanning -0.5 < $[Fe/H]$ < +0.5 for more than 20 M-giants.

Knowing the star formation history of the NSC is important because it allows us to make more accurate predictions of the number of compact objects, including stellar-mass black holes (SBHs), neutron stars (NSs) and white dwarfs (WDs) at the Galactic center, and their rates of mergers for interpreting gravitational wave detections like those from LIGO. Such predictions have been explored assuming different mass profiles (e.g., Baumgardt et al. 2004; Alexander et al. 2007). Morris (1993) reported a total mass of remnants of 0.4 - 5 × 10^6 $M_\odot$, assuming a high low-mass cut-off to the IMF (1 $M_\odot$). Maness et al. (2007) expected a significant mass of dark remnants from a top-heavy IMF. Löckmann et al. (2010) favored a canonical IMF and predicted ∼2.5 × 10^4 SBHs and NSs for every 1.5 × 10^6 $M_\odot$ of total cluster mass. Hailey et al. (2018) reported observations of a dozen quiescent X-ray binaries which contain a SBH, and estimated conservatively ∼600 - 1000 quiescent BH low-mass X-ray binaries (qBH-LMXBs) in the inner 1 pc (or ∼300 - 500 if some observed sources are rotation-powered millisecond pulsars, rMSPs). Generozov et al. (2018) predicted 1 - 4 × 10^4 BHs within the central parsec today, and ∼60 - 200 accreting BH-XRBs currently in the central parsec that formed from tidal capture of stars by BHs. Mori et al. (2021) further confirmed these X-ray sources and reported a lower predicted number of BH-LMXBs with ∼500 - 630 (or ∼240 - 300) in the central parsec. These predictions of BH X-ray binaries provide a lower limit to the total number of BHs in the central parsec. The current limitation is that predictions of compact objects and their merger rates have assumed a canonical IMF and a solar metallicity, which may have large impacts on the resulting compact remnant properties.

In this work, we construct the star formation history of the NSC with the first metallicity constraints. We make updated predictions of the number of compact objects and the resulting gravitational wave merger rates at the Galactic center. The datasets used in this work are described in Section 2. Section 3 presents the methods we use to model the cluster and fit the star formation history. Section 4 reports the results of the star formation history and the impacts of the metallicity constraints on the cluster age. Section 5 further discusses the implications and impacts of the resulting star formation history on the number of compact objects and their merger rates. We conclude with a summary in Section 6.

2. DATASETS

The data for late-type stars used in this work to construct the star formation history of the NSC are from a combination of AO and seeing-limited observations.

2.1. *AO dataset*

A spectroscopic survey of a sample of 83 late-type stars (F-type or later) within a radius of 1 pc from the central SMBH yielded metallicity measurements, $[M/H]$, for all of those stars (Do et al. 2015) (also see details in Støstad et al. 2015). The original spectra were obtained with the medium-spectral-resolution Near-Infrared Integral Field Spectrograph (NIFS) on the Gemini North telescope with the natural-guide-star and laser-guide-star AO system ALTAIR. NIFS provides the observed spectra in the K broadband filter (1.99-2.40 μm) with a spectra resolution of R ∼ 5,000 and a spatial resolution of 115-165 mas. The observations between 2012 May and 2014 May span a projected radius of 8-22 arcsec (0.3-0.9 pc) from Sgr A*, covering a total surface area of 81 $arcsec^2$, approximately 0.15 pc^2 at a distance of 8 kpc. See Figure 3-1 for the location of the fields.

Late-type stars were classified as stars that exhibit strong CO bandheads and Na I doublet absorption lines

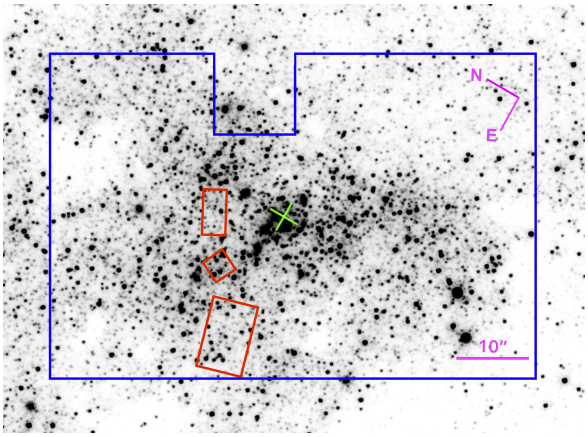

Figure 3-1. Datasets for late-type stars used in this work. Red regions are the Gemini NIFS AO observations (Do et al. 2015), while the blue region shows the VLT KMOS seeing-limited observations (Feldmeier-Krause et al. 2017). The orientation of the Galactic plane runs horizontally through the figure. The green cross in the center shows the position of Sgr A*. The background image is from the HST WFC3-IR observations of the NSC (GO-12182, PI Do).

at 2.2062 and 2.2090 μm, and more precisely classified using the equivalent width (EW) measurements of the lines of these features. For each stellar spectrum, physical parameters were fitted simultaneously with the MARCS synthetic spectral grid (Gustafsson et al. 2008) using the STARKIT code (Kerzendorf & Do 2015): T_{eff}, log g, $[M/H]$, and radial velocity (v_z). We also report the temperature measurements of CO-T_{eff} as derived from the calibrated $T_{eff} - EW_{CO}$ relation (see Appendix B for details). The stars in the sample have a large metallicity range (-1.27 < $[M/H]$ < 0.96), with a mean uncertainty of 0.32 dex. All 83 stars are confirmed to be NSC members after considering different contamination sources and potential biases.

The K_s-band and H-band photometry was obtained by matching the spectroscopic detections to the photometric catalog from Schödel et al. (2010). The matching process was performed by searching stars with location and estimated K magnitudes. The photometry was corrected for dust extinction, A_{Ks}, using the extinction map and extinction law of Schödel et al. (2010). We correct for observational incompleteness of the field using the overall completeness curve derived in Støstad et al. (2015). The overall completeness (both photometric and spectroscopic) is the average likelihood of detecting and classifying stars as a function of stellar brightness. The average total photometric and spectroscopic completeness across the whole field is ∼74% at K_s = 15.5 mag. Do et al. (2015) restricted the analysis to stars with signal-to-noise ratios (S/Ns) greater than 35. We obtained the completeness by multiplying a ratio at each magnitude bin, calculated as the fraction of stars studied by Do et al. (2015) divided by the number of stars in the whole sample. The resulting completeness curve for this dataset shows 50% completeness at K_s ∼15.5 mag.

2.2. *Seeing-limited dataset*

Metallicity determinations were made by Feldmeier-Krause et al. (2017) using a spectroscopic survey of 687 late-type stars within a radius of 1.5 pc from the central SMBH. The original spectra were obtained with seeing-limited observations using the medium-resolution integral-field spectrograph KMOS at the Very Large Telescope (VLT) in the K band filter (∼1.934-2.460 μm). The spectral resolution, R, varies between 3310 and 4660 for 23 different active IFUs on the KMOS detectors with a standard deviation of 300 over all IFUs. The observations on 2013 September 23 covered an area of 2700 $arcsec^2$, approximately 4 pc^2 at a distance of 8 kpc. See Figure 3-1 for the location of the fields.

Late-type stars were classified as stars that exhibit prominent CO bandheads and the Na I doublet absorption lines at 2.2062 and 2.2090 μm, and further confirmed by the measurements of EW_{CO} and EW_{Na}. Each spectrum was fitted with synthetic PHOENIX grid (Husser et al. 2013) using the STARKIT code (Kerzendorf & Do 2015). And the stellar effective temperature was further measured using the calibrated $T_{eff} - EW_{CO}$ relation (see Appendix B). The sample stars have a large metallicity range (-1.25 < $[M/H]$ < 1.00), with a mean uncertainty of 0.27 dex. All 687 stars are confirmed to be NSC members after color analysis to exclude foreground or background sources.

The K_s-band and H-band photometry was obtained by matching spectroscopic detections to the photometric catalogs from Schödel et al. (2010) and Nogueras-Lara et al. (2019). The photometry was corrected for dust extinction using the extinction map and extinction law of Schödel et al. (2010). Stellar extinction values (A_{Ks}) were extracted from the extinction map, which covers 70% of the sample. For stars outside the field of view of the Schödel et al. (2010) extinction map, we used the Nogueras-Lara et al. (2019) extinction map. We correct for observational incompleteness using the completeness from Feldmeier-Krause et al. (2015) and determine separately for stars at different projected radial distances from Sgr A*. The resulting completeness curve for the dataset shows a 50% completeness at K_s ∼14.0 mag.

2.3. *Comparison between the two datasets*

The seeing-limited dataset (50% complete at K_s = 14.0 mag) presents a larger spectroscopic sample

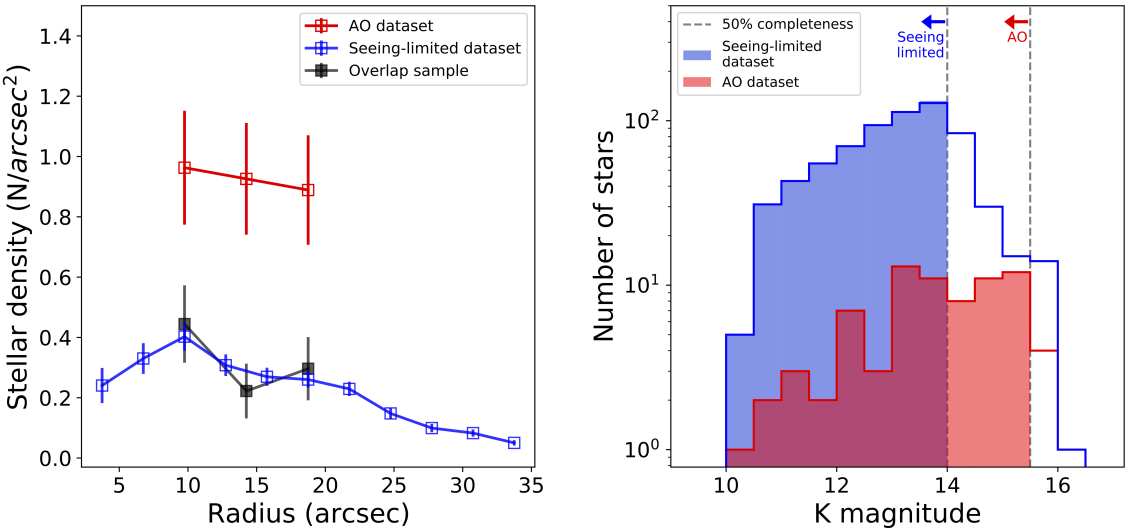

Figure 3-2. Left: Stellar density for two datasets and the overlap sample as a function of distance from Sgr A*. The uncertainties are calculated as $\sqrt{N_{stars}}$/AREA in each radial bin. The seeing-limited dataset (Feldmeier-Krause et al. 2017) enables a larger sample with a much wider coverage, but is limited to a shallower depth. The AO dataset (Do et al. 2015) is deeper in spectroscopic sensitivity, with a much higher stellar density in the observed region. **Right**: Background non-shaded histograms (solid-line edges) show the observed luminosity function of all stars from the AO dataset (red) and the seeing-limited dataset (blue) respectively. Vertical dashed lines mark the detection limits at 50% completeness for each dataset. Shaded regions represent the stars used in this work that are above the 50% completeness.

Table 3-1. Datasets

	Properties	Dataset1	Dataset2	Overlap
Spatial-Related	Atmospheric Correction?	Yes (AO)	No (Seeing-limited)	–
	Angular Resolution, Average (*arcsec*)	0.14 ± 0.03	1.0 ± 0.3	–
	Limiting K mag (50% completeness)	15.5	14.0	14.0
	Sky Coverage ($arcsec^2$)	81	2700	81
	Number of Stars	83	687	27
Spectral-Related	Spectral Resolution	5,400	4,000 ± 700	–
	Spectral Range (μm)	1.99 - 2.40	1.93 - 2.46	–
	Spectral Grid	MARCS	PHOENIX	–
Reference		Do et al. (2015)	Feldmeier-Krause et al. (2017)	–

(N_{stars} = 687) with a much wider coverage (∼2700 $arcsec^2$) than the AO sample. The large sample is essential to obtain robust measurements of the stellar population across the whole field of view. The AO dataset (50% complete at K_s = 15.5 mag) presents a deeper spectroscopic sample with fewer stars (N_{stars} = 83) and a smaller coverage (∼81 $arcsec^2$). The AO spectroscopy is most useful in the innermost dense region and achieves a depth 1.5 magnitudes fainter than the seeing-limited spectroscopy. In the overlapped region between the two datasets, 27 stars were detected in both surveys. See Table 3-1 for the summary. The left panel of Figure 3-2 presents the stellar density for two datasets and the overlap sample as a function of distance from Sgr A*. The right panel of Figure 3-2 presents the luminosity functions of observed stars from the AO and the seeing-limited dataset respectively. In this work, we only use the stars brighter than the 50% completeness in each dataset.

3. METHODOLOGY

In this section, we describe how we model the properties of the NSC by generating synthetic clusters and applying a Bayesian framework (section 3.1 and 3.2). We introduce the prior on the model parameters (section 3.3) and the sampling technique (section 3.4). We present five star-formation history models in section 3.5 and the model selection criteria in section 3.6. The fitter tests on simulated clusters are summarized in section 3.7.

3.1. *Generating a synthetic cluster*

We use a forward-modeling approach to derive the cluster properties by comparing the observational input data to a synthetic cluster within a Bayesian framework. We start with the example of generating a single-age cluster. We use SPISEA, an open-source Python package (Hosek et al. 2020) for simulating simple stellar populations (SSPs), to generate a cluster. The advantage of SPISEA is the ability to control 13 input parameters when generating a cluster. Intrinsic properties (T_{eff}, $log(g)$, etc) and synthetic photometry are assigned for stars spanning the range from pre-main sequence to post-main sequence types. Figure 3-3 presents the top-level diagram of the SPISEA code workflow. The variables used in the cluster modeling are: the cluster age ($log(t)$), cluster metallicity ($\overline{[M/H]}$), total cluster mass (M_{cl}), IMF slope (α), distance to the cluster (d), average extinction ($\overline{A_{Ks}}$), residual differential extinction after the extinction map correction (ΔA_{Ks}), and the minimum and maximum stellar mass (m_{min}, m_{max}) of the IMF. Here we only consider a one-segment IMF with a slope of α between the stellar mass of m_{min} and m_{max}. See Table 3-2 for the summary. We also specify the fixed inputs used in the cluster modeling: stellar evolution model, atmosphere model, extinction law, photometric filters, multiplicity and initial-final mass relation (IFMR).

We use SPISEA to build a theoretical isochrone, which defines the stellar properties at a given age as a function of initial stellar mass, for a given set of model variables and specified inputs. We use the most recent MESA Isochrones and Stellar Tracks (MIST) of the v1.2 stellar evolution model with rotation (Choi et al. 2016; Dotter 2016), to determine the stellar physical properties. MIST is the only end-to-end self-consistent stellar evolution model to produce stars from pre-main-sequence to the post-main-sequence, which avoids merging multiple models; it also agrees broadly with the observations for less massive stars. We use a merged atmosphere model: an ATLAS9 grid (Castelli & Kurucz 2004) for $T_{eff} > 5500$ K and a PHOENIX grid (version 16; Husser et al. 2013) for $T_{eff} < 5000$ K; and the average in the T_{eff} transition region. The intrinsic spectral energy distributions (SEDs) are generated from the atmosphere model, and applied with the total extinction ($\overline{A_{Ks}}$) and the extinction law from Schödel et al. (2010). The synthetic photometry is then calculated by convolving the extinguished SEDs with the K_s and H filter transmission functions.

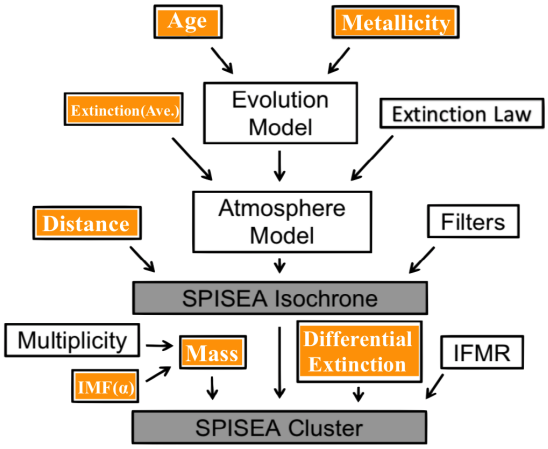

Figure 3-3. Diagram of the SPISEA code (Hosek et al. 2020). The white boxes represent the fixed inputs specified in the modeling while the orange boxes represent the model variables (see Table 3-2). The grey boxes represent the primary SPISEA outputs of the Isochrone and Cluster objects.

We use SPISEA to generate a star cluster, given an isochrone, M_{cl}, ΔA_{Ks}, IMF, and multiplicity within the defined IMF stellar mass range. SPISEA also simulates the differential extinction of stars by perturbing the photometry by a random step from a Gaussian distribution ($\mu = 0$, $\sigma = \Delta A_{Ks}$) at each filter.

3.2. *Bayesian Analysis*

We use a forward-modeling approach to derive the cluster properties by comparing the observational input data to a synthetic cluster within a Bayesian framework. The input observational data includes: stellar K_s magnitude, (H - K_s) *color*, effective temperature (T_{eff}), extinction value (A_{Ks}), metallicity measurement ($[M/H]$) of individual stars, and the total number of observed stars (N_{obs}). See Table 3-2 for summary. The detailed methodology has been described in Lu et al. (2013) and Hosek et al. (2019). The task is to consider the parameter degeneracy and observational uncertainties, and fit the cluster parameters simultaneously. We expand and improve the methodology to a 3-dimensional fitting that for the first time includes stellar measurements of K_s magnitude, *color* and T_{eff} in the modelings, and considers metallicity constraints.

Table 3-2. Model Cluster Variables

	Parameter	Description
Input data	K_s	Stellar K_s magnitude
	color	Stellar (H - K_s) color
	T_{eff}	Stellar effective temperature
	A_{Ks}	Stellar extinction
	$[M/H]$	Stellar metallicity
	N_{obs}	Number of observed stars
Model variable	*logt*	Cluster age
	$\overline{[M/H]}$	Cluster Metallicity
	M_{cl}	Total initial cluster mass[a]
	α	IMF slope
	d	Distance to the cluster
	$\overline{A_{Ks}}$	Average extinction
	ΔA_{Ks}	Differential extinction
	m_{min}	IMF minimum stellar mass
	m_{max}	IMF maximum stellar mass

NOTE—
[a] M_{cl} models the cluster mass with stellar mass between m_{min} and m_{max} (0.8 and 120 $M_\odot$, respectively), over which the IMF is sampled in the cluster modeling.

In order to correct for differential extinction, we differentially deredden the observed stellar K_s magnitude and (H - K_s) *color* to the average extinction value $\overline{A_{Ks}}$ of the input dataset using the extinction map. We define the $K_{s,dered}$ and $color_{dered}$ as the differentially dereddened magnitude and color of the observed stars.

We use Bayes theorem to derive the best-fit cluster model,

$$P(\Theta|\boldsymbol{k}_{obs}, N_{obs}, [M/H]) = \frac{\mathcal{L}(\boldsymbol{k}_{obs}, N_{obs}, [M/H]|\Theta) \cdot P(\Theta)}{P(\boldsymbol{k}_{obs}, N_{obs}, [M/H])} \quad (1)$$

where $\{\boldsymbol{k}_{obs}, N_{obs}, [M/H]\}$ is the input data (see Table 3-2), and $\boldsymbol{k}_{obs}$ is the set of $\{K_{s,dered},\ color_{dered},\ T_{eff}\}$ measurements for the N_{obs} stars observed. Θ is the cluster model defined by the set of model variables $\Theta = \{t,\ \overline{[M/H]},\ M_{cl},\ \alpha,\ d,\ \overline{A_{Ks}},\ \Delta A_{Ks}\}$. $\mathcal{L}(\boldsymbol{k}_{obs}, N_{obs}, [M/H]|\Theta)$ is the likelihood function of observing the data given the model Θ, $P(\Theta)$ captures the prior knowledge on the model variables, and $P(\boldsymbol{k}_{obs}, N_{obs}, [M/H])$ is the sample evidence as a normalizing factor. This calculation results in the posterior probability distributions $P(\Theta|\boldsymbol{k}_{obs}, N_{obs}, [M/H])$ for the given model variables Θ.

The likelihood function is composed of three independent components,

$$\mathcal{L}(\boldsymbol{k}_{obs}, N_{obs}, [M/H]|\Theta) = p(\boldsymbol{k}_{obs}|\Theta) \cdot p(N_{obs}|\Theta) \cdot p([M/H]|\Theta). \quad (2)$$

- $p(\boldsymbol{k}_{obs}|\Theta)$: the probability of observing the distribution of stars in the $\boldsymbol{k}_{obs} = \{K_{s,dered}, color_{dered}, T_{eff}\}$ space.
- $p(N_{obs}|\Theta)$: the probability of detecting the number of observed cluster stars N_{obs} given the observational completeness.
- $p([M/H]|\Theta)$: the probability of measuring the observed $[M/H]$ values for the observed stars.

For the first term $p(\boldsymbol{k}_{obs}|\Theta)$, we calculate the probability of observing the sample of stars by multiplying the individual observed stars' probabilities,

$$p(\boldsymbol{k}_{obs}|\Theta) = \prod_{i=1}^{N_{obs}} p(\boldsymbol{k}_{obs,i}|\Theta) \quad (3)$$

The probability of observing the i^{th} star $p(\boldsymbol{k}_{obs,i}|\Theta)$, given the observed $\{K_{s,dered}, color_{dered}, T_{eff}\}$, is obtained by the probability distribution derived from synthetically "observing" a simulated cluster. We first calculate the intrinsic probability distribution $p(\boldsymbol{k}_{int}|\Theta)_{int}$ for stars in the synthetic cluster. The synthetic cluster is generated given the model Θ with model parameters described in section 3.1 and Table 3-2,

$$p(\boldsymbol{k}_{int}|\Theta)_{int} = Simulated\ Cluster(\Theta) \circledast G(\boldsymbol{\mu}, \boldsymbol{\sigma}) \quad (4)$$

where $\boldsymbol{k}_{int} = \{K_s,\ color,\ T_{eff}\}$ is the distribution of synthetic stellar properties in the model cluster; $G(\boldsymbol{\mu}, \boldsymbol{\sigma})$ is a Gaussian distribution with the mean as the generated values $\boldsymbol{k}_{int}$, and standard deviation from observational errors $\boldsymbol{\sigma} = \{\sigma_{Ks},\ \sigma_{color},\ \sigma_{T_{eff}}\}$. We bin the *Simulated Cluster* stars in 3 dimensions: K_s, $color(H-K_s)$ and T_{eff}. In each dimension, we represent each star as a Gaussian distribution with the mean equal to the generated value, and standard deviation equal to the expected measurement uncertainties based on observations. To reduce the stochastic sampling effects and obtain a more accurate estimate of the probability distribution, all model clusters are generated with a total mass of $5 \times 10^7 M_\odot$.

The intrinsic probability distribution $p(\boldsymbol{k}_{int}|\Theta)_{int}$ is multiplied by the completeness cube $C(\boldsymbol{k}_{int})$ to match the data, and then normalized, to give the probability distribution of observing a star in the model cluster,

$$p(\boldsymbol{k}_{int}|\Theta)_{obs} = \frac{p(\boldsymbol{k}_{int}|\Theta)_{int} \cdot C(\boldsymbol{k}_{int})}{\iiint_V p(\boldsymbol{k}_{int}|\Theta)_{int} \cdot C(\boldsymbol{k}_{int}) d\boldsymbol{k}_{int}} \quad (5)$$

where the completeness cube $C(\boldsymbol{k}_{int})$ is constructed from the observational completeness curve (as a function of K_s, see sections 2.1 and 2.2) and is applied to the 3-dimensional binned simulated cluster $\{K_s, color, T_{eff}\}$, assuming consistency along the axis of color and T_{eff}.

The probability of observing $\boldsymbol{k}_{obs,i}$ for a given star in the input observed data is then calculated by

$$p(\boldsymbol{k}_{obs,i}|\Theta) = \boldsymbol{k}_{obs,i} \cdot p(\boldsymbol{k}_{int}|\Theta)_{obs} \tag{6}$$

The resulting first term of the likelihood is calculated from feeding all stars' probabilities $p(\boldsymbol{k}_{obs,i}|\Theta)$ into equation (3).

For the second term, $p(N_{obs}|\Theta)$, we calculate the probability of obtaining the number of stars we could observe given the cluster model. We apply the observational completeness cube to the synthetic cluster to get the total number of stars (N_{sim}) that we would expect to observe from the model. We then linearly scale the number of stars to the mass of the cluster model to obtain the expected number of observed stars, N_e:

$$N_e = N_{sim} \times \frac{M_{cl}}{5 \times 10^7} \tag{7}$$

The likelihood of observing the number of cluster stars N_{obs} is then taken as a Poisson distribution:

$$p(N_{obs}|\Theta) = \frac{N_e^{N_{obs}} \times e^{-N_e}}{N_{obs}!} \tag{8}$$

For the last term, $p([M/H]|\Theta)$, we model the cluster metallicity distribution as a Gaussian from stellar metallicity measurements $[M/H]$. For each star i, the likelihood of measuring $[M/H]_i$ is

$$p([M/H]_i|\Theta) = \frac{1}{\sqrt{2\pi}\sigma_{total,i}} \times exp(-\frac{([M/H]_i - \overline{[M/H]})^2}{2\sigma_{total,i}^2}) \tag{9}$$

where $[M/H]_i$ and $\sigma_{[M/H],i}$ are the measured stellar metallicity and uncertainty. $\overline{[M/H]}$ is the cluster model metallicity. $\sigma_{\overline{[M/H]}}$ is the intrinsic metallicity dispersion of the NSC, and is conservatively estimated from the standard deviation of the observed sample (0.32).

$\sigma_{total,i} = \sqrt{\sigma^2_{[M/H],i} + \sigma^2_{\overline{[M/H]}}}$. The overall likelihood of metallicity measurements is calculated by multiplying the likelihoods of individual stars together:

$$p([M/H]|\Theta) = \prod_{i=1}^{N_{obs}} p([M/H]_i|\Theta) \tag{10}$$

3.3. *Prior knowledge on the model variables*

We use uniform priors on the model variables: cluster age, cluster metallicity, total cluster mass, and differential extinction. The lower and upper limits of the cluster age are set from the typical age range of late-type stars (30 Myr to 13 Gyr). The upper limit of cluster metallicity ($\overline{[M/H]} = +0.5$) is set from the theoretical stellar evolutionary models (Choi et al. 2016). The upper limit of the cluster differential extinction ($\Delta A_{Ks} = 0.5$) is set with a conservative 5-σ limit, which is 5 times the total uncertainty (systematic and statistical) of the extinction map (Schödel et al. 2010).

Additional prior knowledge is introduced on the model variables: the distance to the cluster and the cluster average extinction ($\overline{A_{Ks}}$). In this work, a Gaussian distributed prior is applied to the distance (μ = 8030 pc, σ = 200 pc) as obtained from the accurate measurements of the Galactic center distance in the literature (Gravity Collaboration et al. 2019; Do et al. 2019). The average extinction ($\overline{A_{Ks}}$) adopts a Gaussian-distributed prior with the mean, μ, being the average of stellar extinction values A_{Ks} of the dataset from the extinction map (Schödel et al. 2010), and the standard deviation, σ, being the total uncertainty (systematic and statistical) of the extinction map.

Simulated synthetic clusters are used to identify possible degeneracies between parameters, and probe the impact of the prior on the fitting results. Several parameters show correlations. The moderate correlation between the cluster age and IMF slope also results in a correlation between the total cluster mass and the cluster age, or the IMF slope. The most massive stars have disappeared at older ages, and thus the total cluster mass would increase to match the observed number of stars brighter than the detection limit. We note that, for late-type stars in our datasets, the stellar mass range is so small that the observations could not constrain the cluster IMF slope in the independent fit. Therefore, we assume that the IMF slope is either a Kroupa IMF ($\alpha = -2.3 \pm 0.36$ for stars with $m > 0.5 M_\odot$, Kroupa 2002) or a top-heavy IMF ($\alpha = -1.7 \pm 0.20$, Lu et al. 2013), and use the corresponding Gaussian distribution as the IMF prior in the fits.

3.4. *Sampling Posterior Probability Distributions with MultiNest*

We use a nested sampling technique (Skilling 2004) called MultiNest (Feroz & Hobson 2008; Feroz et al. 2009), which is a publicly available multi-modal nested sampling algorithm, to obtain detailed probability distribution for cluster parameters given limited observations. This method accounts for the biases from stochas-

Table 3-3. Star Formation History Models

Model	Name	Description	Fitting Parameters
1	Single burst	One burst of star formation	log(t), $\overline{[M/H]}$, M_{cl}, α, d, $\overline{A_{Ks}}$, ΔA_{Ks}
2	Two bursts	Two bursts of star formation	log(t$_1$), log(t$_2$), $\overline{[M/H]}_1$, $\overline{[M/H]}_2$, Fraction$_{M,1}$, M_{cl}, α, d, $\overline{A_{Ks}}$, ΔA_{Ks}
3	Three bursts	Three bursts of star formation	log(t$_1$), log(t$_2$), log(t$_3$), $\overline{[M/H]}_1$, $\overline{[M/H]}_2$, $\overline{[M/H]}_3$, Fraction$_{M,1}$, Fraction$_{M,2}$, M_{cl}, α, d, $\overline{A_{Ks}}$, ΔA_{Ks}
4	Linear SFR	Continuous star formation with a linearly increasing/decreasing SFR[a]	m, $\overline{[M/H]}$, M_{cl}, α, d, $\overline{A_{Ks}}$, ΔA_{Ks}
5	Exponential SFR	Continuous star formation with an exponentially increasing/decreasing SFR[b]	λ, $\overline{[M/H]}$, M_{cl}, α, d, $\overline{A_{Ks}}$, ΔA_{Ks}

Note—
[a] SFR(t) $\propto mt$, where t is the elapsed lookback time starting at 30 Myr and extending as far as 10 Gyr.
[b] SFR(t) $\propto e^{-\lambda t}$, where t is the elapsed lookback time starting at 30 Myr and extending as far as 10 Gyr.

tic sampling of stellar masses, and is less computationally expensive ($\sim$ 5 - 10 times shorter than using the Markov chain Monte Carlo method) with more accuracy in our cases (Lu et al. 2013). For each round of iteration, MultiNest fixes a number of live points to sample the parameter space and calculate the established Bayesian evidence at each point position. The same number of points converge into smaller and smaller patches around the center of the most probable regions until the change of evidence is no longer higher than the selected tolerance value. Here we adopt 600 live points, an evidence tolerance of 0.5, and a sampling efficiency of 0.8 to perform this simulation with a well-sampled parameter space and high efficiency. This MultiNest algorithm is executed by using the python wrapper module PyMultinest (Buchner et al. 2014).

3.5. *Deriving the Star Formation History*

We fit several star formation history models in this work (see summary in Table 3-3):

- One burst of star formation, which is similar to the single age population in the bulge (Genzel et al. 2003).
- Multiple bursts of star formation. We fit up to three bursts in order to distinguish between theoretical models under the current observational uncertainties. See model 2, 3 in Table 3-3. Within each burst, we assume a single metallicity.
- Continuous star formation between 30 Myr and 10 Gyr ago (e.g., Figer et al. 2004). The star formation rate (SFR) is either linearly or exponentially increasing/decreasing. See model 4, 5 in Table 3-3.

3.6. *Model selection and information criteria*

We perform model selection among different star formation history models based on the Bayesian information criterion (BIC). BIC is independent of the prior and penalizes the complexity of the model (number of parameters). For each model, BIC is defined as:

$$BIC = -2ln(\widehat{\mathcal{L}}) + kln(N) \tag{11}$$

where $\widehat{\mathcal{L}}$ is the achieved maximum value of the likelihood function for each model, k is the total number of free parameters used in each model, and N is the number of observed data points used in the modeling. BIC is minimized in the model selection, e.g. the model with the lowest BIC is preferred. Furthermore, we also use the Bayesian evidence (also called "Bayes factor") and the Akaike information criterion (AIC, e.g., Gelman et al. 2013) to further confirm our selection of star formation history models.

3.7. *Testings on Simulated Clusters*

We test our Bayesian methodology by generating a synthetically "observed" cluster, and inputting the simulated sample back to the fitter to derive the probability distribution function for each parameter using the Bayesian inference techniques as described above. See Appendix A for details on the fitter tests. Figure 3-16 in the Appendix shows the output posterior probability distribution for simulated single-age cluster's properties. Each input parameter falls well within the 68% (1σ equivalent) confidence interval of the posterior probability density function. We further examine the fitter on synthetic clusters with different ages, IMFs, multiplicity, metallicity properties, and star formation history

Table 3-4. Model selection between star formation history models

Dataset	Fit	Model	ΔBIC[a]
AO	1	single burst	0
	2	two bursts	**-10.9**
	3	three bursts	0.3
	4	linear SFR	9.8
	5	exponential SFR	6.4
Seeing-limited	1	single burst	0
	2	two bursts	**-3.3**
	3	three bursts	12.0
	4	linear SFR	22.7
	5	exponential SFR	16.9

Note—
[a] We compare the BIC within each dataset. BIC of models is minimized in the model selection, e.g. the mode with the lowest BIC is preferred.

models. Our Bayesian inference methodology is always able to recover the input properties with no significant systematic biases in the tests on synthetic clusters.

4. RESULTS

In this section, we present the fitting results on the AO and seeing-limited datasets independently. Section 4.1 shows that the two-bursts star formation history model is favored by both datasets after model selection. Section 4.2 and 4.3 present the resulting age, metallicity, and other cluster properties from the two-bursts modeling on each dataset respectively. Section 4.4 reports the impact of metallicity constraints on the age estimates of the NSC. We report that the most likely age of the main population of the NSC is ∼3 Gyr younger than that obtained if one assumes solar metallicity as has been done in earlier studies. Section 4.5 further assesses the systematic uncertainties and biases on the cluster age, and presents arguments for why our reported star formation history and cluster properties are robust.

4.1. *Model selection*

The observed data including K_s magnitude, (H - K_s) *color*, extinction (A_{K_s}), effective temperature (T_{eff}), and metallicity ($[M/H]$) of individual stars, and their uncertainties were used in the Bayesian inference to determine the star formation history of the NSC. As introduced in section 2.1 and 2.2, we measure the stellar T_{eff} from the spectra in two ways: CO-T_{eff}, derived from the CO equivalent width; and Starkit-T_{eff}, derived from full spectrum fitting (also see Appendix B for details). Here we present the results based on the CO-T_{eff} method and further discuss the Starkit-T_{eff} in section 4.5.2. We modeled the cluster's physical properties using two datasets independently. For each dataset, we fit the parameters listed in Table 3-3 for different star formation history models including single burst, two bursts, three bursts, continuous star formation with either a linear SFR or an exponential SFR.

Table 3-4 summarizes the ΔBIC between each model for 5 fits on the AO dataset and seeing-limited datasets respectively. The quantities are useful to assess the models favored by the measurements (see section 3.6). The model with the lowest BIC is preferred. For both datasets, the observations show a strong evidence for the two bursts star formation history model (shown in bold in Table 3-4). We further confirm our selection of star formation history model with the Bayesian evidence and the AIC, which all come to the same conclusion. We will show the results from the two bursts model in the rest of the paper for both datasets.

4.2. *AO dataset*

Ten free parameters are fitted to the AO dataset with the two-bursts star-formation history model: mass fraction of burst 1, age of burst 1, age of burst 2, metallicity of burst 1, metallicity of burst 2, total initial cluster mass (in the observed region), distance to the cluster, IMF slope (α), average extinction, and differential extinction. We report the results based on two IMF scenarios (see section 3.3) with either a Kroupa IMF ($\alpha = -2.3 \pm 0.36$, Kroupa 2002) or a top-heavy IMF ($\alpha = -1.7 \pm 0.20$, Lu et al. 2013).

Figure 3-4 shows the 1D posterior probability distributions from the Multinest Bayesian analysis for five of the parameters in the two-bursts modeling assuming a Kroupa and a top-heavy IMF respectively. See Table 3-5 for the fitting results of all parameters with the median and 68% (1σ equivalent) Bayesian confidence intervals, along with the adopted priors. The confidence intervals are calculated by first finding the 50^{th} percentile of the marginalized 1D posterior probability distribution and then stepping away from the center until the integrated probability reaches 68%. We also report the Maximum A Posterior (MAP) value for each parameter.

Here is the summary of the fitting results. With the assumption of **(1) the Kroupa IMF:** the bulk of the stellar mass (93% ± 3%) is modeled to have formed 5.0 $^{+3.4}_{-2.3}$ Gyr ago (Age_{MAP} = 4.7 Gyr), and is metal-rich ($\overline{[M/H]}$ = 0.45 ± 0.05). The burst 2 with 7% ± 3% of the stellar mass is modeled to form 0.8 $^{+3.8}_{-0.7}$ Gyr ago (Age_{MAP} = 1.4 Gyr), and is metal-poor ($\overline{[M/H]}$ = -1.10 $^{+0.30}_{-0.25}$). **(2) top-heavy IMF:** the bulk stellar mass (93%

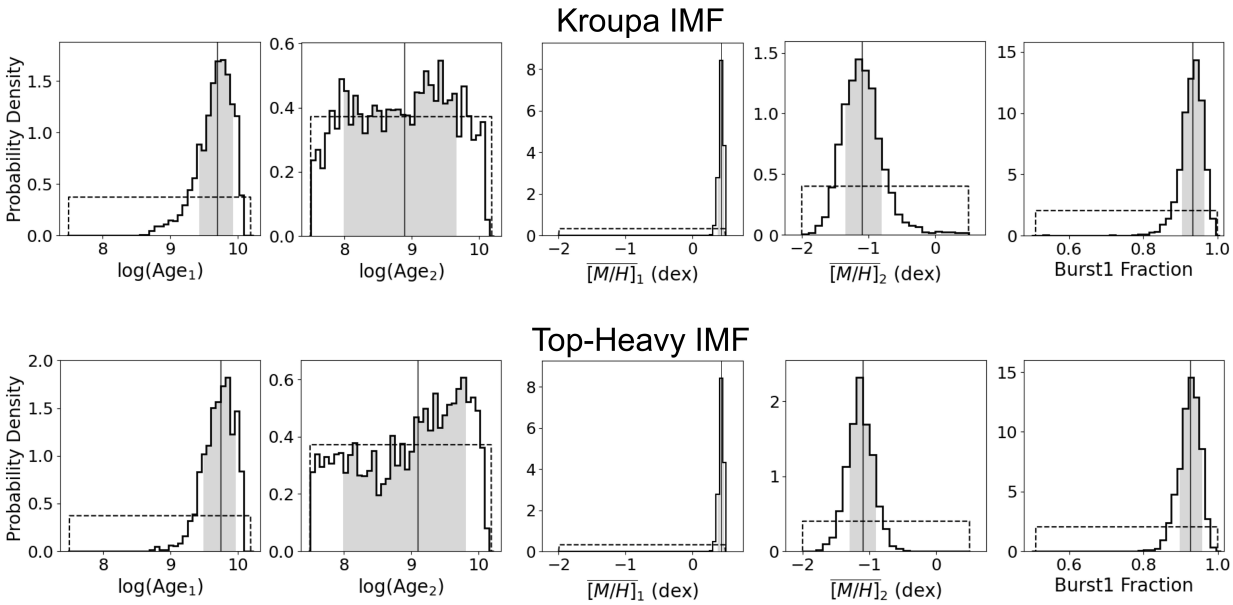

Figure 3-4. Observed marginalized 1D posterior probability density functions of age and metallicity for each burst and the mass fraction of burst 1, based on our two-bursts star-formation history model fitted to the the **AO dataset**. The histograms show the results from the MultiNest Bayesian analysis assuming a Kroupa IMF (**top panels**), and a top-heavy IMF (**bottom panels**) respectively. The vertical solid line shows the weighted median. The shaded region shows the 68% (1σ equivalent) Bayesian confidence interval. The dashed line shows the adopted prior probability distribution. The resulting constraints on the age of burst 1, metallicity of both bursts, and the mass fraction are significant compared with the prior probability distributions. The constraint on the age of burst 2 is relatively weak.

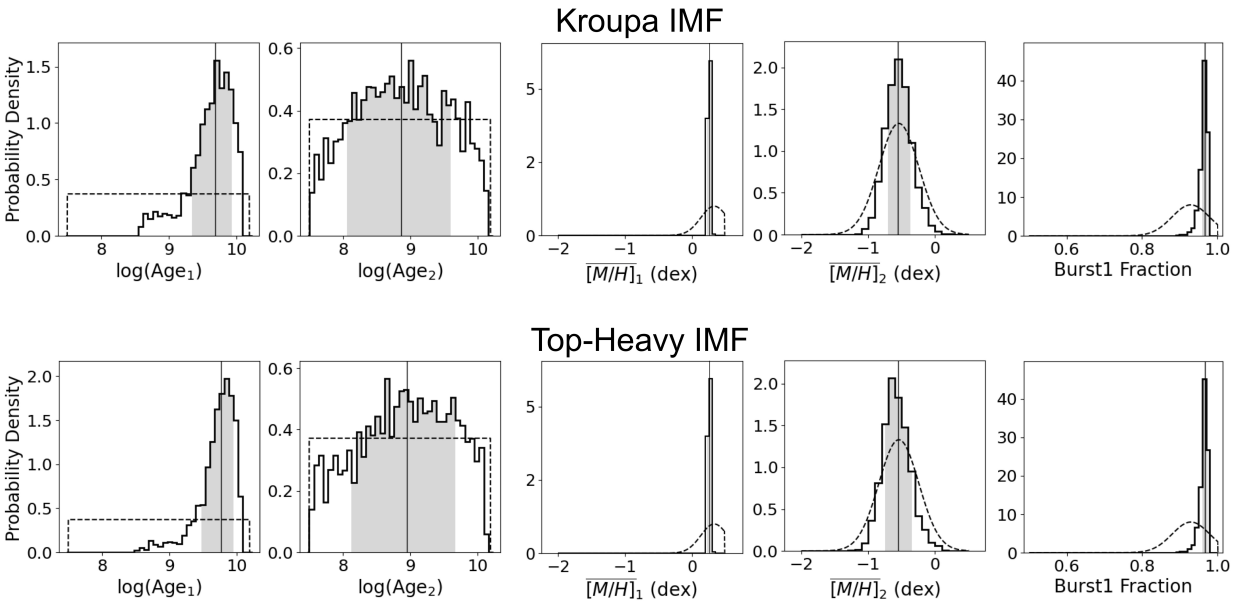

Figure 3-5. Observed marginalized 1D posterior probability density functions from the two-bursts star-formation history model fitted to the **seeing-limited dataset**. The resulting constraints on the age, metallicity, and the mass fraction of burst 1 are significant compared with the prior probability distributions. The constraint on the age of burst 2 is relatively weak. The constraint on the metallicity of burst 2 is largely a reflection of the prior.

$\pm$ 3%) is modeled to form 5.5 $^{+3.4}_{-2.5}$ Gyr ago (Age$_{MAP}$ = 5.6 Gyr), and is metal-rich ($\overline{[M/H]} = 0.45 \pm 0.05$).

Table 3-5. Fitting results for the AO dataset

	Kroupa IMF				Top-heavy IMF			
Cluster properties	MAP[a]	Median	68% interval	Prior[b]	MAP	Median	68% interval	Prior
Mass fraction (burst 1)	0.93	0.93	[0.90, 0.96]	U(0,1)	0.93	0.93	[0.90, 0.96]	U(0,1)
Age of burst 1 (Gyr)	4.7	5.0	[2.7, 8.4]	U_{log}(7.5, 10.12)	5.6	5.5	[3.0, 8.9]	U_{log}(7.5, 10.12)
Age of burst 2 (Gyr)	1.4	0.8	[0.1, 4.6]	U_{log}(7.5, 10.12)	3.2	1.3	[0.1, 6.0]	U_{log}(7.5, 10.12)
Metallicity of burst 1	0.45	0.45	[0.40, 0.50]	U(-2.0, 0.5)	0.45	0.45	[0.40, 0.50]	U(-2.0, 0.5)
Metallicity of burst 2	-1.10	-1.10	[-1.35, -0.80]	U(-2.0, 0.5)	-1.10	-1.10	[-1.30, -0.90]	U(-2.0, 0.5)
Cluster mass[c] ($10^5 M_\odot$)	0.8	1.2	[0.7, 1.7]	U(0.1, 3.0)	4.5	4.2	[2.5, 6.1]	U(0.1, 8.0)
Distance (pc)	8058	8031	[7904, 8158]	G(8030, 200)	7966	8033	[7909, 8156]	G(8030, 200)
IMF slope (α)	-2.37	-2.26	[-2.47, -2.07]	G(-2.30, 0.36)	-1.65	-1.66	[-1.77, -1.55]	G(-1.70, 0.20)
Average extinction	2.61	2.64	[2.56, 2.71]	G(2.64, 0.15)	2.64	2.64	[2.56, 2.72]	G(2.64, 0.15)
Differential extinction	0.12	0.19	[0.07, 0.37]	U(0, 0.5)	0.10	0.21	[0.07, 0.37]	U(0, 0.5)

OTE—
[a] Property values to get the Maximum A posterior (MAP).
[b] U(min, max): Uniform distribution between min and max. G(μ, σ): Gaussian distribution with mean μ and standard deviatic σ.
[c] Total initial cluster mass in the observed region.

Table 3-6. Fitting results for the seeing-limited dataset

	Kroupa IMF				Top-heavy IMF			
Cluster properties	MAP	Median	68% interval	Prior	MAP	Median	68% interval	Prior
Mass fraction (burst 1)	0.98	0.97	[0.96, 0.98]	G(0.93, 0.05)	0.98	0.97	[0.96, 0.98]	G(0.93, 0.05)
Age of burst 1 (Gyr)	5.0	4.9	[2.7, 8.7]	U_{log}(7.5, 10.12)	5.6	5.6	[3.0, 8.9]	U_{log}(7.5, 10.12)
Age of burst 2 (Gyr)	0.8	0.7	[0.1, 4.3]	U_{log}(7.5, 10.12)	0.4	0.9	[0.1, 4.8]	U_{log}(7.5, 10.12)
Metallicity of burst 1	0.30	0.30	[0.25, 0.35]	G(0.33, 0.20)	0.30	0.30	[0.25, 0.35]	G(0.33, 0.20)
Metallicity of burst 2	-0.70	-0.55	[-0.70, -0.35]	G(-0.54, 0.30)	-0.55	-0.55	[-0.75, -0.35]	G(-0.54, 0.30)
Cluster mass ($10^6 M_\odot$)	2.1	1.9	[1.3, 2.6]	U(0.2, 3.5)	8.4	8.0	[4.9, 12.2]	U(1.0, 17.0)
Distance (pc)	8033	8041	[7915, 8162]	G(8030, 200)	8041	8034	[7906, 8156]	G(8030, 200)
IMF slope (α)	-2.28	-2.31	[-2.50, -2.12]	G(-2.30, 0.36)	-1.69	-1.66	[-1.78, -1.55]	G(-1.70, 0.20)
Average extinction	2.79	2.77	[2.69, 2.86]	G(2.76, 0.15)	2.81	2.77	[2.69, 2.85]	G(2.76, 0.15)
Differential extinction	0.21	0.20	[0.07, 0.35]	U(0, 0.5)	0.09	0.20	[0.08, 0.36]	U(0, 0.5)

Burst 2, with 7% ± 3% of the stellar mass, is modeled to form 1.3 $^{+4.7}_{-1.2}$ Gyr ago (Age$_{MAP}$ = 3.2 Gyr), and is metal-poor ($\overline{[M/H]}$ = -1.10 ± 0.20). The age of burst 2 is poorly constrained owing to the small fraction of the total sample size represented by this burst, and consequently the small observed sample size. See Figure 3-11 and 3-12 for the two-dimensional posterior probability density functions.

As discussed in section 3.3, some properties including the total cluster mass, IMF slope and the age show moderate correlations (also see Figures 3-11 and 3-12). At older ages, the most massive stars have disappeared and the total initial cluster mass needs to be increased to match the observed numbers of stars. Assuming a top-heavy IMF results in a higher total cluster mass than when a Kroupa IMF is assumed (4.2 $^{+1.9}_{-1.7}$ × 10^5 $M_\odot$ and 1.2 $^{+0.5}_{-0.5}$ × 10^5 $M_\odot$, respectively). In summary, the fitting results from the two IMF profiles show very consistent modeling within the uncertainties on all cluster properties, except for the total cluster mass.

4.3. *Seeing-limited dataset*

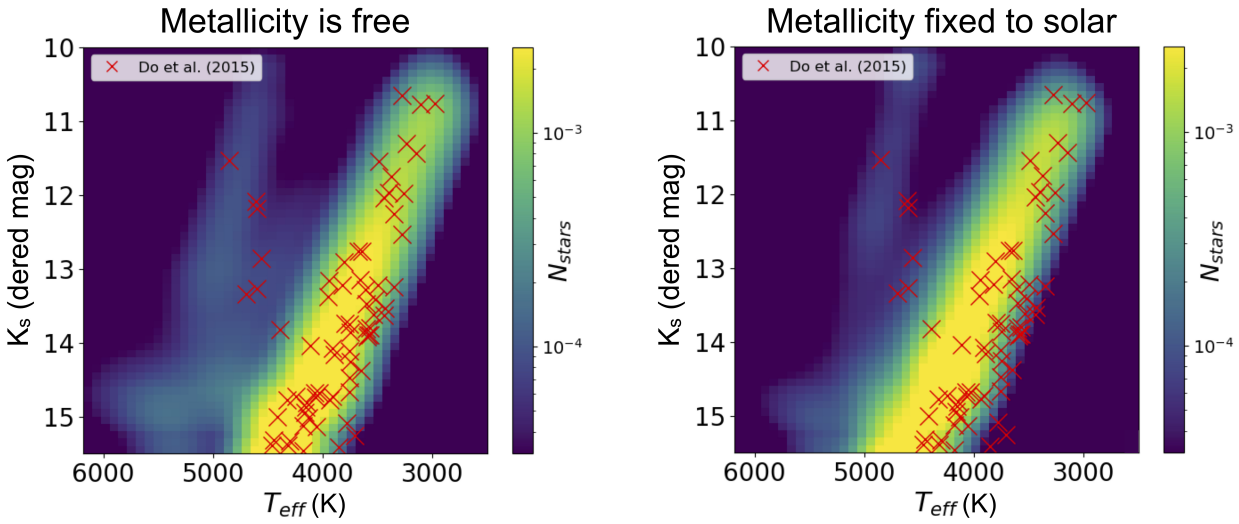

Figure 3-6. Left: Comparison between the observed AO dataset (Do et al. 2015, red crosses) and the predicted Hess diagram with fitting weights from our best-fit star-formation history using the first metallicity constraints. The observed dataset is differentially dereddened at K_s band. The cluster model has been convolved with observational uncertainties and modified by the completeness correction. The AO dataset is well characterized by the two-bursts model of star formation. The bulk stellar mass ($\sim 90\%$) is older and metal-rich (bright strip). The minor group is relatively younger and metal-poor (upper left). **Right:** Comparison between the observed dataset and the predicted Hess diagram with the assumption of solar metallicity ($\overline{[M/H]} = 0$) for all stars in the NSC. With fixed solar metallicity, the age of the bulk stellar mass was modeled to be $\sim$3 Gyr older. Furthermore, we note that, by including metallicity as a free parameter **(left panel)**, our models are able to account for low-temperature red giants that were previously difficult to fit.

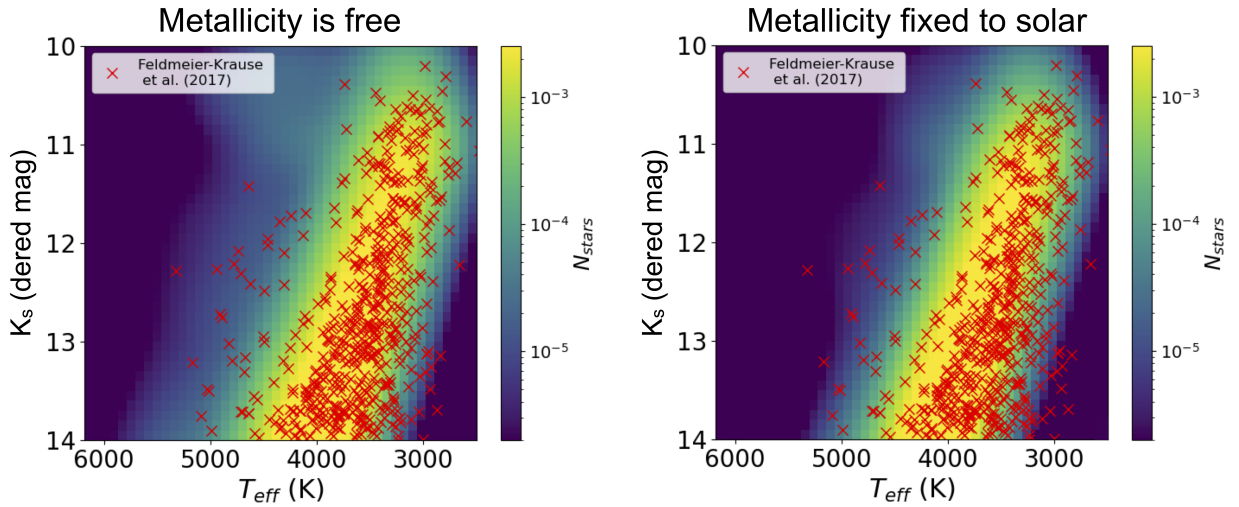

Figure 3-7. Left: Comparison between the observed seeing-limited dataset (Feldmeier-Krause et al. 2017, red crosses) and the predicted Hess diagram with fitting weights from our best-fit star-formation history with metallicity constraints. The observed dataset is well characterized by the two-bursts star-formation model. **Right:** Comparison between the observed dataset and the predicted Hess diagram with the assumption of solar metallicity ($\overline{[M/H]} = 0$) for all stars in the NSC.

Similarly, ten free parameters are fitted in the two-bursts star-formation history model to the seeing-limited dataset under two assumptions of IMF. Specifically, we include the prior knowledge (see Table 3-6) on the mass fraction and metallicity of each burst from the dynamical modeling on this dataset (Do et al. 2020).

Figure 3-5 shows the resulting 1D posterior probability distributions for five of the parameters assuming a Kroupa IMF and a top-heavy IMF respectively. Table 3-6 displays the fitting results for all parameters with their median and 68% (1σ equivalent) Bayesian confidence intervals, the calculated MAP value, and the adopted priors.

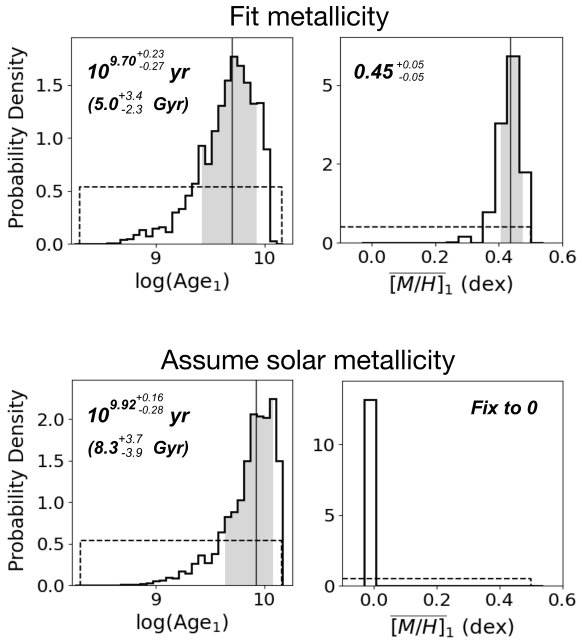

Figure 3-8. Observed marginalized 1D posterior probability density functions for age and metallicity of NSC stars formed in burst 1, assuming a Kroupa IMF in our modeling of the AO dataset. The vertical solid line shows the weighted median. **Top panels:** burst metallicity constrained by stellar metallicity measurements, and the bulk of the stellar mass was modeled to be 5.0 $^{+3.4}_{-2.3}$ Gyr old and metal-rich ($\overline{[M/H]}$ = 0.45 ± 0.05). **Bottom panels:** assuming that stars have solar metallicity, as done by previous works, yields an age of 8.3 $^{+3.7}_{-3.9}$ Gyr. The most likely age for the main population of the NSC is ∼3 Gyr older than our determination if we assume a solar metallicity for all stars.

A summary of the fitting results for the seeing-limited dataset is as follows: with the assumption of **(1) the Kroupa IMF:** the bulk of the stellar mass (97% ± 1%) is modeled to have formed 4.9 $^{+3.8}_{-2.2}$ Gyr ago (Age$_{MAP}$ = 5.0 Gyr), and is metal-rich ($\overline{[M/H]}$ = 0.30 ± 0.05). Burst 2, with 3% ± 1% of the stellar mass, is modeled to have formed 0.7 $^{+3.6}_{-0.6}$ Gyr ago (Age$_{MAP}$ = 0.8 Gyr), and is metal-poor ($\overline{[M/H]}$ = -0.55 $^{+0.20}_{-0.15}$). **(2) top-heavy IMF:** the bulk of the stellar mass (97% ± 1%) is modeled to have formed 5.6 $^{+3.3}_{-2.6}$ Gyr ago (Age$_{MAP}$ = 5.6 Gyr), and is metal-rich ($\overline{[M/H]}$ = 0.30 ± 0.05). Burst 2 with 3% ± 1% of the stellar mass is modeled to have formed 0.9 $^{+3.9}_{-0.8}$ Gyr ago (Age$_{MAP}$ = 0.4 Gyr), and is metal-poor ($\overline{[M/H]}$ = -0.55 ± 0.20). Similar to the AO dataset, the age of burst 2 is poorly constrained. Figures 3-13 and 3-14 provide the two-dimensional posterior probability density functions.

Assuming a top-heavy IMF results in a higher total cluster mass than when a Kroupa IMF is assumed (8.0 $^{+4.2}_{-3.1}$ × 10^6 $M_\odot$ and 1.9 $^{+0.7}_{-0.6}$ × 10^6 $M_\odot$, respectively). In summary, the fitting results from the two alternative IMF profiles show very consistent modeling within the uncertainties on all cluster properties, except for the total cluster mass.

A comparison of the fitting results for the seeing-limited and deeper AO datasets shows consistency between them. In particular, we report consistent age estimates from both datasets for each of the star formation bursts. See the following sections 4.4 and 4.5 for further investigations of the impact of metallicity and systematic uncertainties on the cluster age. Further comparison between the results for each dataset are presented in Appendix C. Regardless of which IMF is assumed, the model prediction for the total current cluster mass is in agreement with the dynamical measurements (e.g., Schödel et al. 2009; Chatzopoulos et al. 2015). No IMF assumption was ruled out by our analyses. The slightly higher mass fraction of burst 1 in the seeing-limited dataset compared to that of the AO dataset is due to the shallower seeing-limited observations and a conservative K magnitude cut (K = 14 mag). A comparison of the observed dataset and the modeled Hess diagram from the inferred parameters of the star-formation history fits is shown in Figure 3-6 (AO dataset) and Figure 3-7 (seeing-limited dataset).

4.4. *Impact of metallicity constraints*

In this work, we report the star formation history of the NSC with the first metallicity constraints as obtained from individual stellar metallicity measurements. In order to understand the impact of metallicity measurements on the age estimates of the NSC, we compare the fitting results with and without metallicity constraints. To assess the effect of modeling metallicity as a free parameter, we repeated the fit of the star formation history with the assumption of fixed solar metallicity ($\overline{[M/H]}$ = 0) for all stars in the NSC as has been done by earlier studies (e.g., Pfuhl et al. 2011). All fitting configurations and priors on the rest of the parameters are consistent for fair comparison. Since the age constraints on the minor group (burst 2) are relatively poor, here we only examine the impact of metal-

Table 3-7. Fitted metallicity vs. fixed solar metallicity for burst 1[a]

		Fit metallicity			Fix to solar metallicity		
Dataset	IMF	Age (Gyr)	$\overline{[M/H]}$	ΔBIC[b]	Age (Gyr)	$\overline{[M/H]}$	ΔBIC[b]
AO	Kroupa	$5.0\ ^{+3.4}_{-2.3}$	0.45 ± 0.05	0	$8.3\ ^{+3.7}_{-3.9}$	0	35.8
	Top-heavy	$5.5\ ^{+3.4}_{-2.5}$	0.45 ± 0.05	-12.0	$8.4\ ^{+3.8}_{-3.5}$	0	37.3
Seeing-limited	Kroupa	$4.9\ ^{+3.8}_{-2.2}$	0.30 ± 0.05	0	$7.9\ ^{+3.5}_{-3.4}$	0	146.5
	Top-heavy	$5.6\ ^{+3.3}_{-2.6}$	0.30 ± 0.05	2.2	$8.7\ ^{+3.0}_{-3.9}$	0	155.2

Note—
[a] The bulk of the stellar mass of the NSC.
[b] We compare the BIC within each dataset. The model with the lowest BIC is preferred.

licity constraints on the age of the bulk of the stellar mass (burst 1). See Table 3-7 for the fitting results and the ΔBIC when we model the metallicity as a free parameter, compared to those with a fixed solar metallicity. The fitted-metallicity models are overwhelmingly preferred over the fixed-solar-metallicity models. When metallicity is fixed to be solar, the median age of the NSC main population increases by $\sim$3 Gyr. For $\sim$90% of the stellar mass, this assumption results an age of $8.3\ ^{+3.7}_{-3.9}$ Gyr (Kroupa IMF) and $8.4\ ^{+3.8}_{-3.5}$ Gyr (top-heavy IMF) from the AO dataset, and $7.9\ ^{+3.5}_{-3.4}$ Gyr (Kroupa IMF) and $8.7\ ^{+3.0}_{-3.9}$ Gyr (top-heavy IMF) from the seeing-limited dataset. The systematic bias to higher ages is due to the fact that high-metallicity stars tend to be cooler and less luminous.

In summary, the most likely age for the NSC main population reported in this work with metallicity constraints is $\sim$3 Gyr younger than that obtained if one assumes solar metallicity. See Figure 3-8 for an example of the comparison with and without metallicity constraints. The comparison of the observed and best-fit modeled Hess diagram from the inferred parameters with and without metallicity constraints are shown in Figures 3-6 and 3-7. Furthermore, we note that, by including metallicity as a free parameter, our models are able to account for low-temperature red giants that were previously difficult to fit.

4.5. *Systematic uncertainties on the cluster age*

We further assess the accuracy of our age estimates of the NSC by considering the impact of systematic errors from the following effects: (i) assumptions regarding the IMF profiles, (ii) using different methods to measure stellar effective temperature (T_{eff}), (iii) priors on the average extinction ($\overline{A_{Ks}}$), (iv) limited metallicity range covered by theoretical stellar evolutionary models and (v) being observed with different spectral resolution, and anlyzed using different spectral grids. Our analyses lead us to conclude that these possible systematic uncertainties do not lead to any substantial bias in the age estimates presented in this work. The reported star formation history and cluster properties, as well as the impact of metallicity constraints, are robust and reliable.

4.5.1. *IMF assumptions*

In order to understand the impacts from the IMF assumptions (see section 3.3), we modeled the star formation history and cluster's physical properties with two IMF scenarios independently: a Kroupa IMF ($\alpha = -2.3 \pm 0.36$, Kroupa 2002) or a top-heavy IMF ($\alpha = -1.7 \pm 0.20$, Lu et al. 2013). Tables 3-5 and 3-6 summarize the comparison of the fitting properties. For both datasets, assuming a top-heavy IMF results in a slightly older age for each burst. The possible systematic offset may come from the moderate correlation between the IMF slope and the cluster age. However, the age difference (either on the median or MAP value) due to the IMF assumptions is always smaller than 1 Gyr, which is much smaller than the 1σ equivalent uncertainty on the age from the 68% Bayesian confidence intervals. No additional systematic uncertainty (or rescaling of the two IMF assumptions) is suggested by the fits. Furthermore, we investigated the impact of metallicity constraints under the two IMF assumptions independently (also see section 4.4 and Table 3-7). Any potential age bias attributable to uncertainties associated with the two IMF assumptions is negligible compared to the age difference resulting from imposing the metallicity measurements, compared to assuming solar metallicity. The impact of metallicity constraints that we report is robust.

4.5.2. *Methods of measuring stellar effective temperature*

We assess the possibility of a systematic offset of cluster age resulting from two different methods of measuring stellar effective temperature: CO-T_{eff}, derived from the calibrated T_{eff}-EW_{CO} (CO equivalent

width) relation (Feldmeier-Krause et al. 2017); and STARKIT T_{eff}, derived from full-spectrum fitting using the STARKIT code (Kerzendorf & Do 2015) with synthetic grids. See Appendix B for details. We followed the same methodology and repeated the modeling of the star-formation history and other cluster properties with Starkit T_{eff}. For both datasets, the differential impact on the fitting results of using the Starkit T_{eff} compared to using CO-T_{eff} is very small (see Table 3-9). No additional systematic uncertainty is suggested by the T_{eff} assumptions adopted for the fits. We further investigated the impact of metallicity constraints using the different T_{eff} independently (see Table 3-9). The age bias due to the different T_{eff} assumptions is negligible, and the impact of metallicity constraints that we present in this work is still robust.

4.5.3. *Priors on model parameters*

Since the extinction and cluster age show moderate correlations, we further investigate the possible systematic uncertainty from the fitting priors adopted for the average extinction ($\overline{A_{Ks}}$, see section 3.3). We tested the fitting bias by repeating the modelings using a more conservative uniform prior on the $\overline{A_{Ks}}$ covering a 5-σ range around the mean of stellar extinction values. The results are consistent and show that no additional systematic bias needs to be considered.

4.5.4. *Limitation of theoretical stellar evolutionary models*

One limitation is that the current upper limit of the metallicity available in all theoretical evolutionary models is $\overline{[M/H]} = +0.5$ (∼3 times solar). The range is limited by the analysis on the opacities and the equation of state (Choi et al. 2016). Both AO and seeing-limited datasets have a fraction of stars with metallicity measurements higher than $[M/H] = +0.5$, though they are more likely subject to greater systematic uncertainties (Do et al. 2015). The posterior distribution of metallicity of burst 1 modeled from the AO dataset has a distribution that peaks near the edge of the grids at $\overline{[M/H]} = +0.5$. This may bring some systematic uncertainties on the resulting cluster age estimates. With improved grids covering a larger metallicity range in the future, we may expect an even younger age of the NSC's main population. Our results present a conservative estimate on the impact of metallicity constraints on the cluster age (see section 4.4).

4.5.5. *Different spectral resolution and grids for two datasets*

We investigate the possible systematic offsets between the two datasets that were observed with different spectral resolution, and analyzed using different spectral grids. As discussed in Feldmeier-Krause et al. (2017), the absolute metallicity measurements above $[M/H] = +0.3$ and below $[M/H] = -0.5$ from the seeing-limited observations are difficult to measure and calibrate to higher accuracy due to the lower spatial and spectral resolution than that of AO. Thus, the systematic uncertainties for those measurements are potentially underestimated. Furthermore, they investigated the influence of spectral resolution, and claimed that a lower spectral resolution would result in a lower $[M/H]$ measurement by a systematic shift of 0.1 dex. We further investigated the effects by re-fitting the AO spectra using the PHOENIX grid for the 27 common stars of the two datasets. The re-fitted metallicity measurements show that both the resolution of the spectra and the grids have about the same effect on the overall difference between the two datasets. In summary, the 27 common stars between two surveys have consistent metallicity measurements within the uncertainties, indicating that the two datasets with different spectral resolution and grids are in reasonable agreement.

In this work, the mean metallicity of the bulk stellar mass (burst 1) is modeled to be 0.45 ± 0.05 (from AO dataset), and 0.30 ± 0.05 (from seeing-limited dataset). They are in good agreement within 2σ difference. In the following, we will use an average metallicity of 0.35 ± 0.05 for subsequent predictions of compact objects and merger rates. The small offset is a reflection of the systematic effects from the two datasets listed above. The mean metallicity of the metal-poor burst from the two datasets are also consistent within 2σ difference. Our reported fitting results represent a robust estimate of the systematic uncertainties introduced from the two datasets. Of particular note, in this work we assume a single metallicity for each burst. We do not model the metallicity dispersion due to the fact that the metallicity spread in the distribution ($\sigma \sim 0.35$) is roughly comparable to the uncertainties on the individual stellar metallicity measurements ($\Delta \sim 0.32$). We may need more data with a higher accuracy in the future to measure the intrinsic dispersion of the metallicity for each burst.

In summary, the systematic uncertainties and bias analyses show that the assumptions on the IMF profiles, methods of measuring stellar effective temperatures, priors on the parameters, limitation of current theoretical stellar evolutionary models and the use of different spectral grids for datasets do not lead to any substantial bias in the estimation of the cluster age presented in this work. The reported star formation history and cluster properties, as well as the impact of metallicity constraints are robust and confident.

Table 3-8. Predicted number of compact objects

Model	IMF	$\overline{[M/H]}$	N_{BH}	N_{NS}
(1)	Kroupa	0.35	1.0±0.2 $\times 10^4$	0.6±0.1 $\times 10^4$
(2)	Kroupa	0	0.9±0.2 $\times 10^4$	1.5±0.3 $\times 10^4$
(3)	Top-heavy	0.35	4.1±0.7 $\times 10^4$	1.4±0.3 $\times 10^4$
(4)	Top-heavy	0	3.4±0.6 $\times 10^4$	2.8±0.5$\times 10^4$

NOTE—
Predictions for every 10^6 $M_\odot$. For each type of compact objects, we report a ∼18% uncertainty on the predicted number.

4.6. *Predicted number of compact objects and their merger rates*

4.6.1. *Compact objects*

One important outcome of the star formation history of the NSC is that it allows us to predict the type and number of compact objects including stellar mass black holes (SBHs), neutron stars (NSs) and white dwarfs (WDs). We calculate the predicted number of compact objects via SPISEA with our most updated star formation history, the first metallicity constraints on the NSC, realistic multiplicity properties (Lu et al. 2013) and the adopted initial-final mass relation (IMFR, Spera et al. 2015; Kalirai et al. 2008).

We predict 1.0 × 10^4 BHs, 6.0 × 10^3 NSs and 3.8 × 10^5 WDs for every 10^6 $M_\odot$ (∼18% uncertainty for each type), with a super-solar metallicity ($\overline{[M/H]}$ = 0.35) and a Kroupa IMF (α = -2.3 ± 0.36, m > 0.8$M_\odot$). See Table 3-8. The fractional uncertainties were estimated by calculating the number of compact objects 500 times and drawing from uncertainties on the IMF and total cluster mass. Assuming the NSC with a total current cluster mass of 2.5 × 10^7 $M_\odot$ (Schödel et al. 2014), we then predict 2.5 × 10^5 BHs, 1.5 × 10^5 NSs and 8.7 × 10^6 WDs in the NSC. Of particular note, the predicted number of neutron stars in this work, when metallicity measurements are included, decreases by a factor of 2 - 4 (see Figure 3-9) compared to earlier predictions, based on the assumption of solar metallicity.

We also predict the number of compact objects under two IMF assumptions: Kroupa and a top-heavy IMF. The IMF profile of the NSC has a significant impact on the resulting compact remnants populations. For a given metallicity, a top-heavy IMF predicts a factor of 3 - 6 times more BHs and 2 - 3 times more NSs than a Kroupa IMF. See Table 3-8 for the summary and Figure 3-9 for the comparison of predicted number of compact objects with different IMF profiles.

4.6.2. *BH-BH merger rate*

We calculate the predicted number of BH-BH mergers N_{merge} that has occurred at the Galactic center,

$$N_{merge} = N_{binary} \cdot f_{stable} \cdot f_{merge} \quad (12)$$

- N_{binary}: Number of massive binary star systems that will form BH-BH binaries at the end of stellar evolution. Calculated for a total cluster mass of 2.5 × 10^7 $M_\odot$, with the updated star formation history, IMF assumption, realistic multiplicity properties and the adopted IMFRs.

- f_{stable}: Fraction of BH-BH binary systems that will produce stable binaries (2.5% - 4.5%; Petrovich & Antonini 2017) and not be torn apart by supernovae.

- f_{merge}: Fraction of stable BH-BH binaries that will eventually merge within 1 Gyr (5.8% - 17%; Petrovich & Antonini 2017; Hoang et al. 2018)

We predict 2.2 × 10^4 (Kroupa IMF) or 2.3 × 10^5 (top-heavy IMF) BH-BH binaries in the NSC, assuming a total cluster mass of 2.5 × 10^7 $M_\odot$.

Currently the fraction of BH-BH mergers modeled from dynamical simulations has only considered the central 0.4 pc (Petrovich & Antonini 2017; Hoang et al. 2018), where the majority of massive early-type stars are found. We thus scale the total predicted number of BH-BH mergers across the NSC down to only those within r = 0.4 pc, based on the 3-dimensional BH radial density profile. The BH number density distribution generally follows a power-law density cusp with n(r) $\propto$ $r^{-\beta}$ near the central SMBH, with the indice range of $7/4 < \beta < 11/4$ covering both severe and weak (Buhcall-Wolf profile) mass segregation scenarios (Alexander & Hopman 2009). With the radial density profile, we predict 0.8-1.0 × 10^4 (Kroupa IMF) or 8.2-9.9 × 10^4 (top-heavy IMF) BH-BH binaries in the central 0.4 pc. By applying to the factors of f_{stable} and f_{merge} in equation 12, we predict a BH-BH merger rate in the range of 0.01-0.16 $Gpc^{-3}yr^{-1}$ (Kroupa IMF) or 0.10-3.03 $Gpc^{-3}yr^{-1}$ (top-heavy IMF). The rate per volume assumes a number density of galaxies of ∼0.02 Mpc^{-3} (e.g., Conselice et al. 2005; Kopparapu et al. 2008). See Figure 3-9 (right) for the comparison of the BH-BH merger rates calculated from two IMF assumptions with a range of possible radial density profiles and different ellipticities (from 0.1 to 1) for the NSC. A top-heavy IMF predicts the BH-BH mergers with a rate up to ∼19 times higher than that with a Kroupa IMF.

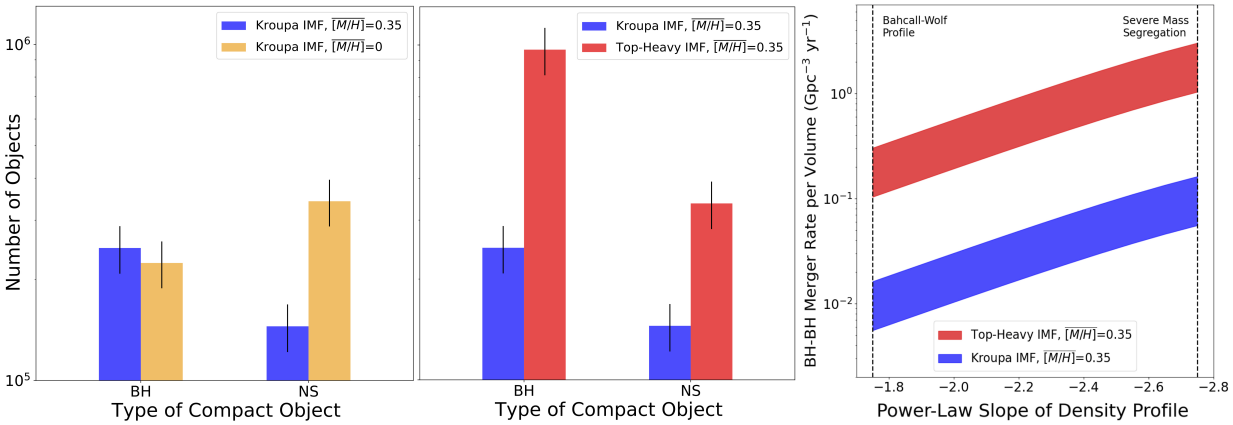

Figure 3-9. IMF and metallicity are crucial properties for predicting the number of compact objects and their merger rates at the Galactic center. **Left panel**: The high metallicity of the main population of the NSC ($\overline{[M/H]}$ = 0.35, blue bar) predicts 2 - 4 times fewer neutron stars than those assuming a solar metallicity ($\overline{[M/H]}$ = 0, yellow bar). **Middle panel**: A cluster with a top-heavy IMF (α = -1.7 $\pm$ 0.2, red) produces 3 - 6 times more black holes and 2 - 3 times more neutron stars than a cluster with a Kroupa IMF. **Right panel**: Comparison of the predicted BH-BH merger rate per volume assuming different IMFs, as calculated from a range of possible 3-d radial density profile of BHs with a power-law indice range of $7/4 < \beta < 11/4$ (Alexander & Hopman 2009) covering both severe and weak (Buhcall-Wolf profile) mass segregation scenarios. The width in the band corresponds to the assumption of ellipticity of the NSC from 0.1 to 1. The top-heavy IMF predicts the BH-BH mergers with a rate of up to 19 times higher than that with a Kroupa IMF.

5. DISCUSSION

5.1. *Comparison with previous work*

Previously the star formation history measurements have assumed a solar metallicity and found the NSC to be 5 - 12 Gyr old. Blum et al. (2003) measured the star formation history from spectroscopy of the most luminous AGB stars in the inner 5 pc, and reported that ∼75% of stars formed more than 5 Gyr ago. Maness et al. (2007) reported AO spectroscopy of late-type stars in the central 1 pc and favored continuous star formation over the last 12 Gyr with a top-heavy IMF. Pfuhl et al. (2011) presented AO spectroscopy for late-type stars in the central 1 pc, and reported that ∼80% of the stellar mass formed more than 5 Gyr ago. Due to the limited metallicity measurements, these spectroscopic studies all assumed a solar metallicity for all stars in the NSC, which would bring large bias on the age estimates as a result of age-metallicity degeneracy. Schödel et al. (2020) presented the star formation history study based on only photometry. They established the K luminosity function for a large sample of stars (down to K∼19 mag) and reported that the age of the cluster could range from 2 to 12 Gyr depending on metallicity assumptions.

In this work, we include metallicity measurements for the first time in modeling the star formation history of the Milky Way NSC. When metallicity is included as a free parameter, we find that the main population of the NSC is metal-rich and likely younger (5.0 $^{+3.4}_{-2.3}$ Gyr). Including metallicity systematically results in a younger age than previous studies (5 - 12 Gyr), there is some overlap in the certainties with previously reported ages. When metallicity is fixed to be solar, the median age increases by ∼3 Gyr. This assumption results an age of 8.3 $^{+3.7}_{-3.9}$ Gyr for ∼90% of the stellar mass, which is in agreement with previous studies with solar metallicity assumption. This bias to higher ages is due to the fact that high metallicity stars tend to be cooler and less luminous. It is therefore important to include metallicity constraints in the star formation history of the NSC.

Our conclusions are consistent with the age of the younger burst in the high metallicity model of Schödel et al. (2020). Schödel et al. (2020) fit for the fraction of stars formed in 17 age bins ranging from 0.03 to 13 Gyr. While this work did not include metallicity measurements, they did explore different metallicity assumptions. For the highest metallicity assumption of 2 times solar, they find that 30% of stars formed at 4 Gyr and 50% of stars formed at 13 Gyr. The 4 Gyr population is consistent with our measurements, but we do not find the older 13 Gyr population. The differences between the two analyses may be from a number of different factors. Schödel et al. (2020) used only Ks photometry while our work uses spectroscopically measured temperatures and H and Ks photometry. Schödel et al. (2020) Ks photometry is deeper (down to K∼19 mag) but properties such as temperature and metallicity require spec-

troscopy to accurately measure. The two analyses also use different fit parameters. Our work considers additional model variables including the total cluster mass, distance to the cluster, IMF slope and differential extinction. Future deeper spectroscopic observations will help to clarify whether the ancient 13 Gyr burst exists in the NSC.

In this work, we test different star formation models and find that a single burst of star formation can explain the origin of 90% of the stars. Previous studies (e.g., Blum et al. 2003; Maness et al. 2007; Pfuhl et al. 2011; Schödel et al. 2020) modeled star formation in this region with a fixed number of age bins and fitting the star formation rate in each bin. The inferred star formation rates range from 0.5×10^{-4} to 8×10^{-4} $M_{\odot}$/yr, but those studies did not do a model comparison to assess whether a single burst can fit most of the data. This is important as star formation in a single burst would imply a star formation rate that could be much higher for a short time. Formation of $\sim 10^7$ $M_{\odot}$ in stars would suggest an extraordinary starburst at the Galactic center during the formation of the NSC. Future work with more stars will be able to test our conclusions with more complex star formation history models.

5.2. *Implication for the co-evolution of the NSC, the SMBH and the bulge*

Surveys of galaxies similar to the Milky Way have shown that their galactic nuclei are often occupied by a massive object of either a NSC, a SMBH, or both (Neumayer et al. 2020). Their NSC mass generally scales with the mass of the bulge (M_{bulge}) and the total stellar mass of the host-galaxy (M_{galaxy}). The scaling relations between the M_{galaxy} and the mass of the central massive object indicate that the SMBH, the NSC and the bulge are undergoing mutual evolution and linked by similar physical mechanisms (e.g. Ferrarese et al. 2006; Georgiev et al. 2016). Specifically, the Milky Way galaxy is the best-studied example for the coexistence of NSC and SMBH (e.g. Ghez et al. 2008; Gillessen et al. 2009; Schödel et al. 2014; Feldmeier et al. 2014) in galaxies with the $M_{galaxy} \sim 10^{10} M_{\odot}$, which represents the transition region between the high-mass galaxies with SMBH dominated and the low-mass galaxies with NSC dominated (e.g., Graham & Spitler 2009; Neumayer & Walcher 2012).

While the existence of a scaling relation between NSC mass and galaxy properties suggest co-evolution of galactic nuclei and their inner bulge regions, our measurement of a younger age of the NSC calls this into question for the Milky Way. We find that roughly 90% of the stellar mass of the NSC formed $5.0\ ^{+3.4}_{-2.3}$ Gyr ago. In comparison, the bulk of the metal-rich stellar population of the Galactic bulge has an age of 10 ± 2.5 Gyr (Zoccali et al. 2003). In addition, SMBHs are believed to build in at early times and have existed in the galaxy more than 12 Gyr ago (e.g., Fan et al. 2001; Volonteri 2010). The younger age of the NSC suggests that the NSC, the SMBH and the bulge might not be co-eval. If the NSC and SMBH in the Milky Way is not just two types of a single central massive object, it means that there are likely different physical processes that regulate their growth and evolution.

5.3. *Implication for the formation of the NSC*

A metallicity and age for the Milky Way NSC may offer constraints on its formation mechanisms. The formation of the NSC is still poorly understood, but two main scenarios of the formation process have been proposed. One is in-situ scenario (Milosavljević 2004), where gas falls onto the center of the galaxy and then triggers star formation within the cluster or the accretion of star clusters formed in the vicinity. The other is migration scenario (Tremaine et al. 1975), where globular clusters that formed elsewhere migrate towards the central region through dynamical friction mechanism, and then fall in and merge with each other (Andersen et al. 2008; Antonini 2013). Both scenarios could also operate at the same time. The two formation scenarios imprint specific observable signatures on the ages and metallicities of the stellar population of NSC. If the in-falling globular clusters were the main contributions to the stars in the NSC, we would expect a large fraction of mass with a very old age and a sub-solar metallicity which are comparable to typical globular clusters. Most globular clusters in the Milky Way (more than 95%) have a low metallicity with $\overline{[M/H]} < -0.3$ (Harris 2010), and an age older than 11.2 Gyr (Krauss & Chaboyer 2003). This work showing a younger age ($\sim$5 Gyr old) and a higher metallicity($\overline{[M/H]} \sim 0.35$) for the bulk stellar mass of the NSC, is inconsistent with the globular clusters in-falling scenario as a dominant mechanism for the main population of the NSC.

The high-metallicity and relatively young age ($\sim$ 5 Gyr) suggests that the bulk of the NSC formed in-situ. Chemical evolution models suggest that the chemical enrichment of the Galactic center can occur very rapidly at time scales of 0.1 - 0.7 Gyr (Grieco et al. 2015). The higher metallicity of the NSC also follows the trend in the the Galactic inner disk or the Galactic bulge, where the stellar metallicities are generally higher towards the Galactic center (Trevisan et al. 2011; Bensby et al. 2013; Feltzing & Chiba 2013).

While the bulk of the cluster may have formed in-situ, about 10% of the stars have metallicity at half-solar or less, which is consistent with an infall of a globular cluster or dwarf galaxy. These lower metallicity stars also appear to have different kinematic signatures than the super-solar metallicity stars, which is the further evidence that the two groups of stars may have different origins (Do et al. 2020). Furthermore, the alpha elemental abundances of the low-metallicity population are also consistent with an infalling cluster or dwarf galaxy (Bentley et al. 2022). Age constraints on the low metallicity stars could help to differentiate between the formation scenarios. Simulations from Arca Sedda et al. (2020) of an infall of a star cluster in a galactic nucleus using N-body simulations suggest that the infall of a massive star clusters should occur in ∼0.1 - 3 Gyr ago to remain the current distinguishable kinematic features as observed. However, our model has poor age constraints on the lower metallicity stars due to their small sample size. Additional age constraints will be important to assess whether this population is consistent with the results of these simulations.

5.4. *Implications of the predicted number of compact objects and their merger rates*

5.4.1. *The "missing-pulsar problem"*

This work predicts 2 - 4 times fewer neutron stars with a super-solar metallicity ($\overline{[M/H]} \sim 0.35$), compared to earlier predictions assuming a solar metallicity. Two major effects result a smaller number of predicted number of neutron stars at the Galactic center. With a higher metallicity, an increased mass loss by the stellar wind on the main-sequence is expected (e.g., Kudritzki et al. 1987; Leitherer et al. 1992; Vink et al. 2001). Metallicity also impacts the supernova explosion process which determines the remnant mass of the progenitor (e.g., Fryer et al. 2012). With a higher metallicity, higher supernova progenitor masses are necessary to produce neutron stars (e.g., Poelarends et al. 2008). Both of these factors lead to smaller remnant mass, and thus more white dwarfs compared to neutron stars. In addition, neutron stars occupy in a small range of masses (1.4 - 3 $M_\odot$), and thus are more sensitive to fraction changes in the remnant masses than stellar mass black holes, which occupy a greater range in masses (Figure 3-10).

If the Galactic center has fewer neutron stars than expected, then this may help us understand the "missing-pulsar problem". The astronomical community has surveyed for decades at the Galactic center without detecting a population of pulsars as expected (e.g., Johnston et al. 1995; Bates et al. 2011; Torne et al. 2021). Here we show that the number of pulsars we expect depends on stellar metallicity, which should be considered when evaluating how many pulsars are "missing" at the Galactic center.

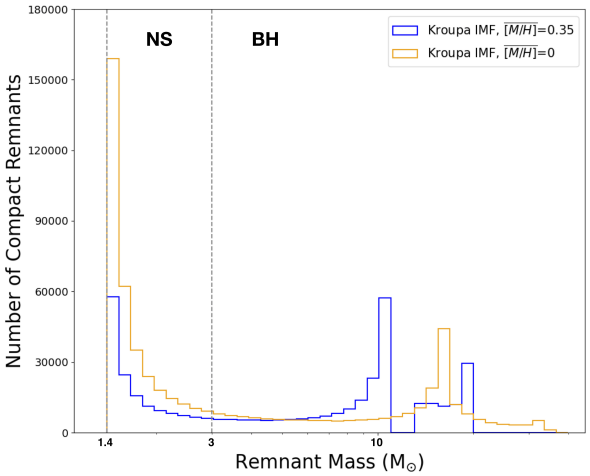

Figure 3-10. Predicted number of compact remnants as a function of remnant mass with a super-solar metallicity reported in this work ($\overline{[M/H]} = 0.35$, blue) or a solar metallicity ($\overline{[M/H]} = 0$, yellow). Dashed lines show the thresholds to differentiate WD and NS (M_{rem} = 1.4 $M_\odot$), NS and BH (M_{rem} = 3 $M_\odot$). Metallicity impacts both the mass loss by stellar wind and the supernova explosion process, and thus the remnant mass. A high metallicity ($\overline{[M/H]} = 0.35$) predicts 2 - 4 times fewer neutron stars as a result of smaller remnant masses. Neutron stars occupy in a small range of masses (1.4 - 3 $M_\odot$), and thus are more sensitive to fraction changes in the remnant masses than stellar mass black holes.

5.4.2. *Gravitational-wave merger rate*

Since 2016, the Advanced Laser Interferometer Gravitation-Wave Observatory (LIGO) and VIRGO have enabled direct detections of gravitational waves from in-spiraling compact object binaries (LIGO Scientific Collaboration & Virgo Collaboration 2016a,b, 2017; Abbott et al. 2016a,b,c, 2017a,b). The location and rate of these gravitational wave sources are important for understanding their nature. Dense star clusters such as NSCs at the center of galaxies are thought to be the major source of these mergers since these regions are expected to be abundant in SBHs and BH-BH binaries with higher merger rates (Antonini et al. 2010; Portegies Zwart & McMillan 2000; Wen 2003; O'Leary et al. 2006, 2009, 2016; Kocsis & Levin 2012; Antonini & Perets 2012; Antonini et al. 2014; Rodriguez et al. 2016b; VanLandingham et al. 2016; Bartos et al. 2017b; Stone et al. 2017; Hoang et al. 2018).

The center of the Milky Way offers us the ideal prototype for constraining the compact object population of galactic nuclei and gravitational-wave merger rates. Previous studies reported a BH-BH merger rate in the proximity of galactic nuclei with a range of 0.6-15 $Gpc^{-3}yr^{-1}$ (Petrovich & Antonini 2017) or 1-3 $Gpc^{-3}yr^{-1}$ (Hoang et al. 2018). In this work, with our updated star formation history of the NSC, we predict a BH-BH merger rate in the range of 0.01-0.16 $Gpc^{-3}yr^{-1}$ (Kroupa IMF) or 0.10-3.03 $Gpc^{-3}yr^{-1}$ (top-heavy IMF). We find that the predicted number of black hole mergers are most sensitive to the IMF, IMFR, and the density profile. The number of black holes are not very sensitive to metallicity, so these values are consistent with previous literature predictions.

5.4.3. *Improving compact object predictions*

The most important factors on the predicted number of compact objects and their merger rates are: the IMF, IFMR, and the compact object density profile. Currently the observations are not deep enough to constrain the cluster IMF simultaneously with the star formation history. Additional observations of stars with metallicity measurements will allow us to fit for the IMF. In addition, the IFMR prescription also affects the number of compact objects predicted for a given star formation history and is a function of stellar properties (e.g., Heger et al. 2003; Sukhbold et al. 2018). Better calibrations of the IFMR will lead directly to more accurate predictions at the Galactic center. Finally, the density profile of compact objects is largely unknown due to the difficulty of observing these objects close to the supermassive black hole. X-ray observations of accreting stellar mass black holes suggest a 3-d radial density profile with a power-law index in a range between 2.1 and 2.7 (Hailey et al. 2018; Mori et al. 2021). Stellar measurements disagree on the density profile, which range from core-like (Do et al. 2009) to cups-like profiles (Schödel et al. 2020). We present here a range of predictions based on different density profiles, but better constraints on this 'dark cusp' will help to narrow the range of predictions.

6. CONCLUSION

We model the star formation history of the Milky Way NSC, incorporating constraints on the metallicity for the first time from a large sample of stellar metallicity measurements. We use spectroscopy and photometry of 770 late-type giants along with a Bayesian inference methodology to derive the star formation history and global properties of the cluster. We test different star formation models (continuous, single-burst, multiple bursts) and find that a two-bursts star formation model is strongly favored. The bulk of the stars (93% ± 3%) is metal-rich ($\overline{[M/H]} = 0.45 \pm 0.05$) with an age of $5.0\ ^{+3.4}_{-2.3}$ Gyr. The minor group with 7% ± 3% of stellar mass is metal-poor ($\overline{[M/H]}$ = -1.10 $\pm\ ^{+0.30}_{-0.25}$) with a younger age of $0.8\ ^{+3.8}_{-0.7}$ Gyr. By including metallicity as a free parameter, our models are able to account for low-temperature red giants that were previously difficult to fit. The bulk of the stars in the NSC is likely younger than previously reported. We find that the age of the stars is systematically younger by ∼3 Gyr when metallicity is included compared to assuming all stars are solar metallicity. This younger age for the NSC could challenge the mutual evolution scenario of the NSC, the central SMBH and the inner bulge. The younger age and the supersolar metallicity for the bulk stellar mass may also challenge the globular clusters in-falling scenario for the main population of the NSC.

This work also updates the predictions of the number of compact objects at the Galactic center and the rate at which they merge using our updated star formation history models. We predict 2.5×10^5 BHs, 1.5×10^5 NSs and 8.7×10^6 WDs in the NSC assuming a total cluster mass of $2.5 \times 10^7\ M_\odot$. Specifically, when metallicity constraints are included, we predict 2 - 4 times fewer neutron stars compared to earlier predictions, which may introduce to a new path to further understand the so-called "missing pulsar problem" at the Galactic center. We also predict 2.2×10^4 (Kroupa IMF) or 2.3×10^5 (top-heavy IMF) BH-BH binaries in the NSC, and a BH-BH merger rate ranging from 0.01-3 $Gpc^{-3}yr^{-1}$ depending on the IMF and density profile.

Future deeper spectroscopic observations and larger spatial coverage of the NSC would be crucial to extend our understanding of the star formation history of the NSC. In particular, the detection of a main-sequence turnoff with spectroscopy reaching K ∼ 19 mag (predicted for a 5 Gyr population) will greatly improve the age estimate of the NSC. Moreover, higher spatial and spectral resolution observations are required to place tighter constraints on the population of subsolar metallicity stars and their origins.

The authors would like to thank Smadar Naoz, Kelly Kosmo O'Neil, Bao-Minh Hoang, and other members of the UCLA Galactic Center group for providing helpful comments and discussions. The primary support for this work was provided by NSF AAG grant NSF AAG AST-1909554. Additional support was received from the UCLA Galactic Center Star Society. This research uses the Galactic Center Orbit Initiative (GCOI) catalogue based on the data obtained from W. M. Keck Observatory. The W. M. Keck Observatory is operated as a scientific partnership among the California Institute of

Technology, the University of California, and the National Aeronautics and Space Administration. The authors wish to recognize that the summit of Maunakea has always held a very significant cultural role for the indigenous Hawaiian community. We are most fortunate to have the opportunity to observe from this mountain. The Observatory was made possible by the generous financial support of the W. M. Keck Foundation.

REFERENCES

Abbott, B. P., Abbott, R., Abbott, T. D., et al. 2016, Physical Review X, 6, 041015

Abbott, B. P., Abbott, R., Abbott, T. D., et al. 2016, PhRvL, 116, 061102

Abbott, B. P., Abbott, R., Abbott, T. D., et al. 2016, PhRvD, 93, 122003

Abbott, B. P., Abbott, R., Abbott, T. D., et al. 2017, PhRvL, 119, 141101

Abbott, B. P., Abbott, R., Abbott, T. D., et al. 2017, ApJL, 851, L35

Alexander, R. D., Begelman, M. C., & Armitage, P. J. 2007, ApJ, 654, 907

Alexander, T. & Hopman, C. 2009, ApJ, 697, 1861

Allen, D. A., Hyland, A. R., & Hillier, D. J. 1990, MNRAS, 244, 706

Andersen, D. R., Walcher, C. J., Böker, T., et al. 2008, ApJ, 688, 990. doi:10.1086/592342

Antonini, F., Faber, J., Gualandris, A., et al. 2010, ApJ, 713, 90

Antonini, F. & Perets, H. B. 2012, ApJ, 757, 27

Antonini, F. 2013, ApJ, 763, 62. doi:10.1088/0004-637X/763/1/62

Antonini, F., Murray, N., & Mikkola, S. 2014, ApJ, 781, 45

Arca Sedda, M., Gualandris, A., Do, T., et al. 2020, ApJL, 901, L29. doi:10.3847/2041-8213/abb245

Bartko, H., Martins, F., Fritz, T. K., et al. 2009, ApJ, 697, 1741

Bartko, H., Martins, F., Trippe, S., et al. 2010, ApJ, 708, 834

Bartos, I., Kocsis, B., Haiman, Z., et al. 2017, ApJ, 835, 165

Bastian, N., Covey, K. R., & Meyer, M. R. 2010, ARA&A, 48, 339

Bates, S. D., Johnston, S., Lorimer, D. R., et al. 2011, MNRAS, 411, 1575. doi:10.1111/j.1365-2966.2010.17790.x

Baumgardt, H., Makino, J., & Ebisuzaki, T. 2004, ApJ, 613, 1143

Becklin, E. E. & Neugebauer, G. 1968, ApJ, 151, 145

Bensby, T., Yee, J. C., Feltzing, S., et al. 2013, A&A, 549, A147. doi:10.1051/0004-6361/201220678

Bentley, R. O., Do, T., Kerzendorf, W., et al. 2022, ApJ, 925, 77. doi:10.3847/1538-4357/ac3910

Blum, R. D., Ramírez, S. V., Sellgren, K., et al. 2003, ApJ, 597, 323

Boehle, A., Ghez, A. M., Schödel, R., et al. 2016, ApJ, 830, 17

Bohlin, R. C., Mészáros, S., Fleming, S. W., et al. 2017, AJ, 153, 234

Buchner, J., Georgakakis, A., Nandra, K., et al. 2014, A&A, 564, A125

ArXiv Astrophysics e-prints, astro-ph/0405087

Chatzopoulos, S., Fritz, T. K., Gerhard, O., et al. 2015, MNRAS, 447, 948. doi:10.1093/mnras/stu2452

Chen, Z., Gallego-Cano, E., Do, T., et al. 2019, ApJL, 882, L28

Choi, J., Dotter, A., Conroy, C., et al. 2016, ApJ, 823, 102

Do, T., Ghez, A. M., Morris, M. R., et al. 2009, ApJ, 703, 1323

Do, T., Lu, J. R., Ghez, A. M., et al. 2013, ApJ, 764, 154

Do, T., Kerzendorf, W., Winsor, N., et al. 2015, ApJ, 809, 143

Do, T., Hees, A., Ghez, A., et al. 2019, Science, 365, 664. doi:10.1126/science.aav8137

Do, T., David Martinez, G., Kerzendorf, W., et al. 2020, ApJL, 901, L28. doi:10.3847/2041-8213/abb246

Dorn-Wallenstein, T. Z. & Levesque, E. M. 2018, ApJ, 867, 125

Dotter, A. 2016, ApJS, 222, 8

Eckart, A. & Genzel, R. 1997, MNRAS, 284, 576

Eisenhauer, F., Genzel, R., Alexander, T., et al. 2005, ApJ, 628, 246

Fan, X., Strauss, M. A., Schneider, D. P., et al. 2001, AJ, 121, 54. doi:10.1086/318033

Feldmeier, A., Neumayer, N., Seth, A., et al. 2014, A&A, 570, A2. doi:10.1051/0004-6361/201423777

Feldmeier-Krause, A., Neumayer, N., Schödel, R., et al. 2015, A&A, 584, A2

Feldmeier-Krause, A., Kerzendorf, W., Neumayer, N., et al. 2017, MNRAS, 464, 194

Feldmeier-Krause, A., Kerzendorf, W., Do, T., et al. 2020, MNRAS, 494, 396

Feltzing, S. & Chiba, M. 2013, NewAR, 57, 80. doi:10.1016/j.newar.2013.06.001

Feroz, F. & Hobson, M. P. 2008, MNRAS, 384, 449

Feroz, F., Hobson, M. P., & Bridges, M. 2009, MNRAS, 398, 1601

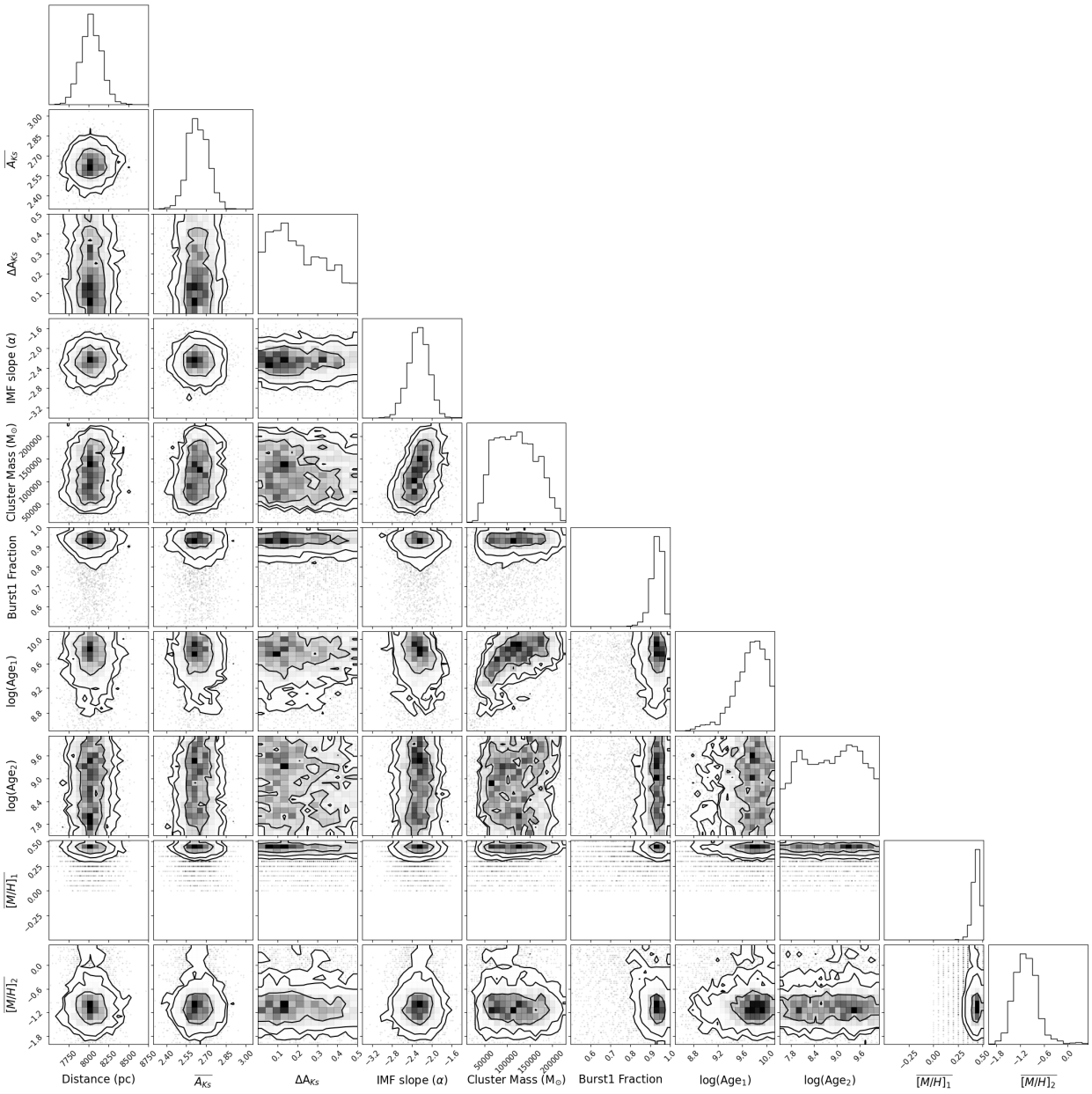

Figure 3-11. Two-dimentional posterior probability density functions for the observed NSC's properties from modeling the AO dataset (Do et al. 2015) assuming a Kroupa IMF. Here we show the results from the MultiNest Bayesian analysis on the two-bursts star formation model after the model selection. The overplotted contours give 68%, 95%, and 99% confidence intervals.

Ferrarese, L., Côté, P., Dalla Bontà, E., et al. 2006, ApJL, 644, L21. doi:10.1086/505388

Figer, D. F., Rich, R. M., Kim, S. S., et al. 2004, ApJ, 601, 319

Forrest, W. J., Shure, M. A., Pipher, J. L., et al. 1987, The Galactic Center, 155, 153

Frogel, J. A., Stephens, A., Ramírez, S., et al. 2001, AJ, 122, 1896. doi:10.1086/323079

Fryer, C. L., Belczynski, K., Wiktorowicz, G., et al. 2012, ApJ, 749, 91. doi:10.1088/0004-637X/749/1/91

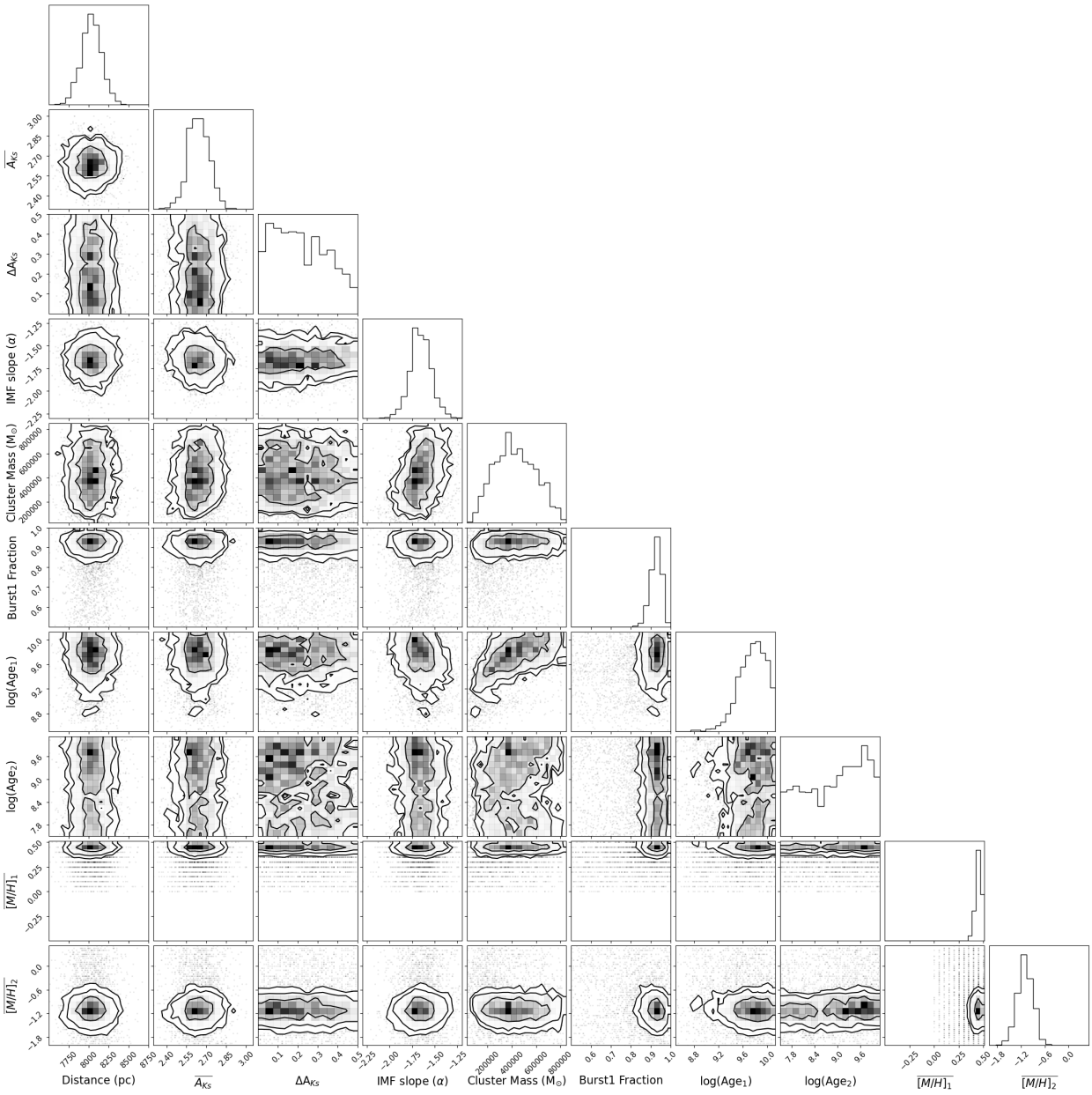

Figure 3-12. Two-dimentional posterior probability density functions for the observed NSC's properties from modeling the AO dataset (Do et al. 2015) assuming a top-heavy IMF.

Gelman, A., Carlin, J.B., Stern, H.S., Dunson, D.B., Vehtari, A., & Rubin, D.B. (2013). Bayesian Data Analysis (3rd ed.). Chapman and Hall/CRC. https://doi.org/10.1201/b16018

Generozov, A., Stone, N. C., Metzger, B. D., et al. 2018, MNRAS, 478, 4030. doi:10.1093/mnras/sty1262

Genzel, R., Pichon, C., Eckart, A., et al. 2000, MNRAS, 317, 348

Genzel, R., Schödel, R., Ott, T., et al. 2003, Nature, 425, 934

Georgiev, I. Y., Böker, T., Leigh, N., et al. 2016, MNRAS, 457, 2122. doi:10.1093/mnras/stw093

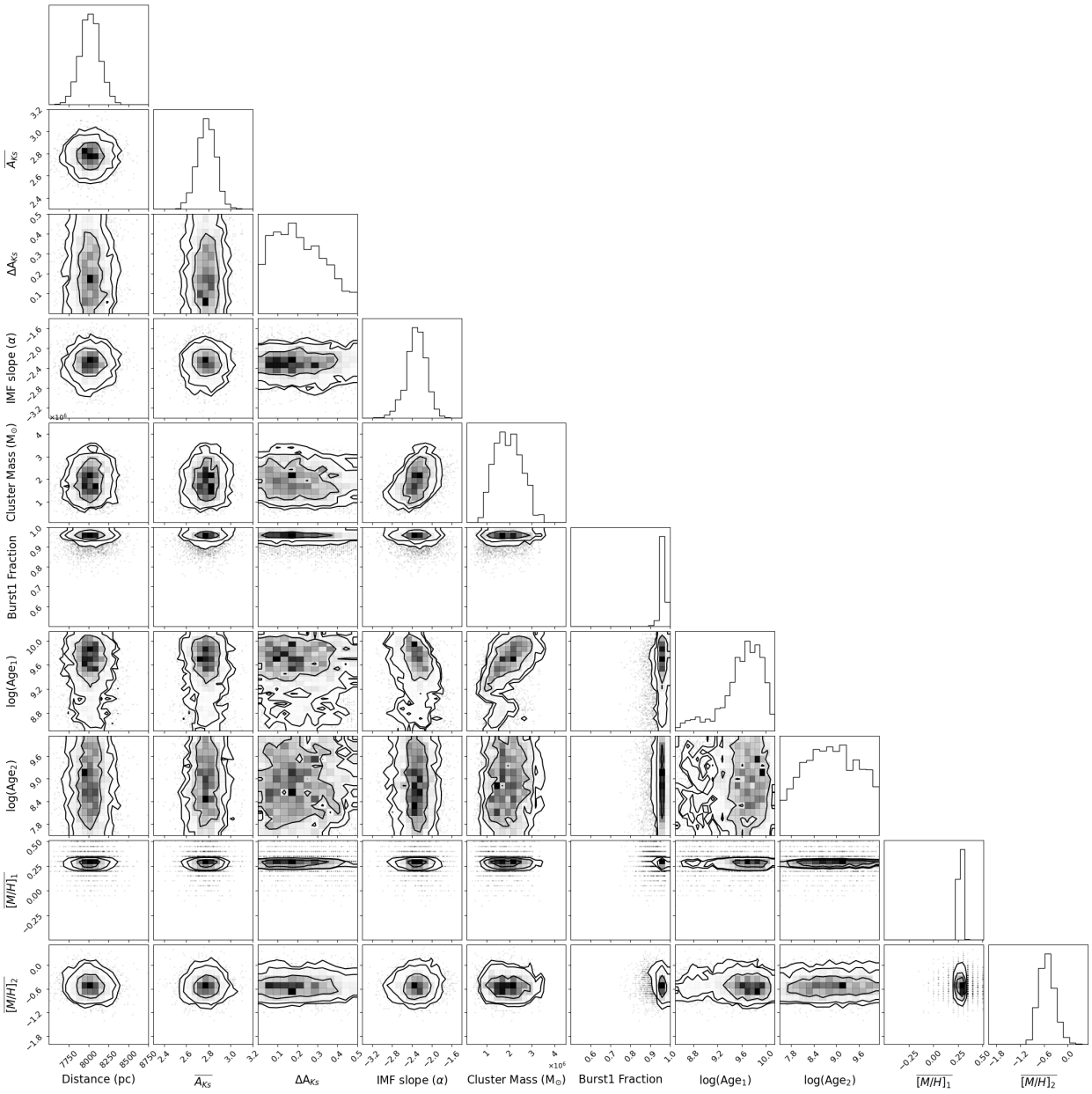

Figure 3-13. Two-dimentional posterior probability density functions for the observed NSC's properties from modeling the seeing-limited dataset (Feldmeier-Krause et al. 2017) assuming a Kroupa IMF.

Ghez, A. M., Klein, B. L., Morris, M., & Becklin, E. E. 1998, ApJ, 509, 678

Ghez, A. M., Morris, M., Becklin, E. E., Tanner, A., & Kremenek, T. 2000, Nature, 407, 349

Ghez, A. M., Salim, S., Hornstein, S. D., et al. 2005a, ApJ, 620, 744

Ghez, A. M., Hornstein, S. D., Lu, J. R., et al. 2005b, ApJ, 635, 1087

Ghez, A. M., Salim, S., Weinberg, N. N., et al. 2008, ApJ, 689, 1044. doi:10.1086/592738

Gillessen, S., Eisenhauer, F., Trippe, S., et al. 2009, ApJ, 692, 1075. doi:10.1088/0004-637X/692/2/1075

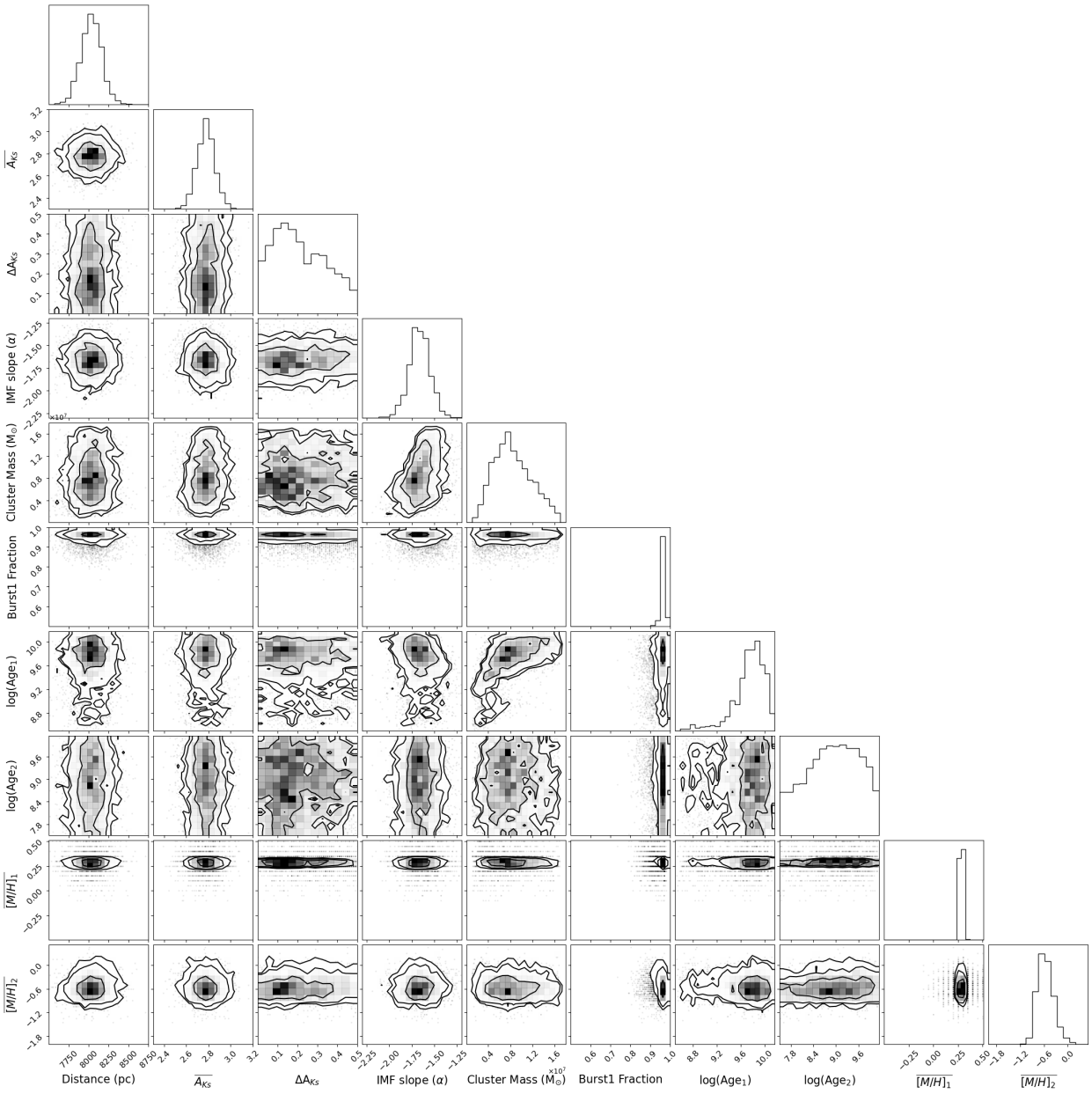

Figure 3-14. Two-dimentional posterior probability density functions for the observed NSC's properties from modeling the seeing-limited dataset (Feldmeier-Krause et al. 2017) assuming a top-heavy IMF.

Graham, A. W. & Spitler, L. R. 2009, MNRAS, 397, 2148. doi:10.1111/j.1365-2966.2009.15118.x

Gravity Collaboration, Abuter, R., Amorim, A., et al. 2019, A&A, 625, L10. doi:10.1051/0004-6361/201935656

Grieco, V., Matteucci, F., Ryde, N., et al. 2015, MNRAS, 450, 2094. doi:10.1093/mnras/stv729

Gustafsson, B., Edvardsson, B., Eriksson, K., et al. 2008, A&A, 486, 951. doi:10.1051/0004-6361:200809724

Hailey, C. J., Mori, K., Bauer, F. E., et al. 2018, Nature, 556, 70

Hanson, M. M., Conti, P. S., & Rieke, M. J. 1996, ApJS, 107, 281

Harris, W. E. 2010, arXiv:1012.3224

Heger, A., Fryer, C. L., Woosley, S. E., et al. 2003, ApJ, 591, 288
Hoang, B.-M., Naoz, S., Kocsis, B., et al. 2018, ApJ, 856, 140
Mori, K., Hailey, C. J., Schutt, T. Y. E., et al. 2021, ApJ, 921, 148. doi:10.3847/1538-4357/ac1da5
Hosek, M. W., Lu, J. R., Anderson, J., et al. 2019, ApJ, 870, 44
STSci poster
Hosek, M. W., Lu, J. R., Lam, C. Y., et al. 2020, arXiv:2006.06691
Husser, T.-O., Wende-von Berg, S., Dreizler, S., et al. 2013, A&A, 553, A6 161
Johnston, S., Walker, M. A., van Kerkwijk, M. H., et al. 1995, MNRAS, 274, L43. doi:10.1093/mnras/274.1.L43
Kalirai, J. S., Hansen, B. M. S., Kelson, D. D., et al. 2008, ApJ, 676, 594
Kent, S. M. 1992, ApJ, 387, 181
Kerzendorf, W. & Do, T. 2015, Zenodo
Kocsis, B. & Levin, J. 2012, PhRvD, 85, 123005
Kozai, Y. 1962, AJ, 67, 591
Krabbe, A., Genzel, R., Drapatz, S., et al. 1991, ApJL, 382, L19
Krauss, L. M. & Chaboyer, B. 2003, Science, 299, 65. doi:10.1126/science.1075631
Kroupa, P. 2002, Science, 295, 82. doi:10.1126/science.1067524
Kudritzki, R. P., Pauldrach, A., & Puls, J. 1987, A&A, 173, 293
Larkin, J., Barczys, M., Krabbe, A., et al. 2006, Proc. SPIE, 6269, 62691A
Launhardt, R., Zylka, R., & Mezger, P. G. 2002, A&A, 384, 112
Leitherer, C., Robert, C., & Drissen, L. 1992, ApJ, 401, 596. doi:10.1086/172089
Abbott, B. P., Abbott, R., Abbott, T. D., et al. 2016, PhRvL, 116, 241103
Abbott, B. P., Abbott, R., Abbott, T. D., et al. 2016, PhRvL, 116, 061102
Abbott, B. P., Abbott, R., Abbott, T. D., et al. 2017, PhRvL, 118, 221101
Lidov, M. L. 1962, Planet. Space Sci., 9, 719
Löckmann, U., Baumgardt, H., & Kroupa, P. 2010, MNRAS, 402, 519
Lu, J. R., Ghez, A. M., Hornstein, S. D., et al. 2009, ApJ, 690, 1463
Lu, J. R., Do, T., Ghez, A. M., et al. 2013, ApJ, 764, 155
Maness, H., Martins, F., Trippe, S., et al. 2007, ApJ, 669, 1024
Martins, F., Genzel, R., Hillier, D. J., et al. 2007, A&A, 468, 233
McKee, C. F. & Ostriker, E. C. 2007, ARA&A, 45, 565
Merritt, D. 2013, Dynamics and Evolution of Galactic Nuclei (Princeton, NJ: Princeton Univ. Press)
Milosavljević, M. 2004, ApJL, 605, L13. doi:10.1086/420696
Morris, M. 1993, ApJ, 408, 496
Nayakshin, S. & Sunyaev, R. 2005, MNRAS, 364, L23
Neumayer, N. & Walcher, C. J. 2012, Advances in Astronomy, 2012, 709038. doi:10.1155/2012/709038
Neumayer, N., Seth, A., & Böker, T. 2020, A&A Rv, 28, 4. doi:10.1007/s00159-020-00125-0
Nogueras-Lara, F., Schödel, R., Gallego-Calvente, A. T., et al. 2019, A&A, 631, A20
O'Leary, R. M., Rasio, F. A., Fregeau, J. M., et al. 2006, ApJ, 637, 937
O'Leary, R. M., Kocsis, B., & Loeb, A. 2009, MNRAS, 395, 2127
O'Leary, R. M., Meiron, Y., & Kocsis, B. 2016, ApJL, 824, L12
Paumard, T., Genzel, R., Martins, F., et al. 2006, ApJ, 643, 1011
Petrovich, C. & Antonini, F. 2017, ApJ, 846, 146
Pflamm-Altenburg, J. & Kroupa, P. 2006, MNRAS, 373, 295
Pfuhl, O., Fritz, T. K., Zilka, M., et al. 2011, ApJ, 741, 108
Poelarends, A. J. T., Herwig, F., Langer, N., et al. 2008, ApJ, 675, 614. doi:10.1086/520872
Portegies Zwart, S. F. & McMillan, S. L. W. 2000, ApJL, 528, L17
Primot, J., Rousset, G., & Fontanella, J. C. 1990, Journal of the Optical Society of America A, 7, 1598
Raithel, C. A., Sukhbold, T., & Özel, F. 2018, ApJ, 856, 35
Rayner, J. T., Cushing, M. C., & Vacca, W. D. 2009, ApJS, 185, 289
Rich, R. M., Ryde, N., Thorsbro, B., et al. 2017, AJ, 154, 239
Rodriguez, C. L., Morscher, M., Wang, L., et al. 2016, MNRAS, 463, 2109
Ryde, N. & Schultheis, M. 2015, A&A, 573, A14
Ryde, N., Fritz, T. K., Rich, R. M., et al. 2016, ApJ, 831, 40
Salpeter, E. E. 1955, ApJ, 121, 161. doi:10.1086/145971
Schödel, R., Ott, T., Genzel, R., et al. 2002, Nature, 419, 694
Schödel, R., Merritt, D., & Eckart, A. 2009, A&A, 502, 91. doi:10.1051/0004-6361/200810922
Schödel, R., Najarro, F., Muzic, K., et al. 2010, A&A, 511, A18
Schödel, R., Yelda, S., Ghez, A., et al. 2013, MNRAS, 429, 1367

Schödel, R., Feldmeier, A., Kunneriath, D., et al. 2014, A&A, 566, A47

Schödel, R., Nogueras-Lara, F., Gallego-Cano, E., et al. 2020, A&A, 641, A102. doi:10.1051/0004-6361/201936688

Skilling, J. 2004, American Institute of Physics Conference Series, 735, 395

Spera, M., Mapelli, M., & Bressan, A. 2015, MNRAS, 451, 4086. doi:10.1093/mnras/stv1161

Stone, N. C., Metzger, B. D., & Haiman, Z. 2017, MNRAS, 464, 946

Støstad, M., Do, T., Murray, N., et al. 2015, ApJ, 808, 106

Sukhbold, T., Ertl, T., Woosley, S. E., et al. 2016, ApJ, 821, 38

Sukhbold, T., Woosley, S. E., & Heger, A. 2018, ApJ, 860, 93

Torne, P., Desvignes, G., Eatough, R. P., et al. 2021, A&A, 650, A95. doi:10.1051/0004-6361/202140775

Tremaine, S. D., Ostriker, J. P., & Spitzer, L. 1975, ApJ, 196, 407. doi:10.1086/153422

Trevisan, M., Barbuy, B., Eriksson, K., et al. 2011, A&A, 535, A42. doi:10.1051/0004-6361/201016056

VanLandingham, J. H., Miller, M. C., Hamilton, D. P., et al. 2016, ApJ, 828, 77. doi:10.3847/0004-637X/828/2/77

Vink, J. S., de Koter, A., & Lamers, H. J. G. L. M. 2001, A&A, 369, 574. doi:10.1051/0004-6361:20010127

Volonteri, M. 2010, A&A Rv, 18, 279. doi:10.1007/s00159-010-0029-x

Wen, L. 2003, ApJ, 598, 419

Witzel, G., Martinez, G., Hora, J., et al. 2018, ApJ, 863, 15

Yelda, S. 2012, Ph.D. Thesis

Zoccali, M., Renzini, A., Ortolani, S., et al. 2003, A&A, 399, 931. doi:10.1051/0004-6361:20021604

APPENDIX

A. FITTER TESTINGS

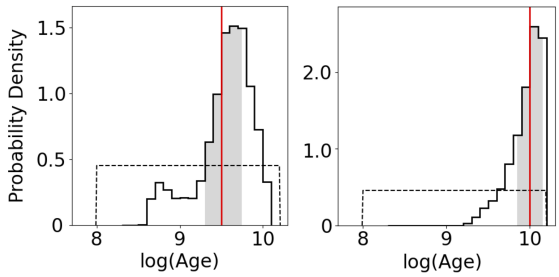

Figure 3-15. Test cluster's marginalized 1D posterior probability density function for a simulated cluster with an age of 3.2 Gyr (log(Age) = 9.5, left), and an age of 10 Gyr (log(Age) = 10, right). A uniform prior probability distribution is used in the fits (black dashed line). The input age (red line) always falls within the 68% (1σ equivalent) Bayesian confidence interval (grey shaded region). Our Bayesian inference methodology is able to recover both moderate and old cluster ages with no substantial systematic biases.

We test our Bayesian methodology by generating a synthetically "observed" cluster, and throwing the simulated sample back to the fitter to derive the probability distribution function for each parameter using the Bayesian inference techniques as described in section 3.2. All clusters were generated at a distance of 8030 pc, an extinction of $A_{Ks} = 2.7$, a differential extinction of $\Delta A_{Ks} = 0.2$, and with a cluster mass aiming to result in a similar number of late-type stars to our observed sample (∼80 stars for AO observations, and ∼700 stars for seeing-limited observations). Photometric and spectroscopic uncertainties for simulated cluster stars are added as the Gaussian distribution from the observational uncertainties. We examine the fitter on synthetic clusters with different ages, IMFs, multiplicity, metallicity properties, and star formation history models. Our Bayesian inference methodology is always able to recover the input properties with no substantial systematic biases in the tests on synthetic clusters. We present detailed fitter testings on the cluster age and each star formation history model in the following sections.

A.1. *Age*

Cluster age is correlated with several parameters in the model fitting. We note moderate correlations between the cluster age, IMF slope, cluster mass and average extinction. Here to understand the correlations between parameters and the reliability of the fitter on estimating the age, we simulate clusters at different ages ranging from 0.2 Gyr to 10 Gyr. Each simulated cluster is fitted using our Bayesian inference methods, and then used to examine the fitting results on cluster properties. Figure 3-15 shows two examples of resulting probability distributions for ages of the simulated clusters with a moderate age of 3.2 Gyr (log(Age) = 9.5), and an old age of 10 Gyr (log(Age) = 10). Through the whole test range of age, the input age and other cluster properties are always recovered within the 68% (1σ equivalent) confidence region of the fitting distribution. Our Bayesian inference methodology is able to recover the age of the cluster with no significant systematic biases.

A.2. *Star formation history models*

We explore the reliability of the fitter by testing the Bayesian inference methods on all star formation history models summarized in section 3.5.

(1) Single burst: The fits on the single burst star formation history model have been well tested through single-age synthetic cluster modelings. See Figure 3-16 for one example. A handful of similar cluster tests were performed with different ages, masses, IMF slopes, parameter priors, and the input and output parameters always agree very well within the 68% (1σ equivalent) confidence intervals.

(2) Two bursts: For multiple bursts, we assume that all stars in the NSC from different bursts have the same observational physical conditions including the same distance (d), average extinction (A_{Ks}), differential extinction (ΔA_{Ks}) and a constant IMF slope for all subgroups of the NSC. For i^{th} burst, we model the age $\log(t_i)$, the metallicity $\overline{[M/H]}_i$ and the mass fraction of the single star burst (also see Table 3-3).

Figure 3-17 shows one example of the output posterior probability distributions on fitting one synthetic cluster including two bursts: **burst 1** with an age of 4 Gyr ($\log(\mathrm{Age}_1) = 9.6$), mass fraction of 90% and metallicity of $\overline{[M/H]}_1 = 0.3$; **burst 2** with an age of 0.13 Gyr ($\log(\mathrm{Age}_2) = 8.1$), mass fraction of 10% and metallicity of $\overline{[M/H]}_2$ = -1.45. The total cluster mass of the two bursts was set to produce comparable total number of stars as observed in the dataset. Similar cluster tests were performed with different ages, mass fraction and metallicity of the two bursts, and the input and output parameters always agree very well within the 68% (1σ equivalent) confidence interval.

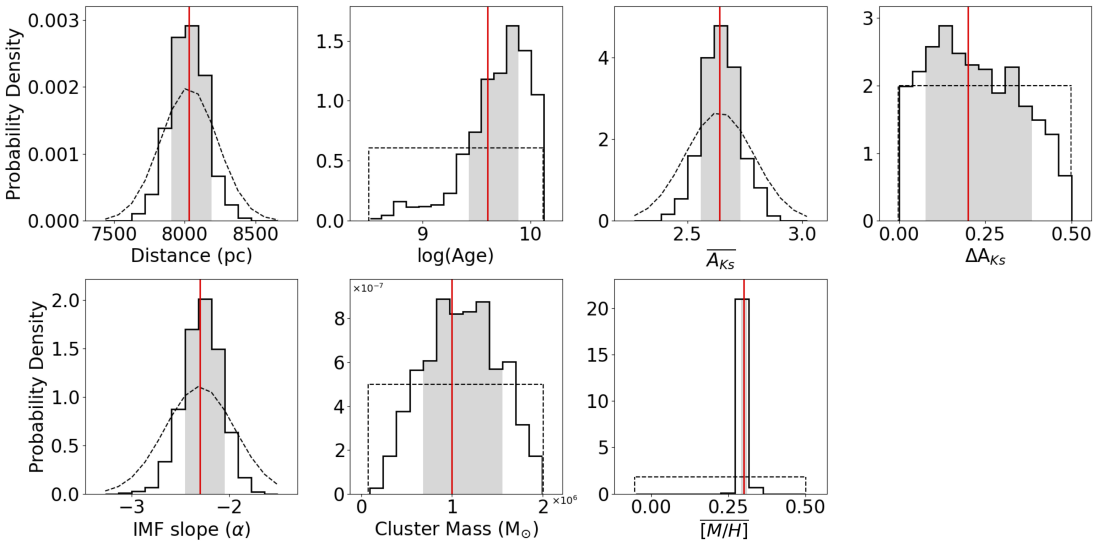

Figure 3-16. Single age test-cluster's marginalized 1D posterior probability density functions for each fitting parameter. The input values for the single-age cluster's distance, age, average extinction (A_{Ks}), differential extinction (ΔA_{Ks}), IMF slope, initial cluster mass, and metallicity are shown as a vertical red line. Each parameter falls well within the 68% (1σ equivalent) confidence interval of the distribution (grey shaded regions). The confidence intervals are calculated by first finding the 50^{th} percentile of the posterior in probability distribution and then stepping away from the center until the integrated probability reached 68% (1σ equivalent).

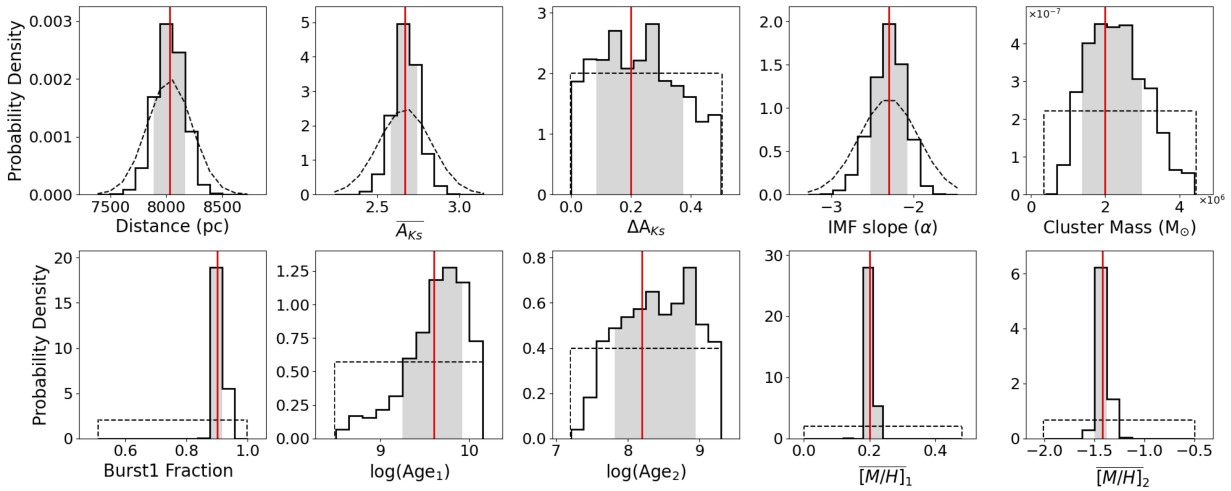

Figure 3-17. Two-bursts star formation history model testing. The input values for the cluster including two bursts of star formation are: distance to the cluster, average extinction (A_{Ks}), differential extinction (ΔA_{Ks}), IMF slope, total cluster mass, mass fraction of burst 1, age of burst 1, age of burst 2, metallicity of burst 1, and metallicity of burst 2 (see vertical red lines). Each parameter falls well within the 68% (1σ equivalent) confidence interval of the distribution (grey shaded regions).

(3) Three bursts: Similar to the two bursts model, Figure 3-18 shows one example of the output posterior probability distributions on fitting one synthetic cluster including three bursts: **burst 1** with an age of 6.3 Gyr ($\log(\text{Age}_1) = 9.8$), mass fraction of 70% and metallicity of $\overline{[M/H]}_1 = 0.45$; **burst 2** with an age of 1.6 Gyr ($\log(\text{Age}_2) = 9.2$), mass fraction of 21% and metallicity of $\overline{[M/H]}_2 = 0$; **burst 3** with an age of 0.32 Gyr ($\log(\text{Age}_3) = 8.5$), mass fraction of 9% and metallicity of $\overline{[M/H]}_3 = -1.05$. Similar cluster tests were performed with different ages, mass fraction and metallicity of the three bursts, and the input and output parameters al-

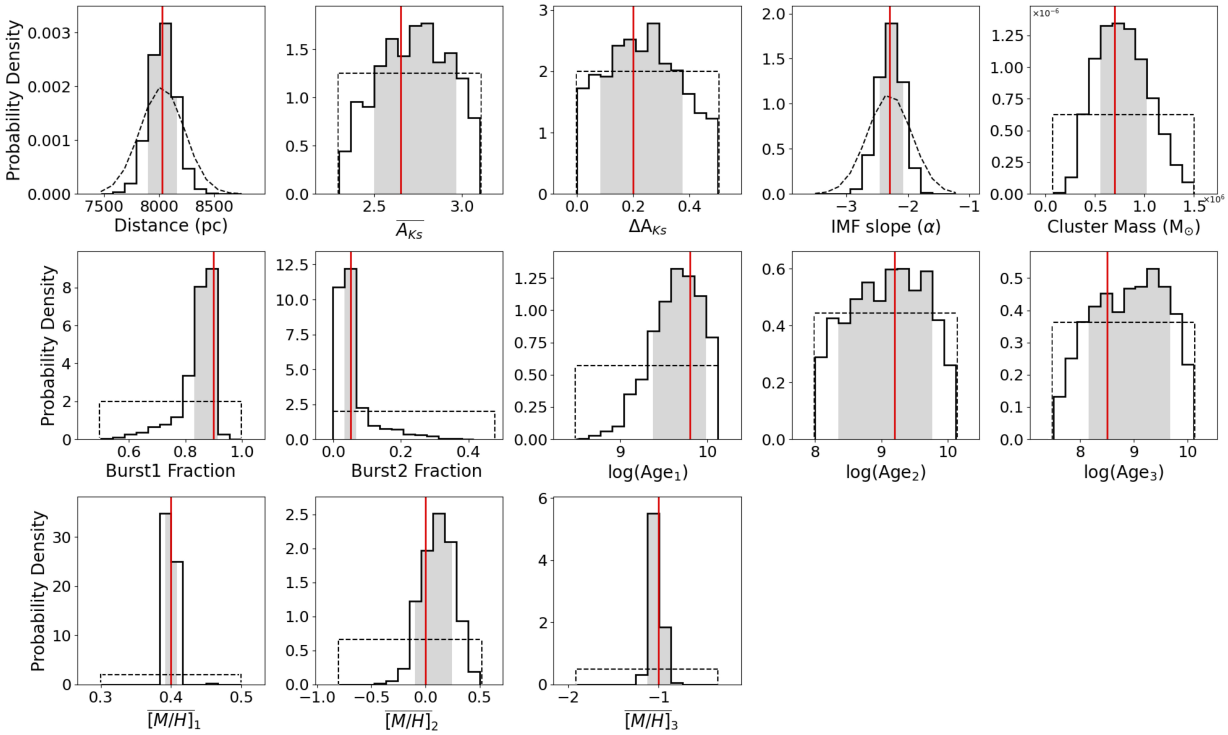

Figure 3-18. Three-bursts star formation history model testing. The input values for the cluster including three bursts of star formation are: distance to the cluster, average extinction (A_{Ks}), differential extinction (ΔA_{Ks}), IMF slope, total cluster mass, mass fraction of burst 1, mass fraction of burst 2, age of burst 1, age of burst 2, age of burst 3, metallicity of burst 1, metallicity of burst 2, and metallicity of burst 3 (see vertical red lines). Each parameter falls well within the 68% (1σ equivalent) confidence interval of the distribution (grey shaded regions).

ways agree very well within the 68% (1σ equivalent) confidence interval. The fitter is reliable to characterize the multiple bursts signatures from our observed sample.

(4) Continuous star formation with a linear SFR: Continuous star formation between 30 Myr and 10 Gyr ago, with a linearly increasing/decreasing SFR(t) $\propto mt$. For continuous star formation, we assume that all stars in the NSC have the same metallicity. Figure 3-19 shows one example of the output posterior probability distributions on fitting the synthetic cluster from continuous star formation with a linearly increasing SFR (m = 0.25). Similar tests were performed with different linearly change rates (either increasing or decreasing), and the input and output parameters always agree very well within the 68% (1σ equivalent) confidence interval.

(5) Continuous star formation with an exponential SFR: Continuous star formation between 30 Myr and 10 Gyr ago, with an exponentially increasing/decreasing SFR(t) $\propto e^{\lambda t}$. Similarly, we assume that all stars in the NSC have the same metallicity. Figure 3-20 shows one example of the output posterior probability distributions on fitting the synthetic cluster from continuous star formation with an exponentially increasing SFR (λ = -2.0). Similar tests were performed with different exponentially change rates (either increasing or decreasing), and the input and output parameters always agree very well within the 68% (1σ equivalent) confidence interval.

B. MEASUREMENTS OF STELLAR EFFECTIVE TEMPERATURE

Two different methods are used to measure the stellar effective temperature T_{eff} from the spectra:

1) CO-T_{eff}: derived from the well-calibrated relation of the T_{eff} with the CO equivalent width EW_{CO} using the stars of the spectral library (Feldmeier-Krause et al. 2017), where the EW_{CO} was defined by Frogel et al. (2001)

$$T_{eff} = 5677^{\pm 21} K - 106.3^{\pm 3.0} K \mathring{A}^{-1} \times EW_{CO} \quad \text{(B1)}$$

where EW_{CO} is in Å, and T_{eff} in K. The uncertainties are the formal fit uncertainties by fitting the template stars and the residual scatter is 163 K. The uncertainties on the CO indices $\sigma_{EW_{CO}}$ are computed based on

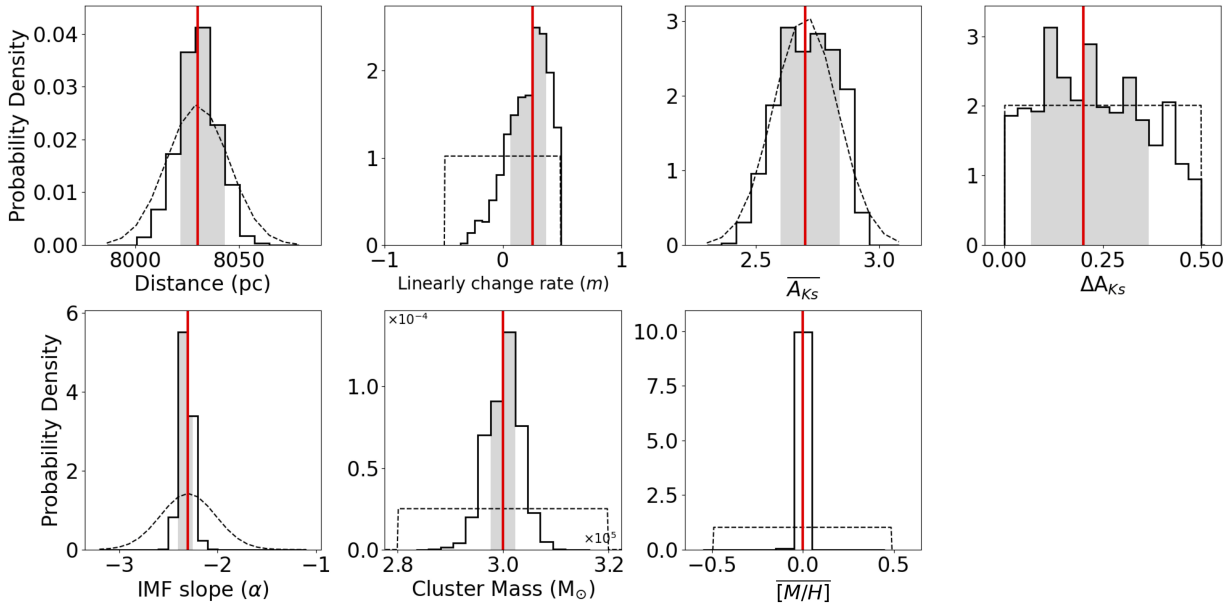

Figure 3-19. Linear SFR model testing. The input values for the continuous star formation with a linearly increasing/decreasing SFR are: distance to the cluster, linearly change rate (m), average extinction (A_{Ks}), differential extinction (ΔA_{Ks}), IMF slope, initial cluster mass, and metallicity (see vertical red lines). Each parameter falls well within the 68% (1σ equivalent) confidence interval of the distribution (grey shaded regions).

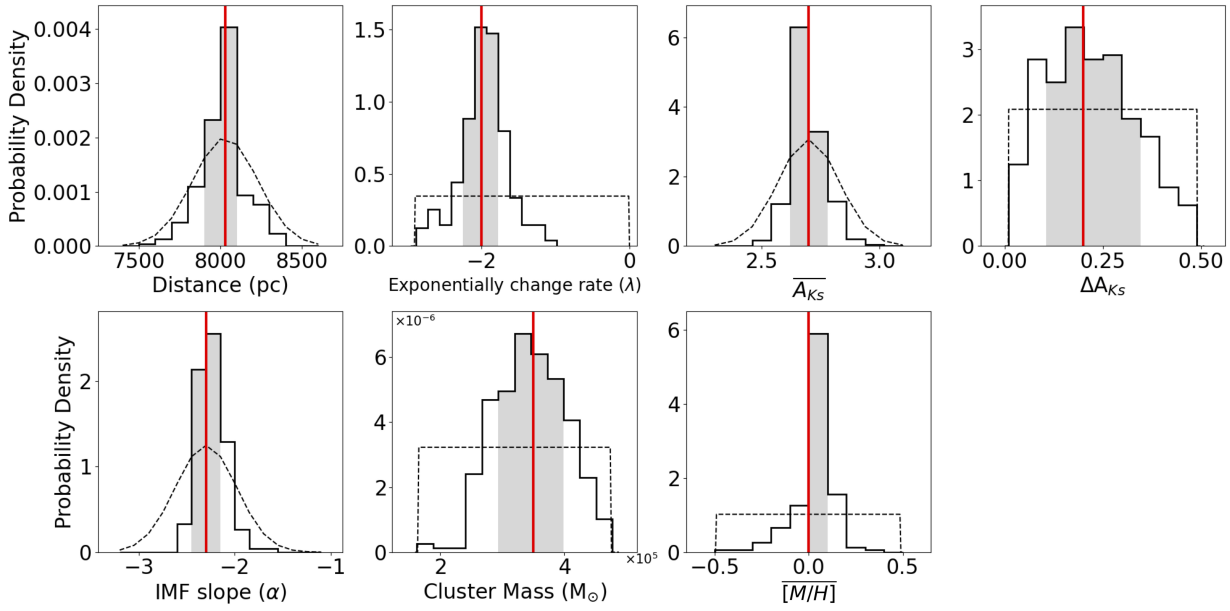

Figure 3-20. Exponential SFR model testing. The input values for the continuous star formation with an exponentially increasing/decreasing SFR are: distance to the cluster, exponentially change rate (λ), average extinction (A_{Ks}), differential extinction (ΔA_{Ks}), IMF slope, initial cluster mass, and metallicity (see vertical red lines). Each parameter falls well within the 68% (1σ equivalent) confidence interval of the distribution (grey shaded regions).

500 Monte Carlo runs of adding the noise. The statistical uncertainty on the effective temperature $\sigma_{T_{eff},stats}$

Table 3-9. Results from CO-T_{eff} vs. Starkit T_{eff}

		Age (Gyr) in this work		Age (Gyr) with fixed $\overline{[M/H]}$	
Dataset	IMF	with CO-T_{eff}	with Starkit T_{eff}	with CO-T_{eff}	with Starkit T_{eff}
AO	Kroupa	$5.0^{+3.4}_{-2.3}$	$4.5^{+3.8}_{-2.4}$	$8.3^{+3.7}_{-3.9}$	$7.4^{+3.4}_{-3.9}$
	Top-heavy	$5.5^{+3.4}_{-2.5}$	$4.8^{+3.4}_{-2.3}$	$8.4^{+3.8}_{-3.5}$	$7.6^{+3.1}_{-4.3}$
Seeing-limited	Kroupa	$4.9^{+3.8}_{-2.2}$	$4.8^{+3.2}_{-1.8}$	$7.9^{+3.5}_{-3.4}$	$7.4^{+3.3}_{-4.0}$
	Top-heavy	$5.6^{+3.3}_{-2.6}$	$5.5^{+2.8}_{-2.3}$	$8.7^{+3.0}_{-3.9}$	$8.3^{+3.2}_{-3.0}$

$= 106.3 \times \sigma_{EW_{CO}}$, and the systematic uncertainty is $\sigma_{T_{eff},sys}$ ∼163 K. The total uncertainty $\sigma_{T_{eff},tot}$ is then calculated by adding statistical and systematic uncertainties in quadrature.

2) Starkit-T_{eff}, derived from full spectrum fitting using STARKIT code (Kerzendorf & Do 2015) with synthetic grids. The code interpolates on a grid of synthetic spectra and then utilizes the Bayesian sample MultiNest in the fits. The AO observed spectra were fitted to a MARCS grid (Gustafsson et al. 2008) of synthetic models while the seeing-limited spectra were fitted to a PHOENIX grid (Husser et al. 2013). Several sources of uncertainties are considered including the statistical uncertainty, interpolation uncertainty between spectra grids, and systematic uncertainty by comparing to standard spectral library in the literature. The total uncertainty $\sigma_{T_{eff},tot}$ is then calculated by adding all these in quadrature.

See Table 9 and 10 for the summary of the stellar effective temperature measurements and the uncertainties from the two different methods for each dataset respectively.

C. COMPARISON BETWEEN THE AO & SEEING-LIMITED RESULTS

The star formation history results that are modeled from two datasets with different detection depth and spatial coverage are in great agreement. The star formation history of the NSC shows no substantial discrepancy at different distances to the Galactic center within the central ∼1.5 pc. In total we have included ∼25% of the total cluster mass covering the central ∼4 pc^2 at a distance of 8 kpc. By modeling the two datasets independently, we can investigate if there are systematic differences between the datasets and assess the accuracy of our results. We fitted independently the two datasets that were observed using different telescopes and instruments, and analyzed using different spectral grids. Importantly, we obtain consistent age estimates for both bursts from the star formation history modelings. The possible systematic uncertainties we discussed (see section 4.5) have been well represented in our reported 68% confidence interval, and thus our reported results are robust and confident.

The deeper AO dataset seems to be more useful in modeling the star formation history. The NIFS AO observations with higher spatial and spectral resolution are more sensitive to differentiate supersolar and subsolar metallicity stars (see details in Do et al. 2015; Feldmeier-Krause et al. 2017). Furthermore, the deeper AO observations are able to detect the fainter and low-metallicity stars below K = 14 mag, enabling a more intrinsic estimate of the mass fraction of each burst and a better constraint on the age of the metal-poor population. In the future, AO observations with wider area coverage, as well as a higher spectral resolution, will be helpful to further constrain the star formation history. In addition, the James Webb Space telescope will have the ability to obtain spectra with increased depth and wavelength coverage, and thus will largely increase the number of the observed subsolar metallicity stars and help to place constraints on the origin of their progenitors.

Table 3-10. Summary of AO Observations

Name	R.A.	Dec.	K_S	$K_{S,err}$	H	H_{err}	A_{K_S}	T^a_{eff}	$\sigma_{T_{eff}}$	$T^b_{eff,*}$	$\sigma_{T_{eff,*}}$	[M/H]	$\sigma_{[M/H]}$
	(°)	(°)						(K)	(K)	(K)	(K)		
E5-1-001	266.421656	-29.007947	12.01	0.01	14.19	0.01	2.66	3260	171	3497	413	0.96	0.32
E5-1-002	266.421449	-29.007402	12.61	0.01	14.51	0.01	2.47	3673	168	3671	414	0.55	0.32
E5-1-003	266.421601	-29.007516	13.15	0.01	15.11	0.01	2.50	3611	170	3597	414	0.85	0.32
E5-1-006	266.422173	-29.007711	14.74	0.01	16.78	0.01	2.60	3936	173	4076	417	0.44	0.32
E5-1-007	266.421681	-29.007874	15.39	0.03	17.32	0.02	2.61	3853	172	3754	414	0.40	0.32
E5-1-008	266.421608	-29.007622	15.05	0.01	17.34	0.02	2.54	4059	174	3915	418	0.43	0.32
E5-1-009	266.421230	-29.007891	14.80	0.01	16.47	0.01	2.70	4246	173	4511	419	0.40	0.32
E5-1-012	266.421322	-29.007822	15.22	0.01	17.37	0.02	2.59	3703	173	4072	420	0.63	0.32
E5-1-015	266.421532	-29.007911	15.73	0.05	17.86	0.03	2.68	4322	173	4180	415	0.25	0.32
E5-1-016	266.421840	-29.008002	15.53	0.01	17.59	0.03	2.64	4238	172	4145	414	0.13	0.32
E5-1-026	266.421795	-29.007727	16.22	0.16	17.72	0.03	2.58	4359	175	4310	418	-0.05	0.33
E5-1-042	266.421690	-29.007519	14.95	0.01	16.92	0.01	2.50	3781	173	4161	417	0.56	0.32
E5-2-001	266.421751	-29.008980	11.34	0.01	13.57	0.01	2.67	3234	166	3519	413	0.73	0.32
E5-2-003	266.421207	-29.008605	13.96	0.01	16.40	0.01	2.77	4386	170	3932	419	0.02	0.32
E5-2-004	266.421605	-29.008783	13.90	0.01	16.11	0.01	2.68	3750	169	3808	414	0.39	0.32
E5-2-005	266.421344	-29.008380	14.24	0.01	15.96	0.01	2.83	4116	173	4328	415	0.40	0.32
E5-2-006	266.421058	-29.008749	14.34	0.01	16.46	0.01	2.81	3895	175	4071	418	0.45	0.32
E5-2-009	266.421439	-29.008438	14.88	0.01	17.02	0.02	2.83	4032	172	4251	423	0.00	0.33
E5-2-010	266.421814	-29.008436	15.07	0.02	17.01	0.02	2.70	4411	169	4434	416	0.18	0.32
E5-2-011	266.421830	-29.008697	15.37	0.02	17.49	0.03	2.66	4302	171	4613	415	0.16	0.32
E5-2-019	266.421633	-29.008886	15.60	0.01	17.58	0.03	2.66	4128	174	4131	415	0.11	0.32
E5-2-020	266.421490	-29.008619	15.68	0.02	17.96	0.03	2.72	4211	175	4066	420	0.42	0.32
E6-1-001	266.422516	-29.007563	11.99	0.01	14.09	0.01	2.66	3394	167	3687	413	0.60	0.32
E6-1-002	266.422538	-29.008311	12.81	0.01	14.96	0.01	2.68	3640	168	3737	414	0.47	0.32
E6-1-003	266.422846	-29.008244	13.27	0.01	15.67	0.01	2.65	3350	168	3656	414	0.65	0.32
E6-1-004	266.422846	-29.007752	13.35	0.01	15.33	0.01	2.71	4603	166	4155	413	-0.12	0.32
E6-1-005	266.422526	-29.008094	13.79	0.01	15.61	0.01	2.68	3792	167	3974	414	0.33	0.32
E6-1-006	266.423015	-29.008235	13.85	0.02	16.05	0.02	2.68	3567	170	3720	414	0.51	0.32
E6-1-008	266.422681	-29.008124	14.79	0.01	16.89	0.01	2.69	3912	173	3986	416	0.43	0.32
E6-1-009	266.422414	-29.007941	14.86	0.01	16.57	0.01	2.67	4145	168	4358	413	0.41	0.32
E6-1-010	266.422611	-29.007941	15.45	0.03	17.98	0.04	2.69	4463	170	4590	417	-0.04	0.32
E6-2-001	266.422891	-29.008638	13.03	0.01	15.01	0.01	2.75	3801	166	3859	414	0.43	0.32
E6-2-002	266.421986	-29.008802	13.46	0.01	15.62	0.01	2.68	3521	168	3759	413	0.39	0.32
E6-2-003	266.422894	-29.008522	13.96	0.01	16.47	0.01	2.69	3567	172	3687	414	0.63	0.32
E6-2-004	266.422091	-29.008830	14.00	0.01	16.67	0.01	2.73	3587	171	3730	415	0.42	0.32
E6-2-005	266.422392	-29.008638	14.78	0.01	17.03	0.01	2.74	3753	174	3836	414	0.64	0.32
E6-2-006	266.422313	-29.008699	14.79	0.01	16.91	0.01	2.74	4074	172	3898	419	0.53	0.32
E6-2-008	266.422592	-29.008627	15.25	0.01	17.41	0.02	2.75	4180	171	4063	415	0.24	0.32
E6-2-009	266.422491	-29.009074	15.06	0.01	17.12	0.02	2.75	4162	171	4422	416	0.16	0.32

Table 3-10 *continued*

Table 3-10 *(continued)*

Name	R.A.	Dec.	K_S	$K_{S,err}$	H	H_{err}	A_{K_S}	T^a_{eff}	$\sigma_{T_{eff}}$	$T^b_{eff,*}$	$\sigma_{T_{eff,*}}$	[M/H]	$\sigma_{[M/H]}$
	(°)	(°)						(K)	(K)	(K)	(K)		
E7-1-001	266.423336	-29.008446	10.82	0.01	13.31	0.02	2.67	3102	166	3479	413	0.73	0.32
E7-1-002	266.423761	-29.008069	11.69	0.01	13.04	0.04	2.77	3491	167	3662	413	0.56	0.32
E7-1-003	266.423634	-29.008363	12.11	0.01	14.17	0.02	2.70	3436	172	3591	414	0.76	0.32
E7-1-004	266.423279	-29.008110	12.26	0.02	14.39	0.02	2.63	3348	170	3594	414	0.72	0.32
E7-1-005	266.423491	-29.008396	13.44	0.01	15.50	0.02	2.70	3946	173	3888	417	0.39	0.32
E7-1-022	266.423501	-29.007857	14.82	0.02	16.56	0.03	2.67	4321	174	4218	425	0.44	0.32
E7-2-001	266.423437	-29.008635	11.45	0.01	13.77	0.01	2.65	3150	168	3524	413	0.74	0.32
E7-2-002	266.423253	-29.009038	14.28	0.01	16.51	0.03	2.66	3745	168	3801	414	0.39	0.32
E7-2-006	266.423345	-29.008846	15.42	0.01	17.53	0.04	2.66	4319	168	4313	416	0.17	0.32
N1-1-001	266.417952	-29.005541	13.22	0.02	15.31	0.02	2.63	3821	171	3644	414	0.68	0.32
N1-1-002	266.417282	-29.005447	13.32	0.01	15.34	0.02	2.61	4698	166	4198	413	-0.91	0.32
N1-1-003	266.418187	-29.005311	13.92	0.01	16.20	0.02	2.64	3595	170	3844	416	0.48	0.32
N1-1-004	266.418072	-29.005577	14.06	0.01	16.10	0.02	2.62	3908	174	3988	417	0.36	0.32
N1-1-005	266.417949	-29.005136	13.57	0.02	15.69	0.02	2.58	3536	170	3658	414	0.75	0.32
N1-1-007	266.418098	-29.005341	14.37	0.01	16.54	0.02	2.62	3653	174	3851	415	0.61	0.32
N1-1-045	266.417993	-29.005805	12.11	0.01	14.15	0.01	2.56	4602	165	4212	413	-1.14	0.32
N1-2-001	266.418717	-29.005886	13.32	0.02	15.45	0.03	2.80	3659	167	3929	415	0.40	0.32
N1-2-002	266.418956	-29.005591	13.34	0.02	15.82	0.03	2.75	3496	168	3706	413	0.67	0.32
N1-2-003	266.418577	-29.005422	13.50	0.03	15.88	0.03	2.66	3602	171	3689	413	0.65	0.32
N1-2-004	266.418847	-29.005677	13.94	0.02	16.17	0.03	2.82	3755	169	3844	413	0.36	0.32
N1-2-006	266.418768	-29.005533	14.93	0.02	17.03	0.03	2.68	4156	176	4204	420	0.39	0.32
N2-1-001	266.418676	-29.004597	12.08	0.01	14.59	0.01	2.96	3373	169	3593	413	0.69	0.32
N2-1-002	266.418234	-29.004755	12.12	0.01	14.19	0.03	2.66	4604	164	4358	413	-1.06	0.32
N2-1-003	266.417977	-29.004608	12.84	0.01	14.90	0.01	2.61	4555	172	4260	415	-1.2	0.32
N2-1-004	266.417990	-29.004844	13.13	0.01	14.74	0.02	2.60	3938	175	3909	415	0.18	0.32
NE-1-001	266.420502	-29.006774	10.44	0.01	12.57	0.01	2.42	3276	167	3558	414	0.80	0.32
NE-1-002	266.419562	-29.006672	10.72	0.01	12.90	0.01	2.59	2980	168	3447	414	0.90	0.32
NE-1-003	266.419572	-29.006766	11.45	0.01	13.60	0.01	2.55	4851	164	4125	413	-1.27	0.32
NE-1-005	266.419832	-29.006436	12.39	0.01	14.50	0.01	2.48	3273	168	3517	413	0.89	0.32
NE-1-007	266.419912	-29.006980	13.53	0.01	15.48	0.01	2.35	3598	171	3710	414	0.65	0.32
NE-1-008	266.420185	-29.006444	13.44	0.01	15.68	0.01	2.44	3435	169	3625	415	0.81	0.32
NE-1-009	266.419689	-29.006630	13.48	0.01	15.46	0.01	2.57	3434	168	3683	413	0.56	0.32
NE-1-010	266.420267	-29.006791	13.93	0.01	15.92	0.01	2.45	3756	172	3769	417	0.62	0.32
NE-1-011	266.419810	-29.006936	14.21	0.01	16.14	0.01	2.37	3753	170	3829	414	0.56	0.32
NE-1-012	266.420366	-29.006586	14.47	0.01	16.40	0.01	2.36	4063	173	4239	418	0.48	0.32
NE-1-013	266.420356	-29.006480	14.78	0.01	16.73	0.01	2.40	4132	173	3885	422	0.33	0.32
NE-1-014	266.420493	-29.007016	15.26	0.01	17.17	0.02	2.43	4173	175	4241	417	0.03	0.32
NE-1-018	266.420131	-29.006819	15.05	0.01	16.91	0.01	2.37	4442	173	4354	417	0.20	0.33
NE-1-025	266.419753	-29.007022	15.33	0.01	17.27	0.02	2.38	4013	168	4224	419	0.55	0.32

Table 3-10 *continued*

Table 3-10 *(continued)*

Name	R.A.	Dec.	K_S	$K_{S,err}$	H	H_{err}	A_{K_S}	T^a_{eff}	$\sigma_{T_{eff}}$	$T^b_{eff,*}$	$\sigma_{T_{eff,*}}$	[M/H]	$\sigma_{[M/H]}$
	(°)	(°)						(K)	(K)	(K)	(K)		

[a] CO-$Teff$ derived from $Teff$-EW_{CO} relation.

[b] Starkit-$Teff$ derived from full spectrum fitting using the STARKIT code (Kerzendorf & Do 2015).

Table 3-11. Summary of seeing-limited Observations

Id	R.A.	Dec.	K_S	$K_{S,err}$	H	H_{err}	A_{K_S}	$T_{eff,CO}$	$\sigma_{T_{eff,CO}}$	$T_{eff,*}$	$\sigma_{T_{eff,*}}$	[M/H]	$\sigma_{[M/H]}$
	(°)	(°)						(K)	(K)	(K)	(K)		
1	266.41675	-29.010296	9.95	0.01	12.07	0.01	2.51	2982	251	3190	209	0.87	0.31
5	266.41571	-29.012167	10.54	0.01	12.80	0.01	2.66	3119	164	3301	206	0.13	0.25
6	266.42401	-29.003611	10.57	0.90	12.65	0.90	2.78	3408	181	3374	205	0.14	0.25
14	266.42093	-29.004204	10.34	0.01	12.53	0.01	2.56	2976	166	3250	217	0.31	0.24
16	266.41727	-29.013838	10.65	0.90	13.02	0.90	2.94	3450	173	3200	205	0.31	0.25
17	266.42236	-29.006290	10.34	0.01	12.68	0.01	2.47	2940	163	3463	282	-0.37	0.24
19	266.41556	-29.013939	10.65	0.90	12.94	0.90	2.77	3258	209	3300	205	0.25	0.25
24	266.41565	-29.009136	10.43	0.02	13.00	0.02	2.69	3100	166	3043	205	0.73	0.24
28	266.41629	-29.003059	10.51	0.02	12.75	0.01	2.58	3025	170	3334	209	0.28	0.25
31	266.42523	-29.005554	10.73	0.90	13.40	0.90	3.10	3743	799	3852	219	0.09	0.31
37	266.40793	-29.012726	10.76	0.90	13.21	0.90	3.21	2789	173	3163	268	0.73	0.38
42	266.41089	-29.015068	10.77	0.91	14.02	0.90	3.07	2825	220	3051	205	0.76	0.25
44	266.42050	-29.006775	10.44	0.01	12.57	0.01	2.43	2866	182	3479	229	0.10	0.33
48	266.42209	-29.002333	10.81	0.01	12.55	0.01	2.69	2977	340	3369	211	0.22	0.26
51	266.41922	-29.007935	10.54	0.01	12.82	0.02	2.64	3072	196	3389	205	0.31	0.24
52	266.41379	-29.015020	10.81	0.90	13.34	0.90	2.91	2870	174	3067	205	0.83	0.24
55	266.41501	-29.005209	10.58	0.02	12.54	0.03	2.57	3240	228	3412	206	0.31	0.25
57	266.41592	-29.004692	10.63	0.02	12.58	0.01	2.53	3318	168	3405	209	0.25	0.25
61	266.41907	-29.007301	10.52	0.01	12.81	0.01	2.67	3153	163	3273	208	0.43	0.30
65	266.41504	-29.012383	12.36	0.02	14.55	0.04	2.57	3928	171	3763	209	-1.00	0.24
66	266.41663	-29.004574	10.54	0.01	12.56	0.01	2.38	3426	163	3394	205	0.30	0.24
69	266.41797	-29.010990	10.00	0.02	12.61	0.02	2.87	2801	210	3165	205	1.00	0.25
73	266.41498	-28.998943	10.87	0.90	13.14	0.90	2.87	2849	257	3362	205	0.42	0.24
74	266.42505	-29.006744	10.88	0.90	13.65	0.90	3.25	2181	184	3332	209	0.39	0.24
78	266.41608	-29.005465	10.70	0.01	13.03	0.01	2.62	3240	169	3379	216	0.28	0.31
84	266.41422	-29.016352	10.91	0.90	14.06	0.90	3.03	3051	181	3632	206	0.50	0.24
85	266.41571	-29.005150	10.73	0.01	13.12	0.02	2.65	3720	241	3721	205	-0.54	0.30
87	266.41946	-29.004255	10.77	0.01	12.97	0.01	2.67	3251	221	3324	209	0.37	0.29
90	266.41409	-29.010923	13.39	0.01	15.15	0.02	2.38	3365	172	3348	216	0.34	0.24
92	266.41473	-29.006163	10.76	0.01	13.17	0.02	2.72	2970	169	3265	205	0.58	0.24
94	266.42093	-29.001326	10.94	0.01	12.93	0.01	2.84	3082	168	3296	222	0.41	0.28

Table 3-11 *continued*

Table 3-11 *(continued)*

Id	R.A.	Dec.	K_S	$K_{S,err}$	H	H_{err}	A_{K_S}	$T_{eff,CO}$	$\sigma_{T_{eff,CO}}$	$T_{eff,*}$	$\sigma_{T_{eff,*}}$	[M/H]	$\sigma_{[M/H]}$
	(°)	(°)						(K)	(K)	(K)	(K)		
101	266.41956	-29.006672	10.72	0.01	12.90	0.01	2.59	3331	241	3460	224	0.54	0.38
105	266.42227	-29.009150	10.97	0.01	13.85	0.01	2.68	3132	167	3044	205	0.73	0.24
107	266.41208	-29.013832	10.98	0.90	13.32	0.90	2.98	2596	172	3388	205	0.40	0.26
110	266.41656	-29.009279	10.81	0.01	13.04	0.02	2.58	2797	177	3374	207	0.62	0.33
121	266.42197	-29.005337	10.87	0.01	12.89	0.01	2.42	3006	172	3460	205	0.19	0.24
126	266.42343	-29.002001	11.03	0.01	13.54	0.01	2.86	3169	183	3064	205	0.83	0.24
130	266.41577	-29.014538	11.05	0.90	13.42	0.90	2.99	3316	175	3530	206	-0.15	0.25
133	266.41586	-29.002373	11.08	0.02	13.47	0.02	2.67	2801	178	3389	205	0.47	0.24
134	266.41455	-28.999651	11.05	0.90	13.37	0.90	2.85	3302	169	3405	205	0.19	0.25
137	266.42233	-29.003618	11.07	0.01	13.28	0.01	2.52	2762	164	3400	205	0.36	0.25
138	266.42401	-29.007814	11.07	0.90	13.62	0.90	2.77	3166	163	3395	205	0.15	0.25
145	266.41492	-29.012680	11.08	0.90	13.42	0.90	2.46	3253	163	3379	207	0.29	0.24
146	266.41501	-29.006264	10.81	0.01	13.12	0.01	2.68	3007	320	3340	211	0.40	0.32
152	266.41864	-29.003736	11.03	0.02	13.68	0.03	2.80	3040	273	3477	233	0.01	0.31
154	266.42386	-29.003574	11.11	0.90	14.21	0.90	2.79	3529	178	3069	205	0.85	0.25
156	266.41779	-29.002705	10.98	0.01	13.42	0.01	2.68	2477	438	3262	208	0.48	0.25
165	266.41904	-29.007879	10.88	0.01	13.36	0.02	2.73	3421	164	3352	215	0.25	0.24
167	266.42270	-29.001617	11.14	0.01	12.95	0.01	2.73	3507	378	3440	205	0.32	0.27
168	266.41925	-29.007391	11.09	0.01	13.26	0.01	2.56	3538	168	3399	205	0.40	0.24
171	266.41672	-29.008722	11.03	0.01	13.16	0.02	2.57	3479	178	3509	217	0.17	0.25
173	266.42154	-29.004095	11.15	0.01	13.31	0.01	2.60	3023	168	3421	205	0.34	0.25
184	266.41571	-29.014446	11.20	0.90	13.69	0.90	2.99	3102	175	3399	206	0.28	0.25
186	266.41544	-29.004692	11.08	0.01	13.28	0.02	2.60	3019	331	3373	206	0.23	0.24
191	266.42169	-29.005253	11.01	0.01	13.02	0.01	2.41	3148	205	3488	208	0.05	0.29
216	266.42258	-29.007032	11.03	0.01	12.77	0.01	2.57	3364	170	3778	257	0.06	0.25
224	266.41919	-29.002748	11.30	0.01	13.86	0.01	2.77	3240	175	3395	205	0.25	0.24
225	266.42316	-29.002224	11.31	0.01	13.73	0.01	2.78	2704	175	3396	206	0.47	0.25
226	266.42151	-29.000822	11.31	0.90	13.64	0.90	2.97	3087	225	3514	258	-0.03	0.27
234	266.41425	-29.011614	11.34	0.01	13.36	0.01	2.33	3260	179	3439	205	0.29	0.24
235	266.42065	-29.008093	11.17	0.01	13.34	0.01	2.59	3302	167	3586	223	-0.22	0.33
236	266.41345	-29.010067	11.34	0.01	14.00	0.01	2.72	3208	163	3201	205	0.28	0.24
238	266.42035	-29.009640	11.31	0.01	13.87	0.01	3.03	2998	200	3373	205	0.22	0.24
242	266.41809	-28.999863	11.36	0.90	14.00	0.90	3.41	3214	177	3401	205	0.28	0.24
251	266.41699	-29.005293	11.20	0.02	13.42	0.02	2.57	3276	208	3385	205	0.41	0.24
253	266.42142	-29.004925	11.29	0.01	13.35	0.01	2.47	3084	175	3514	223	0.22	0.24
256	266.41687	-29.002863	11.37	0.01	13.47	0.01	2.56	3259	165	3415	222	0.78	0.25
257	266.41953	-29.002182	11.40	0.01	13.67	0.01	2.92	3335	163	3394	205	0.32	0.24
265	266.41858	-29.012802	11.42	0.90	13.59	0.90	2.79	3760	409	3527	226	0.44	0.28
268	266.41302	-29.013050	11.43	0.90	13.54	0.90	2.71	2932	372	3391	206	0.50	0.25
270	266.42044	-29.007963	11.79	0.01	13.90	0.01	2.59	4465	165	3803	210	-0.19	0.24

Table 3-11 *continued*

Table 3-11 *(continued)*

Id	R.A.	Dec.	K_S	$K_{S,err}$	H	H_{err}	A_{K_S}	$T_{eff,CO}$	$\sigma_{T_{eff,CO}}$	$T_{eff,*}$	$\sigma_{T_{eff,*}}$	[M/H]	$\sigma_{[M/H]}$
	(°)	(°)						(K)	(K)	(K)	(K)		
280	266.41675	-29.014807	11.45	0.90	13.98	0.90	3.02	3406	164	3382	205	0.28	0.25
285	266.41278	-29.009092	11.46	0.01	13.37	0.01	2.88	3742	167	3424	206	0.12	0.24
290	266.42029	-29.004440	11.31	0.01	13.46	0.01	2.54	2829	175	3404	205	0.48	0.24
304	266.42285	-29.004103	11.51	0.01	13.17	0.01	2.60	3616	168	3740	305	-0.21	0.24
305	266.41614	-28.999004	11.52	0.90	13.61	0.90	2.86	4642	172	3793	205	-0.89	0.25
307	266.41742	-29.003508	11.51	0.01	13.81	0.01	2.56	3072	258	3415	226	0.38	0.28
309	266.41376	-29.015631	11.52	0.90	13.84	0.90	2.96	3348	249	3437	205	0.32	0.24
310	266.42328	-29.006380	11.23	0.02	13.69	0.02	2.70	3047	175	3401	205	0.20	0.24
315	266.41718	-29.004700	9.66	0.01	12.23	0.01	2.51	3662	170	2300	206	-0.75	0.24
316	266.42520	-29.006914	11.53	0.90	14.40	0.90	3.11	2681	164	3310	206	0.48	0.25
323	266.42041	-29.010298	11.55	0.01	14.37	0.01	2.88	2933	170	3311	208	0.45	0.25
338	266.42166	-29.012245	11.58	0.01	13.98	0.01	2.79	3522	167	3339	211	0.44	0.32
347	266.42178	-29.006201	11.39	0.01	13.36	0.01	2.37	3288	175	3513	206	-0.03	0.25
351	266.42050	-29.004311	11.47	0.01	13.41	0.01	2.54	4108	165	3821	233	-1.14	0.32
354	266.41382	-29.007954	11.44	0.02	14.30	0.04	2.98	3422	175	3290	206	0.59	0.25
358	266.41495	-29.010553	11.63	0.01	13.57	0.01	2.43	3637	171	3395	205	0.28	0.25
362	266.42343	-29.008638	11.45	0.01	13.77	0.01	2.65	3214	241	3400	206	0.38	0.24
363	266.41376	-29.010965	11.64	0.01	13.77	0.01	2.40	3429	195	3509	231	0.17	0.26
365	266.42191	-29.005045	11.52	0.01	13.60	0.01	2.48	3394	165	3647	209	0.22	0.26
368	266.41388	-29.002548	11.65	0.01	13.86	0.01	2.62	3821	166	3440	205	-0.19	0.24
376	266.40753	-29.013672	11.68	0.90	14.23	0.90	3.31	3315	182	3345	213	0.55	0.26
378	266.41571	-29.015787	11.69	0.90	14.22	0.90	3.27	3425	177	3410	211	0.30	0.24
379	266.40878	-29.009350	11.69	0.90	14.59	0.90	3.22	2760	238	3403	205	0.42	0.24
385	266.41907	-29.005041	11.51	0.02	13.60	0.02	2.73	3287	194	3368	207	0.43	0.27
386	266.41687	-29.011995	11.47	0.01	13.66	0.03	2.63	3181	197	3404	206	0.42	0.24
390	266.42126	-29.001127	11.72	0.90	13.99	0.90	3.07	3404	253	3370	228	0.46	0.36
392	266.41754	-29.011990	11.34	0.02	14.28	0.03	2.72	2920	188	3044	205	0.77	0.24
406	266.41614	-29.015436	11.76	0.90	14.27	0.90	3.16	3369	186	3413	206	0.36	0.25
407	266.40695	-29.011070	11.76	0.90	14.76	0.90	3.46	3339	362	3376	206	-0.12	0.25
422	266.41626	-29.009604	11.69	0.01	13.85	0.02	2.56	3172	186	3353	211	0.56	0.30
425	266.41077	-29.014553	11.82	0.90	14.60	0.90	3.01	2876	165	3298	205	0.68	0.24
427	266.42172	-29.006935	11.68	0.01	13.69	0.01	2.46	3142	163	3470	205	0.11	0.24
434	266.41736	-29.014042	11.85	0.90	14.72	0.90	2.97	3835	181	3254	205	0.77	0.34
438	266.42114	-29.009212	11.64	0.01	14.00	0.01	2.75	3067	169	3394	205	0.40	0.28
439	266.41681	-29.002293	11.78	0.02	14.02	0.01	2.75	3291	320	3360	207	0.35	0.28
440	266.41663	-29.009872	13.84	0.02	15.88	0.03	2.46	3118	486	3383	215	0.26	0.34
441	266.41653	-29.008242	11.65	0.02	13.90	0.03	2.72	3625	176	3455	205	0.20	0.25
444	266.41855	-29.010599	11.54	0.02	13.99	0.04	2.76	3283	243	3393	205	0.33	0.25
448	266.41800	-29.005814	12.11	0.01	14.15	0.01	2.59	5324	169	4047	205	-1.25	0.24
449	266.42599	-29.005480	11.89	0.90	14.99	0.90	3.03	3063	199	3333	222	0.42	0.29

Table 3-11 *continued*

Table 3-11 *(continued)*

Id	R.A.	Dec.	K_S	$K_{S,err}$	H	H_{err}	A_{K_S}	$T_{eff,CO}$	$\sigma_{T_{eff,CO}}$	$T_{eff,*}$	$\sigma_{T_{eff,*}}$	[M/H]	$\sigma_{[M/H]}$
	(°)	(°)						(K)	(K)	(K)	(K)		
450	266.41809	-28.998802	11.89	0.90	14.32	0.90	3.07	3176	177	3396	205	0.29	0.25
453	266.40903	-29.011761	11.90	0.90	14.12	0.90	3.13	3031	163	3403	205	0.47	0.24
456	266.41974	-29.003576	11.87	0.02	14.10	0.03	2.79	3542	225	3520	300	-0.04	0.36
462	266.41647	-29.013035	11.92	0.90	14.31	0.90	2.64	3161	200	3403	205	0.56	0.25
464	266.41858	-29.002287	11.96	0.04	14.25	0.04	2.75	3598	246	3626	215	-0.27	0.26
468	266.41626	-29.002348	11.89	0.01	14.10	0.02	2.69	3162	260	3401	206	0.69	0.25
470	266.41745	-29.007996	11.92	0.02	14.06	0.03	2.66	4458	188	3961	206	-0.64	0.25
474	266.41443	-29.002247	11.95	0.01	14.30	0.01	2.63	4735	170	4052	207	-1.18	0.25
475	266.41867	-29.011787	11.69	0.03	14.49	0.04	2.79	3289	180	3402	207	0.12	0.25
478	266.41571	-29.008177	12.01	0.02	14.11	0.03	2.85	4129	431	3514	208	0.12	0.25
482	266.41818	-29.006348	11.72	0.01	13.95	0.01	2.75	3405	220	3643	271	-0.10	0.29
488	266.42297	-29.010637	11.98	0.01	14.31	0.01	2.54	3429	270	3354	214	0.39	0.34
489	266.40771	-29.012438	11.98	0.90	14.51	0.90	3.16	3266	167	3403	205	0.41	0.25
490	266.42026	-29.011614	11.98	0.01	15.09	0.01	3.16	3173	232	3386	206	0.19	0.24
492	266.42215	-29.001673	11.99	0.01	14.27	0.01	2.81	2994	168	3410	205	0.44	0.24
493	266.41113	-29.008364	11.99	0.01	14.78	0.01	2.91	3382	196	3425	205	0.31	0.24
498	266.41498	-29.008699	12.00	0.01	14.51	0.02	2.98	4352	163	3647	206	-0.34	0.24
500	266.41260	-29.008354	11.75	0.04	14.04	0.04	2.75	3378	165	3491	243	0.62	0.29
506	266.41730	-29.001766	12.02	0.02	14.49	0.02	2.88	3240	187	3388	205	0.36	0.24
510	266.41660	-29.013130	12.04	0.90	14.36	0.90	2.63	3572	409	3405	205	0.39	0.27
518	266.42172	-29.004902	11.88	0.01	14.09	0.01	2.58	3373	174	3546	231	0.18	0.24
519	266.41663	-29.005119	11.85	0.01	14.07	0.02	2.52	2966	183	3398	205	0.45	0.24
524	266.40759	-29.011082	12.08	0.90	15.34	0.90	3.47	3033	172	3333	209	0.66	0.24
525	266.42297	-29.003731	12.08	0.01	14.42	0.01	2.80	2929	175	3399	207	0.51	0.25
526	266.41330	-29.002993	15.59	0.02	17.85	0.05	2.66	3295	164	3598	243	0.99	0.26
531	266.41345	-29.006804	11.90	0.01	14.21	0.02	2.94	4241	163	3742	212	-0.80	0.24
538	266.42416	-29.007343	12.12	0.90	14.46	0.90	2.87	3249	327	3601	228	-0.03	0.30
540	266.41626	-29.002419	11.98	0.02	14.15	0.02	2.68	3422	165	3417	205	0.36	0.24
546	266.41440	-29.011454	12.15	0.01	14.12	0.01	2.38	3129	166	3423	206	0.48	0.24
547	266.41696	-29.008257	12.24	0.02	14.49	0.02	2.74	4942	356	3825	206	0.02	0.24
551	266.42194	-29.004950	12.12	0.01	14.68	0.01	2.66	2663	175	3398	207	0.65	0.25
553	266.42059	-29.006168	11.93	0.01	13.59	0.01	2.46	3604	169	3899	205	0.12	0.25
571	266.41821	-29.012957	12.19	0.91	14.42	0.90	2.80	3234	249	3356	212	0.54	0.24
582	266.41641	-29.007080	12.18	0.01	14.95	0.01	2.81	3751	178	3514	209	-0.12	0.24
583	266.42252	-29.007563	11.99	0.01	14.09	0.01	2.66	3664	182	3778	249	0.02	0.24
584	266.41797	-29.008503	11.92	0.01	14.14	0.01	2.57	2299	169	3339	228	0.78	0.37
588	266.41943	-29.001991	12.22	0.01	14.69	0.01	2.94	3287	204	3402	205	0.46	0.25
589	266.41809	-29.013887	12.22	0.91	14.50	0.91	2.78	3507	173	3592	205	0.27	0.25
590	266.42166	-29.007198	11.94	0.01	14.25	0.01	2.43	3362	174	3619	222	0.53	0.25
591	266.40894	-29.007990	12.23	0.90	15.23	0.90	3.27	2906	203	3396	205	0.50	0.24

Table 3-11 *continued*

Table 3-11 *(continued)*

Id	R.A.	Dec.	K_S	$K_{S,err}$	H	H_{err}	A_{K_S}	$T_{eff,CO}$	$\sigma_{T_{eff,CO}}$	$T_{eff,*}$	$\sigma_{T_{eff,*}}$	[M/H]	$\sigma_{[M/H]}$
	(°)	(°)						(K)	(K)	(K)	(K)		
592	266.42484	-29.002094	12.23	0.90	14.18	0.90	2.57	4307	164	4138	214	-0.17	0.28
597	266.41748	-29.011641	11.86	0.01	14.43	0.02	2.70	3412	227	3653	402	0.16	0.31
598	266.42496	-29.007315	12.24	0.90	15.39	0.90	3.05	3156	163	3406	205	0.38	0.25
605	266.42365	-29.008354	12.11	0.01	14.17	0.02	2.69	3337	249	3583	270	0.05	0.32
606	266.40707	-29.013386	12.25	0.90	15.59	0.90	3.25	2946	163	3052	205	0.77	0.24
608	266.41614	-29.004025	12.01	0.01	14.20	0.02	2.51	3213	164	3422	205	0.37	0.24
611	266.40781	-29.012098	12.26	0.90	15.59	0.90	3.15	2761	166	3309	217	0.50	0.24
621	266.41391	-29.010311	12.27	0.01	14.21	0.01	2.59	3408	262	3574	230	0.19	0.27
622	266.41507	-29.004053	12.29	0.02	14.54	0.03	2.64	4623	175	3084	207	0.52	0.25
626	266.41727	-29.006521	12.35	0.01	15.06	0.01	2.90	3389	166	3206	205	0.63	0.25
627	266.42130	-29.012211	12.28	0.01	14.70	0.01	2.84	3643	164	3348	205	0.45	0.25
628	266.41809	-29.009865	12.13	0.01	14.39	0.02	2.79	4311	184	4723	227	-0.38	0.24
629	266.42166	-29.007940	12.01	0.01	14.19	0.01	2.64	3374	179	3357	213	0.62	0.28
631	266.42416	-29.005165	12.30	0.90	15.10	0.90	2.90	3197	229	3410	205	0.44	0.24
632	266.41528	-29.016600	12.30	0.90	14.62	0.90	3.12	3375	164	3415	205	0.39	0.24
635	266.42303	-29.004759	12.30	0.01	14.95	0.01	2.71	3324	172	3444	205	0.15	0.29
652	266.41376	-29.012100	12.34	0.01	13.79	0.01	2.35	4895	401	3980	228	-1.22	0.24
654	266.41531	-29.000746	12.34	0.90	14.50	0.90	2.84	3609	176	3479	206	0.01	0.25
656	266.41812	-29.009113	12.29	0.01	14.33	0.01	2.51	3351	165	3409	205	0.56	0.26
661	266.41440	-29.013138	12.35	0.90	14.43	0.90	2.46	3457	260	3539	233	0.11	0.33
662	266.41867	-29.004597	12.08	0.01	14.59	0.01	2.96	3468	166	3433	207	0.29	0.25
667	266.42236	-29.010098	14.27	0.01	16.33	0.01	2.53	3451	164	3526	230	0.03	0.37
670	266.41278	-29.011522	12.35	0.01	14.72	0.01	2.50	3627	169	3644	434	0.25	0.28
675	266.41519	-29.015194	12.36	0.90	14.90	0.90	3.30	2968	426	3405	206	0.59	0.26
682	266.41718	-29.007048	12.16	0.01	14.11	0.01	2.75	3428	278	3494	244	0.78	0.32
688	266.41403	-29.010353	14.35	0.02	16.50	0.02	2.55	4561	168	3951	276	-0.97	0.33
692	266.41202	-29.006178	12.25	0.01	14.58	0.01	2.79	3645	177	3460	205	0.21	0.25
693	266.41248	-29.008341	12.39	0.01	14.53	0.01	2.75	3399	268	3343	211	0.85	0.25
694	266.42059	-29.005875	12.07	0.01	14.16	0.01	2.45	3089	373	3498	268	0.51	0.25
696	266.42026	-29.003000	12.39	0.01	14.69	0.01	2.67	3433	164	3401	205	0.50	0.24
697	266.40927	-29.014820	12.39	0.90	14.73	0.90	3.01	3430	201	3623	205	-0.22	0.25
699	266.41824	-29.004759	12.12	0.01	14.19	0.03	2.67	4782	180	4101	384	-0.73	0.31
701	266.41409	-29.008251	12.20	0.02	14.79	0.03	2.78	3565	179	3403	206	0.43	0.24
703	266.41696	-29.007376	12.69	0.01	15.19	0.02	2.77	3730	452	3427	211	0.72	0.25
708	266.40878	-29.009220	12.42	0.90	14.84	0.90	3.10	3450	228	3375	205	0.18	0.25
712	266.41525	-29.008928	12.31	0.02	14.68	0.03	2.75	3505	191	3380	208	0.47	0.24
726	266.41760	-29.009958	12.54	0.01	14.79	0.02	2.65	3470	163	3414	205	0.43	0.25
727	266.41812	-29.013445	12.46	0.90	15.12	0.90	2.85	3445	246	3583	227	0.32	0.31
732	266.41443	-29.009901	12.48	0.01	14.40	0.01	2.44	3749	167	3429	205	0.37	0.25
734	266.41260	-29.008162	12.34	0.04	15.06	0.04	2.74	3412	301	3399	205	0.48	0.24

Table 3-11 *continued*

Table 3-11 *(continued)*

Id	R.A.	Dec.	K_S	$K_{S,err}$	H	H_{err}	A_{K_S}	$T_{eff,CO}$	$\sigma_{T_{eff,CO}}$	$T_{eff,*}$	$\sigma_{T_{eff,*}}$	[M/H]	$\sigma_{[M/H]}$
	(°)	(°)						(K)	(K)	(K)	(K)		
736	266.41614	-29.013872	12.48	0.90	14.85	0.90	2.74	3401	166	3399	205	0.57	0.26
741	266.42221	-29.009548	12.49	0.01	14.72	0.01	2.62	3422	193	3401	205	0.58	0.24
744	266.41953	-29.012537	12.49	0.90	14.78	0.90	2.74	3294	163	3389	206	0.57	0.28
748	266.41205	-29.007483	12.40	0.02	15.27	0.02	2.82	3027	234	3331	224	0.76	0.27
753	266.41879	-29.008213	12.29	0.01	14.03	0.02	2.68	3868	180	3493	210	0.17	0.25
754	266.41623	-29.004189	12.36	0.01	14.42	0.02	2.53	3429	164	3658	403	0.34	0.38
758	266.42307	-29.004883	12.25	0.03	14.88	0.03	2.69	3031	164	3487	239	0.50	0.28
763	266.42313	-29.006020	12.39	0.02	14.57	0.03	2.60	3537	175	3575	207	0.15	0.25
766	266.42380	-29.006126	12.52	0.90	14.86	0.90	2.87	3331	163	3715	207	-0.05	0.24
770	266.40967	-29.007736	12.53	0.90	15.53	0.90	3.21	3305	187	3358	206	0.35	0.24
771	266.41827	-29.000378	12.53	0.90	15.69	0.90	3.59	3307	358	3366	209	0.23	0.31
775	266.41800	-29.008432	12.15	0.04	14.57	0.03	2.57	3873	207	3691	463	0.63	0.28
778	266.42093	-29.009659	12.55	0.01	14.65	0.01	2.73	3577	190	3556	215	0.35	0.29
779	266.41702	-29.012520	12.55	0.90	15.23	0.90	2.70	3412	202	3429	205	0.27	0.24
783	266.41983	-29.006035	12.38	0.01	14.45	0.01	2.50	3245	164	3444	208	0.31	0.24
786	266.41586	-28.998631	12.55	0.90	15.16	0.90	2.92	3399	192	3384	206	0.44	0.28
791	266.41669	-29.002781	12.52	0.01	14.86	0.01	2.62	3621	175	3639	209	-0.11	0.25
792	266.42261	-29.006411	12.01	0.01	14.82	0.01	2.49	3398	198	3518	233	0.15	0.26
804	266.42245	-29.006784	12.24	0.01	14.40	0.01	2.51	3210	164	3738	312	0.31	0.25
805	266.41498	-29.014784	12.58	0.90	15.06	0.90	2.89	3578	186	3870	211	-0.02	0.24
809	266.41205	-29.006685	12.53	0.01	14.85	0.02	2.78	3537	197	3903	205	0.11	0.25
814	266.41864	-29.007214	12.49	0.01	14.82	0.01	2.78	3535	167	3467	207	0.79	0.25
816	266.41608	-29.015982	12.60	0.90	15.15	0.90	3.23	3330	175	3515	207	0.73	0.25
821	266.42212	-29.004391	12.60	0.01	14.65	0.01	2.54	3350	214	3903	205	0.09	0.25
824	266.41885	-29.011356	12.24	0.02	14.64	0.04	3.05	3277	173	3406	205	0.54	0.30
830	266.41983	-29.006441	12.39	0.01	14.50	0.01	2.47	3064	311	3411	209	0.56	0.25
831	266.41479	-29.006573	12.40	0.01	14.62	0.02	2.75	3601	171	3409	207	0.44	0.26
836	266.41190	-29.005968	12.52	0.01	14.80	0.02	2.84	3695	189	3387	208	0.41	0.28
837	266.41818	-28.998991	12.62	0.90	14.97	0.90	3.07	4715	190	3971	214	-0.52	0.24
851	266.41428	-29.012781	12.65	0.90	14.60	0.90	2.44	3900	169	4218	207	0.00	0.25
856	266.41803	-29.003960	12.53	0.01	14.62	0.02	2.61	3611	169	3566	259	0.19	0.25
862	266.41690	-29.008066	12.59	0.02	14.82	0.03	2.61	4109	181	3625	209	0.59	0.26
867	266.41409	-29.003403	12.70	0.01	14.94	0.01	2.49	3084	175	3900	207	0.01	0.25
869	266.41327	-29.012655	12.69	0.90	14.72	0.90	2.66	3684	179	3746	212	0.46	0.31
871	266.42059	-29.011789	12.69	0.01	15.64	0.01	3.17	3370	164	3424	205	0.38	0.25
876	266.41241	-29.011311	12.70	0.01	15.52	0.01	2.65	3295	168	3431	205	0.34	0.25
877	266.42050	-29.003620	12.62	0.02	14.86	0.02	2.72	3217	165	3709	209	0.34	0.25
881	266.41800	-29.007368	12.66	0.02	14.82	0.02	2.56	3260	229	3330	206	0.83	0.27
886	266.42365	-29.002209	15.65	0.03	18.12	0.07	2.87	3558	166	3690	296	0.79	0.25
889	266.41821	-29.015991	12.72	0.90	15.48	0.90	3.22	3150	218	3465	247	0.45	0.30

Table 3-11 *continued*

Table 3-11 *(continued)*

Id	R.A.	Dec.	K_S	$K_{S,err}$	H	H_{err}	A_{K_S}	$T_{eff,CO}$	$\sigma_{T_{eff,CO}}$	$T_{eff,*}$	$\sigma_{T_{eff,*}}$	[M/H]	$\sigma_{[M/H]}$
	(°)	(°)						(K)	(K)	(K)	(K)		
894	266.41449	-29.014227	12.72	0.90	15.01	0.90	2.64	3424	166	3375	206	0.50	0.25
898	266.41446	-29.010950	12.73	0.01	14.78	0.01	2.37	2965	300	3384	206	0.88	0.28
903	266.41110	-29.011145	12.74	0.01	15.66	0.01	2.89	2968	186	3293	208	0.61	0.29
904	266.41171	-29.011250	12.74	0.01	15.30	0.01	2.95	3366	274	3399	206	0.42	0.25
905	266.41492	-29.008863	12.48	0.01	14.85	0.02	2.68	3545	221	3404	205	0.51	0.24
907	266.41757	-29.004734	12.63	0.01	14.76	0.01	2.52	3450	166	3396	205	0.51	0.25
910	266.41837	-29.003201	12.88	0.01	15.43	0.01	2.78	3012	197	3394	205	0.67	0.25
917	266.41772	-29.001163	12.82	0.01	15.40	0.01	3.10	4497	177	3898	211	-1.03	0.24
918	266.42145	-29.007406	12.61	0.01	14.51	0.01	2.47	3939	169	3896	205	0.17	0.24
925	266.41364	-29.009142	12.72	0.01	15.06	0.01	2.71	3598	164	3681	368	0.02	0.24
930	266.41541	-29.010298	12.61	0.03	14.70	0.02	2.45	3535	351	3602	284	0.27	0.27
931	266.42325	-29.003578	12.78	0.01	15.45	0.01	2.93	3992	179	3505	205	0.58	0.25
939	266.42230	-29.005709	12.65	0.01	14.60	0.01	2.41	3872	175	3420	211	0.83	0.33
943	266.41476	-29.003391	12.66	0.01	14.74	0.01	2.46	3423	170	3477	223	0.39	0.33
944	266.41476	-29.015236	12.79	0.90	15.08	0.90	3.08	3880	165	3531	230	0.19	0.24
945	266.41592	-29.013023	12.79	0.90	14.98	0.90	2.73	3504	485	3390	247	0.27	0.34
949	266.42102	-29.007717	12.60	0.01	14.67	0.01	2.54	3642	167	3713	213	-0.13	0.25
954	266.41260	-29.013672	12.81	0.90	14.76	0.90	2.90	3483	164	3505	205	0.88	0.26
959	266.41043	-29.007265	12.81	0.90	15.53	0.90	3.18	2912	269	3410	206	0.64	0.28
960	266.41779	-29.006075	12.43	0.01	14.72	0.01	2.74	3571	164	3413	205	0.41	0.24
963	266.42264	-29.004353	15.65	0.03	18.05	0.04	2.55	3682	166	3668	212	0.77	0.28
964	266.41470	-29.010609	14.98	0.01	16.95	0.03	2.46	3783	186	3502	205	1.00	0.24
968	266.41867	-29.013489	12.82	0.90	15.04	0.90	2.80	3638	241	3496	244	0.78	0.37
977	266.41934	-29.007116	12.68	0.01	14.76	0.01	2.56	3258	383	3748	344	0.32	0.27
979	266.41800	-29.003510	12.83	0.01	14.98	0.01	2.65	3309	165	3673	212	0.58	0.24
987	266.41492	-29.014647	12.84	0.90	15.28	0.90	2.82	3696	171	3730	304	0.07	0.25
988	266.41895	-29.004152	12.87	0.02	15.44	0.03	2.78	3516	185	3448	206	0.24	0.27
990	266.42139	-29.009720	12.84	0.01	15.50	0.01	2.66	3211	169	3399	205	0.31	0.27
991	266.41589	-29.001415	12.82	0.01	15.05	0.01	2.73	3452	170	3492	228	0.44	0.28
994	266.41937	-29.009338	13.09	0.01	15.28	0.02	2.78	3732	164	3716	207	0.47	0.27
999	266.41635	-29.003559	12.99	0.01	15.10	0.01	2.50	3627	166	3634	219	0.25	0.24
1004	266.41736	-29.017534	12.85	0.90	16.17	0.90	3.47	3447	169	3406	205	0.34	0.24
1006	266.41461	-29.003693	12.78	0.01	14.83	0.01	2.48	3113	164	3453	259	0.75	0.24
1007	266.42178	-29.006525	12.69	0.01	15.18	0.01	2.38	3642	164	3887	206	-0.19	0.27
1008	266.42642	-29.004353	12.86	0.90	15.83	0.90	3.22	3151	234	3398	205	0.52	0.25
1009	266.42389	-29.002943	12.86	0.90	15.21	0.90	2.77	3557	175	3913	205	0.14	0.24
1015	266.42084	-29.005308	14.81	0.02	16.65	0.02	2.42	4797	191	4411	215	-0.89	0.28
1028	266.42532	-29.003208	12.88	0.90	15.03	0.90	2.88	3835	173	3476	222	0.36	0.29
1040	266.41788	-29.010601	12.80	0.01	15.08	0.02	2.70	3691	185	3687	350	0.02	0.25
1046	266.41537	-29.005014	12.85	0.01	14.76	0.02	2.58	3519	243	3922	207	0.12	0.31

Table 3-11 *continued*

Table 3-11 *(continued)*

Id	R.A.	Dec.	K_S	$K_{S,err}$	H	H_{err}	A_{K_S}	$T_{eff,CO}$	$\sigma_{T_{eff,CO}}$	$T_{eff,*}$	$\sigma_{T_{eff,*}}$	[M/H]	$\sigma_{[M/H]}$
	(°)	(°)						(K)	(K)	(K)	(K)		
1047	266.41727	-29.011795	12.68	0.02	14.96	0.03	2.62	4128	177	3924	209	-0.63	0.34
1049	266.41971	-29.001760	12.90	0.01	15.56	0.01	2.88	3416	198	3668	428	0.41	0.28
1050	266.41675	-29.012566	12.91	0.90	15.19	0.90	2.72	3276	244	3420	217	0.76	0.33
1051	266.42337	-29.003422	12.91	0.01	15.36	0.01	2.97	3345	170	3883	206	-0.04	0.26
1058	266.42145	-29.002750	15.49	0.02	17.59	0.04	2.71	4710	167	4029	225	-0.23	0.25
1060	266.42145	-29.011246	12.92	0.01	15.09	0.01	2.69	3882	168	3537	206	0.30	0.25
1068	266.41653	-29.006496	12.72	0.01	14.98	0.01	2.76	3619	369	3357	217	0.64	0.33
1070	266.41599	-29.001604	12.98	0.01	14.97	0.02	2.72	4825	165	4195	212	-0.63	0.28
1071	266.41571	-29.010422	12.93	0.01	14.79	0.01	2.45	3935	175	4390	222	-0.41	0.26
1079	266.41599	-29.012703	12.95	0.90	15.18	0.90	2.70	3620	195	3773	269	0.00	0.28
1080	266.41840	-29.008720	12.81	0.01	14.81	0.01	2.56	3725	196	3654	405	0.26	0.38
1086	266.41412	-29.014639	12.96	0.90	15.08	0.90	2.82	3582	185	3405	205	0.48	0.24
1092	266.42081	-29.004541	12.67	0.01	14.89	0.01	2.51	3072	177	3897	205	0.70	0.25
1100	266.41412	-29.011169	12.97	0.01	14.85	0.01	2.33	3582	396	3764	218	0.08	0.27
1106	266.42172	-29.010563	12.97	0.01	15.19	0.01	2.62	3463	175	3475	215	0.82	0.26
1108	266.42148	-29.011766	12.98	0.01	15.21	0.01	2.82	3315	201	3367	215	0.47	0.25
1109	266.41705	-29.010752	12.63	0.01	14.75	0.01	2.52	3773	282	3399	205	0.52	0.24
1110	266.42422	-29.003529	12.98	0.90	15.23	0.90	2.74	4496	203	3476	295	0.83	0.27
1112	266.41644	-29.014996	12.98	0.90	15.46	0.90	3.07	3628	166	3611	221	0.93	0.25
1113	266.41074	-29.011730	12.87	0.91	15.86	0.92	3.23	3235	180	3373	206	0.49	0.24
1121	266.42245	-29.010098	15.66	0.03	17.94	0.04	2.55	3062	175	3806	224	0.94	0.26
1124	266.41739	-29.010471	12.83	0.01	14.87	0.02	2.64	4501	164	4121	219	-0.33	0.30
1125	266.41452	-29.003633	12.84	0.01	14.95	0.01	2.48	3146	239	3386	206	0.66	0.32
1127	266.40714	-29.012390	13.00	0.90	15.21	0.90	3.17	3915	175	4077	208	0.02	0.26
1135	266.42236	-29.002581	13.01	0.01	15.10	0.01	2.71	4254	186	4152	234	-0.28	0.29
1136	266.42233	-29.003403	13.01	0.01	15.12	0.01	2.57	3650	169	3635	208	0.00	0.25
1138	266.41150	-29.008324	13.01	0.01	15.40	0.01	2.80	3446	165	3412	205	0.34	0.24
1144	266.41913	-29.004314	12.86	0.02	15.39	0.03	2.74	3679	166	3611	326	0.23	0.34
1145	266.41812	-29.014215	13.02	0.90	15.32	0.90	2.79	3755	283	3516	331	0.41	0.25
1146	266.41940	-29.005552	12.81	0.01	14.94	0.01	2.63	3446	170	3893	206	0.20	0.33
1147	266.42505	-29.004974	13.02	0.90	15.86	0.90	2.96	3518	167	3701	279	0.16	0.24
1148	266.42209	-29.011602	13.03	0.01	15.43	0.01	2.79	3549	190	3398	205	0.85	0.27
1151	266.41605	-29.008072	13.41	0.02	15.68	0.04	2.76	4401	280	3549	208	-0.22	0.28
1153	266.41068	-29.005999	12.87	0.91	15.36	0.91	3.12	3430	165	3493	234	0.51	0.25
1155	266.41544	-29.008190	12.99	0.02	15.52	0.03	3.03	4907	273	3744	303	-0.31	0.28
1161	266.41727	-29.012365	12.81	0.02	15.00	0.03	2.76	3529	164	3500	227	0.34	0.25
1163	266.41681	-29.004583	12.93	0.01	14.89	0.01	2.38	4015	181	4495	215	0.02	0.27
1165	266.41925	-29.004295	13.05	0.01	15.26	0.01	2.68	3836	303	3777	344	-0.05	0.35
1171	266.41095	-29.011372	13.06	0.01	16.29	0.01	2.96	3493	184	3701	208	-0.48	0.28
1177	266.41281	-29.009876	15.85	0.03	18.98	0.18	3.06	3544	164	3814	206	0.75	0.26

Table 3-11 *continued*

Table 3-11 *(continued)*

Id	R.A.	Dec.	K_S	$K_{S,err}$	H	H_{err}	A_{K_S}	$T_{eff,CO}$	$\sigma_{T_{eff,CO}}$	$T_{eff,*}$	$\sigma_{T_{eff,*}}$	[M/H]	$\sigma_{[M/H]}$
	(°)	(°)						(K)	(K)	(K)	(K)		
1178	266.40952	-29.014214	13.07	0.90	15.41	0.90	2.85	3890	164	4067	212	0.09	0.25
1184	266.41785	-29.007839	12.75	0.04	14.95	0.03	2.58	4202	538	3792	244	0.28	0.37
1189	266.41965	-29.010170	13.17	0.01	15.49	0.03	2.68	2925	175	3328	215	0.95	0.26
1193	266.41766	-29.015926	13.08	0.90	15.45	0.90	3.21	3760	220	3327	211	0.48	0.31
1206	266.41742	-29.003832	12.92	0.01	14.94	0.01	2.52	3738	186	3902	205	0.05	0.25
1210	266.41266	-29.010744	13.10	0.01	15.80	0.01	2.72	3479	215	3454	213	0.52	0.25
1211	266.42053	-29.008406	12.86	0.01	14.95	0.01	2.58	3300	271	3843	219	-0.03	0.34
1220	266.41403	-29.006220	13.12	0.01	15.58	0.01	2.78	3431	175	3885	215	0.02	0.26
1227	266.42291	-29.008631	13.03	0.01	15.01	0.01	2.75	3799	234	3911	206	-0.16	0.26
1230	266.42450	-29.004244	13.12	0.90	15.67	0.90	2.77	3420	164	3502	246	0.37	0.24
1233	266.41498	-29.001451	13.12	0.01	15.27	0.01	2.61	4265	216	3936	211	-0.82	0.26
1239	266.42484	-29.006716	13.13	0.90	15.71	0.91	3.25	3300	240	3293	210	0.94	0.25
1248	266.41638	-28.999792	13.15	0.90	15.17	0.90	2.86	4098	175	3450	215	0.01	0.26
1250	266.41071	-29.011463	13.15	0.90	16.03	0.90	3.22	3158	164	3393	205	0.40	0.26
1255	266.42407	-29.004765	13.15	0.90	15.47	0.90	2.76	3584	230	3681	366	0.08	0.26
1259	266.41965	-29.011335	13.16	0.01	15.68	0.01	3.06	3873	224	3613	207	-0.11	0.26
1263	266.41000	-29.014530	13.17	0.90	16.27	0.90	2.84	3643	377	3814	207	0.11	0.25
1264	266.41492	-29.003098	13.08	0.01	15.15	0.01	2.49	3739	306	3519	227	0.59	0.34
1270	266.41766	-29.010380	12.97	0.01	15.30	0.02	2.64	3545	175	3896	215	-0.04	0.26
1271	266.41907	-29.003124	12.92	0.01	15.24	0.03	2.84	3844	335	3798	252	-0.10	0.30
1281	266.41589	-29.001749	15.25	0.02	17.39	0.04	2.73	3351	167	3646	273	0.98	0.24
1288	266.41064	-29.012886	13.19	0.90	15.47	0.90	3.13	3381	175	3657	215	0.78	0.27
1302	266.41574	-29.016493	13.20	0.90	15.56	0.90	3.20	3205	179	3743	317	0.37	0.31
1307	266.41895	-29.013653	13.21	0.90	15.38	0.90	2.79	3636	244	3747	245	0.85	0.31
1310	266.41315	-29.010544	13.21	0.01	15.92	0.01	2.69	3879	421	3599	227	0.25	0.38
1314	266.41632	-29.005119	13.10	0.01	15.06	0.02	2.50	3920	175	3724	215	-0.56	0.26
1316	266.41693	-29.011318	13.15	0.01	15.60	0.02	2.76	3504	257	3647	215	0.57	0.31
1317	266.41925	-29.009899	13.02	0.01	15.13	0.02	2.65	3790	191	3901	205	0.07	0.24
1325	266.42322	-29.003342	13.23	0.01	15.53	0.01	2.95	3538	313	3920	205	0.15	0.24
1329	266.41916	-29.010277	12.94	0.02	15.09	0.02	2.60	3825	375	3396	207	0.43	0.27
1331	266.42084	-29.009041	13.20	0.01	15.35	0.01	2.75	3911	221	3918	207	0.10	0.29
1341	266.42160	-29.007521	13.15	0.01	15.11	0.01	2.49	3979	324	3687	208	0.19	0.29
1344	266.41483	-29.005974	13.39	0.01	15.62	0.02	2.70	4025	175	3721	226	0.16	0.26
1352	266.41525	-29.005028	13.11	0.01	15.16	0.02	2.52	3839	170	3514	263	0.17	0.37
1357	266.42139	-29.012569	13.25	0.90	15.59	0.90	2.98	3259	230	3463	235	0.36	0.28
1362	266.42093	-29.005245	13.51	0.01	15.38	0.01	2.41	4334	238	3569	220	0.53	0.27
1367	266.41428	-29.013044	13.27	0.90	15.25	0.90	2.51	3536	173	3880	211	0.14	0.32
1374	266.41840	-29.005167	13.08	0.01	15.08	0.02	2.63	5167	215	4687	446	-0.65	0.28
1382	266.41415	-29.010031	13.28	0.01	15.36	0.01	2.56	4229	175	3542	215	-0.17	0.26
1387	266.41809	-29.007925	13.33	0.03	15.44	0.03	2.50	4563	257	3461	300	0.19	0.25

Table 3-11 *continued*

Table 3-11 *(continued)*

Id	R.A.	Dec.	K_S	$K_{S,err}$	H	H_{err}	A_{K_S}	$T_{eff,CO}$	$\sigma_{T_{eff,CO}}$	$T_{eff,*}$	$\sigma_{T_{eff,*}}$	[M/H]	$\sigma_{[M/H]}$
	(°)	(°)						(K)	(K)	(K)	(K)		
1397	266.41266	-29.002357	13.30	0.01	15.62	0.01	2.87	4791	175	4467	224	-0.87	0.26
1398	266.41379	-29.012920	13.30	0.90	15.22	0.90	2.57	3549	253	3413	205	0.44	0.25
1402	266.41620	-29.009214	13.24	0.01	15.41	0.02	2.59	3346	175	3596	215	0.20	0.26
1404	266.41779	-28.999891	13.30	0.90	15.74	0.90	3.28	4080	178	3682	368	0.06	0.28
1409	266.41971	-29.012054	13.30	0.01	16.17	0.01	2.80	3412	164	3396	205	0.96	0.24
1425	266.42636	-29.004766	13.31	0.90	15.79	0.90	3.09	3787	164	3905	205	-0.20	0.25
1428	266.42413	-29.008787	13.32	0.90	15.71	0.90	2.96	2967	171	3404	206	0.69	0.27
1429	266.41727	-29.005453	13.32	0.01	15.34	0.02	2.60	5034	170	4151	313	-0.04	0.30
1438	266.41684	-29.004688	13.14	0.01	15.12	0.01	2.40	3957	180	3568	215	0.71	0.26
1443	266.42291	-29.004393	13.33	0.01	15.35	0.01	2.65	3988	285	3582	340	0.19	0.26
1447	266.42279	-29.006817	13.17	0.01	15.25	0.01	2.52	3310	330	3583	280	0.79	0.26
1455	266.41891	-29.010996	13.06	0.03	15.48	0.04	2.91	3689	175	3575	215	0.26	0.26
1462	266.42523	-29.004967	13.35	0.90	15.62	0.90	2.92	4318	219	3910	206	0.02	0.27
1465	266.41507	-29.010630	13.35	0.01	15.36	0.01	2.44	3408	308	3695	368	0.17	0.29
1466	266.41611	-29.003786	13.28	0.02	15.39	0.02	2.53	3535	165	3486	250	0.49	0.31
1487	266.42514	-29.003004	13.37	0.90	15.49	0.90	2.61	4224	175	3679	215	0.28	0.26
1491	266.41852	-29.010424	13.12	0.03	15.28	0.04	2.73	3556	165	3562	289	0.59	0.25
1497	266.41553	-29.005039	13.32	0.01	15.50	0.02	2.62	3142	175	3903	215	0.03	0.26
1499	266.42398	-29.002485	13.38	0.90	15.39	0.90	2.69	3505	175	3416	215	0.70	0.26
1500	266.42426	-29.003393	13.38	0.90	15.61	0.90	2.64	3775	180	3358	207	0.72	0.27
1503	266.41876	-29.005274	13.10	0.03	15.25	0.02	2.66	3699	217	3898	206	0.12	0.25
1504	266.41714	-29.000154	13.38	0.90	15.55	0.90	2.93	3429	175	3418	215	0.40	0.26
1505	266.41510	-29.009163	13.34	0.01	15.35	0.02	2.50	4107	245	3966	227	-0.37	0.28
1509	266.41196	-29.016159	13.39	0.90	16.76	0.91	3.34	3151	165	3398	205	0.75	0.38
1512	266.41290	-29.013212	13.39	0.90	15.28	0.90	2.71	3328	180	3908	215	-0.13	0.26
1515	266.41641	-29.015362	13.39	0.90	15.82	0.90	3.15	3165	168	3881	217	-0.12	0.25
1519	266.42123	-29.003683	13.39	0.01	15.24	0.01	2.74	4027	182	4025	272	-0.31	0.29
1521	266.41962	-29.014248	13.39	0.90	15.77	0.90	2.93	3731	175	3922	215	0.43	0.26
1528	266.41660	-29.012918	13.41	0.90	15.64	0.90	2.65	2414	175	3530	215	0.92	0.26
1530	266.41492	-29.000210	13.41	0.90	15.92	0.90	2.83	3552	164	3876	212	0.00	0.25
1539	266.42029	-29.006161	13.34	0.01	15.33	0.01	2.41	2870	244	4093	325	0.16	0.27
1545	266.41330	-29.014585	13.43	0.90	15.50	0.90	3.03	3834	175	3647	215	0.49	0.26
1551	266.42252	-29.010786	13.43	0.01	15.72	0.01	2.45	3750	173	3721	254	0.69	0.28
1552	266.42538	-29.006886	13.43	0.90	16.25	0.90	3.05	2838	172	3483	238	0.59	0.26
1561	266.41595	-29.005693	14.06	0.01	16.16	0.01	2.66	4702	175	3615	224	0.19	0.27
1577	266.41397	-29.013943	13.45	0.90	15.60	0.90	2.60	3590	224	3778	283	0.12	0.25
1582	266.41428	-29.007017	13.34	0.01	15.97	0.02	3.05	3617	195	3516	334	0.37	0.38
1585	266.41592	-29.001009	13.46	0.90	15.66	0.90	2.91	4683	175	4105	288	-0.60	0.27
1589	266.40784	-29.010241	13.46	0.90	15.98	0.90	3.30	3629	165	3562	209	0.41	0.38
1592	266.40933	-29.008156	13.47	0.90	16.05	0.90	3.32	3467	166	3401	205	0.43	0.25

Table 3-11 *continued*

Table 3-11 *(continued)*

Id	R.A.	Dec.	K_S	$K_{S,err}$	H	H_{err}	A_{K_S}	$T_{eff,CO}$	$\sigma_{T_{eff,CO}}$	$T_{eff,*}$	$\sigma_{T_{eff,*}}$	[M/H]	$\sigma_{[M/H]}$
	(°)	(°)						(K)	(K)	(K)	(K)		
1593	266.40756	-29.011965	13.47	0.90	16.37	0.90	3.17	3379	165	3398	205	0.42	0.25
1594	266.41891	-29.001204	13.49	0.02	16.58	0.03	3.09	3653	175	3396	215	0.42	0.26
1596	266.42261	-29.006084	13.35	0.01	14.98	0.01	2.43	4082	175	3909	215	0.03	0.26
1597	266.41913	-29.010094	13.48	0.02	15.76	0.02	2.59	3822	187	3528	270	0.56	0.32
1604	266.42319	-29.001587	13.47	0.01	15.65	0.01	2.78	3790	168	3660	288	0.94	0.25
1609	266.42075	-29.009022	13.32	0.01	15.54	0.01	2.72	3968	175	3947	215	0.10	0.26
1614	266.41202	-29.008722	13.49	0.01	15.68	0.01	2.81	3339	175	3484	215	0.91	0.26
1621	266.42438	-29.006681	13.49	0.90	16.35	0.91	3.27	3285	278	3860	213	-0.10	0.25
1624	266.41968	-29.001667	13.49	0.01	16.22	0.01	2.89	3800	171	3430	206	0.36	0.25
1630	266.41727	-29.004953	13.28	0.02	15.32	0.03	2.53	4081	215	3817	211	-0.17	0.25
1631	266.42282	-29.008221	13.27	0.01	15.67	0.01	2.65	3679	314	3888	205	0.06	0.27
1640	266.41422	-29.009130	13.30	0.01	15.29	0.02	2.51	4104	418	3799	237	0.17	0.26
1642	266.42340	-29.009787	13.51	0.01	15.47	0.01	2.59	4048	253	3940	211	-0.19	0.24
1650	266.41522	-29.002235	13.64	0.02	15.99	0.03	2.69	3042	199	3708	215	0.74	0.25
1652	266.41711	-29.009640	13.39	0.01	15.45	0.02	2.47	3345	175	3849	215	0.65	0.26
1653	266.41455	-29.001780	13.46	0.01	15.59	0.01	2.56	4006	181	3899	205	-0.14	0.25
1658	266.41626	-29.000544	13.53	0.90	15.57	0.90	2.91	3944	182	3913	205	-0.13	0.28
1660	266.41794	-29.005545	13.22	0.02	15.31	0.02	2.63	3836	166	3670	416	0.28	0.26
1664	266.41785	-29.013163	13.53	0.90	15.74	0.90	2.82	4103	180	3665	215	0.29	0.26
1667	266.41684	-29.000731	13.53	0.90	16.26	0.90	3.21	3597	173	3356	210	0.56	0.25
1669	266.41400	-29.015829	13.53	0.90	15.67	0.90	3.02	3909	818	3807	243	-0.01	0.25
1677	266.41736	-29.009998	13.61	0.01	15.69	0.03	2.67	3750	179	3509	215	0.52	0.26
1680	266.41684	-28.998081	13.54	0.90	15.74	0.90	2.88	3450	167	3595	210	0.69	0.28
1696	266.41895	-29.005600	13.34	0.02	15.82	0.03	2.75	3037	170	3911	206	0.15	0.25
1699	266.41055	-29.007355	13.18	0.92	15.67	0.95	3.19	3450	180	3407	205	0.57	0.27
1700	266.41873	-29.005890	13.32	0.02	15.45	0.03	2.80	3114	189	3906	206	-0.01	0.25
1716	266.40738	-29.012524	13.57	0.90	15.97	0.90	3.16	3484	166	3536	211	0.89	0.26
1717	266.41382	-29.008245	13.52	0.03	15.84	0.04	2.87	4028	175	3897	215	0.00	0.26
1721	266.41684	-28.999475	13.58	0.90	15.65	0.90	2.70	4056	172	3747	222	0.19	0.26
1722	266.41763	-29.003658	13.35	0.01	15.26	0.01	2.61	5017	177	4139	225	-0.75	0.28
1723	266.42279	-29.005619	13.44	0.01	15.63	0.02	2.44	3527	216	3688	216	0.05	0.25
1726	266.41394	-29.000601	13.58	0.90	15.59	0.90	2.71	3664	175	3583	217	0.48	0.26
1727	266.42014	-29.006233	13.36	0.01	15.38	0.01	2.41	3838	175	3949	215	-0.15	0.26
1729	266.41962	-29.008511	13.64	0.01	15.48	0.02	2.70	4156	171	3945	218	0.13	0.29
1742	266.42218	-29.011038	13.60	0.01	15.79	0.01	2.62	3593	273	3808	274	0.07	0.28
1748	266.42371	-29.005051	13.60	0.01	15.85	0.01	2.69	3618	187	3789	220	-0.08	0.25
1755	266.41837	-28.999825	13.61	0.90	16.32	0.90	3.47	3458	176	3661	392	0.34	0.29
1756	266.41324	-29.011593	13.61	0.01	15.40	0.01	2.41	4066	177	3995	215	-0.13	0.26
1760	266.42264	-29.009279	13.61	0.01	15.77	0.01	2.62	3698	272	3908	205	0.05	0.26
1767	266.41885	-29.009039	14.48	0.02	16.47	0.03	2.63	4276	211	3781	234	-0.05	0.25

Table 3-11 *continued*

Table 3-11 *(continued)*

Id	R.A.	Dec.	K_S	$K_{S,err}$	H	H_{err}	A_{K_S}	$T_{eff,CO}$	$\sigma_{T_{eff,CO}}$	$T_{eff,*}$	$\sigma_{T_{eff,*}}$	[M/H]	$\sigma_{[M/H]}$
	(°)	(°)						(K)	(K)	(K)	(K)		
1770	266.41858	-29.005438	13.50	0.03	15.88	0.03	2.66	3469	275	3843	261	0.08	0.28
1781	266.41989	-29.002373	14.50	0.01	16.88	0.02	2.69	3931	175	3617	224	0.67	0.26
1787	266.41971	-29.009071	13.73	0.02	16.02	0.03	2.65	3294	175	3939	215	0.31	0.26
1793	266.42456	-29.006603	13.64	0.90	16.31	0.90	3.30	2955	219	3551	275	0.50	0.26
1797	266.41492	-29.003897	13.50	0.01	15.62	0.02	2.53	3741	351	3906	206	0.14	0.25
1800	266.41394	-29.013393	13.64	0.91	15.40	0.90	2.61	3111	175	3174	215	-0.05	0.26
1804	266.42511	-29.002193	13.64	0.90	15.68	0.90	2.60	4046	176	3735	277	0.46	0.35
1808	266.41702	-29.009539	13.69	0.01	15.76	0.02	2.49	3847	179	4008	230	-0.13	0.26
1819	266.42010	-29.002823	13.65	0.01	15.80	0.01	2.66	3982	175	3854	215	0.22	0.26
1824	266.41818	-29.006947	13.59	0.01	15.79	0.01	2.59	3800	175	3491	220	0.89	0.26
1826	266.41135	-29.013887	13.65	0.90	16.90	0.90	3.19	3218	175	3400	215	0.69	0.26
1831	266.41446	-29.005604	13.39	0.01	15.46	0.02	2.65	4105	175	3680	215	-0.42	0.26
1834	266.41522	-29.002043	13.69	0.02	15.96	0.03	2.73	3941	175	3898	215	0.06	0.26
1848	266.41193	-29.014835	13.66	0.90	16.66	0.90	3.11	2976	174	3401	205	0.74	0.26
1849	266.42563	-29.002613	13.66	0.90	15.69	0.90	2.67	3860	231	3907	206	0.12	0.26
1857	266.41782	-29.004032	13.41	0.01	15.60	0.01	2.55	3508	169	3864	261	0.48	0.28
1859	266.41580	-29.010866	13.34	0.01	15.46	0.02	2.49	3277	167	3563	257	0.55	0.25
1860	266.41653	-29.002901	13.62	0.01	15.68	0.01	2.57	3904	199	3902	215	-0.04	0.26
1870	266.41461	-29.007505	15.31	0.02	17.86	0.06	2.89	4529	180	3169	224	0.89	0.26
1871	266.41992	-29.006971	13.53	0.01	15.48	0.01	2.35	3622	297	3623	343	0.43	0.26
1875	266.41418	-29.006748	13.52	0.01	15.82	0.02	2.85	3360	186	3621	356	0.86	0.25
1885	266.41727	-29.010700	14.19	0.01	16.83	0.02	2.60	3819	224	3753	273	0.22	0.26
1887	266.40778	-29.013887	13.68	0.90	16.01	0.90	3.31	3521	166	3659	422	0.35	0.34
1896	266.41901	-29.009604	13.47	0.01	15.69	0.01	2.78	3369	169	3456	213	0.86	0.27
1898	266.42151	-29.004648	13.28	0.01	15.52	0.01	2.55	3654	538	3411	357	0.34	0.30
1901	266.40875	-29.009541	13.70	0.90	16.51	0.90	3.31	3941	181	3381	215	0.75	0.28
1903	266.41901	-29.010345	13.74	0.03	16.04	0.02	2.62	3425	179	3758	224	0.72	0.26
1904	266.41321	-29.015574	13.70	0.90	15.88	0.90	3.02	3852	172	3707	257	-0.05	0.28
1906	266.41354	-29.008898	13.65	0.01	15.92	0.02	2.71	4224	277	3923	210	-0.07	0.26
1908	266.41611	-28.999445	13.70	0.90	15.91	0.90	2.81	3942	182	3771	263	0.15	0.31
1914	266.42130	-29.006514	13.66	0.01	15.67	0.01	2.39	3751	175	3821	215	0.21	0.26
1921	266.41812	-29.009661	13.28	0.01	15.75	0.01	2.75	4006	175	3853	215	0.53	0.26
1923	266.42181	-29.006735	13.61	0.01	15.49	0.01	2.44	4292	340	3951	214	-0.17	0.31
1926	266.41541	-29.001644	13.72	0.01	15.81	0.01	2.69	4042	336	3611	219	0.02	0.28
1932	266.41327	-29.008123	13.82	0.04	16.16	0.05	2.81	3614	175	3302	224	0.92	0.26
1934	266.41260	-29.006172	13.57	0.01	16.28	0.02	2.83	4034	169	3945	264	-0.07	0.38
1936	266.41788	-29.007971	13.90	0.04	15.93	0.01	2.57	3846	176	3457	224	0.98	0.26
1938	266.42197	-29.007074	13.60	0.01	15.58	0.01	2.43	3467	210	4014	238	0.02	0.25
1944	266.41525	-29.010221	15.26	0.04	17.32	0.04	2.45	4127	170	3695	352	0.66	0.34
1953	266.42404	-29.006180	13.74	0.90	16.28	0.90	2.92	3899	219	3755	211	0.00	0.25

Table 3-11 *continued*

Table 3-11 *(continued)*

Id	R.A.	Dec.	K_S	$K_{S,err}$	H	H_{err}	A_{K_S}	$T_{eff,CO}$	$\sigma_{T_{eff,CO}}$	$T_{eff,*}$	$\sigma_{T_{eff,*}}$	[M/H]	$\sigma_{[M/H]}$
	(°)	(°)						(K)	(K)	(K)	(K)		
1954	266.41599	-29.007069	13.57	0.01	16.20	0.02	2.89	3601	175	3691	215	-0.32	0.26
1959	266.41666	-29.003410	13.76	0.01	15.45	0.01	2.45	4129	175	4050	219	-0.29	0.26
1961	266.40921	-29.007526	13.74	0.90	16.13	0.90	3.34	3224	175	3437	215	0.86	0.27
1969	266.41791	-29.004957	13.62	0.02	15.67	0.03	2.56	3398	192	3645	443	0.11	0.29
1975	266.41492	-29.014006	13.75	0.90	16.10	0.90	2.63	3532	175	3458	215	0.50	0.26
2000	266.41965	-29.005619	13.78	0.01	15.88	0.01	2.56	4099	255	3970	402	0.25	0.25
2002	266.41125	-29.014507	13.76	0.90	16.19	0.90	3.36	4671	175	4068	234	-0.55	0.30
2018	266.41534	-29.010584	14.57	0.03	16.60	0.03	2.42	3791	286	3690	237	0.98	0.26
2024	266.42096	-29.003439	13.77	0.01	15.99	0.01	2.79	3795	169	3492	221	0.59	0.29
2026	266.41794	-29.005152	13.57	0.02	15.69	0.02	2.58	3811	168	3723	313	0.17	0.25
2030	266.41098	-29.010225	13.77	0.01	15.73	0.01	2.65	4006	317	3900	205	0.01	0.24
2033	266.42062	-29.010000	15.62	0.02	17.96	0.04	2.89	3630	166	3919	338	0.82	0.25
2040	266.41559	-29.005575	13.61	0.01	15.54	0.01	2.67	3974	180	3924	223	-0.10	0.26
2062	266.42090	-29.007627	13.55	0.01	15.63	0.01	2.52	4449	175	3934	230	0.22	0.27
2064	266.41586	-28.998327	13.80	0.90	15.96	0.90	3.01	4593	197	3899	261	-0.03	0.30
2070	266.42017	-29.006453	13.44	0.01	15.68	0.01	2.43	3219	499	3467	326	0.90	0.27
2071	266.41550	-29.008944	14.25	0.02	16.52	0.03	2.85	2712	184	3581	224	0.17	0.26
2076	266.42422	-29.002779	13.81	0.90	16.05	0.91	2.60	4174	177	3996	224	-0.13	0.27
2085	266.41943	-29.012499	13.81	0.90	16.22	0.90	2.75	3212	180	3861	256	0.84	0.28
2092	266.41476	-29.003168	13.78	0.01	15.69	0.01	2.48	4505	256	4180	226	-0.17	0.29
2099	266.41879	-29.008915	13.59	0.01	15.26	0.02	2.59	3988	454	3929	223	0.11	0.28
2105	266.42032	-29.000406	13.82	0.90	16.51	0.90	3.15	3814	173	3709	344	0.19	0.28
2111	266.41660	-29.000641	13.82	0.90	16.39	0.90	3.02	4089	175	4048	224	-0.02	0.26
2112	266.42087	-29.002171	13.82	0.01	16.35	0.01	2.74	3550	175	3425	224	0.66	0.26
2113	266.42297	-29.001698	14.99	0.03	17.10	0.04	2.78	4118	175	4326	224	0.53	0.26
2115	266.41895	-29.012487	13.83	0.90	15.99	0.90	2.80	3238	175	3598	224	0.98	0.26
2123	266.41492	-29.011126	13.83	0.01	15.63	0.01	2.39	3610	285	3930	356	0.01	0.27
2124	266.41635	-29.001572	13.70	0.02	16.12	0.02	2.72	3785	169	3919	206	0.27	0.29
2129	266.41782	-29.011810	14.83	0.01	17.38	0.03	2.75	4072	371	3998	216	0.94	0.24
2131	266.41946	-29.007629	13.77	0.01	15.78	0.01	2.49	3710	291	3935	207	0.25	0.26
2136	266.41534	-29.001410	13.89	0.02	15.92	0.02	2.62	3629	181	3507	224	0.79	0.27
2137	266.41251	-29.006887	13.69	0.02	16.11	0.03	2.89	3288	169	3663	232	0.69	0.26
2139	266.42319	-29.003031	13.84	0.01	16.66	0.01	2.82	3793	261	3705	225	-0.04	0.25
2142	266.42188	-29.004375	13.84	0.01	15.78	0.01	2.61	3002	184	4312	241	0.93	0.26
2144	266.41614	-29.009445	13.76	0.01	15.88	0.03	2.56	3237	180	3757	215	0.91	0.26
2147	266.41464	-29.002703	13.73	0.01	15.71	0.01	2.60	4157	174	3958	218	-0.26	0.25
2153	266.40790	-29.011442	13.85	0.90	16.84	0.90	3.17	3344	175	3308	224	0.87	0.27
2156	266.41904	-29.005932	13.73	0.02	15.65	0.03	2.74	5090	184	3517	215	-0.10	0.28
2163	266.42245	-29.004362	13.85	0.01	15.72	0.01	2.53	3591	175	3534	224	0.63	0.27
2164	266.41602	-29.010801	14.96	0.02	16.98	0.03	2.51	5214	176	5297	235	-0.57	0.28

Table 3-11 *continued*

Table 3-11 *(continued)*

Id	R.A.	Dec.	K_S	$K_{S,err}$	H	H_{err}	A_{K_S}	$T_{eff,CO}$	$\sigma_{T_{eff,CO}}$	$T_{eff,*}$	$\sigma_{T_{eff,*}}$	[M/H]	$\sigma_{[M/H]}$
	(°)	(°)						(K)	(K)	(K)	(K)		
2167	266.42700	-29.003567	13.86	0.90	16.80	0.91	3.25	3463	234	3325	207	0.77	0.34
2181	266.42529	-29.003366	13.86	0.90	16.26	0.90	2.92	4161	189	3910	224	0.16	0.29
2184	266.41931	-29.004824	13.74	0.02	15.88	0.01	2.80	3296	175	3952	220	0.49	0.26
2188	266.42108	-29.008650	13.61	0.01	15.93	0.01	2.82	3456	175	3587	216	0.87	0.26
2189	266.41925	-29.001663	13.70	0.05	16.69	0.02	3.01	3741	168	3305	211	0.80	0.33
2194	266.41986	-29.011341	13.86	0.01	16.52	0.01	3.11	3842	175	3489	224	0.62	0.38
2196	266.42062	-29.009682	13.87	0.01	16.41	0.01	2.81	3812	175	3694	224	0.20	0.26
2198	266.41800	-29.001871	13.74	0.02	15.88	0.03	2.82	4253	175	3889	215	0.12	0.26
2203	266.41479	-29.009274	13.68	0.01	15.72	0.02	2.47	4544	166	3230	215	0.87	0.25
2211	266.41766	-29.005871	13.58	0.01	15.63	0.01	2.73	3571	185	3958	219	0.15	0.26
2213	266.41415	-29.003168	13.58	0.01	15.66	0.01	2.54	4222	175	4004	221	0.12	0.26
2216	266.42093	-29.008656	13.92	0.01	16.06	0.01	2.82	3263	175	4346	224	0.33	0.26
2236	266.40900	-29.012369	13.89	0.90	17.13	0.90	3.27	3316	317	3652	212	0.78	0.31
2239	266.41953	-29.006277	13.93	0.01	16.05	0.02	2.57	3767	180	3695	224	0.17	0.26
2242	266.41281	-29.013845	13.89	0.90	16.21	0.90	2.86	3576	178	3711	248	0.46	0.27
2255	266.41547	-28.998924	13.90	0.90	16.10	0.90	2.92	3572	180	3879	227	0.26	0.26
2264	266.41565	-29.005659	14.13	0.01	16.31	0.02	2.69	4001	175	3708	224	0.18	0.26
2270	266.42542	-29.004419	13.91	0.90	16.37	0.90	2.98	3385	176	3512	211	0.74	0.38
2286	266.41135	-29.012089	13.91	0.01	16.56	0.01	3.01	3813	227	3390	212	0.77	0.28
2310	266.41846	-29.004160	13.67	0.01	15.93	0.02	2.72	3663	175	3371	215	0.87	0.26
2319	266.42062	-29.002625	13.94	0.01	16.10	0.01	2.70	3233	194	3704	218	0.49	0.25
2320	266.41635	-28.999981	13.94	0.90	16.38	0.90	2.95	3796	272	3853	247	0.26	0.28
2323	266.42383	-29.006687	13.94	0.90	16.23	0.91	2.87	3884	327	3850	224	-0.31	0.25
2328	266.41776	-29.005516	13.98	0.01	16.22	0.02	2.61	4273	183	3731	239	0.96	0.26
2329	266.41916	-29.004398	13.73	0.02	15.93	0.03	2.76	4640	187	3366	215	-0.35	0.27
2333	266.41714	-29.013994	13.94	0.91	16.25	0.90	2.85	3587	175	3428	224	0.97	0.26
2345	266.41391	-29.003092	13.95	0.01	15.99	0.01	2.54	3636	255	3491	239	0.31	0.26
2353	266.41574	-29.003061	13.96	0.01	16.00	0.01	2.55	4981	190	4464	238	-0.33	0.29
2355	266.41843	-29.004951	13.60	0.01	15.78	0.01	2.71	3847	175	3765	217	0.65	0.29
2357	266.41779	-28.999481	13.96	0.90	16.34	0.90	3.17	3612	176	3496	224	0.17	0.27
2371	266.42154	-29.007578	13.79	0.01	15.80	0.01	2.54	3825	175	3411	224	0.29	0.28
2386	266.42026	-29.014256	13.97	0.90	17.06	0.90	3.02	4711	177	4207	224	-0.41	0.28
2387	266.41977	-29.008863	13.54	0.01	15.79	0.02	2.67	3705	278	3994	267	0.17	0.28
2388	266.42508	-29.002645	13.97	0.90	16.08	0.90	2.67	3942	175	3398	224	0.70	0.28
2401	266.41483	-29.010294	13.99	0.01	16.22	0.01	2.43	4322	291	3348	213	0.54	0.31
2405	266.41113	-29.005711	13.96	0.01	15.98	0.01	2.88	3949	310	3713	279	0.69	0.36
2407	266.41000	-29.009678	13.99	0.90	16.62	0.90	3.15	3735	330	3886	207	0.06	0.25
2411	266.42191	-29.001961	14.00	0.01	16.15	0.01	2.87	4347	177	4629	239	0.27	0.26
2412	266.41943	-29.003786	13.82	0.01	16.03	0.02	2.75	3625	175	3437	235	0.57	0.28
2425	266.41510	-29.011354	14.00	0.01	15.98	0.01	2.55	4087	175	3476	224	0.64	0.26

Table 3-11 *continued*

Table 3-11 *(continued)*

Id	R.A.	Dec.	K_S	$K_{S,err}$	H	H_{err}	A_{K_S}	$T_{eff,CO}$	$\sigma_{T_{eff,CO}}$	$T_{eff,*}$	$\sigma_{T_{eff,*}}$	[M/H]	$\sigma_{[M/H]}$
	(°)	(°)						(K)	(K)	(K)	(K)		
2427	266.41638	-29.010605	13.94	0.01	16.02	0.02	2.51	3409	182	3928	224	0.11	0.26
2449	266.41656	-29.011148	15.61	0.02	17.65	0.04	2.57	3499	175	3717	230	0.93	0.26
2467	266.42035	-29.003611	14.02	0.01	16.13	0.01	2.75	3411	175	4170	224	-0.04	0.27
2497	266.40799	-29.011366	14.04	0.90	16.47	0.90	3.16	3356	227	3520	245	0.97	0.24
2498	266.42068	-29.009270	14.00	0.01	16.11	0.01	2.66	3780	179	3846	231	-0.37	0.26
2509	266.42682	-29.004519	14.04	0.90	16.51	0.90	3.22	3997	212	3746	442	0.50	0.27
2514	266.42279	-29.010157	14.05	0.01	16.08	0.01	2.54	4747	175	4211	224	-0.53	0.26
2523	266.42645	-29.005098	14.05	0.90	16.53	0.90	3.11	3742	175	3453	224	0.97	0.26
2524	266.42221	-29.002899	14.05	0.01	16.10	0.02	2.61	4125	175	3943	224	-0.69	0.26
2525	266.41125	-29.014950	14.05	0.90	17.28	0.91	3.33	2932	175	3400	224	0.65	0.26
2536	266.41544	-29.010441	15.54	0.03	17.27	0.04	2.42	4322	190	4397	245	0.54	0.29
2537	266.41501	-29.003698	13.94	0.02	15.95	0.02	2.54	3709	178	3913	224	0.22	0.26
2553	266.42099	-29.013466	14.06	0.90	16.74	0.90	3.03	3505	175	3849	224	0.66	0.26
2581	266.40823	-29.011982	14.08	0.90	16.45	0.90	3.14	3246	213	3776	334	0.54	0.33
2583	266.41690	-29.001455	14.06	0.03	16.23	0.03	2.93	3780	262	3881	227	0.14	0.36
2588	266.41223	-29.008587	14.15	0.01	16.56	0.02	2.76	3734	193	3511	224	0.68	0.28
2592	266.41681	-29.017212	14.08	0.90	17.07	0.90	3.28	4064	182	4064	224	-0.01	0.27
2594	266.41418	-29.000767	14.08	0.90	16.12	0.90	2.96	3807	265	4068	249	0.36	0.37
2604	266.42224	-29.010675	14.61	0.01	16.14	0.02	2.46	3880	261	3839	221	0.97	0.24
2612	266.41226	-29.010082	14.09	0.01	16.54	0.01	2.94	3480	177	3958	224	0.56	0.26
2622	266.42032	-29.003258	14.10	0.01	16.34	0.01	2.68	3761	179	3533	227	0.68	0.29
2623	266.42252	-29.008083	13.79	0.01	15.61	0.01	2.68	3845	205	3698	220	0.51	0.33
2628	266.41199	-29.006006	14.23	0.01	16.38	0.02	2.83	3898	423	4030	251	-0.35	0.25
2638	266.42209	-29.008804	14.00	0.01	16.67	0.01	2.73	3798	175	3876	224	0.17	0.26
2653	266.42300	-29.008209	13.85	0.02	16.05	0.02	2.67	3586	188	3928	209	0.34	0.26
2657	266.41739	-28.998842	14.12	0.90	16.22	0.90	2.69	3982	254	3928	213	-0.19	0.36
2659	266.41776	-29.009951	14.04	0.01	16.25	0.02	2.70	4331	178	3754	228	-0.09	0.31
2666	266.40930	-29.014652	14.12	0.90	16.46	0.90	3.10	3594	179	3391	224	0.90	0.26
2671	266.41815	-29.009424	14.20	0.01	16.29	0.02	2.61	4119	179	3418	224	0.01	0.26
2683	266.42361	-29.004406	11.85	0.04	14.13	0.04	2.73	3542	166	3454	205	0.23	0.24
2685	266.41702	-28.998262	14.13	0.90	16.27	0.90	2.87	3661	180	3912	224	0.27	0.26
2688	266.42487	-29.006514	14.13	0.90	16.97	0.91	3.30	3278	201	3578	225	-0.21	0.28
2702	266.42340	-29.005886	14.53	0.02	16.78	0.02	2.63	3964	180	3981	222	-0.60	0.28
2704	266.41470	-29.009069	13.53	0.01	15.62	0.02	2.49	4314	344	3666	214	-0.22	0.33
2710	266.40616	-29.012201	14.14	0.90	16.80	0.90	3.37	3622	175	3724	224	0.37	0.26
2716	266.42032	-29.002659	14.15	0.01	16.04	0.01	2.65	3225	175	3592	224	0.95	0.26
2718	266.42523	-29.002253	14.15	0.90	16.14	0.90	2.58	4484	180	3899	224	0.03	0.26
2722	266.40884	-29.010603	14.15	0.90	16.69	0.91	3.34	3945	189	3770	211	-0.12	0.25
2725	266.41580	-28.997906	14.15	0.90	16.30	0.90	3.01	4986	173	4446	424	-0.42	0.29
2732	266.42380	-29.005814	14.15	0.90	16.34	0.90	2.85	3538	225	3677	393	0.27	0.30

Table 3-11 *continued*

Table 3-11 *(continued)*

Id	R.A.	Dec.	K_S	$K_{S,err}$	H	H_{err}	A_{K_S}	$T_{eff,CO}$	$\sigma_{T_{eff,CO}}$	$T_{eff,*}$	$\sigma_{T_{eff,*}}$	[M/H]	$\sigma_{[M/H]}$
	(°)	(°)						(K)	(K)	(K)	(K)		
2759	266.42224	-29.002773	15.34	0.02	17.48	0.03	2.61	3501	175	4024	228	0.49	0.26
2779	266.42624	-29.003439	14.17	0.90	16.86	0.91	2.96	3641	184	3828	239	0.28	0.33
2780	266.42139	-29.001745	15.88	0.02	18.22	0.06	2.85	4097	175	4045	243	0.54	0.27
2788	266.41525	-29.013418	14.18	0.90	16.24	0.90	2.62	4561	175	3581	224	-0.46	0.29
2795	266.41675	-29.011026	14.09	0.01	16.19	0.02	2.53	3964	218	3985	256	0.24	0.27
2802	266.41745	-29.002836	14.34	0.01	16.38	0.02	2.55	3758	221	3468	263	0.41	0.27
2823	266.42349	-29.005426	14.12	0.03	16.11	0.03	2.62	4149	175	3789	224	-0.52	0.26
2824	266.41281	-29.002218	14.19	0.01	16.66	0.01	2.88	3844	175	3474	224	0.02	0.26
2828	266.42188	-29.004633	14.20	0.01	16.35	0.02	2.79	3457	177	3523	224	-0.13	0.27
2837	266.42084	-29.012793	14.20	0.90	16.57	0.91	3.00	4210	175	4035	224	-0.34	0.26
2847	266.42731	-29.003298	14.21	0.90	16.60	0.91	3.15	4391	176	3912	224	0.10	0.26
2852	266.42114	-29.003057	14.21	0.01	16.40	0.01	2.75	3366	201	3816	222	0.66	0.33
2856	266.41986	-29.005211	14.17	0.01	16.50	0.01	2.70	4516	175	4190	224	-0.19	0.26
2880	266.41913	-29.012434	14.22	0.90	16.34	0.90	2.72	3511	179	3999	224	0.42	0.27
2884	266.41608	-29.010653	14.22	0.01	16.76	0.01	2.51	4233	176	4439	224	0.16	0.26
2899	266.42389	-29.007181	14.23	0.90	16.40	0.90	2.84	3367	168	3899	224	-0.01	0.26
2906	266.41611	-29.003536	14.07	0.02	16.10	0.02	2.54	3813	178	3610	224	0.05	0.26
2910	266.42352	-29.001492	14.23	0.01	16.13	0.01	2.78	4169	181	3834	226	0.03	0.28
2974	266.40948	-29.009998	14.26	0.90	16.81	0.90	3.31	4698	185	4184	240	-0.76	0.30
2997	266.41846	-28.999363	14.27	0.90	16.97	0.90	3.34	4363	182	3342	227	0.45	0.29
3021	266.41501	-29.006832	13.76	0.01	16.05	0.02	2.75	3942	326	3866	242	-0.36	0.25
3030	266.42325	-29.001465	14.28	0.01	16.66	0.01	2.78	3276	190	3996	240	0.11	0.28
3041	266.42065	-29.012106	14.29	0.01	16.65	0.01	3.09	3436	175	3902	224	0.00	0.26
3078	266.42221	-29.001997	14.31	0.01	16.41	0.01	2.92	3857	182	4045	239	0.12	0.27
3091	266.42700	-29.003218	14.31	0.90	16.77	0.91	3.14	4586	179	3965	224	-0.46	0.28
3101	266.41760	-29.001745	14.02	0.01	16.47	0.02	2.88	4155	316	3895	212	-0.05	0.25
3108	266.41324	-29.007954	14.18	0.04	17.06	0.05	2.83	3905	182	3644	231	0.87	0.28
3119	266.41156	-29.007223	14.25	0.01	16.29	0.02	2.88	3774	190	4062	224	0.10	0.26
3128	266.41632	-29.001673	14.43	0.02	16.70	0.03	2.69	4226	182	3953	224	-0.30	0.27
3144	266.42236	-29.002993	14.33	0.01	16.24	0.01	2.60	4068	175	3961	224	-0.30	0.26
3181	266.41125	-29.006653	14.34	0.03	16.76	0.05	2.90	3940	183	3787	224	0.31	0.32
3190	266.41748	-28.998602	14.35	0.90	16.30	0.91	2.70	3605	279	3823	243	0.06	0.25
3191	266.41391	-29.009911	15.15	0.02	17.05	0.03	2.59	5466	175	3925	224	-1.06	0.28
3203	266.41751	-29.005054	14.19	0.02	16.23	0.02	2.49	4025	172	3837	317	-0.21	0.37
3239	266.41681	-28.999672	14.37	0.90	16.54	0.90	2.81	4889	181	3662	226	-1.06	0.30
3241	266.42322	-29.010654	14.37	0.01	17.27	0.02	2.58	3469	175	3458	224	0.16	0.26
3290	266.42453	-29.006178	14.39	0.90	16.75	0.90	3.30	4198	192	4063	255	-0.07	0.29
3293	266.42346	-29.007198	14.36	0.01	16.55	0.01	2.61	4148	171	3913	206	0.11	0.28
3325	266.42447	-29.004820	14.41	0.90	16.76	0.91	2.76	3315	184	4104	224	0.92	0.26
3330	266.42273	-29.005919	14.77	0.01	16.77	0.02	2.46	3805	176	3930	229	0.64	0.27

Table 3-11 *continued*

Table 3-11 *(continued)*

Id	R.A.	Dec.	K_S	$K_{S,err}$	H	H_{err}	A_{K_S}	$T_{eff,CO}$	$\sigma_{T_{eff,CO}}$	$T_{eff,*}$	$\sigma_{T_{eff,*}}$	[M/H]	$\sigma_{[M/H]}$
	(°)	(°)						(K)	(K)	(K)	(K)		
3349	266.41473	-29.008512	14.56	0.01	17.12	0.03	2.88	3973	179	3715	224	0.06	0.26
3392	266.41913	-29.005436	14.47	0.03	16.76	0.03	2.79	3782	182	3890	233	0.13	0.29
3399	266.41714	-28.999853	14.44	0.90	16.40	0.90	2.81	5258	177	3658	224	-0.30	0.27
3416	266.42050	-29.000370	14.44	0.90	17.12	0.90	3.27	3867	244	3447	244	0.33	0.34
3430	266.41672	-29.012074	14.34	0.04	16.67	0.05	2.68	3179	182	3940	224	0.18	0.28
3495	266.42081	-29.006136	14.40	0.01	16.34	0.01	2.46	3350	183	3552	224	0.09	0.26
3555	266.41565	-29.014706	14.49	0.91	17.53	0.91	3.04	3285	185	3899	224	0.05	0.26
3584	266.41745	-29.005234	15.15	0.03	17.34	0.04	2.56	5177	201	3559	232	0.26	0.29
3587	266.41806	-29.005356	14.37	0.01	16.54	0.02	2.63	4166	177	4077	224	0.14	0.28
3644	266.41705	-29.003355	14.46	0.01	16.42	0.02	2.44	3951	186	4115	224	-0.48	0.28
3648	266.40964	-29.012684	14.53	0.90	16.59	0.90	2.93	3825	183	3919	224	0.10	0.29
3657	266.40897	-29.011299	14.53	0.90	16.75	0.90	3.15	3993	191	3898	231	-0.10	0.27
3712	266.42444	-29.005718	14.55	0.90	17.80	0.91	3.05	3753	176	3517	261	0.12	0.27
3743	266.41763	-28.999210	14.56	0.90	17.10	0.90	2.72	4515	187	4236	224	-0.32	0.27
3750	266.41284	-29.009504	14.56	0.01	17.05	0.01	2.90	4136	176	3764	224	-0.59	0.28
3753	266.40686	-29.011229	14.57	0.91	17.36	0.91	3.47	3496	175	3628	224	0.67	0.29
3774	266.41815	-29.003092	14.63	0.01	16.94	0.03	2.79	3249	167	3394	209	0.90	0.26
3858	266.41812	-29.015493	14.60	0.90	17.12	0.90	3.12	3991	190	3474	231	0.90	0.28
3917	266.41669	-29.001600	14.62	0.01	16.99	0.01	2.71	4153	184	4242	233	-0.10	0.30
3961	266.41031	-29.013763	14.63	0.91	16.61	0.91	2.85	3634	854	3838	228	-0.03	0.27
4117	266.42221	-29.008068	14.89	0.01	16.90	0.01	2.61	4671	282	4243	228	0.00	0.35
4327	266.41629	-28.998655	14.73	0.90	16.87	0.91	2.87	4796	196	4479	275	-0.24	0.31
4334	266.41605	-29.005186	14.46	0.01	16.62	0.02	2.61	3472	181	4038	224	-0.14	0.27
4397	266.41754	-28.999607	14.76	0.90	16.90	0.90	2.95	4827	253	3697	267	-0.74	0.26
4622	266.42093	-29.004595	14.30	0.01	16.33	0.01	2.49	3847	190	3925	224	0.70	0.27
4694	266.41629	-29.011095	14.65	0.02	16.84	0.02	2.57	3781	185	3981	231	0.97	0.26
4731	266.42380	-29.008951	14.85	0.90	17.08	0.90	2.92	3116	181	3978	224	0.40	0.26
4792	266.42078	-29.003967	15.52	0.02	17.61	0.03	2.56	4289	188	3734	224	0.18	0.27
4983	266.41919	-29.000832	14.91	0.90	17.38	0.91	3.53	4332	195	3789	229	-0.31	0.27
5038	266.42200	-29.006519	14.73	0.01	16.21	0.01	2.37	4386	204	4044	250	-0.53	0.32
5311	266.41653	-29.013405	14.99	0.90	17.05	0.90	2.63	3884	266	3490	215	0.98	0.26
5334	266.42200	-29.002966	14.99	0.01	16.88	0.01	2.59	4258	175	3864	224	0.62	0.26
5488	266.42264	-29.003649	15.03	0.01	17.28	0.01	2.63	3752	192	3753	229	0.44	0.28
5639	266.41345	-29.001505	15.06	0.01	17.41	0.01	2.73	3439	175	3758	224	0.99	0.26
6056	266.42313	-29.002724	15.14	0.01	17.41	0.01	2.83	3428	175	3807	224	0.68	0.26
6385	266.42120	-29.001240	11.69	0.01	13.98	0.01	2.89	2844	175	3298	206	-0.26	0.25
6620	266.41772	-29.003418	15.18	0.01	17.29	0.03	2.59	4449	175	3926	226	0.33	0.26
6668	266.41565	-29.013695	15.23	0.91	17.51	0.91	2.74	3825	425	3771	215	0.84	0.26
6735	266.41388	-29.003359	15.24	0.01	17.55	0.02	2.51	3259	175	3918	224	-0.06	0.26
8187	266.41495	-29.002350	15.41	0.01	17.47	0.03	2.71	3787	178	4195	224	0.85	0.26

Table 3-11 *continued*

CHAPTER 4

Conclusions

The development of high angular resolution technology and methodology in the near-infrared (NIR) has fundamentally transformed our vision and understanding of the center of the Milky Way galaxy. The large telescopes on the ground allow us to resolve individual stars in this extreme environment, producing a wide-range of discoveries to understand the complete picture. The recently improved speckle holography technique has led to the reanalysis of the speckle imaging data of the Galactic center and the capability to detect Sgr A* in early years. The advent of integral field spectroscopy has enabled a large sample of stellar metallicity measurements and revealed a remarkably wide range of metallicity distribution of the stars in the nuclear star cluster (NSC). The studies presented in this dissertation have investigated the long-term NIR accretion properties of the supermassive black hole (SMBH) at the center of the Milky Way, and the star formation history in this vicinity under the extreme environment.

We presented new NIR measurements of Sgr A* as observed from Keck Telescope over a decade in which it was previously inaccessible at these wavelengths. With the application of the speckle holography technique, we are able to monitor Sgr A* with deeper detections covering a time baseline of 7 years, and study its variability addressing timescales ten times longer than published works. Sgr A* was stable from 1998 to 2005 and showed no extraordinary flux excursions during this time. The brightness and its variability is consistent over 22 years by comparing to the extrapolation modeled from the AO-based short timescale studies, indicating that the known 245 minutes still remains the dominant break timescale. Further-

more, the periapse passage of the extended, dusty object G1, experiencing tidal disruption, did not result in any measureable change of the mean accretion rate onto Sgr A*.

We also reconstructed the star formation history of the Milky Way's NSC with the first metallicity constraints from a large sample of stellar metallicity measurements. Along with photometry and spectroscopically derived temperature, we developed a Bayesian inference approach in the analysis. We find that the NSC population strongly favors a a two-component model. The dominant component ($\sim$ 93% of the mass) is metal-rich ($\overline{[M/H]} \sim 0.45$), with an age of 5^{+3}_{-2} Gyr. The most likely age for the NSC main population is $\sim$3 Gyr younger than that obtained if one assumes solar metallicity as has been done in earlier studies. The reported younger age would challenge the mutual evolution scenario of the NSC, the central SMBH and the inner bulge; and also challenge the globular cluster in-falling scenario as the dominant formation mechanisms. The minor component ($\sim$ 7% of the mass) is metal-poor ($\overline{[M/H]} \sim$ -1.10) with an uncertain age. Our metallicity-dependent models are able to, for the first time, account for low-temperature red giants that were previously difficult to fit. When metallicity constraints are included, we predict 2 - 4 times fewer neutron stars compared to earlier predictions assuming solar metallicity. This may introduce a new path to understand the so-called "missing pulsar problem" at the Galactic center.

Bibliography

Abbott, B. P., Abbott, R., Abbott, T. D., et al. 2016, Physical Review X, 6, 041015

Abbott, B. P., Abbott, R., Abbott, T. D., et al. 2016, PRL, 116, 061102

Abbott, B. P., Abbott, R., Abbott, T. D., et al. 2016, PRD, 93, 122003

Abbott, B. P., Abbott, R., Abbott, T. D., et al. 2017, PRL, 119, 141101

Abbott, B. P., Abbott, R., Abbott, T. D., et al. 2017, ApJL, 851, L35

Alexander, R. D., Begelman, M. C., & Armitage, P. J. 2007, ApJ, 654, 907

Alexander, T. & Hopman, C. 2009, ApJ, 697, 1861

Allen, D. A., Hyland, A. R., & Hillier, D. J. 1990, MNRAS, 244, 706

Andersen, D. R., Walcher, C. J., Böker, T., et al. 2008, ApJ, 688, 990. doi:10.1086/592342

Antonini, F., Faber, J., Gualandris, A., et al. 2010, ApJ, 713, 90

Antonini, F. & Perets, H. B. 2012, ApJ, 757, 27

Antonini, F. 2013, ApJ, 763, 62. doi:10.1088/0004-637X/763/1/62

Antonini, F., Murray, N., & Mikkola, S. 2014, ApJ, 781, 45

Arca Sedda, M., Gualandris, A., Do, T., et al. 2020, ApJL, 901, L29. doi:10.3847/2041-8213/abb245

Baganoff, F. K., Maeda, Y., Morris, M., et al. 2003, ApJ, 591, 891. doi:10.1086/375145

Balick, B. & Brown, R. L. 1974, ApJ, 194, 265. doi:10.1086/153242

Bartko, H., Martins, F., Fritz, T. K., et al. 2009, ApJ, 697, 1741

Bartko, H., Martins, F., Trippe, S., et al. 2010, ApJ, 708, 834

Bartos, I., Kocsis, B., Haiman, Z., et al. 2017, ApJ, 835, 165

Bastian, N., Covey, K. R., & Meyer, M. R. 2010, ARA&A, 48, 339

Bates, S. D., Johnston, S., Lorimer, D. R., et al. 2011, MNRAS, 411, 1575. doi:10.1111/j.1365-2966.2010.17790.x

Baumgardt, H., Makino, J., & Ebisuzaki, T. 2004, ApJ, 613, 1143

Becklin, E. E. & Neugebauer, G. 1968, ApJ, 151, 145

Bensby, T., Yee, J. C., Feltzing, S., et al. 2013, A&A, 549, A147. doi:10.1051/0004-6361/201220678

Blum, R. D., Ramírez, S. V., Sellgren, K., et al. 2003, ApJ, 597, 323

Boehle, A., Ghez, A. M., Schödel, R., et al. 2016, ApJ, 830, 17

Bohlin, R. C., Mészáros, S., Fleming, S. W., et al. 2017, AJ, 153, 234

Bower, G. C., Markoff, S., Dexter, J., et al. 2015, ApJ, 802, 69. doi:10.1088/0004-637X/802/1/69

Buchner, J., Georgakakis, A., Nandra, K., et al. 2014, A&A, 564, A125

ArXiv Astrophysics e-prints, astro-ph/0405087

Chatzopoulos, S., Fritz, T. K., Gerhard, O., et al. 2015, MNRAS, 447, 948. doi:10.1093/mnras/stu2452

Chen, Z., Gallego-Cano, E., Do, T., et al. 2019, ApJL, 882, L28

Choi, J., Dotter, A., Conroy, C., et al. 2016, ApJ, 823, 102

Do, T., Ghez, A. M., Morris, M. R., et al. 2009, ApJ, 703, 1323

Do, T., Lu, J. R., Ghez, A. M., et al. 2013, ApJ, 764, 154

Do, T., Kerzendorf, W., Winsor, N., et al. 2015, ApJ, 809, 143

Do, T., Hees, A., Ghez, A., et al. 2019, Science, 365, 664. doi:10.1126/science.aav8137

Do, T., Witzel, G., Gautam, A. K., et al. 2019, ApJL, 882, L27. doi:10.3847/2041-8213/ab38c3

Do, T., David Martinez, G., Kerzendorf, W., et al. 2020, ApJL, 901, L28. doi:10.3847/2041-8213/abb246

Dodds-Eden, K., Porquet, D., Trap, G., et al. 2009, ApJ, 698, 676. doi:10.1088/0004-637X/698/1/676

Dodds-Eden, K., Gillessen, S., Fritz, T. K., et al. 2011, ApJ, 728, 37. doi:10.1088/0004-637X/728/1/37

Dorn-Wallenstein, T. Z. & Levesque, E. M. 2018, ApJ, 867, 125

Dotter, A. 2016, ApJS, 222, 8

Eckart, A., Genzel, R., Hofmann, R., et al. 1995, ApJL, 445, L23

Eckart, A., & Genzel, R. 1996, Nature, 383, 415

Eckart, A. & Genzel, R. 1997, MNRAS, 284, 576

Eckart, A., Baganoff, F. K., Zamaninasab, M., et al. 2008, A&A, 479, 625. doi:10.1051/0004-6361:20078793

Eisenhauer, F., Genzel, R., Alexander, T., et al. 2005, ApJ, 628, 246

Falcke, H., Wilson, A. S., & Simpson, C. 1998, ApJ, 502, 199. doi:10.1086/305886

Fan, X., Strauss, M. A., Schneider, D. P., et al. 2001, AJ, 121, 54. doi:10.1086/318033

Feldmeier, A., Neumayer, N., Seth, A., et al. 2014, A&A, 570, A2. doi:10.1051/0004-6361/201423777

Feldmeier-Krause, A., Neumayer, N., Schödel, R., et al. 2015, A&A, 584, A2

Feldmeier-Krause, A., Kerzendorf, W., Neumayer, N., et al. 2017, MNRAS, 464, 194

Feldmeier-Krause, A., Kerzendorf, W., Do, T., et al. 2020, MNRAS, 494, 396

Feltzing, S. & Chiba, M. 2013, NAR, 57, 80. doi:10.1016/j.newar.2013.06.001

Feroz, F. & Hobson, M. P. 2008, MNRAS, 384, 449

Feroz, F., Hobson, M. P., & Bridges, M. 2009, MNRAS, 398, 1601

Ferrarese, L., Côté, P., Dalla Bontà, E., et al. 2006, ApJL, 644, L21. doi:10.1086/505388

Figer, D. F., Rich, R. M., Kim, S. S., et al. 2004, ApJ, 601, 319

Forrest, W. J., Shure, M. A., Pipher, J. L., et al. 1987, The Galactic Center, 155, 153

Frogel, J. A., Stephens, A., Ramírez, S., et al. 2001, AJ, 122, 1896. doi:10.1086/323079

Genzel, R., Pichon, C., Eckart, A., et al. 2000, MNRAS, 317, 348

Genzel, R., Schödel, R., Ott, T., et al. 2003, Nature, 425, 934

Genzel, R., Eisenhauer, F., & Gillessen, S. 2010, Reviews of Modern Physics, 82, 3121. doi:10.1103/RevModPhys.82.3121

Georgiev, I. Y., Böker, T., Leigh, N., et al. 2016, MNRAS, 457, 2122. doi:10.1093/mnras/stw093

Ghez, A. M., Klein, B. L., Morris, M., & Becklin, E. E. 1998, ApJ, 509, 678

Ghez, A. M., Morris, M., Becklin, E. E., Tanner, A., & Kremenek, T. 2000, Nature, 407, 349

Ghez, A. M., Duchêne, G., Matthews, K., et al. 2003, ApJL, 586, L127. doi:10.1086/374804

Ghez, A. M., Wright, S. A., Matthews, K., et al. 2004, ApJL, 601, L159

Ghez, A. M., Salim, S., Hornstein, S. D., et al. 2005a, ApJ, 620, 744

Ghez, A. M., Hornstein, S. D., Lu, J. R., et al. 2005b, ApJ, 635, 1087

Ghez, A. M., Salim, S., Weinberg, N. N., et al. 2008, ApJ, 689, 1044. doi:10.1086/592738

Gillessen, S., Eisenhauer, F., Trippe, S., et al. 2009, ApJ, 692, 1075. doi:10.1088/0004-637X/692/2/1075

Gillessen, S., Genzel, R., Fritz, T. K., et al. 2012, Nature, 481, 51

Gillessen, S., Plewa, P. M., Eisenhauer, F., et al. 2017, ApJ, 837, 30. doi:10.3847/1538-4357/aa5c41

Graham, A. W. & Spitler, L. R. 2009, MNRAS, 397, 2148. doi:10.1111/j.1365-2966.2009.15118.x

Gravity Collaboration, Abuter, R., Amorim, A., et al. 2018, A&A, 618, L10. doi:10.1051/0004-6361/201834294

Gravity Collaboration, Abuter, R., Amorim, A., et al. 2019, A&A, 625, L10. doi:10.1051/0004-6361/201935656

Gustafsson, B., Edvardsson, B., Eriksson, K., et al. 2008, A&A, 486, 951. doi:10.1051/0004-6361:200809724

Hailey, C. J., Mori, K., Bauer, F. E., et al. 2018, Nature, 556, 70

Hanson, M. M., Conti, P. S., & Rieke, M. J. 1996, ApJS, 107, 281

Harris, W. E. 2010, arXiv:1012.3224

Heger, A., Fryer, C. L., Woosley, S. E., et al. 2003, ApJ, 591, 288

Hoang, B.-M., Naoz, S., Kocsis, B., et al. 2018, ApJ, 856, 140

Hora, J. L., Witzel, G., Ashby, M. L. N., et al. 2014, ApJ, 793, 120

Hornstein, S. D., Ghez, A. M., Tanner, A., et al. 2002, ApJL, 577, L9

Mauerhan, J. C., Morris, M., Walter, F., et al. 2005, ApJL, 623, L25. doi:10.1086/429960

Melia, F. & Falcke, H. 2001, ARA&A, 39, 309. doi:10.1146/annurev.astro.39.1.309

Meyer, L., Do, T., Ghez, A., et al. 2009, ApJL, 694, L87

Mori, K., Hailey, C. J., Schutt, T. Y. E., et al. 2021, ApJ, 921, 148. doi:10.3847/1538-4357/ac1da5

Hosek, M. W., Lu, J. R., Anderson, J., et al. 2019, ApJ, 870, 44

STSci poster

Hosek, M. W., Lu, J. R., Lam, C. Y., et al. 2020, arXiv:2006.06691

Husser, T.-O., Wende-von Berg, S., Dreizler, S., et al. 2013, A&A, 553, A6 161

Johnston, S., Walker, M. A., van Kerkwijk, M. H., et al. 1995, MNRAS, 274, L43. doi:10.1093/mnras/274.1.L43

Kalirai, J. S., Hansen, B. M. S., Kelson, D. D., et al. 2008, ApJ, 676, 594

Kent, S. M. 1992, ApJ, 387, 181

Kerzendorf, W. & Do, T. 2015, Zenodo

Kocsis, B. & Levin, J. 2012, PRD, 85, 123005

Kozai, Y. 1962, AJ, 67, 591

Krabbe, A., Genzel, R., Drapatz, S., et al. 1991, ApJL, 382, L19

Krauss, L. M. & Chaboyer, B. 2003, Science, 299, 65. doi:10.1126/science.1075631

Kroupa, P. 2002, Science, 295, 82. doi:10.1126/science.1067524

Larkin, J., Barczys, M., Krabbe, A., et al. 2006, Proc.SPIE, 6269, 62691A

Launhardt, R., Zylka, R., & Mezger, P. G. 2002, A&A, 384, 112

Abbott, B. P., Abbott, R., Abbott, T. D., et al. 2016, PRL, 116, 241103

Abbott, B. P., Abbott, R., Abbott, T. D., et al. 2016, PRL, 116, 061102

Abbott, B. P., Abbott, R., Abbott, T. D., et al. 2017, PRL, 118, 221101

Lidov, M. L. 1962, Planet. Space Sci., 9, 719

Löckmann, U., Baumgardt, H., & Kroupa, P. 2010, MNRAS, 402, 519

Lu, J. R., Ghez, A. M., Hornstein, S. D., Morris, M., & Becklin, E. E. 2005, ApJL, 625, L51

Lu, J. R., Ghez, A. M., Hornstein, S. D., et al. 2009, ApJ, 690, 1463

Lu, J. R., Do, T., Ghez, A. M., et al. 2013, ApJ, 764, 155

Maness, H., Martins, F., Trippe, S., et al. 2007, ApJ, 669, 1024

Martins, F., Genzel, R., Hillier, D. J., et al. 2007, A&A, 468, 233

McKee, C. F. & Ostriker, E. C. 2007, ARA&A, 45, 565

Merritt, D. 2013, Dynamics and Evolution of Galactic Nuclei (Princeton, NJ: Princeton Univ. Press)

Milosavljević, M. 2004, ApJL, 605, L13. doi:10.1086/420696

Morris, M. 1993, ApJ, 408, 496

Nayakshin, S. & Sunyaev, R. 2005, MNRAS, 364, L23

Neumayer, N. & Walcher, C. J. 2012, Advances in Astronomy, 2012, 709038. doi:10.1155/2012/709038

Nogueras-Lara, F., Schödel, R., Gallego-Calvente, A. T., et al. 2019, A&A, 631, A20

O'Leary, R. M., Rasio, F. A., Fregeau, J. M., et al. 2006, ApJ, 637, 937

O'Leary, R. M., Kocsis, B., & Loeb, A. 2009, MNRAS, 395, 2127

O'Leary, R. M., Meiron, Y., & Kocsis, B. 2016, ApJL, 824, L12

Paumard, T., Genzel, R., Martins, F., et al. 2006, ApJ, 643, 1011

Petrovich, C. & Antonini, F. 2017, ApJ, 846, 146

Pflamm-Altenburg, J. & Kroupa, P. 2006, MNRAS, 373, 295

Pfuhl, O., Fritz, T. K., Zilka, M., et al. 2011, ApJ, 741, 108

Pfuhl, O., Gillessen, S., Eisenhauer, F., et al. 2015, ApJ, 798, 111

Ponti, G., George, E., Scaringi, S., et al. 2017, MNRAS, 468, 2447. doi:10.1093/mnras/stx596

Portegies Zwart, S. F. & McMillan, S. L. W. 2000, ApJL, 528, L17

Press, W. H. 1978, Comments on Astrophysics, 7, 103

Primot, J., Rousset, G., & Fontanella, J. C. 1990, Journal of the Optical Society of America A, 7, 1598

Rafelski, M., Ghez, A. M., Hornstein, S. D., Lu, J. R., & Morris, M. 2007, ApJ, 659, 1241

Raithel, C. A., Sukhbold, T., & Özel, F. 2018, ApJ, 856, 35

Rayner, J. T., Cushing, M. C., & Vacca, W. D. 2009, ApJS, 185, 289

Rich, R. M., Ryde, N., Thorsbro, B., et al. 2017, AJ, 154, 239

Rodriguez, C. L., Morscher, M., Wang, L., et al. 2016, MNRAS, 463, 2109

Ryde, N. & Schultheis, M. 2015, A&A, 573, A14

Ryde, N., Fritz, T. K., Rich, R. M., et al. 2016, ApJ, 831, 40

Salpeter, E. E. 1955, ApJ, 121, 161. doi:10.1086/145971

Schödel, R., Ott, T., Genzel, R., et al. 2002, Nature, 419, 694

Schödel, R., Ott, T., Genzel, R., et al. 2003, ApJ, 596, 1015. doi:10.1086/378122

Schödel, R., Merritt, D., & Eckart, A. 2009, A&A, 502, 91. doi:10.1051/0004-6361/200810922

Schödel, R., Najarro, F., Muzic, K., et al. 2010, A&A, 511, A18

Schödel, R., Yelda, S., Ghez, A., et al. 2013, MNRAS, 429, 1367

Schödel, R., Feldmeier, A., Kunneriath, D., et al. 2014, A&A, 566, A47

Schödel, R., Nogueras-Lara, F., Gallego-Cano, E., et al. 2020, A&A, 641, A102. doi:10.1051/0004-6361/201936688

Sitarski, B., Do, T., Witzel, G., et al. 2014, American Astronomical Society Meeting Abstracts #223, 223, 238.05

Skilling, J. 2004, American Institute of Physics Conference Series, 735, 395

Spera, M., Mapelli, M., & Bressan, A. 2015, MNRAS, 451, 4086. doi:10.1093/mnras/stv1161

Stone, N. C., Metzger, B. D., & Haiman, Z. 2017, MNRAS, 464, 946

Støstad, M., Do, T., Murray, N., et al. 2015, ApJ, 808, 106

Sukhbold, T., Ertl, T., Woosley, S. E., et al. 2016, ApJ, 821, 38

Sukhbold, T., Woosley, S. E., & Heger, A. 2018, ApJ, 860, 93

Torne, P., Desvignes, G., Eatough, R. P., et al. 2021, A&A, 650, A95. doi:10.1051/0004-6361/202140775

Tremaine, S. D., Ostriker, J. P., & Spitzer, L. 1975, ApJ, 196, 407. doi:10.1086/153422

Trevisan, M., Barbuy, B., Eriksson, K., et al. 2011, A&A, 535, A42. doi:10.1051/0004-6361/201016056

Valencia-S., M., Eckart, A., Zajaček, M., et al. 2015, ApJ, 800, 125

Volonteri, M. 2010, A&ARv, 18, 279. doi:10.1007/s00159-010-0029-x

Wen, L. 2003, ApJ, 598, 419

Witzel, G., Ghez, A. M., Morris, M. R., et al. 2014, ApJL, 796, L8

Witzel, G., Sitarski, B. N., Ghez, A. M., et al. 2017, ApJ, 847, 80

Witzel, G., Martinez, G., Hora, J., et al. 2018, ApJ, 863, 15

Yelda, S. 2012, Ph.D. Thesis

Yusef-Zadeh, F., Bushouse, H., Dowell, C. D., et al. 2006, ApJ, 644, 198. doi:10.1086/503287

Yusef-Zadeh, F., Wardle, M., Dodds-Eden, K., et al. 2012, AJ, 144, 1. doi:10.1088/0004-6256/144/1/1

Zoccali, M., Renzini, A., Ortolani, S., et al. 2003, A&A, 399, 931. doi:10.1051/0004-6361:20021604